2020

Accretion variability in young, low-mass stellar systems

BOSTON UNIVERSITY

GRADUATE SCHOOL OF ARTS AND SCIENCES

Dissertation

ACCRETION VARIABILITY IN YOUNG, LOW-MASS STELLAR SYSTEMS

by

CONNOR EDWARD ROBINSON

B.A., University of Montana, 2014
M.A., Boston University, 2016

Submitted in partial fulfillment of the

requirements for the degree of

Doctor of Philosophy

2020

Approved by

First Reader

Catherine C. Espaillat, PhD
Associate Professor of Astronomy

Second Reader

Philip S. Muirhead, PhD
Assistant Professor of Astronomy

Acknowledgments

First and foremost, I thank my wife, Emma, and my family who have supported me during every step of this journey. Without their support, this would not have been possible.

Next, I would like to thank the advisors and professors who have guided me along my path in the academy. In particular, I thank my graduate academic advisor and mentor Catherine Espaillat; the co-advisor for my first paper, Dr. James Owen; my undergraduate advisor, Professor Nate McCrady; the second-reader of this dissertation, Professor Philip Muirhead; and Professor Nuria Calvet.

I have enjoyed and appreciated the support and close friendships of the graduate students and postdocs at Boston University. In particular, I would like to thank the members of my research group with whom I commiserated and triumphed. In particular, I thank both of our excellent postdocs Álvaro Ribas and Enrique Macías who have been both good friends and excellent mentors. I thank Dan Feldman, who guided me as a young graduate student. I thank Sierra Grant, who has been there through it all and is an excellent source of fierce, friendly banter that has made graduate school miles more enjoyable.

Outside of my research group, I thank my graduate cohort for the constant support and camaraderie that we developed very early in graduate school. In particular, I thank Eunkyu Han, who graciously put up with my many questions.

ACCRETION VARIABILITY IN YOUNG, LOW-MASS STELLAR SYSTEMS

CONNOR EDWARD ROBINSON

Boston University, Graduate School of Arts and Sciences, 2020

Major Professor: Catherine C. Espaillat, Associate Professor of Astronomy.

ABSTRACT

Through the study of accretion onto the young, low-mass stars known as T Tauri Stars (TTS), we can better understand the formation of our solar system. Gas is funneled along stellar magnetic field lines into magnetospheric accretion columns where it reaches free-fall velocities and shocks at the stellar surface, generating emission that carries information about the inner regions of the protoplanetary disk. Accretion is a variable process, with characteristic timescales ranging from minutes to years. In this dissertation, I use simulations, models, and observations to provide insight into the driving forces of mass accretion rate variability on timescales of minutes to weeks and the structure of the inner disk.

Using hydrodynamic simulations, I find that steady-state, transonic accretion occurs naturally in the absence of any other source of variability. If the density in the inner disk varies smoothly in time with roughly day-long time-scales (e.g., due to turbulence), traveling shocks develop within the accretion column, which lead to rapid increases in the accretion luminosity followed by slower declines.

I present the largest *Hubble Space Telescope* (*HST*) spectral variability study of TTS to date. I infer mass accretion rates and accretion column surface coverage using newly updated accretion shock models. I find typical changes in the mass

accretion rate of roughly 10% and moderate changes in the surface coverage on week timescales. Individual peculiar epochs and objects are further discussed. I find that the inner disk is inhomogeneous and that dust may survive near the magnetic truncation radius.

Next, I link two-minute cadence light curves from the Transiting Exoplanet Survey Satellite (*TESS*) to accretion using ground-based U-band photometry. Additional *HST* observations for one target enable more detailed connections between *TESS* light curves and accretion. I also use the *TESS* light curves to identify rotation periods and patterns of quasi-periodicity.

Finally, I connect hydrodynamic simulations, accretion shock models, and stellar rotation to predict signatures of a turbulent inner disk. I generate light curves from these models to make comparisons to previous month-long photometric monitoring surveys of TTS using metrics of light curve symmetry and periodicity.

Contents

List of Tables

List of Figures

List of Abbreviations

Abbreviation	Full Name
1D	One Dimensional
3D	Three Dimensional
2MASS	2 Micron All-Sky Survey
Å	Angstrom
ACF	Autocorrelation Function
ALMA	Atacama Large Millimeter Array
APD	Aperiodic Dipper
au	Astronomical Unit
B	Burster
CCD	Charge-coupled Device
cm	centimeter
CoRoT	Convection, Rotation and planetary Transits (ESA mission)
COS	Cosmic Origins Spectrograph (HST instrument)
CTTS	Classical T Tauri Star
CWT	Continous Wavelet Transform
d	day
DSHARP	Disk Substructures at High Angular Resolution Project
EB	Eclipsing Binary
FFI	Full-Frame Images
FIR	Far Infrared
g	Gram

FUV	Far Ultraviolet
GO	General Observer
GP	Gaussian Process
HBC	Herbig & Bell, Catalog
HD	Hydrodynamic
HST	*Hubble Space Telescope*
IR	Infrared
K	Kelvin
kG	Kilogauss
L	Long Timescale
LDT	Lowell Discovery Telescope
MAMA	Multi-Anode Micro-channel Array
MCMC	Markov Chain Monte Carlo
MESA	Modules for Experiments in Stellar Astrophysics
MIST	MESA Isochrones and Stellar Tracks
MHD	Magnetohydrodynamic
mjd	Modified Julian Day
MP	Multiperiodic
MRI	Magnetohydrodynmaic Instability
N	Non-variable
NGC	New General Catalog
NIR	Near Infrared
nLTE	non-local thermodynamic equilibrium
NUV	Near Ultraviolet
P	Purely Periodic Symmetric
PI	Principal Investigator

PyRAF	Python Image Reduction and Analysis Facility
QPD	Quasi-periodic Dipper
QPS	Quasi-periodic Symmetric
RECX	ROSAT Eta Cha X-ray
s	Second
S	Purely Stochastic
SZ	Southern Zwicky
ROSAT	Roentgen Satellite
SED	Spectral Energy Distribution
SPOC	Science Processing Operations Center
STIS	Space Telescope Imaging Spectrograph
STSDAS	Space Telescope Science Data Analysis System
STScI	Space Telescope Science Institute
TDB	Temps Dynamique Barycentrique (Barycentric Dynamical Time)
TESS	*Transiting Exoplanet Survey Satellite*
TTS	T Tauri Star
TWA	TW Hya Association
U	Unclassifiable
ULLYSES	Ultraviolet Legacy Library of Young Stars as Essential Standards
UV	Ultraviolet
WTTS	Weak-lined T Tauri Star
yr	Year
YSO	Young Stellar Object

1

Introduction

The first theory that resembled our current understanding of the process of the formation of our solar system was the nebular hypothesis proposed by Emanuel Swedenborg in 1734 in the volume "Principia Rerum Naturalium" (Swedenborg, 1734), the first of three folios in his "Opera Philosophica et Mineralia". The idea of the nebular hypothesis, which describes the solar system forming from a primordial cloud which eventually flattens into a disk and forms the planets from the residual material, was expanded upon by the German philosopher Immanuel Kant in 1755 in "Allgemeine Naturgeschichte und Theorie des Himmels" (Kant, 1755). Roughly 40 years after the publication of that work, the French mathematician Pierre-Simon Laplace, formulated his similar vision of origins of the solar system in his 1796 five-volume "Traité de Mécanique Céleste" (Laplace, 1798), where he posited that the circular nature of the orbits was a consequence of their in situ formation history. One of the issues to solve with Laplace's model was the distribution of angular momentum and mass within the disk. Over 99% of the mass of the solar system resides in the sun but only 1% of the angular momentum (the remainder is in the orbits of the surrounding planets). Both are difficult to reconcile under his model, so the model fell out of favor for many years.

Other models rose to explain the origins of the solar system. Solar activity was proposed as a way of powering large prominences that condense into protoplanets (Chamberlin, 1901; Moulton, 1905). Alternative models included tidal interactions

with nearby massive stars (Jeans, 1917). Lyttleton (1961) suggested the accretion of material from the passage of the sun through a dense cloud could lead to the formation of the solar system. Capture models were re-visited by Woolfson (1964) who considered the interaction between a large protostar and the young sun. A modern form of the nebular hypothesis was presented by Prentice (1978), who introduced supersonic turbulence, which would explain some of the outflows associated with young, low-mass stars and solve some of issues associated with the original Laplacian model.

1.1 Observational Evidence for Protoplanetary Disks

The first connection of the variable stars known as T Tauri Stars (TTS) (identified by Joy, 1945) to pre-main-sequence stars came from the work of Ambartsumian (1947, 1949, 1952, 1954) and Parenago (1950). This connection was solidified and more widely recognized following the work of Herbig (1962). Early observational support for protoplanetary disks around TTS came in the form of excess infrared (IR) emission above what one would expect to observe for a bare photosphere. The connection of this excess IR emission to a disk structure was first identified as one of several possibilities by Rucinski (1985). Early *Hubble Space Telescope* images of the Orion star-forming region revealed new support for the hypothesis of the formation of the solar system through protoplanetary disks (O'dell et al., 1993; Bally et al., 1998). These observations found dark, dusty, concentric regions around the central young stars, silhouetted against the bright background of the surrounding H_2 region (see Fig. 1.1). The oblong shape of the dark regions match the morphology of an inclined circumstellar disk.

Observational classifications based on observed IR excesses for young stellar objects (YSOs) were developed by Lada (1987). That work, along with Andre et al. (1993) and Greene et al. (1994), split YSOs into five categories based on α, the

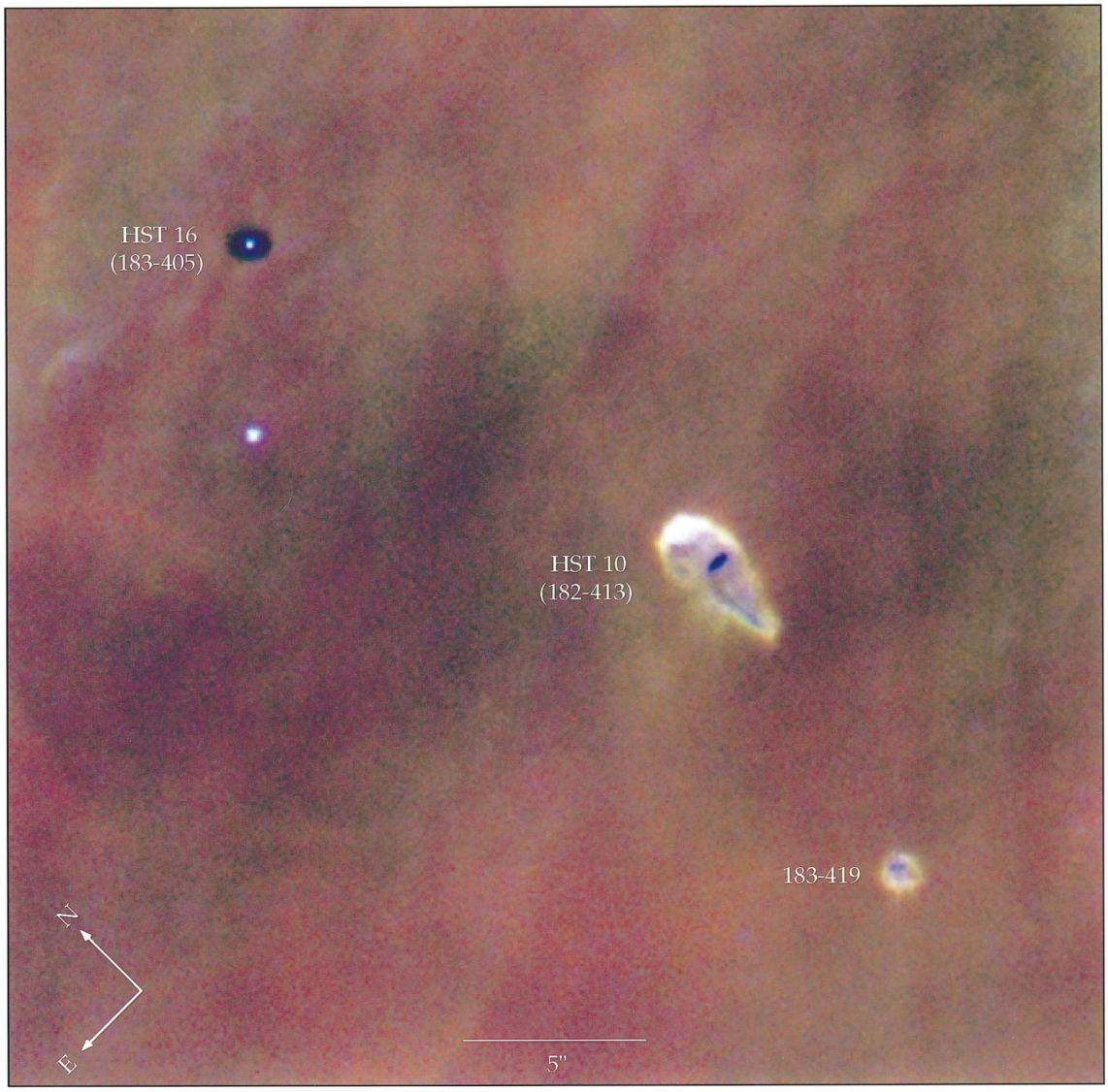

Fig. 1.1: Three-color, narrow-band, Wide Field Planetary Camera 2 *HST* image of several dark "proplyds", or protoplanetary disks, silhouetted against the bright background of the Orion star-forming region. $[N_{II}]$ is in red, H_α is in green, and $[O_I]$ is in blue. Adapted from Bally et al. (1998) with permission.

power-law slope of the spectral energy distribution (SED) in the near-infrared (NIR, 2.2 μm) to the mid-infrared (MIR, 20 μm). These empirical classifications of young stars are central to our current understanding of low-mass star formation after the initial collapse and fragmentation of the primordial molecular cloud. Fig. 1.2 shows several schematics of the different young-stellar object classes as evolution progresses.

Organized by rough evolutionary sequence/age, these classifications are described as follows. Class 0 objects are young protostars that are deeply embedded. These objects are best observed at wavelengths longer than MIR, since light at shorter wavelengths typically cannot permeate their dense envelopes. Class I objects are protostars still embedded in their protostellar envelopes, with SEDs that peak in the MIR to the far-infrared (FIR). "Flat-spectrum objects", as their name implies, have nearly flat SEDs between $2.2\mu m$ and $10\mu m$ are an intermediate stage of evolution proceeding Class I and are likely protostars with the least amount of dust-obscuration (Doppmann et al., 2005).

Class II objects are objects with SEDs that peak in the optical/NIR but still show significant excess above a typical stellar photosphere in the IR and radio wavelengths, which is evidence of a dusty accretion disk and clearing of the natal envelope. The SEDs of Class II objects are subdivided to make inferences about substructures within the disk. Disks with large (several au) inner cavities are known as "transitional disks" (e.g., Strom et al., 1989; Skrutskie et al., 1990; Stassun et al., 2001; Espaillat et al., 2014), and typically have SEDS with weaker NIR excess but still moderate to strong FIR excess. Protoplanetary disks with rings are known as "pretransitional disks" (Espaillat et al., 2007) and generally show strong NIR emission, weaker MIR emission, and stronger FIR emission. Disks without gaps and cavities show excess emission above the photosphere at all IR wavelengths. Class III objects do not show excess above photospheric emission at these wavelengths, and largely

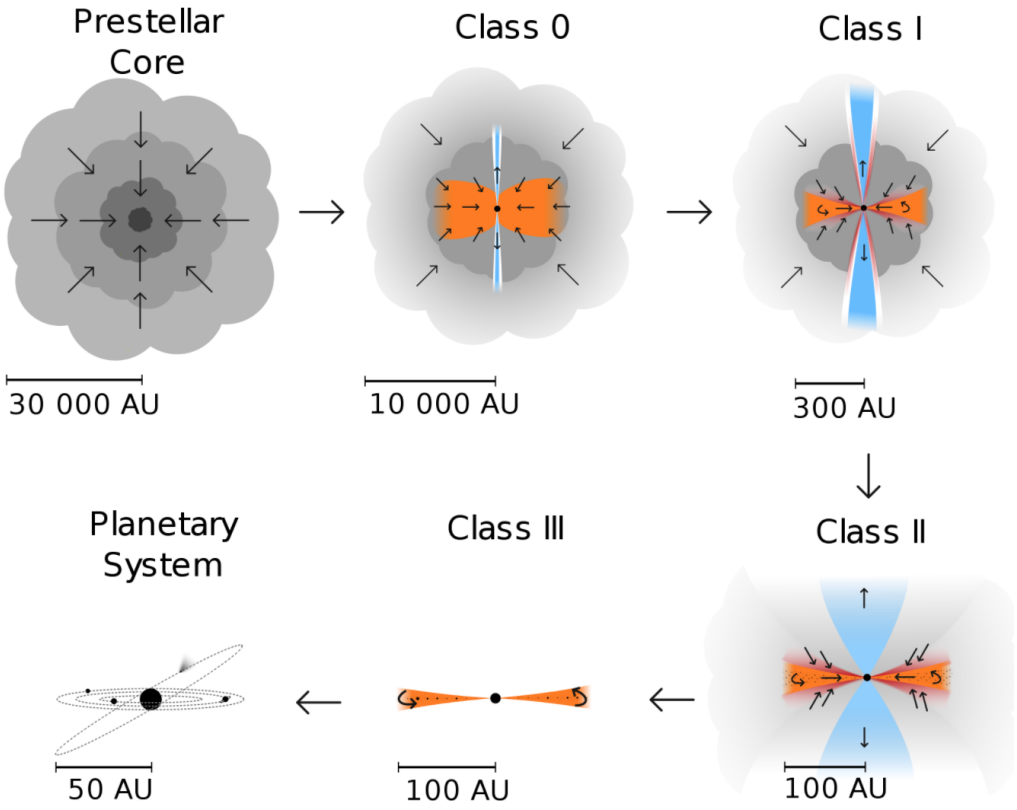

Fig. 1.2: Overview of the evolutionary sequence of young stellar objects. Grey regions show the protostellar envelope. Orange sections display the protoplanetary disk. Finally, blue areas mark winds and jets. Arrows within individual schematics mark the large-scale motion of gas and dust. The prestellar core collapses under self-gravity to form a protostar. Class 0 objects are the most deeply embedded protostars, with the surrounding envelopes that are just starting to fall onto the accretion disk. During Class I, the cloud continues to fall onto the newly formed protoplanetary disk and outflows may begin to emerge. By Class II, the envelope has nearly dispersed, leaving behind an optically thick protoplanetary disk and a directly visible young star. This stage is the primary focus of this dissertation. As the protoplanetary disk evolves and disperses, Class III objects display minimal IR excess. Ultimately, the process ends with a planetary system like our own. As a general trend, the radiation from younger stellar objects tends to peak at redder wavelengths. Note that flat-spectrum objects exist as an intermediate class between Class I and Class II. This figure is adapted from Persson (2014) and is licensed under CC BY 4.0.

resemble main-sequence stars with some exceptions (see Manara et al., 2017, for an optical spectral library of WTTS).

1.2 The Importance of Accretion in Protoplanetary Disks

With the mounting evidence for protoplanetary disks around young stars, a solution to the problem of the distribution of mass and angular momentum in the nebular hypothesis needed to be developed. One part of this solution is viscous accretion, which serves to redistribute mass and angular momentum. Solving the classical equations of mass and angular momentum conservation for a flat, circular and geometrically thin disk with some degree of viscosity reveals that mass spreads towards the star while angular momentum is transported to the outer regions of the disk (see Armitage, 2019, for a review). Molecular viscosity alone is thought to be too weak to evolve protoplanetary disks sufficiently over the current estimates of the ages of protoplanetary disks. Turbulence, as proposed by Shakura & Sunyaev (1973) in their paper regarding black hole accretion disks, may drive angular momentum transport. The Shakura-Sunyaev α prescription describes such a disk, where α is a parameterization of viscosity from turbulence in the disk. α modifies the effective viscosity $\nu = \alpha c_s h$, where c_s is the local sound speed, and h is the local scale height of the disk. If α is constant across the disk, then predictive models can be developed to simulate the structure and estimate the mass of the disk if $\dot{M}$ is known. This makes accurate measurements of the behavior of $\dot{M}$ necessary for unveiling the structure of protoplanetary disks, and thus the formation history of stars and planets.

Accretion also produces the majority of the high-energy radiation field that permeates protoplanetary disks. The FUV field, Lyman-α emission in particular, has a strong influence on disk chemistry because it regulates the chemical abundances of many of the common molecules in protoplanetary disks (e.g., Fogel et al., 2011)

and is an important source of ionization within the disk. Stellar FUV emission may also power photoevaporation that limits the lifetime of the disk (Gorti & Hollenbach, 2009; Gorti et al., 2009). Finally, recent models suggest that accretion may also be a source of cosmic rays that ionize the disk and drive chemistry (Padovani et al., 2016; Gaches & Offner, 2018; Offner et al., 2019).

A low level of ionization in the disk has consequences for turbulence and thus mass and angular momentum transport in the form of the magnetorotational instability (MRI, Balbus & Hawley, 1991; Gammie, 1996). Consider a vertical magnetic field threading the disk. If the ionization fraction is high enough, the material in the disk will be tethered to the magnetic field line. If a slight perturbation is introduced, the two patches of the disk that are connected via the magnetic field line will be at slightly different radii. As time progresses, the patch closer to the star revolves slightly faster around the central star than the more distant patch due to Keplerian motion. This shear increases the magnetic tension between the two patches, causing a torque that transfers angular momentum from the inner patch to the outer patch. As the inner patch loses angular momentum, it falls further towards the star while the outer patch drifts outward. This further increases their radial displacement, leading to an instability that drives turbulence in the disk. As noted before, this turbulence acts as a source of viscosity and can contribute to the large inferred values of α in protoplanetary disks. This instability is thought to occur in the upper layers of the disk, avoiding the "dead-zone" of non-ionized material in the midplane due to shadowing (Gammie, 1996).

1.3 Overview of Disk Structure

The continuum emission at IR and millimeter wavelengths in TTS with disks is dominated by dust emission, despite the typically assumed value of the dust-to-gas

mass ratio being on the order of 1%. Characteristic radii of the dust emission from mm studies range from a few to several hundred au (e.g., Andrews et al., 2009). Typically dust and gas surface densities decrease with radius, but high-resolution observations with the Atacama Large Millimeter Array (ALMA) have revealed significant substructure among disks including gaps, rings, and asymmetries. The Disk Substructures at High Angular Resolution Project (DSHARP, Andrews et al., 2018) is a recent example which demonstrates the variety of detailed substructure observed in protoplanetary disks.

1.3.1 Vertical Structure

A rough analytic model of the vertical disk structure can be developed by assuming that the disk is slowly evolving along axisymmetric static solutions to the fluid equations. The vertical density profile of the disk can be found by assuming that the disk is isothermal and that the pressure support to keep the disk in hydrostatic equilibrium comes solely from a density gradient. Self-gravity of the disk is ignored in this derivation. The momentum equation written under these assumptions is

$$\frac{dP}{dz} = \rho g_z \tag{1.1}$$

where P is the pressure, and g_z is the local acceleration due to gravity. At a given height above the disk midplane, z, and radius, r, and assuming that $z << r$, this transforms into

$$\frac{dP}{dz} = -\frac{GM_\star z}{(r^2+z^2)^{3/2}} \approx \rho\Omega_K^2 z \tag{1.2}$$

where $\Omega_K = \sqrt{GM_\star/r^3}$ is the Keplerian orbital velocity in the midplane for a circular orbit. Writing pressure in terms of the sound speed results in

$$c_s^2\frac{d\rho}{dz} = \Omega_K^2\rho z \tag{1.3}$$

This can be integrated to obtain

$$\rho(z) = \rho_0 \exp(-z^2/2h^2), \tag{1.4}$$

where ρ_0 is the density of the disk at the midplane, and h is the scale height defined as $h \equiv c_s/\Omega_K$. This resulting solution is a Gaussian rather than the typical exponential found in planetary atmospheres because of the scaling of the vertical component of the gravitational force.

This scale height is the ratio of two quantities that are both a function of radius (c_s and Ω_K). The ratio of these thus sets the geometry of the disk. If the decrease in temperature with radius is shallower than $T \propto r^{-3}$, then the disk will be "flared" because the scale height will increase with radius. Such flaring is observed in protoplanetary disks (e.g., Watson & Stapelfeldt, 2007).

More complex models of the disk that include a balance between heating from stellar X-rays & UV emission and cooling from dust & molecules can be qualitatively broken into three distinct layers as outlined by Armitage (2019). The gas and dust in the midplane of the disk have the same temperature, and dust is the dominant source of cooling. At the surface of the disk, the temperatures are hotter than at the midplane and the disk cools via CO rovibrational transitions and dust-gas collisions. This region is primarily heated through photoelectric heating where electrons are freed from graphite grains by the strong stellar UV emission (Draine, 1978). Above this layer is a hot, low-density atmosphere heated by X-ray emission which cools via L_α and other atomic lines.

1.3.2 Radial Structure

Following the prescription of Hartmann (2008), rough estimates of the evolution of the radial structure can be explored by considering the HD fluid equations for a

geometrically thin disk subjected to viscous torques. Under these assumptions, the continuity equation can be written for an axially symmetric disk as

$$r\frac{\partial \Sigma}{\partial t} + \frac{\partial}{\partial r}(r\Sigma u_r) = 0 \tag{1.5}$$

while the momentum equation takes the form

$$r\frac{\partial}{\partial t}(\Sigma r^2 \Omega) + \frac{\partial}{\partial r}(\Sigma u_r r^3 \Omega) = \frac{1}{2\pi}\frac{\partial T}{\partial r} \tag{1.6}$$

where Σ is the surface density, u_r is the radial motion, Ω is the orbital velocity, and T is the viscous torque. Assuming Newtonian viscosity, torque at a given radius can be expressed as

$$T = 2\pi\nu\Sigma r^3 \frac{\partial \Omega}{\partial r}, \tag{1.7}$$

where ν is the viscosity. Next, the term for torque in the momentum equation is replaced with this expression and the second term on the left is separated using the chain rule. After canceling terms by using the continuity equation, the result is

$$\Sigma u_r \frac{\partial}{\partial r}(r^2\Omega) = \frac{1}{r}\frac{\partial}{\partial r}\Big(\nu\Sigma r^3 \frac{\partial \Omega}{\partial r}\Big). \tag{1.8}$$

This can be solved for an expression for u as a function of r and t

$$u_r(r,t) = \frac{1}{\Sigma r}\frac{\partial}{\partial r}\Big[\frac{\frac{\partial}{\partial r}(\nu\Sigma r^3 \frac{\partial \Omega}{\partial r})}{\frac{\partial}{\partial r}(r^2\Omega)}\Big] \tag{1.9}$$

This result can be combined with the continuity equation to solve for the derivative of the surface density with respect to time

$$\frac{\partial \Sigma}{\partial t} = -\frac{1}{r}\frac{\partial}{\partial r}\Big[\frac{\frac{\partial}{\partial r}(\nu\Sigma r^3 \frac{\partial \Omega}{\partial r})}{\frac{\partial}{\partial r}(r^2\Omega)}\Big] \tag{1.10}$$

Assuming that the orbital motion in the disk is Keplerian ($\Omega = \sqrt{\frac{GM}{r^3}}$) and simplifying yields the following final expression for $\frac{\partial \Sigma}{\partial t}$

$$\frac{\partial \Sigma}{\partial t} = \frac{3}{r}\frac{\partial}{\partial r}\Big[r^{1/2}\frac{\partial}{\partial r}(\nu \Sigma r^{1/2})\Big] \tag{1.11}$$

Once an initial density distribution is specified, this equation can be used to find the distribution as a function of time. The family of solutions to this equation shows that initial over-densities spread out over time because of the viscous forces at work in the disk.

While the derivation above considers a simplified thin disk without thermal effects, the temperatures of the dust and gas rise in the inner regions of the disk because of the proximity to the young star (in addition to heating from viscous interactions). When the dust becomes too hot, the grains begin to sublimate. Based on our current understanding of silicate grain properties, this typically occurs roughly at a temperature of 1400K (Draine & Lee, 1984), resulting in a dust sublimation radius between 0.1-0.5 au depending on the stellar luminosity. This phenomenon is observed in protoplanetary disks via the NIR-bright, directly-illuminated dust wall (Muzerolle et al., 2003; D'Alessio et al., 2006). Inwards of the dust sublimation radius, we expect the disk to be mostly dust-free.

1.4 Models of Accretion in the Inner Disk

The gas that moves into the inner regions of the disk must be either accreted onto the star or ejected from the system. Evidence for both accretion and ejection via stellar winds/jets is seen from studies of spectral lines. For example, in some young stars, the H_I 10830 Å line shows both blue-shifted wind absorption and red-shifted absorption arising from material falling towards the star (Edwards et al., 1994). Excess UV and optical emission is observed in some young stars above models of non-

accreting photospheres. This excess is attributed to potential energy from accreted material being transformed into emission. Typical inferred accretion rates for young, low-mass stars are on the order of $10^{-8}\,\mathrm{M_{\odot}yr^{-1}}$ (Hartmann et al., 1998). Young, low-mass stellar objects which are accreting are known as classical T Tauri stars (CTTS), while their non-accreting counterparts are known as weak-lined T Tauri stars (WTTS). In this dissertation, references to populations that include both CTTS and WTTS will be referred to collectively as T Tauri stars (TTS).

1.4.1 Spherical Accretion

Considering the simplified analytic case of spherical accretion can grant insight into more complicated accretion systems with additional physical processes. Here I present the derivation for Bondi accretion (Bondi, 1952). The velocity and density structure of such a system can be solved by starting with the HD fluid equations in spherical coordinates. Next, assume that the flow is in steady-state, purely radial, viscosity-free, isothermal, and that self-gravity is unimportant. Under these assumptions, the continuity and momentum equations become

$$\frac{d}{dr}\left(r^2\rho u\right) = 0 \tag{1.12}$$

$$\rho u\frac{du}{dr} = -\frac{dP}{dr} - \frac{GM_{\star}}{r^2}\rho, \tag{1.13}$$

respectively. The continuity equation can be integrated to obtain

$$r^2\rho u = \kappa, \tag{1.14}$$

where κ is an integration constant. This expression can be rearranged to solve for ρ, resulting in

$$\rho = \frac{\kappa}{r^2 u}. \tag{1.15}$$

Using the ideal gas law, pressure can be replaced with $P = c_s^2\rho$, yielding the momentum equation in the following form

$$\rho u\frac{\partial u}{\partial r} = -c_s^2\frac{\partial \rho}{\partial r} - \frac{GM_\star}{r^2}\rho. \tag{1.16}$$

Dividing this expression by ρ, and then replacing both instances of ρ by the result from the continuity equation results in

$$u\frac{\partial u}{\partial r} = -c_s^2 r^2 u\frac{\partial}{\partial r}\Big(\frac{1}{r^2 u}\Big) - \frac{GM_\star}{r^2}. \tag{1.17}$$

Using the chain rule to split the differential and simplifying results in

$$u\frac{\partial u}{\partial r} = c_s^2\Big[\frac{2}{r} + \frac{1}{u}\frac{\partial u}{\partial r}\Big] - \frac{GM_\star}{r^2}. \tag{1.18}$$

Gathering all of the terms involving $\frac{\partial u}{\partial r}$ on the left side results in

$$\Big[u - \frac{c_s^2}{u}\Big]\frac{\partial u}{\partial r} = \frac{2c_s^2}{r^2}\Big[r - \frac{GM_\star}{c_s^2}\Big]. \tag{1.19}$$

Replacing the differential on the left side with $\frac{\partial u^2}{\partial r}$, and recognizing $\frac{GM_\star}{c_s^2}$ as a critical radius, r_c, the expression can be written

$$\Big[1 - \frac{c_s^2}{u^2}\Big]\frac{\partial u^2}{\partial r} = \frac{4c_s^2}{r^2}[r - r_c] \tag{1.20}$$

This expression can be integrated to obtain the following transcendental equation

$$\frac{u^2}{c_s^2} - \ln\Big(\frac{u^2}{c_s^2}\Big) = 4\ln\Big(\frac{r}{r_c}\Big) + 4\frac{r_c}{r} + C \tag{1.21}$$

From inspection of the family of solutions representing u as a function of r, only two values of C produce solutions that are physical, transonic, and stable. The value of C can be found for these two solutions by setting $u = c_s$ at r_c. After simplifying, it is found for both solutions that $C = -3$.

The transcendental equation can be written in the form of the special Lambert W function (see Cranmer, 2004), which is a solution to equations of the form

$$\ln(A + Bx) + Cx = \ln(D) \tag{1.22}$$

with the solution

$$x = \frac{1}{C} W\Big[\frac{CD}{B} \exp\Big(\frac{AC}{B}\Big)\Big] - \frac{A}{B}. \tag{1.23}$$

Re-arranging and assigning $x \equiv u^2$, the coefficients for the above solution are

$$A = 0 \tag{1.24}$$

$$B = c_s^2 \tag{1.25}$$

$$C = -c_s^2 \tag{1.26}$$

$$D = \Big(\frac{r}{r_c}\Big)^{-4} \exp\Big[4(1 - \frac{r_c}{r}) - 1\Big] \tag{1.27}$$

The final result is a piece-wise function where the real part of the branches of the Lambert W function and the negative root are chosen such that velocity becomes more negative as the flow approaches the star.

$$u^2 = \begin{cases} -c_s^2 W_{-1}\big[-D(r)\big] & r \leq r_c \\ -c_s^2 W_0\big[-D(r)\big] & r \geq r_c \end{cases} \tag{1.28}$$

This result is the Bondi spherical accretion solution (Bondi, 1952). This solution is the only solution that passes smoothly through the transonic radius with velocity increasing as the flow gets closer to the star. This result is analogous to a de Laval nozzle. The radial scaling of the gravitational field and the scale factors of the spherical coordinate system play the role of the effective nozzle shape which changes the cross-sectional area of the flow. This modifies the speed with the critical point being reminiscent of the narrowest part of the nozzle where the flow becomes supersonic.

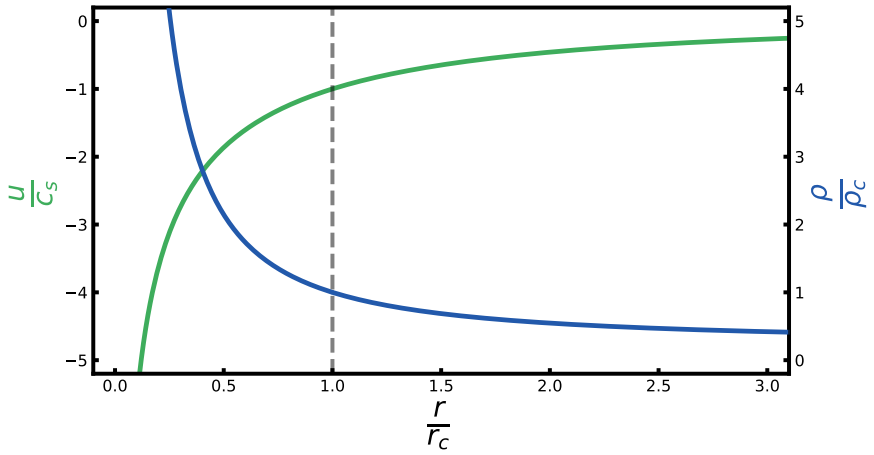

Fig. 1.3: The Bondi accretion solution with velocity shown in green and density shown in blue, plotted in terms of c_s and the density at r_c, ρ_c (scaled such that $\kappa = 1$). r_c, which is the location where the flow transitions smoothly to being supersonic, is marked with the dashed grey line.

The final velocity of the flow at the star depends on the radius of the star and the mass of the star through the expression for r_c. Fig. 1.3 shows the Bondi accretion solution for velocity and density. If the opposite branches of the Lambert W solution were chosen, then this solution would be the famous Parker solar wind solution (Parker, 1958).

1.4.2 Magnetospheric Accretion

Measurements of lines sensitive to broadening through the Zeeman effect reveal magnetic field strengths in TTS on the order of several kG (e.g., Johns-Krull, 2007). If the inner gas disk is sufficiently ionized, then it will be influenced by this strong stellar magnetic field. TTS are known to produce ionizing X-ray and FUV emission, and recent models also suggest that the accretion process itself can produce ionizing cosmic rays (Offner et al., 2019). With this level of ionization and strong magnetic field, the gas in the inner disk is truncated by the magnetosphere. The disrupted gas then flows along the magnetic field line until it collides with the star, forming a

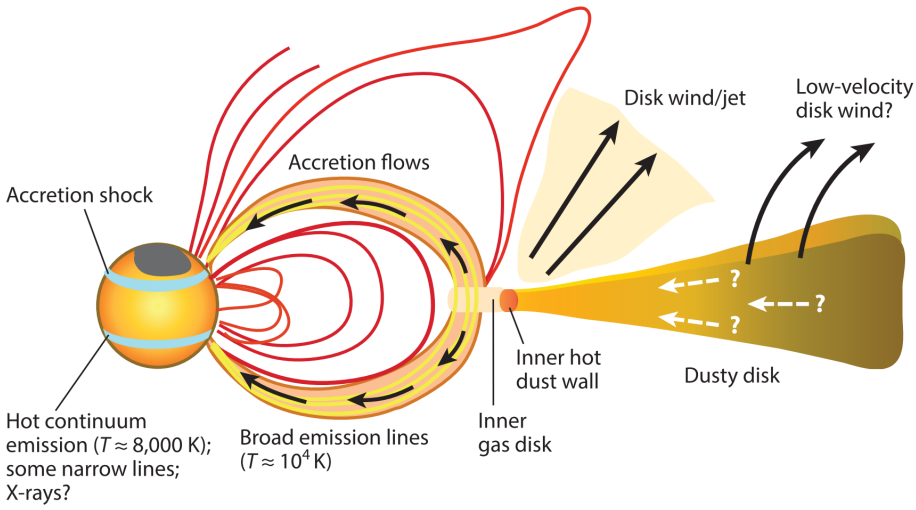

Fig. 1.4: Schematic of the current understanding of magnetospheric accretion and the inner regions of protoplanetary disks. The stellar magnetic field is strong enough to disrupt the inner disk, channeling infalling material along magnetic field lines. As that material impacts the star, hot continuum emission and narrow lines are formed near the shock at the stellar photosphere. Broader emission lines are formed by the material entrained within the stellar magnetosphere. Forbidden lines arise from winds and outflows. Adapted from Hartmann et al. (2016) with permission.

system of magnetospheric accretion. Such a system was considered for the transfer of mass and momentum in neutron stars by Ghosh & Lamb (1979a,b). Bertout et al. (1988) suggested that such a model might also apply to TTS based on the analysis of their light curves of DF Tau. Early work expanding this model for TTS was conducted by Camenzind (1990); Koenigl (1991); Calvet & Hartmann (1992); Shu et al. (1994). A schematic of the current theory of magnetospheric accretion is shown in Fig. 1.4.

This idea is reinforced by the red-shifted components of accretion-sensitive absorption/emission lines observed in CTTS. Typical line shifts are on the order of several hundred km/s, which is comparable to freefall velocity for young stars (Edwards et al., 1994). Similar in-fall velocities are seen in the broad components of FUV lines such as C_{IV} (Ardila et al., 2013). The high in-fall velocities observed

in these line profiles are inconsistent with boundary-layer accretion at the stellar surface, which was a previously proposed scenario for accretion onto young stars.

The structure of the magnetic field can be probed through spectropolarimetric observations of young stars. These observations consist of time-series observations of the polarized signature of Zeeman broadening. The first work to recover the large-scale structure of the magnetic field of a CTTS was Donati et al. (2007). This work found that the photospheric magnetic field is not a pure dipolar, rotation-axis-aligned magnetic field, but instead hosted a large octupolar component tilted by about 20°. Later works using the same technique found a variety of stellar magnetic field structures, ranging from simple axisymmetric dipoles (LkCa 15, Donati et al., 2019) to highly complex (V2247 Oph, Donati et al., 2010a) field structures.

From these spectropolarimetric observations, several trends emerge. In general, the structure of the magnetic field at several stellar radii tends to resemble a dipolar field due to the radial scaling of multipole field strengths. This dipole field is strong enough to disrupt the inner disk. Near the surface of the star, many stars show higher-order complex fields, most commonly octupolar fields. Strong quadrupolar fields are notably absent. If present, they would tend to push accretion hot spots towards the midplane which is not observed. While the stellar magnetic pole tends to be aligned with the rotational axis, misalignments of $10-20°$ are common. Spectropolarimetric observations of line emission, which is thought to be formed in the accretion shock, find typical surface coverages of 10%, often near the poles (Donati et al., 2011b). This is in agreement with the expected size and locations of hot spots formed through magnetospheric accretion.

A rough estimate of the location where the magnetic field truncates the inner disk can be found by setting the ram pressure at the inner edge of the disk equal to

the magnetic pressure from the stellar magnetic field and solving for the radius at which the two are balanced:

$$P_B = P_r. \tag{1.29}$$

In cgs units, the magnetic pressure is $P_B = \frac{B^2}{8\pi}$ and in spherical coordinates, the gas ram pressure can be written in terms of the accretion rate as $P_r = \frac{\dot{M}v}{2r^2}$. Under the assumption that the stellar magnetic field is an axis-aligned dipole and that the escape speed is the relevant velocity scale, this reduces to

$$\frac{r_m}{R\star} \approx \eta \frac{B_\star^{4/7} R_\star^{5/7}}{\dot{M}^{2/7} (2GM_\star)^{1/7}}, \tag{1.30}$$

where η is a factor of order unity that encompasses the complexities in the interaction between the magnetic field and the disk, $B_\star$ is the magnetic field strength at the surface of the star, $R_\star$ is the stellar radius, $M_\star$ is the stellar mass, and G is the gravitational constant. By assuming $\eta = 1$ and writing this in terms of typical values for young stars, we find

$$\begin{aligned} \frac{r_m}{R_\star} = 7.1 \Big(\frac{B_\star}{1\,\mathrm{kG}}\Big)^{4/7} \Big(\frac{\dot{M}}{10^{-8}\,\mathrm{M_\odot\,yr^{-1}}}\Big)^{-2/7} \\ \Big(\frac{M}{0.5\,\mathrm{M_\odot}}\Big)^{-1/7} \Big(\frac{R}{2\,\mathrm{R_\odot}}\Big)^{5/7}, \end{aligned} \tag{1.31}$$

where $M_\odot$ and $R_\odot$ are the solar mass and radius, respectively. From this, we see that the typical value of the magnetic truncation radius is around $7R_\star$. This value of r_m is often comparable to the co-rotation radius, r_{co}, which is the point in the disk where the angular velocity of the Keplerian disk is equal to the angular velocity of the star. Typically, r_m is smaller than the dust-sublimation radius.

The kinetic energy flux of the accretion flow entering the preshock region can be written as

$$F = \frac{1}{2}\rho v_f^3, \tag{1.32}$$

where v_f is the freefall velocity at the stellar surface, given by

$$v_f = \sqrt{\frac{2GM_\star}{R_\star}}\sqrt{1 - \frac{R_\star}{r_m}} \tag{1.33}$$

(Calvet & Gullbring, 1998). The density of the accretion flow can be calculated as a function of $\dot{M}$ and the area of the star covered by accretion shocks, $A = f4\pi R_\star^2$, where f is a filling factor. The density is found with the following expression.

$$\rho = \frac{\dot{M}}{Av_f} \tag{1.34}$$

By combining these two expressions and adopting typical stellar parameters for young stars with a filling factor of 0.01, we find that the hydrogen density of the infalling material is on the order of $5 \times 10^{12} cm^{-3}$.

1.4.3 The Calvet & Gullbring (1998) Accretion Shock Models

Under values typical of TTS, we find that the material in the column is highly supersonic when it collides with the photosphere of the star. This results in a strong shock at the footprint of the magnetic field line. The kinetic energy of the accretion flow is transformed into thermal energy in the postshock region. This heats the material in the postshock region to reach temperatures around 10^6 K, which causes the material in the region to cool predominantly through X-rays as it falls towards the surface of the star. These X-rays are emitted both towards the stellar photosphere and into the overlying preshock region. Because both of these regions are optically thick to X-rays, they absorb the emission, heat up, and re-radiate the energy at UV and optical wavelengths to which they are more optically thin. A widely adopted

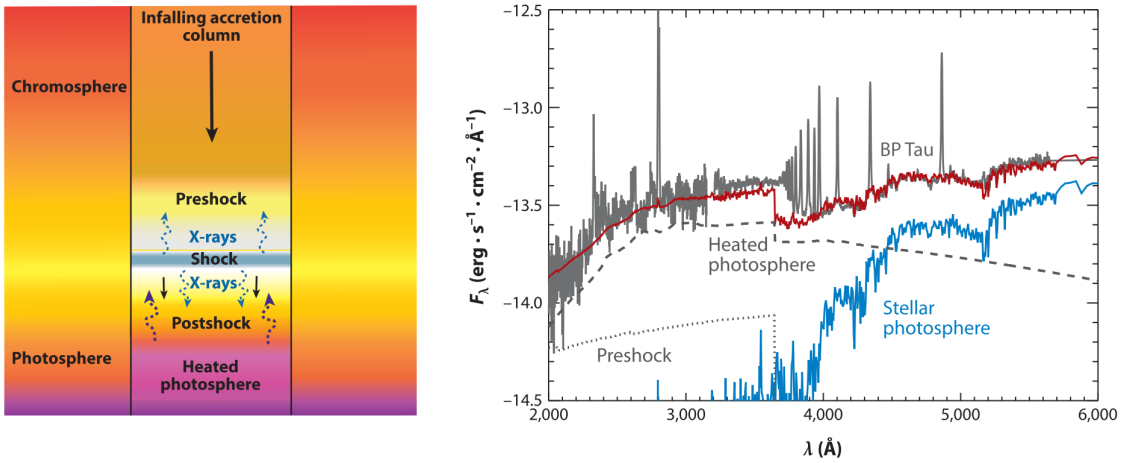

Fig. 1.5: *Left:* Schematic showing the accretion shock model of Calvet & Gullbring (1998). As material falls towards the star, it shocks and transforms its kinetic energy into thermal energy. This thermal energy is re-emitted primarily as X-rays in the postshock region. Half the emission is emitted towards the star, heating the underlying photosphere while the other half heats the preshock region above the shock. These two regions absorb and transform this energy into the UV excess that we observe. *Right:* Spectrum of the CTTS BP Tau (gray) with the total fitted accretion shock model overlaid (red). The heated photosphere and preshock components of the model are shown in dashed and dotted lines respectively. A non-accreting WTTS was used as a spectral template, and is shown in blue. Emission lines are ignored in the fitting process. Adapted from Hartmann et al. (2016) with permission.

model of these regions at the footprint of the stellar magnetic field was developed by Calvet & Gullbring (1998) and is briefly described here. A schematic of this model and a fit to observations of a CTTS are shown in Fig. 1.5.

The structure and the emission of the optically thin postshock region are modeled using the one-dimensional (1D) steady-state hydrodynamic (HD) fluid equations. Under the assumptions that the flow is (1) plane-parallel, (2) strictly along magnetic field lines perpendicular to the stellar surface, (3) well-described by a one-fluid solution, (4) free of instabilities and magnetic effects, and (5) conduction is ignored, the continuity, momentum, and energy HD fluid equations near the stellar surface can

be written

$$\rho v = constant \tag{1.35}$$

$$\rho v \frac{dv}{dz} + \frac{d}{dz}\Big(\frac{\rho k_b T}{\mu m_H}\Big) + g\rho = 0 \tag{1.36}$$

$$\frac{d}{dz}\Big[\rho v\Big(\epsilon + \frac{v^2}{2} + \frac{kT}{\mu m_H} + gz\Big)\Big] = \Lambda(\rho, T) \tag{1.37}$$

where z is the height as measured from the accretion shock, k_b is the Boltzmann constant, μ is the mean molecular mass, m_H is the mass of hydrogen, g is the local gravitational acceleration, ϵ is the internal energy per unit mass, and Λ is the volume emissivity of hot plasma. The boundary conditions are given by the strong shock conditions from the assumed kinematic energy flux.

The structure and emission of the preshock region is calculated by assuming a single density and solving the temperature structure and emission using the non-local thermodynamic radiative transfer (nLTE) code `Cloudy` (Ferland et al., 2017). The heated photosphere is modeled by integrated the hydrostatic equations written in terms of the Rosseland mean opacity (τ_{ross}). The structure at the bottom of the postshock is used as a boundary condition. Both the incident emission from the postshock region and the radiant flux from the stellar interior are considered when calculating the temperature structure of the heated photosphere.

These models find typical lengths of the postshock region to be on the order of $10^5 - 10^6$ cm, while the part of the preshock region where H is fully ionized spans between $10^7 - 10^9$ cm. The range in these lengths accounts for models with different reasonable parameters. As mentioned before, typical temperatures in the postshock region are found to be on the order of 10^6 K, while temperatures in the portion of the preshock where H is fully ionized are typically between 15000 K and 25000 K.

The temperature in the preshock region rapidly drops as the ionizing photons are exhausted, which generally occurs around $0.01\,R_\star$. Characteristic temperatures of the heated photosphere at the depth where the continuum is formed ($\tau_{Ross} = 2/3$) are between $4000 - 8000$ K depending on the kinetic energy flux, and thus the density of the accretion column under the assumption of freefall.

These models solve for the outward continuum emission, which is comprised of the sum of the emission arising from the preshock region and the heated photosphere. The postshock emission is implicitly included since it is used as the incident radiation field on the other two regions. The excess continuum emission typically peaks in the near UV (NUV) under most accretion column densities. The Balmer continuum primarily arises from the preshock region, while the Paschen continuum is dominated by the contribution from the heated photosphere.

Observations of the continuum of young stars can be modeled by treating the filling factor and the kinetic energy flux of the flow as free parameters. Previous work with this model found it necessary to include multiple accretion column densities to reproduce the observed continuum levels (Ingleby et al., 2013, 2015). This suggests that there may be gradients across accretion columns, and/or multiple columns are involved in the accretion process. In most cases, the largest filling factors are associated with lower kinematic energy fluxes ($F = 10^{10} - 10^{11}\,\mathrm{erg\,s^{-1}\,cm^{-2}}$) with typical values of f ranging between $5 - 40\%$. Higher-energy columns ($F = 10^{11} - 10^{12}11\,\mathrm{erg\,s^{-1}\,cm^{-2}}$) typically cover $0.1 - 1\%$ of the stellar surface. The amount of mass carried by high- and low-energy columns are generally comparable but vary from object-to-object and between separate observations of the same object (Ingleby et al., 2015). Fig. 1.6 demonstrates the use of these models on the CTTS GM Aur during three epochs of *HST* Space Telescope Imaging Spectrograph (STIS) observations.

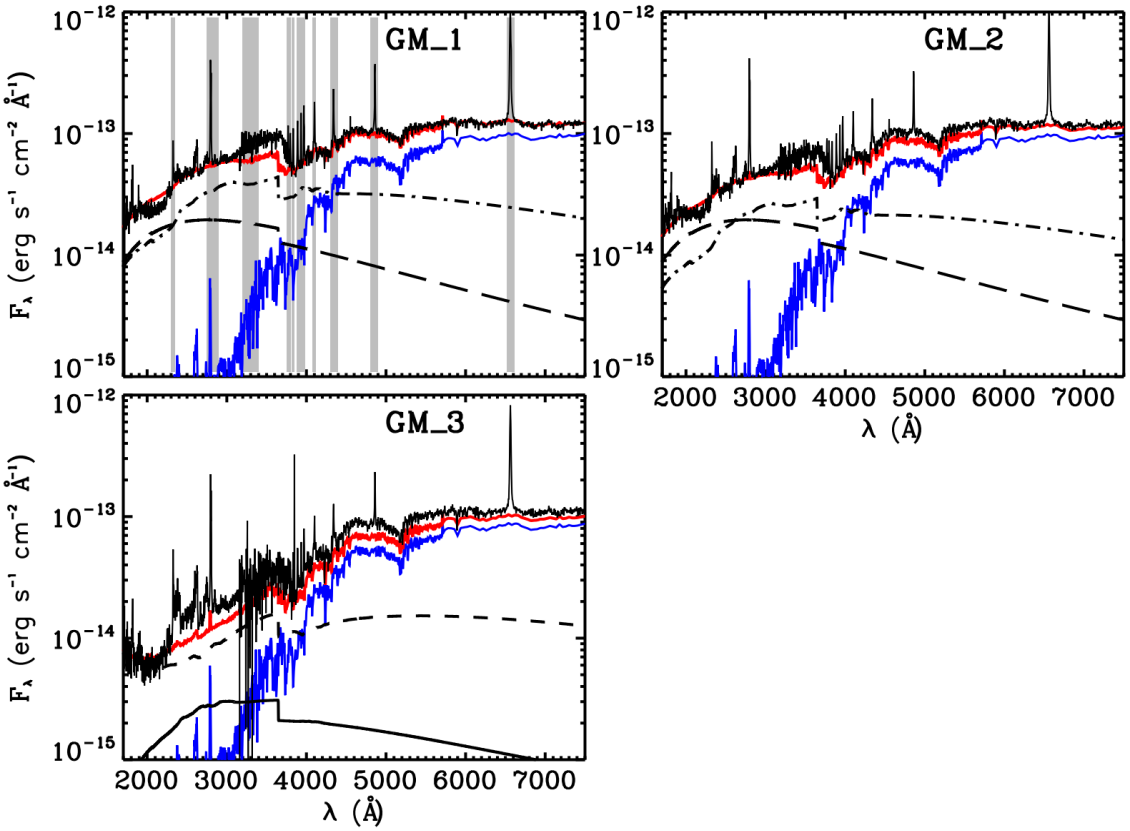

Fig. 1.6: Calvet & Gullbring (1998) accretion shock continuum models fit to three epochs of contemporaneous *HST* STIS observations of GM Aur, a CTTS in the Taurus star-forming region. The de-reddened observations are the black spectra while the sum of the models of the continuum are red and the non-accreting WTTS used as a spectral template is in blue. The gray bars mark regions of strong emission lines that were masked. The black lines represent models with different kinetic energy fluxes, F. The short-dashed, dotted-dashed, solid, and long-dashed lines represent values of $\log F = 10.5, 11, 11.5$ and $12\,\mathrm{ergs}^{-1}\,\mathrm{cm}^{-2}$, respectively. Significant variability is observed across the epochs which is thought to be caused by changes in the accretion rate. The unique wide-coverage of the STIS instrument breaks the degeneracy between accretion column density and surface coverage of accretion shocks. Adapted from Ingleby et al. (2015) with permission.

1.5 Variability in T Tauri Stars

Variability has been a near-ubiquitous characteristic of young, low-mass stars and their disks since their discovery (e.g., Joy, 1945). Variability in TTS is observed across nearly the entire electromagnetic spectrum. The majority of this variability is driven by processes that operate in the inner few au of the disk.

At X-ray wavelengths, sources of variability include flares (TTS are known to be active, e.g., Jackman et al., 2019), and occultation events (Günther et al., 2018). Changes in X-ray spectra related to variable accretion have also been observed. Generally, it is found that X-ray luminosity is anti-correlated with NUV emission (Schneider et al., 2018; Espaillat et al., 2019b). This is thought to occur because of density stratification across the accretion columns on the stellar surface causing harder X-rays to be absorbed by surrounding low-density regions while softer X-rays escape. Significant variability has been observed in both the FUV continuum and in FUV lines associated with accretion and from hot spots and active regions rotating into and out of view (e.g., Ingleby et al., 2015). The NUV and optical also show significant variability in continuum and line emission (e.g., H_α, Thanathibodee et al., 2019) from changes in the accretion rate, rotational modulation of hot and cold spots (e.g., Cody et al., 2014; Venuti et al., 2017), and stellar activity. The observed emission in optical wavelengths and shorter is also affected by variable extinction events thought to be caused by disk warps (AA Tau being the prototypical example, see Bouvier et al., 1999, 2003). The spectra in Fig. 1.6 demonstrate variability thought to be caused by changes in the accretion rate.

The NIR, which traces dust in the inner regions of the disk (including the illuminated wall at the dust sublimation temperature), has been observed to be variable in some cases, with some hints of connections to accretion behavior (Ingleby et al., 2015; Banzatti et al., 2015). At longer IR wavelengths, some objects demonstrate

variability in the form of "see-saw" variability thought to be caused by changes in the wall height (Muzerolle et al., 2009; Espaillat et al., 2011).

Continuum variability at millimeter wavelengths has been observed in FU Orionis objects, which are young, low-mass stars with massive outbursts with $\dot{M}$ up to $10^{-4}\,M_{\odot}\,yr^{-1}$ (Liu et al., 2018; Wendeborn et al., 2020). Variability in mm lines possibly associated with X-ray driven chemistry has been observed for CTTS by Cleeves et al. (2017). Centimeter wavelengths trace ionized regions of the disk via free-free emission, which include the jet. The presence of jets appears to be tethered to accretion, since the mass-loss rates of jets are typically on the order 10% of $\dot{M}$ (Hartigan et al., 1995; Natta et al., 2014). Simultaneous UV-cm observations of TTS hint that variability in the accretion rate may be connected to variability in the jet (Espaillat et al., 2019a).

1.5.1 Classification of Variability

Classification of variability also has a long history in low-mass star formation. Early variability classification schemes were devised by Parenago (1950), which share some similarities to modern metrics of variability. TTS were sorted into categories based on whether the object was more frequently bright, faint, near the mean brightness, or showed no preference for any level of brightness. Herbst et al. (1994) posited that TTS could be broken into three categories: Type I encompassed variability caused by rotational modulation of cold spots; Type II covered changes due to "veiling" (relating to accretion); and Type III, which included early spectral type TTS, showed large amounts of variability with limited changes in veiling.

In recent years, several studies have emerged which leveraged the power of continuous, month-long, space-based monitoring surveys of entire star-forming regions to study optical variability of TTS (Cody et al., 2014; Cody & Hillenbrand, 2018). These works have developed empirical variability classifications based on the ob-

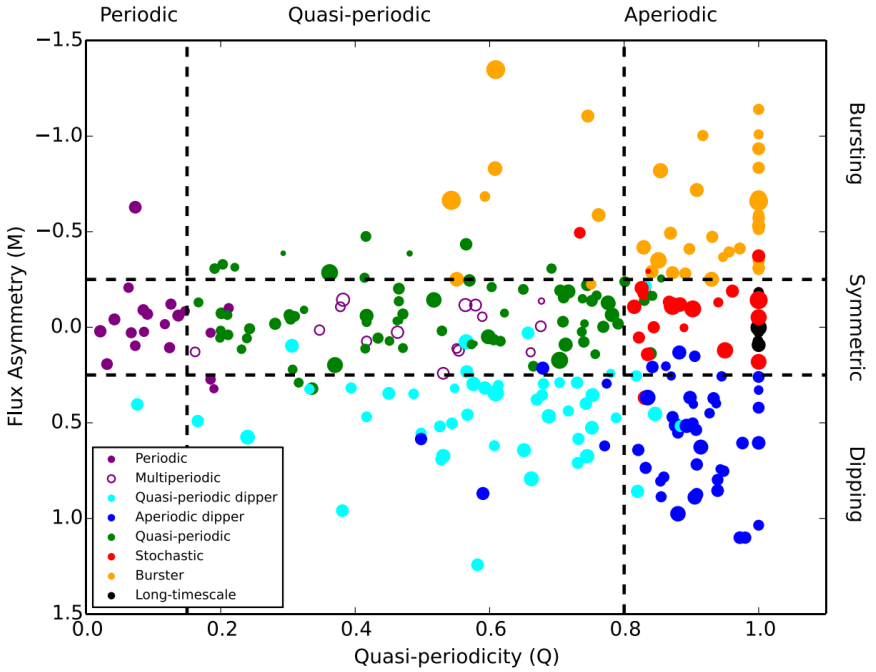

Fig. 1.7: Bivariate plot of the variability metrics, Q and M, which measure periodicity and symmetry around the mean, respectively. Variability classifications are marked by different colors. The points in this figure are from K2 light curves of the TTS in the ρ Oph and Upper Sco star-forming regions. Adapted from Cody & Hillenbrand (2018) with permission.

served behavior of the light curve. In particular, two statistical metrics, Q and M, were created to capture the periodic behavior and the symmetry of the light curve. With these metrics, it becomes possible to identify variability trends for many objects under an automated approach. This approach enables statistics-based studies of the characteristics that drive each type of variability. An example of classification using these metrics for over 100 members of the ρ Oph and Upper Sco star-formation regions is shown in Fig. 1.7.

While more in-depth discussion of these metrics is saved for Chapter 5, I briefly describe here the steps to measure these metrics. To measure the metric associated with periodicity, Q, the period must first be determined. A smoothed, phase-folded

light curve is then subtracted from the original light curve. Finally, Q is calculated by examining the ratio of the residual variance to the original light-curve variance. The value of Q ranges between 0 (purely periodic) to 1 (stochastic). To measure the metric that quantifies symmetry around the mean, M, outliers in the light curve are first removed. A mean is then taken of the top and bottom 5% of the remaining points, and the median flux value of the entire light curve is subtracted. Finally, M is found by dividing this value by the estimated white-noise level. Typical values of M range between -1.5 (largely favoring brightening events) and 1.5 (primarily favoring dimming events).

The combination of these two metrics can be used to create a bi-variate plot where regions of Q-M space can be used to separate objects into empirical variability classes. Trends with accretion, inclination (defined such that a disk with $i = 0°$ is face-on), and the presence of material in the inner disk have been identified within these variability categories. Following Cody & Hillenbrand (2018), these classifications occupy the following ranges of Q-M space.

- *Burster (B):* $M < -0.25$

  These objects exhibit rapid increases in brightness thought to be associated with changes in the accretion rate on timescales of hours to days. Among the variability classes, these are the dominant class for objects that show the largest UV excess from accretion (Stauffer et al., 2015). Bursters in general host more substantial inner disks than the other classifications and inclinations for these objects are typically lower (more face-on), suggesting that we are seeing accretion that is unobscured by their disk (Cody & Hillenbrand, 2018).

- *Purely Periodic Symmetric (P):* $Q < 0.15$ and $-0.25 < M < 0.25$

  The sinusoidal behavior observed in the light curves of purely periodic symmetric objects is thought to primarily arise from rotational modulation of cool

spots on the surface of the star. These objects tend to have weaker accretion and bluer NIR colors, which indicates less material in the inner disk when compared to other classifications (Cody & Hillenbrand, 2018).

- *Quasi-periodic Symmetric (QPS):* $0.15 < Q < 0.85$ and $-0.25 < M < 0.25$
  Quasi-periodic symmetric objects are the largest fraction of variability classes amongst stars included in photometric monitoring surveys of star-forming regions (Cody et al., 2014; Cody & Hillenbrand, 2018). Their light curves show a mix of periodic behavior from rotational modulation and stochastic behavior from accretion/dipping. These objects display a wide range of accretion rates and may require additional sub-categories to fully capture the observed behavior. The dominant mechanism for the variability of many QPS objects appears to be accretion (Venuti et al., 2015), but some of the variability may also be driven by cold-spot modulation for objects with low accretion rates (Cody & Hillenbrand, 2018). Typically, QPS objects show inclinations of $i > 50°$.

- *Purely Stochastic (S):*$Q > 0.85$ and $-0.25 < M < 0.25$
  Like the burster sources, stochastic (also known as aperiodic symmetric) objects tend to show redder colors, indicating significant material in the inner regions of the disk. These objects show little to no evidence of rotational modulation, and unlike bursters, exhibit brightness variations that are symmetric around the mean value of the light curve. Inclinations derived from millimeter observations for these objects are typically low, with $i < 60°$ (Cody & Hillenbrand, 2018). These inclinations are consistent with the idea that we are directly viewing the accretion with limited interference from the dusty disk.

- *Quasi-periodic Dipper (QPD):* $0.15 < Q < 0.85$ and $M > 0.25$
  As the name implies, the light curves of quasi-periodic dippers show quasi-

periodic dimming events thought to be caused by occultations by the accretion disk. In general, QPD sources tend to have higher inclinations ($i > 50°$), which is in agreement with the idea of the dips being caused by occultation of the central star by dust entrained in the co-rotating inner disk/magnetosphere (Bouvier et al., 1999). Dippers tend to be moderately bright in the IR, and tend to have relatively low accretion rates.

- *Aperiodic Dipper (APD):* $Q > 0.85$ and $M > 0.25$

  The light curves of aperiodic dippers show irregular dimming events, also thought to be caused by occulting material in the inner disk. Like QPD sources, aperiodic dippers tend to have higher inclinations.

Four additional classes that fall outside the realm of classification by Q and M are as follows.

- *Long Timescale (L):*

  Several of the light curves of objects in the previously described photometric monitoring programs of star-forming regions show features evolving on timescales much longer than what is typically associated with rotational modulation and accretion. These objects are classified as such if they show trends longer than 30 d timescales.

- *Multiperiodic (MP):*

  Light curves of multiperiodic objects are thought to be generated through the superposition of periodic signals of a P source and its companion. Roughly 40% of the objects considered P sources can also be categorized into the multiperiodic class.

- *Unclassifiable (U):*

Some of the objects included in these samples cannot be classified under the current constraints of the Q and M metrics and do not fall into the miscellaneous categories considered here. As an example, two light curves from the study of Cody & Hillenbrand (2018) feature a single, large, brightening event on an otherwise relatively featureless light curve.

- *Eclipsing Binary (EB)*

  Eclipsing binaries are rare to observe in young star-forming regions. This is because of the strict geometric requirements and that they are essentially unobservable if they are co-planar with an optically thick accretion disk.

- *Non-variable (N)* The final category is non-variable stars. Depending on the star-forming region and the sensitivity of the detector, rates of non-variable stars range from $3 - 19\%$ (Cody et al., 2014; Cody & Hillenbrand, 2018).

Each of these classifications applies to the variability observed on timescales of weeks to months. Variability on shorter timescales is less well characterized, and high-quality short-cadence light curves of TTS are less readily available. Models predict that the accretion column should be inherently unstable to a thermal instability (Langer et al., 1981; Chevalier & Imamura, 1982; Sacco et al., 2008). While hints of variability on short timescales may point to this instability occurring (e.g., Siwak et al., 2018), there are no observations that unambiguously observe this phenomenon. Additionally, several previous studies have failed to detect periodic behavior on the expected timescales at all (Drake et al., 2009; Günther et al., 2010). Clearly, questions remain as to the driving forces of accretion variability in T Tauri stars.

1.6 Goals, Questions, and Outline

The previous sections introduced protoplanetary disks with a focus on the process of magnetospheric accretion and accretion variability in CTTS. The overarching question about CTTS that drives this dissertation is: *What is the structure of the inner disk?* The following chapters in this dissertation will address the following sub-questions to this larger question through the use of accretion variability as a probe of the typically unobservable inner disk.

1.6.1 *Is the accretion column connecting the disk to the star inherently unstable?*

Predictions made by the analytic models of Adams & Gregory (2012) suggest that the accretion column may be unstable under specific conditions relating to the equation of state for pressure and the magnetic field geometry. Chapter 2 presents numerical fluid simulations to test this prediction by constructing a model that solves the system under the same assumptions used by that work. Chapter 4 presents short-cadence *TESS* light curves with simultaneous LDT observations to identify regions of quasi-periodicity that may be explained by thermal instabilities at the base of the accretion column at the star.

1.6.2 *What are the observable accretion signatures of variability driven by the inner disk?*

By identifying signatures of variability driven by the inner disk, a better picture of the structure of the inner disk can be formed. Chapter 2 explores the effect of adding driving functions to simulate turbulence in the inner disk as a source of variability. Chapter 3 presents an updated version of the Calvet & Gullbring (1998) accretion shock models which produce synthetic spectra of the accretion column. The fluid simulations from Chapter 2 are further expanded in Chapter 5 using this accretion shock model to produce synthetic light curves that can be compared to

real observations of accreting young stars and their associated Q and M statistical variability metrics.

1.6.3 *Is the material in the inner disk clumpy or homogenous?*

The small physical extent of the inner gas disk makes resolving it impossible for current traditional observing methods (e.g., coronagraphy and interferometry). Instead, the physical structure of this region is inferred via signatures of accretion. Observations of CTTS suggest that multiple columns may be responsible for transporting material from the inner rim of the gas disk to the stellar surface, but multiepoch observations of individual objects that can be used to address this type of inference are limited. Chapter 3 presents multiepoch UV *HST* spectra of 5 CTTS to test how the mass accretion rate and the distribution of accretion columns with different densities change over time. Additional discussion is included on one object, which displayed evidence of a highly-collimated, dusty accretion column occulting a fraction of the star. Chapter 4 presents additional multiepoch UV *HST* spectra for one well-studied object, which was observed simultaneously by *TESS* in the short-cadence mode.

2

Time-dependent Models of Magnetospheric Accretion onto Young Stars

A similar version of this chapter was published in the Astrophysical Journal by Robinson et al. (2017).

2.1 Introduction

In this chapter, I focus on the innermost region of the disk, and variability due to changes in the accretion rate that occur on day-to-week-timescales. This type of variability is faster than what is expected from viscous processes, since the viscous timescale in the inner disk is on the order of several years (Hartmann, 2008). Proposed sources of variability on these timescales include Rayleigh-Taylor instabilities that produce variable "tongues" of material that flow between magnetic field lines (Kulkarni & Romanova, 2008) and magnetorotational instabilities that can cause changes in the amount of material available for accretion as a function of time (Romanova et al., 2012). A monitoring campaign of NGC 2264 observed multiple accretion signatures that appear to fit these models well (Stauffer et al., 2014), providing motivation for continued modeling of the inner regions of the disk.

The hydrodynamics of gas traveling along magnetic accretion columns has been studied analytically, assuming steady-state flows (e.g., Hartmann et al., 1994; Li,

1996; Koldoba et al., 2002). Under the assumption that the accretion columns are well described by a polytropic equation of state ($P \propto \rho^{1+1/n}$), analytic work suggests a transonic steady-state solution that approaches freefall velocities may not be possible within the accretion columns if the effective polytropic index, n is smaller than a critical value (Adams & Gregory, 2012). These authors developed a coordinate system that follows magnetic field lines aligned with the stellar rotation axis, under the assumption that the magnetic field is strong enough to dominate the flow. This allows for the transformation of the system to a one-dimensional (1D) problem, with semi-analytic steady-state solutions for the isothermal case where $n \to \infty$. The general form for the predicted constraint on the minimum value of n that allows these solutions to exist is $n > \ell + 3/2$, where ℓ is the highest order multipole component of the magnetic field near the star. This constraint only holds in the inner limit where $r \to 0$. The predicted absence of this type of solution under certain conditions may imply the possibility of spontaneous variability generated within accretion columns, even in the case of a constant accretion rate feeding the columns. However, this prediction cannot be tested analytically, and we must appeal to time-dependant numerical calculations.

Expanding upon this analytic work, I present a 1D hydrodynamic simulation of accretion onto a CTTS, using a coordinate construction that follows the accretion columns from the gas disk to the star. I investigate two possible sources of short timescale accretion variability: inherent variability from the inability to reach freefall speeds suggested by Adams & Gregory (2012) and variability driven by turbulence/instabilities at the inner disk edge. In this work, I also study the hydrodynamics within the accretion column and derive possible observable quantities.

This chapter is structured as follows. The construction of the magnetospheric accretion system and the numerical method used to simulate the system are presented

in §2.2 and §2.3. I then present simulations testing for spontaneous variability and discuss their implications in §2.4. Explicit time dependence is then included, the results of which are shown in §2.5. I discuss implications of the simulation on the current understanding of variability within the inner disk and possibilities for observations in §2.6 and conclude in §2.7.

2.2 Model Construction

The magnetic fields of CTTS are strong near the star, in some cases reaching up to 6 kG at the photosphere (Valenti & Johns-Krull, 2004), and as such, I assume that the materials in the accretion columns follow the stellar magnetic field lines, which are unperturbed by the accretion flow and co-rotate with the star (see Koldoba et al., 2002; Adams & Gregory, 2012, for a discussion of the validity of this approximation). The magnetic truncation radius, and thus the inner edge of the disk, is assumed to be co-located with the co-rotation radius for simplicity. The large-scale magnetic field of CTTS is dominated by the dipole component, but some CTTS have significant octupole components (Donati et al., 2011b). In this work, I investigate two field geometries: a pure dipole field and a field formed from the sum of dipole and octupole components. Finally, I take the magnetic field to be constant in time and its axis to be aligned with the rotation axis.

This assumption does prevent the magnetic field lines from becoming twisted from differential rotation, which is an important part of angular momentum transfer within the inner disk (Ustyugova et al., 2006) and could perhaps be a source of variability itself. In regard to the transfer of angular momentum, the timescale in which the rotation period of the star changes ($\sim 10^6$ y; Ustyugova et al., 2006) is many orders of magnitude longer than the roughly week-long timescales this chapter focuses on. Thus, I assume the stellar rotation rate is constant.

2.2.1 Coordinate System

Under the assumptions outlined above, the system can be reduced to a 1D problem using a set of coordinates that follows current-free, axis-symmetric magnetic field lines that co-rotate with the star. Because the magnetic field configuration is current-free, and thus curl-free, it can be described as the gradient of scalar fields, or coordinates, denoted here as (p, q). The coordinate p describes the distance along a given field line, while q describes which field line is being traced. These coordinates are orthogonal; ∇p points along the field line and ∇q points in the poloidal direction, perpendicular to ∇p. The origin of the system is located at the center of the star. A complete formulation of this coordinate system and its associated scale factors can be seen in Adams & Gregory (2012). For the numerical calculations, a grid was constructed along the magnetic field lines (the p coordinate). A magnetic field containing dipole and octupole contributions is given by

$$\begin{aligned}\mathbf{B} = \frac{B_{\rm oct}}{2}\xi^{-5}[(5\cos^2\theta - 3)\cos\theta\,\hat{\boldsymbol{r}} \\ +\frac{3}{4}(5\cos^2\theta - 1)\sin\theta\,\hat{\boldsymbol{\theta}}] \\ +\frac{B_{\rm dip}}{2}\xi^{-3}(2\cos\theta\,\hat{\boldsymbol{r}} + \sin\theta\,\hat{\boldsymbol{\theta}})\end{aligned} \tag{2.1}$$

where ξ the radius from the center of the star given in dimensionless stellar radius units, $\xi \equiv r/R_*$ and θ the colatitude. B_{dip} and B_{oct} are the strengths of the dipole and octupole terms in the multipole expansion of the magnetic field at the stellar surface. The parameter Γ is defined as the ratio of the coefficients of the composite multipole field,

$$\Gamma \equiv \frac{B_{\rm oct}}{B_{\rm dip}}. \tag{2.2}$$

The coordinates q and p can be written in terms of the standard spherical polar coordinates. The coordinate p, which traces along individual magnetic field lines, can be written as

$$p = -\frac{1}{4}\xi^{-4}\Gamma(5\cos^2\theta - 3)\cos\theta - \xi^{-2}\cos\theta\,, \tag{2.3}$$

while the orthogonal coordinate q is given by

$$q = \frac{1}{4}\xi^{-3}\Gamma(5\cos^2\theta - 1)\sin^2\theta + \xi^{-1}\sin^2\theta. \tag{2.4}$$

Two configurations of magnetic fields were used in the simulation, $\Gamma = 0$ and $\Gamma = 10$. Examples of the field lines for the different geometries are shown in Figure 2.1. The addition of the octupole components has a substantial impact on the regions of the accretion column at small radii. Near the surface of the star, the cross-sectional area of the accretion column is greatly reduced in the dipole plus octupole case, compared with the pure dipole configuration, which will lead to increased levels of compression of the flow. Near the surface of the disk, the effect of adding octupole terms is minimal, due to the steep radial fall off of the octupole component, causing the truncation radius to be set almost purely by the strength of the dipole field alone (Gregory et al., 2016).

2.2.2 Hydrodynamic Formulation

As the magnetic field is assumed to be strong enough to force material to only flow along field lines, the magnetic term in the force equation can be eliminated. The angular velocity vector is defined such that $\mathbf{\Omega} = \Omega\hat{z}$, and is aligned with the dipole and octupole moments. Transforming into a non-inertial frame introduces centrifugal force terms. Because the fluid is forced to flow solely along the field lines with no $\hat{\phi}$ components in this frame, the Coriolis term can be eliminated in the 1D force

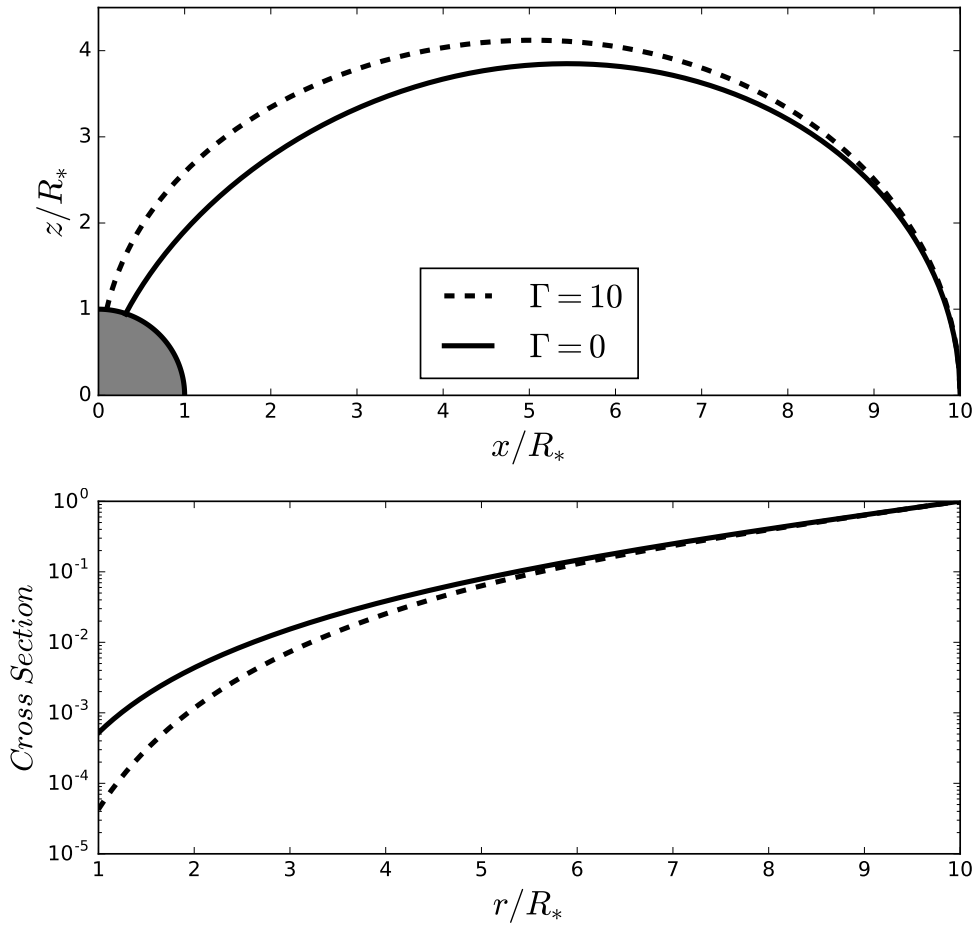

Fig. 2.1: *Top panel:* schematic showing both magnetic field configurations. The solid line traces the field line described by pure dipole fields ($\Gamma = 0$), while the dashed line traces the field line composed of the sum of dipole and octupole components ($\Gamma = 10$). *Bottom panel:* cross-sectional area of the accretion column as function of radius, normalized to the cross-sectional area of the column at the disk. The dipole + octupole field configuration has a smaller cross section near the stellar surface, leading to higher levels of compression as material flows toward the star compared with the pure dipole field configuration.

equation. After these simplifications, the continuity, force, and energy equations take the form

$$\begin{aligned} \frac{\partial \rho}{\partial t} + \nabla \cdot (\rho \mathbf{u}) &= 0 \\ \frac{\partial \mathbf{u}}{\partial t} + (\mathbf{u} \cdot \nabla)\mathbf{u} &= -\frac{1}{\rho}\nabla P - \nabla \Psi - \mathbf{\Omega} \times (\mathbf{\Omega} \times \mathbf{r}) \\ \frac{\partial}{\partial t}(\frac{e}{\rho}) + (\mathbf{u} \cdot \nabla)(\frac{e}{\rho}) &= -\frac{P}{\rho}\nabla \cdot \mathbf{u} \end{aligned} \tag{2.5}$$

where ρ is the density, e is the internal energy, $\mathbf{u}$ is the fluid velocity, Ψ is the gravitational potential, and P is pressure. Pressure, written using an effective adiabatic index $\gamma = (n+1)/n$ and the ideal gas law, takes the form

$$P = (\gamma - 1)e \tag{2.6}$$

The adiabatic sound speed a, derived from the adiabatic equation of state and assuming an ideal hydrogen gas, is written as

$$a = \sqrt{\gamma \frac{k_b T}{m_H}} \tag{2.7}$$

where k_b is the Boltzmann constant, m_H is the mass of a hydrogen atom, and T is the gas temperature.

The governing equations can be written in dimensionless 1D forms along the co-rotating field line. Reference quantities were used to scale ρ, e, and the velocity along the field line, u_p, and can be written as

$$\alpha \equiv \frac{\rho}{\rho_1} \quad u \equiv \frac{u_p}{a_1} \quad \epsilon \equiv \frac{e}{a_1^2 \rho_1} \tag{2.8}$$

where a_1 and ρ_1 are the sound speed and density at the inner edge of the disk. Distances have been written in terms of the stellar radius (ξ), and time has been

scaled using the stellar crossing time for a velocity a_1. This allows us to write the governing equations as

$$\frac{\partial \alpha}{\partial t} = -\frac{\alpha u}{h_p}\Big[\frac{1}{\alpha}\frac{\partial \alpha}{\partial p} + \frac{1}{u}\frac{\partial u}{\partial p} + \frac{1}{h_q h_\phi}\frac{\partial}{\partial p}(h_q h_\phi)\Big] \tag{2.9}$$

$$\begin{aligned}\frac{\partial u}{\partial t} &= -\frac{1}{h_p}\Big[u\frac{\partial u}{\partial p} - \frac{1}{\alpha}\frac{\partial P}{\partial p} - \frac{b}{\xi^7}\frac{\cos\theta f}{H}\Big] \\ &\quad +\omega \sin\theta(\hat{x}\cdot\hat{p})\end{aligned} \tag{2.10}$$

$$\begin{aligned}\frac{\partial}{\partial t}\Big(\frac{\epsilon}{\alpha}\Big) &= -\frac{u}{h_p}\Big[\frac{\partial}{\partial p}\Big(\frac{\epsilon}{\alpha}\Big) - \frac{(\gamma-1)}{u}\frac{\epsilon}{\alpha}\frac{\partial u}{\partial p}\Big] \\ &\quad -\frac{u}{h_p}\Big[\frac{(\gamma-1)}{h_q h_\phi}\frac{\epsilon}{\alpha}\frac{\partial}{\partial p}(h_q h_\phi)\Big]\end{aligned} \tag{2.11}$$

where ω is a dimensionless parameter that measures stellar rotation, $\omega = \Omega R_*/a_1$. The gravitational potential is represented using the dimensionless quantity b, which measures the depth of the gravitational potential well relative to the sound speed, written as $b = GM_*/R_* a_1^2$. More discussion of this dimensionless formulation of the system is provided in Adams & Gregory (2012). The curvilinear coordinate scale factor for the p coordinate is denoted h_p, while f and H are ancillary functions of ξ and θ. The functional forms for these terms, along with an analytic expression for $(\hat{x}\cdot\hat{p})$ are shown in the Appendix.

2.3 Numerical Method

The hydrodynamic problem is solved using the method of finite differencing under a ZEUS-style framework using a time-explicit, multi-step solution procedure (see Stone & Norman 1992). This style of simulation uses a staggered mesh framework in which the density, internal energy, and gravitational potential are zone centered, while the velocity is face centered. The grid is constructed with 'ghost' cells at both ends of the simulation domain, which are used to set boundary conditions. The

velocity, density, and internal energy are updated using operator splitting in two sub-steps: the 'source' update and the 'transport' update.

The numerical method is based on Owen & Adams (2016), who simulated magnetically controlled isothermal outflows from hot Jupiters. In this work, the code has been modified to include the energy equation in the system of hydrodynamic equations. In addition, I have modified the geometry of the problem from a dipole plus vertical field to either a pure dipole or a dipole plus octupole magnetic field configuration, and added the effects of rotation. More discussion of the changes can be found in the Appendix.

2.3.1 Sub-steps

The first step is the source update, in which the velocity and the internal energy are updated by solving finite-difference versions of the governing differential fluid equations. The velocity is updated during the source update, due to gravitational forces and pressure gradients acting along the accretion column. Because the system is in a non-inertial rotating reference frame, the velocity is also updated due to the centrifugal terms that appear in the force equation. The full difference equations are presented in the Appendix. In order to capture shocks, an artificial viscosity is introduced using a full stress tensor formalism. The full stress tensor is need because of the complicated geometry. The full details of this artificial viscosity tensor are presented in Appendix A of Owen & Adams (2016). Finally, the internal energy of the system is updated due to compressional heating in a time-centered manner (Stone & Norman, 1992).

The second step is the transport update in which finite-difference approximations to the integral advection equations are used to update the velocity, density, and internal energy. Reconstruction at the cell boundaries is performed in a second-order manner with a van Leer limiter (see van Leer, 1977).

2.3.2 Boundary Conditions

At the stellar boundary, I apply standard outflow boundary conditions (see Stone & Norman, 1992). At the disk boundary, I used two different approaches. For the steady simulations described in §2.4, the density and internal energy were held fixed, while for the simulations with explicit time variability described in §2.5, the density was varied according to a prescribed time-dependent function and the internal energy was varied such that the ghost cells maintained constant entropy.

2.3.3 Simulation Parameters

The simulations were performed in a dimensionless manner; however, I present the results here in dimensional form in order to compare to real systems. Since the flows are scale-free, the specific values of the density and temperature do not matter inside the simulation.

The material near the footprint at the disk is assumed to have a density of 3×10^{11} cm^{-3}; this is taken from the analytic accretion solutions of Adams & Gregory (2012) for a standard accretion rate of 1×10^{-8} M$_\odot$ yr^{-1} and temperature of $10,000$ K due to heating from UV radiation. Because the cross-sectional area of the accretion column is a function of chosen multipole geometry, the 'standardized $\dot{M}$' values reported in this work are mass fluxes at the star scaled to the equivalent mass flux through an area of 1 cm^2 at the surface of the disk. Mass accretion rates are scaled this way to facilitate comparisons between the two simulated geometries that would otherwise be drawing material from unequal sized magnetic footprints. Converting to the more observationally interesting quantities of the mass flux at the surface of the star can be done by dividing the reported scaled mass flux by the dimensionless cross section of the accretion column, A (see Figure 2.1). For the two geometries discussed in this chapter, $\Gamma = 0$ and $\Gamma = 10$, the ratio of the cross-sectional area of the column

at the stellar surface to the disk is 5.14×10^{-4} and 4.18×10^{-5} respectively. The global stellar accretion rate in terms of a hot spot filling factor, f, and this standardized mass flux can be written as

$$\dot{M}_{global} = f(4\pi R_*^2)\frac{\dot{M}}{A} \tag{2.12}$$

For reference, a young accreting star with $f = 0.03$, $R_* = 1.5\,\mathrm{R}_\odot$ with a mass flux of $\dot{M} = 1.0 \times 10^{-7}\,\mathrm{g\,s^{-1}\,cm^{-2}}$ under the pure dipole construction, will have an accretion rate of $1.3 \times 10^{-9}\,\mathrm{M_\odot yr^{-1}}$ or $1.5 \times 10^{-8}\,\mathrm{M_\odot yr^{-1}}$ under the dipole plus octupole configuration. Both accretion rates are plausible for T Tauri stars (Ingleby et al., 2013).

I can determine the degree to which the flow is magnetically controlled by considering the magnetic plasma β – the ratio of the gas pressure to the magnetic pressure. For a CTTS with a surface magnetic field strength $B_{\rm dip} = 3$ kG (e.g., Johns-Krull, 2007) and an inner disk edge of 10 R_*, the parameter β is $\ll 1$ several scale heights up in the disk where the accretion flow is launched. This finding validates the assumption that the magnetic field is unperturbed by the flow. In the midplane of disk, however, the density is larger and the magnetic plasma β can approach unity. As result, MHD effects could be important in the midplane and hence in setting the location of the truncation radius.

The simulation domain is separated into to 1024 cells (with resolution tests discussed later). I fix the ghost cell used to set boundary conditions at the disk to a height of $0.05\,R_\star$ above the midplane of the disk. Because gravitational potential and velocity gradients are larger near the star, a non-linear grid spacing is adopted to ensure the accuracy of the simulation. The grid spacing is scaled using a power-law such that the resolution near the star is higher than near the disk.

The simulation was initialized with a very small negative velocity. Density throughout the simulation is initially set to the density at the disk. The internal energy of the simulation, e, is set such that the entropy is constant throughout the simulation. Transient behavior from initialization dissipates over the duration of several stellar sound crossing times, and the choice of initial flow profile is not important. Time steps were chosen within the simulation by enforcing a maximum Courant number of 0.5 (Courant et al., 1928). Additionally, the time step was not allowed to increase by more than 30% between subsequent steps.

2.4 Results: Searching for Spontaneous Variability

As introduced previously, prior analytic work suggested that a constraint can be placed on the index n for steady-state solutions that pass smoothly through the sonic point and reach nearly freefall speeds near the star (Adams & Gregory, 2012). If n does not satisfy this constraint, the system may be unable to reach this type of solution. This effect could generate spontaneous variability within the accretion column, and could thereby explain some of the short-term variability observed in TTS. This variability would be predicted to occur when the polytropic index n is sufficiently small (corresponding to a stiff equation of state); i.e., $n < \ell + 3/2$ where ℓ is the highest order multipole with significant contributions to the magnetic field and in the inner limit where $r \to 0$. For the case where the stellar magnetic field is a pure dipole ($\ell = 1$, $\Gamma = 0$), the critical value for n is 2.5.

To test this prediction, a set of simulations were performed above and below this critical value of the polytropic index, with other parameters chosen to be representative of those for CTTS. The simulation set spanned $b = [200, 350, 500]$, and n in the range 2.0–4.7 with a step size of 0.3 (although lower n's and b's were explored; see §2.4.1). Transient effects from initialization dissipated over the course of a few sound

crossing times ($\sim$ days). After these effects subsided, the simulations converged to a steady state and the flow was able to smoothly pass through the sonic point and reach freefall speeds for all combinations of b and n in this set. The condition of steady-state was confirmed by differencing the output velocity information between time steps, yielding accelerations in the regime of numerical rounding error. In order to be sure this was not a numerical issue, additional tests of a steady state flow are described in §2.4.2. Snapshots of an example simulation with values of $n = 2.0$, with $b = 500$ converging to a steady-state solution can be seen in Figure 2.2. The absolute value of the residuals from differencing the density at a chosen point and the density at the same point in the final time step in the simulation is also shown in Figure 2.2. Velocity and density approach the final value with oscillatory behavior, with a linearly decaying amplitude in semi-log space as time progresses, indicating the simulation is indeed, converging toward a steady-state solution.

A second set of simulations was used to simulate systems with octupole + dipole stellar magnetic field geometry using the same distribution of values for b and n. The addition of octupole components increases the amount of compression that occurs near the star, further heating the gas and raising pressure. Spontaneous variability for this field line geometry is predicted to occur when $n < 4.5$. The relative contribution of the octupole moment compared with the dipole moment for the magnetic field, Γ, was fixed to a value of 10 for this set of simulations. These simulations were analyzed using the same method as the pure dipole case, and returned similar results; the simulations converged to a steady state after the initial transient behavior subsided. Again, the velocity was able to reach freefall speeds for each combination of b and n.

2.4.1 Subsonic Simulations

A subset of more extreme simulations with low masses and stiff equations of state were unable to reach a steady-state solution because the flow failed to remain

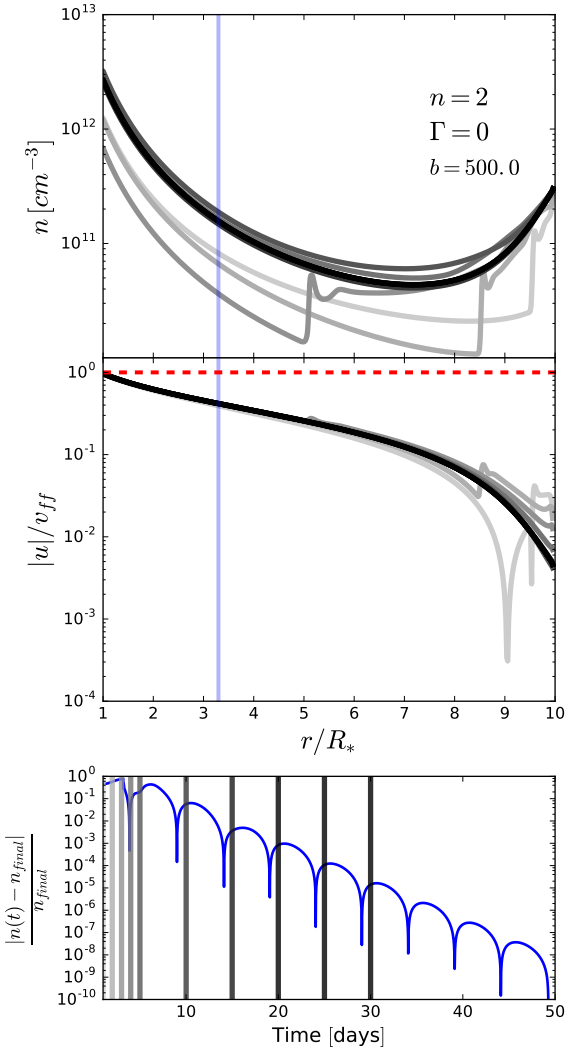

Fig. 2.2: *Top panels:* snapshots of density and speed for a transonic simulation under a dipole magnetic field configuration. The value of n in this simulation is below the predicted critical value of $n = 2.5$, but the flow still converges to steady state. The snapshots are colored such that lines darken as time increases. The dashed red line shows the freefall velocity. *Bottom panel:* absolute difference between the density as a function of time and the density in the final time step at the location of the blue line shown in the top panels. The vertical lines correspond to the snapshots shown in the top panel. The simulation oscillates and converges toward the steady-state solution with an exponentially decaying amplitude.

supersonic after the initial transient phase subsided. The depth of the stellar potential well (b) determines where the sonic point is located along the column, and if it is small enough, the sonic point will lie within the star. In this case, slow ($|u| < 0.1 v_{ff}$) time-variable solutions dominate the flow (analogous to the known time-variable "breeze" solutions; Velli 1994; Del Zanna et al. 1998; Owen & Adams 2016). These solutions occur when b is small, the compression of the flow is high (from octupole magnetic field components), the flow is heated significantly (n is small), and the sonic point criterion cannot be satisfied in the region between the inner edge of the disk and the stellar surface.

The original criterion for non-freefall flow has the form $n < \ell + 3/2$ and thus does not depend on the depth b of the gravitational potential well. On the other the hand, the previous results show departures from freefall flow with sufficiently small values of b. One can understand this behavior as follows. The incoming flow fails to reach freefall speeds when the pressure term does not decrease fast enough relative to the gravitational term as the radius decreases. Under conditions where $n < \ell + 3/2$, the pressure term will always dominate in the limit $\xi \to 0$. As I have shown, however, the small dynamic range of the flow (the disk edge is only an order of magnitude larger than the stellar radius) does not generally allow for the flow to reach the regime (small ξ) where the pressure dominates, so the flow retains nearly freefall speeds. As shown in equations (24 – 26) of Adams & Gregory (2012), the depth b of the gravitational potential well appears as a coefficient in the terms under comparison. As a result, when b is large, the gravitational term dominates over a larger dynamic range (in ξ), and freefall speeds can be reached even when $n < \ell + 3/2$. For small values of b, the gravitational term is less effective at enforcing freefall speeds, and departures can arise (as discussed previously).

Nonetheless, these time-variable subsonic solutions are unlikely to present themselves in the region of parameter space realized by CTTS. Furthermore, observed signatures associated with shocks and high velocity flows at the surface of the star also indicate these solutions are not occurring. Although I reject these subsonic solutions as realistic models for CTTS, they may be relevant for systems with lower masses (e.g., planets and brown dwarfs), should they possess strong octupole (or higher order) magnetic field components. I caution this conjecture needs to be investigated in more detail before any predictions can be made.

2.4.2 Tests

Numerous tests were performed to check that the simulations were producing accurate results to ensure that the lack of spontaneous variability in the transonic solutions was not a spurious result from a numerical error. In any steady-state flow, the Bernoulli potential is constant; the Bernoulli potential of the flow was calculated and was found to converge to a nearly constant value after initial transient effects had dissipated. Figure 2.3 shows the difference between the potential at the disk and the Bernoulli potential along the field line for the simulation shown in Figure 2.2. Although there are deviations from a constant value along the field line, they are small, and the magnitude of the deviations is in part dependent on the resolution of the simulation. Under a resolution of 1024 cells, the maximum deviations are on the order of 0.1%. The largest deviations from a constant potential generally occur near the star where the velocity of the flow is largest and the divergence of the magnetic field lines is steepest. A second simulation is also shown in Figure 2.3 in which the number of cells has been doubled to 2048, yielding maximum deviations from potential at the disk on the order of 0.02%.

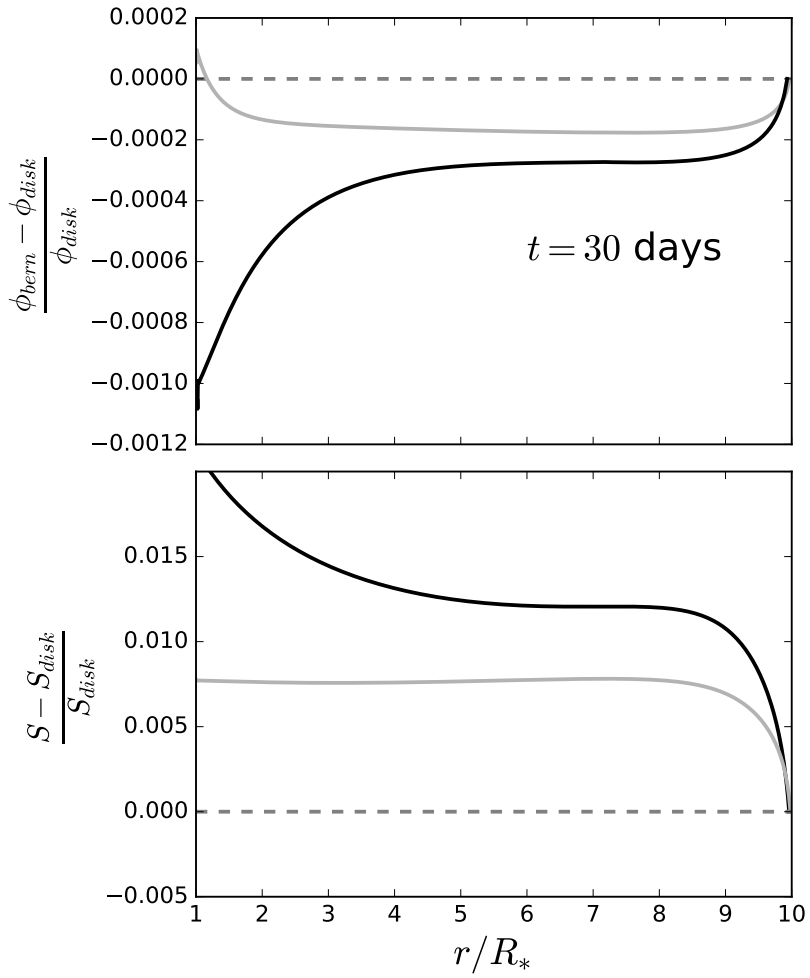

Fig. 2.3: *Top panel*: normalized relative difference in the Bernoulli potential at $t = 30$ sound crossing times for the simulation shown in Figure 2.2 in solid black. A higher resolution simulation, shown in gray, was run with 2048 cells and indicates smaller deviations from the expected constant potential. *Bottom panel*: normalized relative difference between entropy throughout the simulation and entropy at the disk.

The construction of the numerical scheme does not actively ensure that entropy is conserved to machine-limited precision, as I explicitly work with internal energy. This provides another method to test the simulation, as the level of entropy in each cell should converge to a constant value once transient behavior has subsided under an adiabatic equation of state. The entropy of each cell was calculated and then normalized to the value of entropy at the inner edge of the disk. Entropy remained roughly constant throughout the system, with the largest deviations on the order of 1.5%. The bottom panel of Figure 2.3 shows the normalized entropy throughout the simulation shown in Figure 2.2. The same simulation run at the higher resolution is also shown in that panel with significantly smaller deviations, indicating that these deviations from constant entropy will continue to decrease with increasing resolution.

Finally, an analytic solution exists for the isothermal case. This provides a way to test the portions of the simulation not associated with the energy fluid equation. The results for a simulation using dipole geometry run under an isothermal equation of state are compared against the analytic solution in the Appendix. As shown in Figure 7.1, the simulation closely agrees with the analytic result.

2.4.3 Lack of Variability

All of the transonic simulations run with a constant gas disk density converged to steady solutions, with no indication of spontaneous variability, or lack of near freefall velocities close to the stellar surface. The tests of the non-isothermal simulations, in addition to the comparison of an isothermal flow against the analytic result, suggest that the simulation is behaving physically. Instead, the assumptions that went into the prediction of a constraint on the possible values for n by Adams & Gregory (2012) may be insufficient for realistic systems. In particular, those authors note that the assumption of working in the limit where $\xi \to 0$ may not hold where the dynamic range of the system is not sufficiently large. For example, in CTTS the radial range

is only about a factor of 10 from the stellar surface to the disk's edge. The constraint placed on the polytropic index is based on how the thermal pressure compares with the ram pressure in the innermost regions of the system. If the flow is to reach freefall speeds, the ram pressure must dominate over the thermal pressure, which is the case for all of the supersonic simulations. In the cases where n has a value lower than the predicted constraint, the dynamic range of ξ does not appear to be large enough for the density term to dominate, since the minimum value of ξ is necessarily fixed at 1 (the stellar surface) and the other terms cannot be ignored.

2.5 Results: Disk-driven Variability

Following the inability to explain short-term accretion variability through spontaneous variability in the accretion column in the transonic solutions, I ran sets of simulations using time-variable boundary conditions. 3D MHD simulations have shown that density in the inner disk can be highly variable due to turbulence (Romanova et al., 2012). As an approximation to these naturally occurring density perturbations, the density at the inner edge of the disk was modulated manually. Two driving functions were used, sinusoidal oscillations and Gaussian pulses, both on top of a baseline density. These driving functions were chosen for convenience, allowing us to study a well-posed problem, but are unlikely to represent the true density variations in real systems, which are likely to be stochastic. The internal energy, and thus the pressure, at the boundary was set such that the cells at the boundary are varied adiabatically or isothermally in the isothermal models. The simulation was initialized in the same manner as before, and was allowed to evolve for 15 d before the driving functions were initiated, to avoid transients that occur upon initialization. It is shown in the bottom panel of Figure 2.2 that relative de-

partures from the steady-state solution were on the order of 10^{-2} after this amount of time.

In these models, I chose the dimensionless parameters that corresponded to a typical CTTS. These models were constructed with the following stellar properties: $M_* = 0.5\,M_\odot$, $R_{disk} = 10\,R_*$, and $R_* = 1.5\,R_\odot$. This yields a value of $b \sim 750$. Again, the temperature at the disk was assumed to be 10000 K and at a density of $3\times10^{11}\mathrm{cm}^{-3}$. The parameter space formed by Γ, n, the amplitude of the perturbation A, and the timescale of the perturbation was explored to examine the behavior of the accretion column under a variety of conditions.

2.5.1 Isothermal Sinusoidal Driving

In the first set of simulations with driven accretion, the accretion column was assumed to be isothermal and the density at the inner edge of the disk was forced to oscillate sinusoidally with a fixed period, P, and amplitude, A, written as

$$\rho_{disk}(t) = \rho_1[\frac{A}{2}(\sin(\frac{2\pi}{P}t) + 1) + 1]. \tag{2.13}$$

Simulations were run with P = [0.5, 1, 2, 4, 8] d, $\Gamma = [0, 10]$, and $A = [1, 2, 3]$.

The behavior of the flow fell into three regimes, depending on the driving period of the simulation. Simulations of isothermal flows with driving periods shorter than about a day (roughly the stellar sound crossing time) showed smaller amplitudes than the driving function near the stellar surface. This was because the flow could not react fast enough to the changes in density in the outer boundary (i.e., the flow cannot adjust on a time-scale shorter than the sound crossing time). The overdensities in the accretion column were mostly damped out when they collided with the star. The mass accretion rate of a simulation displaying this behavior with $P = 0.5$, $A = 3$, and $\Gamma = 0$ is shown by the orange line in Figure 2.4.

The second regime of behavior was observed in simulations with periods roughly 1d or longer. As the density was modulated at the inner edge of the disk, weak shocks form and then propagate along the field line. Figure 2.4 shows two simulations in this regime in green and purple. These shocks formed because the velocity of the flow was slow in the outer regions of the accretion column, allowing material to build up during periods of high density in the disk, and then fell in the form of a higher-density shock onto the star. The period of the accretion rate oscillations at the star matched the driving period of the boundary condition for all sets of simulation parameters. Finally, if the driving period became much longer than the flow time-scale (tens of days), the flow evolved steadily along the steady-state solutions.

In these driven accretion simulations, density was the quantity manually controlled at the outer boundary, which allowed the mass loss rate to change as a function of model parameters. The averaged mass accretion rate at the star for all of the isothermal simulations is shown in Figure 2.5. Simulations with larger amplitudes show higher mass accretion rates, which was expected because the mean density in the outer regions of the accretion column was higher for larger values of A. Systems driven with shorter periods in most cases had lower accretion rates. This was in part due to sharp peaks in the density, causing pressure gradients both inward and outward, that prevent matter from flowing onto the columns and in some cases even lead to flow away from the star. As the driving period increased, the pressure gradient become shallower. Simulations run with magnetic fields composed of dipole and octupole components showed lower accretion rates than simulations run under the pure dipole field, in agreement with the analytic steady-state solutions presented by Adams & Gregory (2012). In this construction of the magnetic field lines with $R_{disk} = 10\,R_\star$, the net centripetal and gravitational force along the field line was away from the star in the outer regions of the accretion column for both the pure

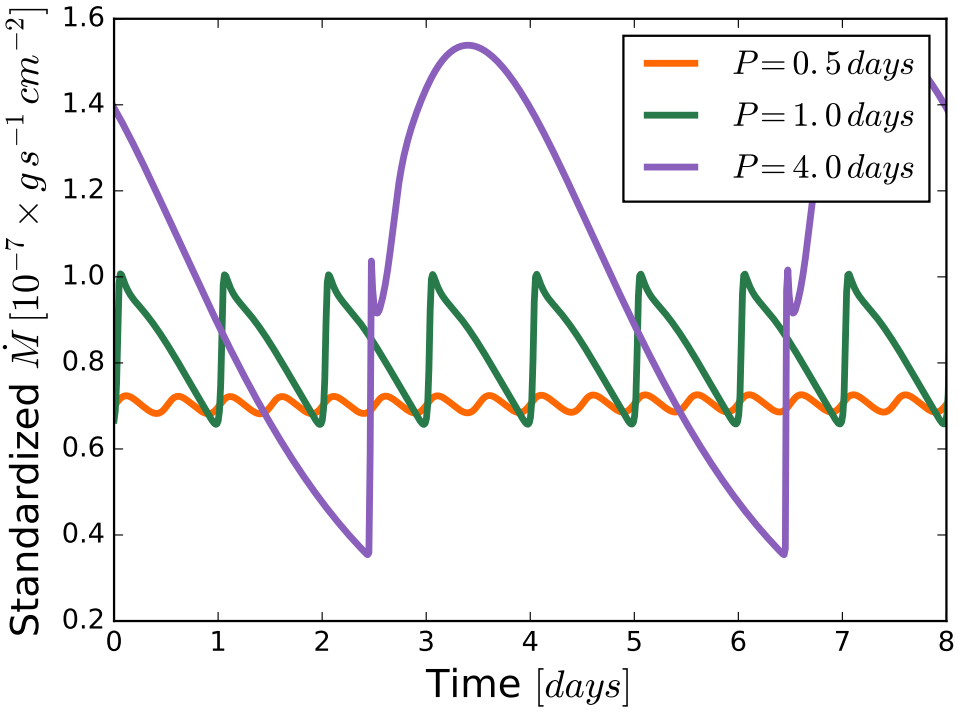

Fig. 2.4: Mass accretion rates near the surface of the star for isothermal simulations with different driving frequencies, written in terms of an equivalent mass flux at the disk. These simulations were run with oscillations with $A = 3$ under a pure dipole field configuration. Simulations with periods longer than roughly one sound crossing time form shocks in the outer regions of the accretion column that then propagate along the field line. Simulations with shorter periods do not shock, and show decreased accretion variability amplitudes compared with the longer period oscillations for the same value of A.

dipole and octupole + dipole configurations. This contributed to slow velocities in these regions.

2.5.2 Non-isothermal Sinusoidal Driving

Another set of simulations with sinusoidal driving density perturbations at the inner edge of the disk were run with values of n = [3.5, 4.5, 5.5], using the same set of periods and amplitudes as for the isothermal case. These simulations exhibit much

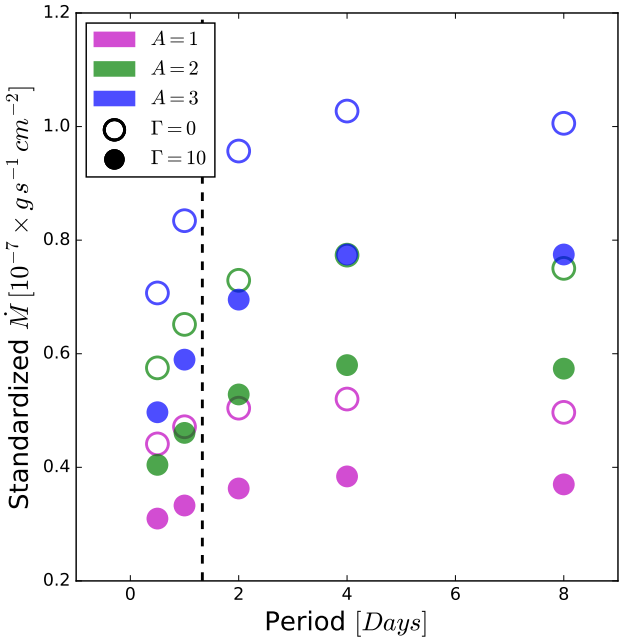

Fig. 2.5: Time averaged accretion rates written in terms of an equivalent mass flux at the disk, for isothermal simulations with sinusoidally driven boundary conditions. Different colors show driving amplitudes, A. Circles are simulations under a pure dipole field geometry, while squares show simulations that have octupole components in addition to dipole components with $\Gamma = 10$.

of the same behavior as seen in the isothermal simulations. Similar to the isothermal case, weak shocks formed in the outer regions of the accretion column in simulations with longer periods ($P > 1$ d). Figure 2.6 shows a snapshot of a simulation with a shock traveling along the accretion column. The shock speed for the inset plot was found using the Rankine–Hugoniot jump condition derived from the continuity equation, using densities and velocities measured on either side of the shock.

The time averaged accretion rate for the non-isothermal simulations is shown in Figure 2.7. Simulations with both short 0.5 d and longer 4.0 d oscillations are plotted to show both regimes of shocking and non-shocking behavior. For all simulations, the average accretion rate decreases as the accretion column becomes closer to isothermal.

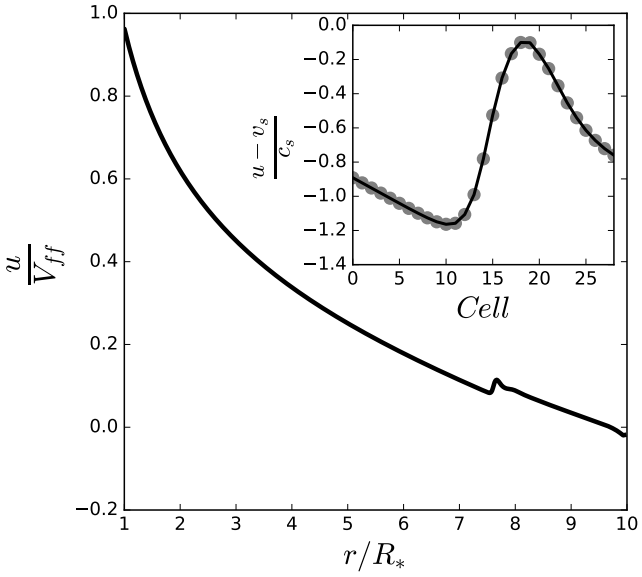

Fig. 2.6: Velocity snapshot in the accretion column for a simulation with sinusoidally driven outer boundaries. The simulation shown has values of $n = 3.5$, $P = 4.0$ d, $A = 3$, and $\Gamma = 0$. A shock forms in the outer regions of the simulation as material piles up and then falls onto the star. The inset shows velocity in the reference frame of the shock in terms of the sound speed. The gray dots in the inset show the location of the edge of each cell, which is where the velocity information is stored on the staggered mesh grid. Similar discontinuities also form in the isothermal simulations with driven accretion.

Changing A, Γ, and P reveals the same patterns as the isothermal models shown in Figure 2.5.

2.5.3 Gaussian Density Pulses

To isolate the effects that a single accretion burst would have on conditions near the stellar surface and test how long it takes the accretion column to relax from a perturbation, simulations were run with boundary conditions that manually varied the density at the disk-magnetosphere footprint as a Gaussian in time. This caused a density pulse to travel along the magnetic field line until it collided with the star, which for appropriate choices of the time-scale was a shock. The density at the inner

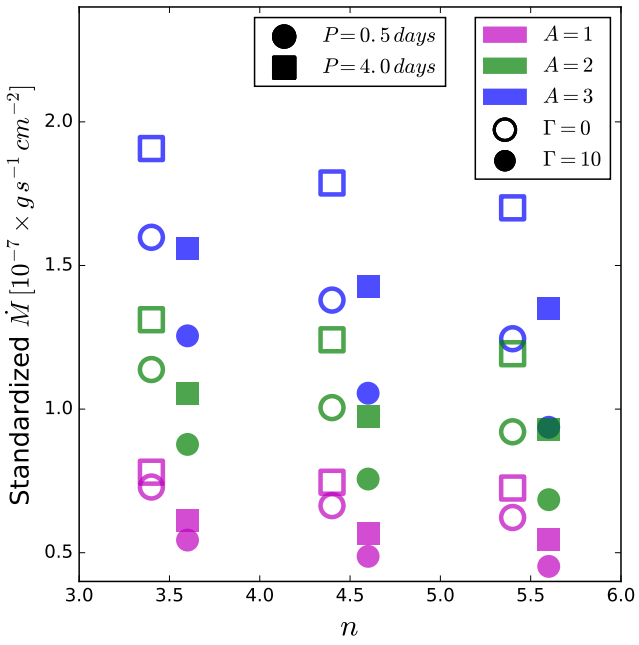

Fig. 2.7: Time averaged accretion rates for non-isothermal sinusoidally driven simulations as a function of n, A, Γ, and P. Open symbols show simulations with periods of 0.5 d, and closed symbols show simulations with 4.0 d periods. The points are shown slightly shifted from their true values of $n = [3.5, 4.5, 5.5]$ for clarity.

edge of the disk during the pulse is described as

$$\rho_{disk}(t) = \rho_1(1 + Ae^{-\frac{t^2}{2\sigma^2}}) \tag{2.14}$$

where A is the amplitude of the driving Gaussian and σ represents the timescale of the pulse.

Figure 2.8 shows the properties of the flow measured near the surface of the star as a function of time for several values of n, including the mass accretion rate, temperature, density, and velocity. The Gaussian density pulses shown have $\sigma = 1$ and $A = 3$. As discussed in section 5.1, the amount of material available for accretion onto the star is a function of the parameters describing the system, even if the time averaged density in the boundary remains the same.

The temperature, density, and velocity were measured near the star during the passage of the density pulse for a set of simulations with $A = [1, 2, 3]$, $\Gamma = [0, 10]$, and $n = [3.5, 4.5, 5.5]$, the results of which are shown in Figure 2.9. The initial values of T, number density, and u for the steady-state solutions, described in Section 4, are also shown in gray. As expected, the polytropic index is important in determining the temperature of the gas. As the polytropic index increases, the temperature of the gas decreases for all simulations and approaches the temperature of the upper layers of the gas disk (10,000 K). The density during and before the pulse is decreased in the simulations with higher polytropic indexes, but the effect is less dramatic than the effect on the temperature within the column. The velocity near the star gradually increases with increasing values of n, but does not quite reach the freefall velocity.

The geometry of the magnetic field lines also plays a critical role in the environment near the star. The field lines converge faster near the star for the octupole + dipole geometry, causing a higher level of compression at small radii compared with the pure dipole configuration. For the most isothermal simulations shown here ($n = 5.5$), while the pulse is passing through, the temperature difference between the pure dipole and the octupole + dipole configurations is on the order of 15,000 K. During steady state, the difference is roughly 8000 K. Density increases by roughly an order of magnitude while the pulse is passing through. The changes in velocity are quite small between the two field configurations, compared with the changes in the density and temperature, as the thermal energy is relatively insignificant compared with the kinetic energy of the flow. The largest change in the velocity between the two configurations for any of the simulations during the passage of the pulse is only $\approx 1.2\%$ of the freefall velocity.

The amount of time it takes the column to relax to its initial state provides a measure of the timescale between discernible accretion events. This timescale was

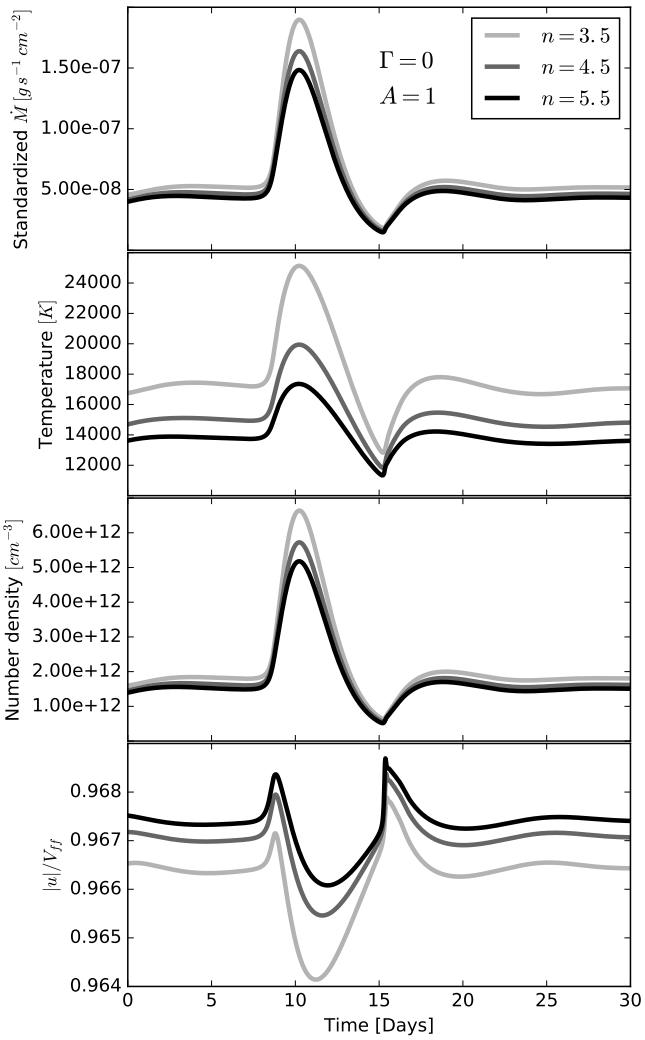

Fig. 2.8: Time-dependant behavior for the calculations with a Gaussian density perturbation, with varying values of the polytropic index. The top panel shows the accretion rate measured at the stellar surface. The next three panels show the pre-shock temperature, density, and velocity measured at the stellar surface.

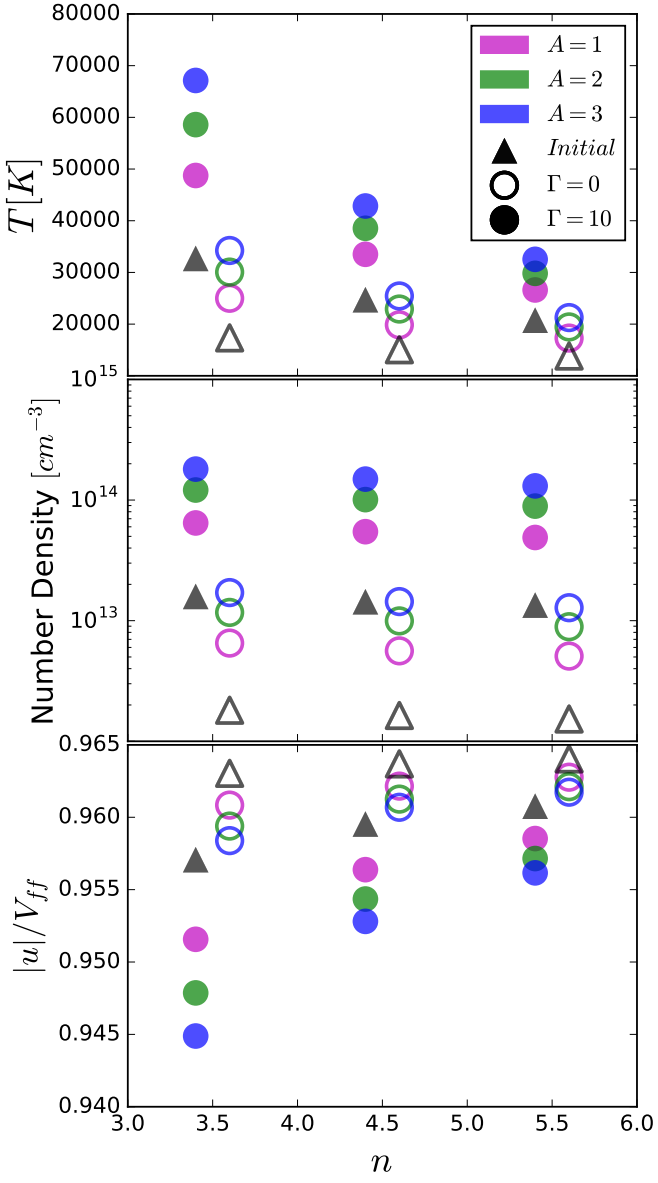

Fig. 2.9: Values of the preshock temperature, density, and velocity taken near the stellar surface during the peak of the density pulse for the Gaussian driven boundary conditions. The points are shown slightly shifted from their values of $n = [3.5, 4.5, 5.5]$ for clarity.

found to be a function of the polytropic index and the geometry of the magnetic field lines. Reminiscent of the bottom panel in Figure 2.2, the absolute value of the residuals between density in a cell near the stellar surface and the same cell at the final time step after the Gaussian pulse has passed can be enclosed within a power-law envelope. The envelope was found for each set of parameters within the sample by taking a finite temporal derivative of the density at a cell near the star, and fitting the residuals with a power-law at the times of the zero crossings.

The slope of the fit, β, and the half-life of the residuals is shown for all of the simulations in this sample in Figure 2.10. The half-life for simulations under the octupole plus dipole magnetic field configuration is $\approx 10\%$ longer than those under a pure dipole configuration. The polytropic index also plays a role in how quickly the accretion column relaxes. Simulations with smaller values of n are more rapidly damped than more isothermal simulations. For comparison, two fully isothermal simulations with $A = 3$ were run for $\Gamma = 0$ and $\Gamma = 10$, and had $t_{1/2} = 2.3$ and 3.1 d, respectively. The amplitude of the initial Gaussian pulse plays a limited role in the relaxation timescale, which suggests a single slope/half-life may be sufficient for describing the behavior of an accretion column undergoing events with similar timescales, while the parameters governing the system remain constant.

2.6 Discussion

I have discovered a new hydrodynamic mechanism that can lead to short-period, rapid changes in the accretion rate onto the star that may explain some of the short-period accretion variability observed in CTTS. I find that smooth time-dependent variability in the inner disk that feeds the magnetospheric accretion column is amplified along the column. Under certain conditions, these variations can shock in the accretion column, leading to rapid, large amplitude changes in the accretion rate

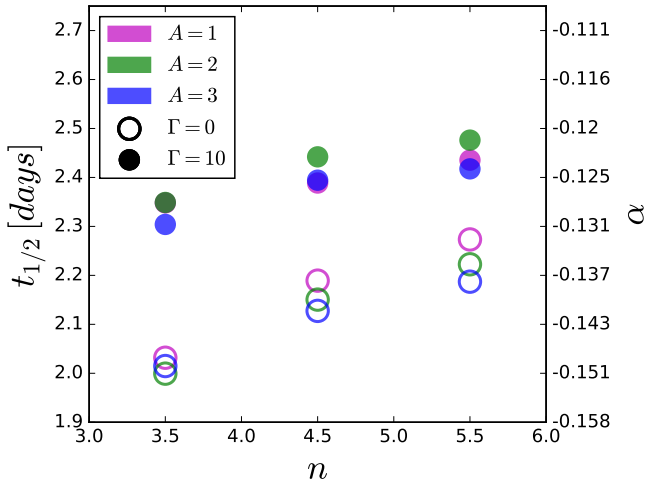

Fig. 2.10: Half-life of the encompassing envelope of the oscillatory residuals from $|\rho(t) - \rho_{final}|$ near the surface of the star after a Gaussian pulse travels through the accretion column. The power-law index of the damped oscillation envelope is shown on the right axis. Gaussian pulses of different amplitudes (A) are shown in different colors, and the two cases of field line geometry are represented by open and closed circles. The width of the driving Gaussian (σ) for these points is 2 d.

onto the star. This is a promising mechanism to explain some of the variable behavior observed in CTTS, as the inner disk that feeds the accretion column is likely to be variable. For example, density variations due to turbulence at the inertial scale have eddy turnover times $\sim \Omega^{-1}$ (e.g., Fromang & Papaloizou, 2006), which at the disk-magnetosphere boundary gives a timescale of order a day with amplitudes of density changes on order unity. Below I discuss the results in the context of recent observations and speculate about the connection between observations and the models.

A monitoring campaign of CTTS in NGC 2264 revealed variability in the light curves of most of the stars with significant UV excesses is dominated by short duration accretion bursts (Stauffer et al., 2014; Venuti et al., 2017, see also Cody et al. (2017) for a comparable campaign utilizing K2). For all of these moderately accreting stars but one (and it was systematically different than the others), the median rise

and fall times were 0.4 and 0.5 d, respectively, measured between the beginning or end of the burst and the center value. Qualitatively, this is comparable to the rise/fall behavior shown by some of the driven accretion scenarios presented here (e.g., the isothermal model driven using the sinusoidal boundary condition with a 1.0 d period shown in Figure 2.4). I also find shorter rise times in the simulations because of the shocking behavior presented in §2.5.1. Although further investigation is required, I speculate that the small asymmetry in the observed rise and fall times is because of the weak shocking behavior, followed by a slower relaxation period. It is important to note that the boundary conditions used in these simulations are continuous, and the buildup of material occurs within the active region of the simulation. Most of the accretion burst dominated light curves presented by Stauffer et al. (2014) did not show periodic structure and instead bursted stochastically, providing inspiration for future simulations with density fluctuations at the outer boundary distributed randomly in time with varying amplitudes. In the case of the variability at the disk being turbulence driven, one naturally expects a range of time-scales rather than a simple periodic signal.

In these simulations, the velocity approaches but never reaches the freefall velocity measured from the inner edge of the disk

$$V_{ff} = \left(\frac{2GM}{R_*}\right)^{1/2}\left(1 - \frac{R_*}{R_{disk}}\right)^{1/2} \tag{2.15}$$

because of the pressure support along the column. This is relevant for popular methods of calculating mass accretion rates that assume the material reaches V_{ff} as it strikes the surface of the star (e.g., Calvet & Gullbring, 1998; Gullbring et al., 1998). Because the kinetic energy flux (ρu^3) has such steep scaling with u, the difference between V_{ff} and the velocities shown in Figure 2.9 can result in calculated accretion rates that differ by up to $\sim 10\%$. Differences in velocities between simulations are

all within $\sim 0.01 V_{ff}$ of each other, so the effect on the calculated accretion rate will be a roughly constant multiplicative factor. As this is a nearly systematic effect for all models that assume $u \rightarrow V_{ff}$, this effect could easily be accounted for in future models of accretion shocks, although it does not drastically improve the accuracy of accretion rate measurements. Typical uncertainties in current measurements of accretion rates are generally much larger than 10%. For example, uncertainties in A_V alone can introduce a factor of two or larger (Ingleby et al., 2015).

As shown in Figure 2.9, the addition of octupole components to the magnetic field drastically increases the density in the accretion column near the stellar surface. The overall average accretion rate for this field configuration in the simulations is decreased slightly because of marginally slower velocities (see Figure 2.9 and Figure 2.7) and a smaller column cross section (Figure 2.1). The increased density in accretion columns with dipole plus octupole fields leads to higher kinetic energy fluxes. Higher kinetic energy fluxes lead to shock emissions that peak at shorter wavelengths (Calvet & Gullbring, 1998). Combined with the smaller column cross section, this suggests that stars with significant octupole components are more likely to show evidence of hotter accretion spots with more limited surface coverage. Because the fractional changes between the initial and final velocity are small while pulses are passing through, changes in the energy flux at the surface of the star closely trace the density profile as a function of time. The thermal component of the energy flux within the column is essentially negligible for all the simulations shown here, as the flow is highly supersonic.

Line emission associated with magnetospheric accretion columns has been observed (e.g., Johns & Basri, 1995a). The simulation in its current form does not explicitly include radiative energy losses, which could play a role in determining the dynamics occurring within the accretion column; rather, they are packaged up into

in the polytropic index. As a first consideration as to its importance, I compare the optically thin cooling timescale to the flow timescale. I note since this uses optically thin cooling, it will provide a maximal estimate of the cooling rate; if any of the lines were to become optically thick, then the cooling rate would be reduced. Figure 2.11 shows the flow timescale, the time it takes for material to flow over a distance where the density changes significantly compared with the cooling timescale derived from optically thin, solar metallicity, equilibrium cooling curves (Schure et al., 2009). The cooling is faster near the surface of the star where the magnetic field lines converge and material within the columns has been heated. Radiative cooling would likely drastically change the temperature structure seen in Figure 2.8. Figure 2.11 reveals cooling may also be significant near the magnetic footprint where the column connects with the disk and the flow velocities are slower. Cooling in the outer region of the accretion column would cause the flow to be more isothermal, affecting the formation process of the small shocks predicted in some of the driven accretion scenarios presented here. That said, discontinuities are present within the isothermal simulations presented.

Because the cooling timescale is proportional to ρ^{-1} for optically thin cooling and density in the simulation is normalized, the cooling timescale could be shifted up and down by changing the value for number density at the disk. The cooling curves shown here were generated assuming a density at the disk of $3 \times 10^{11}\,\mathrm{cm}^{-3}$, yielding a surface mass flux of $1.26 \times 10^{-7}\,\mathrm{g\,s}^{-1}\,\mathrm{cm}^{-2}$. The cooling timescale curve spans such a large range of timescales that even if the density at the disk was decreased by a factor of 10, radiative cooling would still be important within the inner and outer regions of the simulation. Because the mass accretion rate, and thus the density at the disk, can be highly variable, a range of values of the polytropic index are possible, even for a fixed location along the accretion column. If the accretion rate is very low

(e.g., $\dot{M} \approx 10^{-11} M_{\odot}/\mathrm{yr}$), a more adiabatic equation of state is appropriate for the magnetic footprint at the disk ($n \rightarrow 1.5$ for a monatomic ideal gas). For a larger accretion rate, the gas is best approximated by an isothermal equation of state (n $\rightarrow \infty$). Using the simple ρ^{-1} scaling for cooling timescales, estimates of when these regimes occur can be found using Figure 2.11 by scaling the cooling timescale curves inversely with density. The shape of the cooling curve is also itself a function of the polytropic index, so Figure 2.11 only provides a rough guide. Although the inclusion of radiative cooling is a logical next step in the development of this simulation, it would be a significant expansion on the current framework, and thus will be left for future work.

Finally, another source of heating or cooling that could arise is from MHD waves that are explicitly ignored in my treatment. Under an assumed magnetic field of 3 kG the Alfvén crossing time is significantly shorter than the flow crossing time ($\sim$ 20 times shorter). This suggests that Alfvén (and fast) waves[1] are likely too fast to generate the sort of variability that creates these shocks; however, they may be able to transport energy and hence lead changes in the thermodynamics of the flow, which in principle could generate variability. Full MHD simulations are required to investigate the importance of MHD waves on the dynamics and thermodynamics.

The goal of this set of simulations was to expand 1D analytic steady-state solutions into dynamic solutions, allowing us to gain physical insight into their results. The simplicity of the 1D approach of these simulations also allows us to easily compute observable quantities. However, the limitation of 1D comes at the cost of the loss of information associated with 2D and 3D simulations. This includes the naturally occurring instabilities at the disk boundary (e.g., Romanova et al., 2012), which I have artificially replicated with driving functions. We also lose information about

[1] In the low β flows I consider here, the slow wave is essentially the same as sound waves.

anything that occurs in the toroidal direction. That said, the use of a 1D system allows for a higher degree of control over the system, and allows for the connections between theory and simulation. One possible future advancement that could be introduced within this 1D construction is the misalignment of the magnetic field and the stellar rotation axis.

2.7 Conclusions

I have performed 1D hydrodynamic simulations of accretion onto young stars under multipole magnetic field configurations aligned with the rotation axis, using both dipole and dipole plus octupole configurations. Static and time-dependent inflow boundary conditions were used at the inner edge of the disk to investigate the possibility of spontaneous accretion variability and explore the effects of a time-variable accretion rate in the disk. Physical parameters that govern the flow were varied within the range expected in real accreting CTTS. The major conclusions of this chapter are summarized as follows.

1. I found no spontaneous variability is generated within the column, and the flow approaches steady-state freefall solutions for transonic solutions with values of n lower than the constraint suggested by Adams & Gregory (2012). The analytic constraint on n holds only in the limit of small radius $\xi \to 0$. In contrast, I found it is likely that realistic young stellar systems lack the dynamic range in radius necessary for the constraint to come into effect.

2. By introducing time variability in the density at the inner edge of the disk, weak shocks can form in the outer regions of the accretion column and propagate toward the star resulting in rapid, high-amplitude changes in the accretion rate in systems with variability periods longer than roughly a day (of order the sound crossing time). Variability driven with periods less than a day does

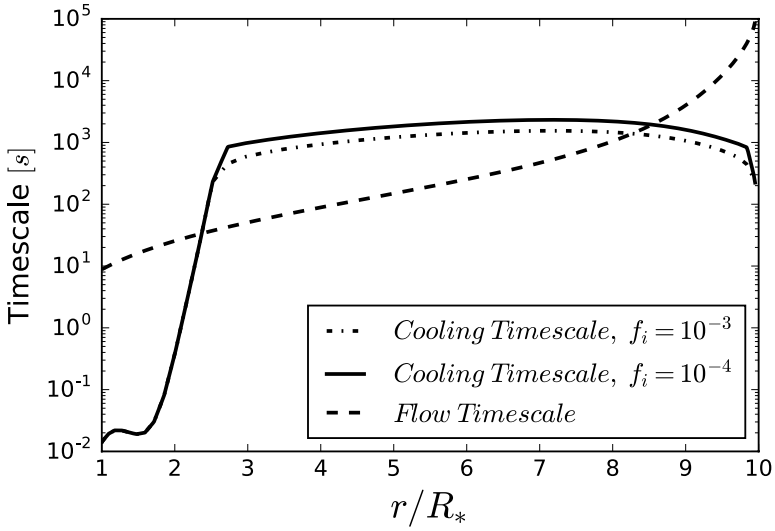

Fig. 2.11: Flow timescales and cooling timescales for the simulation shown in Fig. 2.2 after transients have subsided. Two values of the ionization fraction are shown for regions in the simulation with temperatures under 10^4K. The cooling timescale is faster or comparable to the flow timescale throughout the simulation, suggesting cooling is significant and should be included in future works. The cooling curves shown here are from Schure et al. (2009) and use solar metallicity values.

not appear to shock, and the oscillations in density are damped out, as the flow cannot respond fast enough to the changes. With variability timescales much longer than the flow timescale, the flow profiles closely follow the steady solutions but slowly vary between them, and no shocks form.

3. The rapid increases in accretion rate seen in the simulations are qualitatively comparable to short duration accretion burst dominated variability observed in monitoring campaigns (Stauffer et al., 2014; Venuti et al., 2017, see also Cody et al. (2017) for a comparable campaign utilizing K2). Specifically, the shocks in the accretion columns naturally result in fast accretion rate rise times as the shock hits the star, and slower fall times as the flow relaxes to steady state on the order of the sound crossing time (Figure 2.4).

4. Simulations were run featuring single time-dependent Gaussian density pulses to reveal how the accretion column reacts during both quiescent and high accretion states. Decreasing the polytropic index leads to higher temperatures and higher mass accretion rates. Magnetic fields with dipole plus octupole components lead to much higher densities near the surface of the star, with only slightly lower velocities compared with pure dipolar fields.

5. I find the outer and inner regions of the accretion column are likely to be isothermal, while the central portion may not be. Optically thin cooling timescales of material in the column indicate the temperature profile is more complex than a single adiabatic or isothermal equation of state can provide (Figure 2.11). Additional work to incorporate radiative cooling into this simulation is one possible next step to producing a more physically accurate representation of this system.

I have found short-term variability is not spontaneously generated within the accretion column, at least for my 1D examination of the system under realistic parameters for CTTS. Instead, variability on ∼day timescales is likely driven by instabilities and turbulence near the magnetic footprints of the flow, which can be modulated by shocks forming in the accretion columns. The limitations of this study lie in the assumptions of a polytropic treatment of pressure and the 1D treatment of the accretion column. Despite these limitations, these simulations provide a readily interpretable link between analytic solutions, more complex simulations, and observations. In the future, I expect an approach of the kind developed in this work can be used to directly compute time-dependent observables, such as the UV excess.

3

Multiepoch Ultraviolet *HST* Observations of Accreting Low-mass Stars

A similar version of this chapter was published in the Astrophysical Journal by Robinson & Espaillat (2019).

3.1 Introduction

As discussed in Chapter 1, the accretion shock region transforms the kinetic energy of the column into an observed continuum excess through the following processes. The kinetic energy of the column is transformed into thermal energy in the shock, heating the gas in the postshock region to temperatures of $\sim 10^6$ K. As the gas falls and cools, the energy is primarily reemitted as X-rays both toward and away from the star (Calvet & Gullbring, 1998). The X-ray emission traveling toward the star heats the underlying photosphere, forming a hot spot. Emission traveling away from the star heats the material in the preshock region to temperatures of $\sim 10^4$K. These regions reemit the energy of the accretion column into the observed FUV, NUV, and optical continuum excess (for a review, see Hartmann et al., 2016). This, along with stronger emission lines from accretion processes, distinguishes CTTS from non-accreting WTTS.

While the bolometric luminosity of the UV excess directly depends on the amount of material accreted by the star, the spectral shape of this excess is a function of the density of the accretion column (Calvet & Gullbring, 1998). Higher density

columns emit more FUV/NUV emission, while lower density columns more closely resemble undisturbed photospheric emission, making UV spectra a useful tool for estimating density and surface coverage of accretion columns. These qualities in turn inform us on conditions in the inner regions of the disk. Previous studies have found it necessary to include contributions from accretion columns with a range of energy fluxes in order to explain the observed UV excess (Ingleby et al., 2013, 2015).

Young low-mass stars often exhibit a rich forest of atomic and molecular FUV/NUV emission features. Although present, these lines are not nearly as strong in nonaccreting WTTS, indicating that these lines are primarily produced through the act of accretion (Johns-Krull & Valenti, 2000). The emission lines $C_{IV}\,\lambda1549$ Å, $He_{II}\,\lambda1640$ Å, and $H_{\alpha}\,\lambda6563$ Å are several examples of features that have been shown to correlate with mass accretion rate (Johns-Krull & Valenti, 2000; Calvet et al., 2004; Ingleby et al., 2011; Yang et al., 2012; Ardila et al., 2013; Ingleby et al., 2013). These lines are useful secondary indicators of mass accretion rate when spectra with complete UV-to-optical coverage are unavailable. In addition, these lines provide information about the kinematics of the accretion shock (Ardila et al., 2013).

Several morphological classifications of variability in CTTS have been identified by photometric monitoring campaigns (e.g., Herbst et al., 1994; Alencar et al., 2010; Cody et al., 2014). The configuration of the magnetic field is likely in part responsible for the density and degree of surface coverage of the accretion columns (Adams & Gregory, 2012). Spectropolarimetric measurements of accreting young stars indicate a variety of magnetic field configurations, ranging from well-ordered dipolar fields to complex non-axisymmetric field configurations (e.g., Donati et al., 2010b, 2011c). Periodic accretion signatures associated with well-ordered magnetic fields are also present among objects within these surveys. The collimation by this field is thought to result in accretion columns that impact the star at high stellar latitudes, giving

rise to approximately sinusoidal light curves at the rotational frequency (Kulkarni & Romanova, 2008; Romanova et al., 2008). However, many other CTTS exhibit more chaotic signatures with limited or no obvious periodicity with characteristic timescales of a few days. Two classes of objects with more chaotic light curves that have been identified in previous photometric surveys are "bursters" and "stochastic objects" (e.g., Cody et al., 2014; Cody & Hillenbrand, 2018). These objects exhibit rapid changes in brightness that have been attributed to changes in the mass accretion rate. Stochastic objects tend to show both fading and brightening events, while bursters primarily exhibit brightening events. The median timescales for events from periodogram analysis for both of these types of objects is $\sim$ 20 d, but individual sources have been identified with characteristic timescales ranging from $\sim 2-80$ d. These sorts of timescales make it possible to capture interesting large-scale changes in the accretion rate using observations with roughly week-long cadences. It is also worth noting that smaller-scale accretion variability is also very common in young stars, with timescales ranging down to just a few minutes (e.g., Siwak et al., 2018), which is missed by observations with longer cadences and integration times.

Simulations of magnetospheric accretion onto young stars predict various sources of accretion variability from a variety of instabilities in the inner regions of disks and the magnetosphere (Kulkarni & Romanova, 2008; Romanova et al., 2012; Robinson et al., 2017). Inferences about the magnetic field structure and sources of variability can be made with measurements of the surface coverage of accretion columns from UV spectra of accreting objects while simultaneously measuring the mass accretion rate.

Previous studies with simultaneous FUV to NIR coverage have presented samples of single observations of several objects (Ardila et al., 2013; Ingleby et al., 2013; Thanathibodee et al., 2018), or have interpreted repeated observations of a single

object (Ingleby et al., 2015). Multiple observations of individual objects mitigate systematic effects (e.g., distance and extinction), are required for measurements of variability, and place irregular accretion epochs in context when they might otherwise be considered standard behavior. On the other hand, broader surveys that include observations of many objects provide context for identifying trends and outliers in the global population of young stars (e.g., identifying trends with accretion with age; Hartmann et al., 1998). In short, multiepoch studies with multiple objects are necessary to fully interpret accretion variability within a local and global context.

Here, I present and model contemporaneous FUV–NIR observations of a sample of five well-studied CTTS. In §3.2, I present the sample and describe the observations. In §3.3, I briefly describe the Calvet & Gullbring (1998) accretion shock model and discuss updates to that model. I describe the fitting methods and present mass accretion rates, surface coverages, and line luminosities in §3.4. Interpretation of the results is presented in §3.5, and I conclude in §3.6.

3.2 Sample and Observations

3.2.1 Objects

The sample contains five young accreting stars surrounded by full, transitional (disks with an inner hole), and pre-transitional disks (disks with gaps, e.g., Espaillat et al., 2014). The objects in this sample include DM Tau, GM Aur, SZ 45, TW Hya, and VW Cha. These objects are all relatively well studied and associated with nearby star formation regions. More discussion on each object is presented in §3.5.2.

3.2.2 Weak-Line T Tauri Stars

WTTS are used as spectral templates in this analysis because even non-accreting young stars can have significant chromospheric emission in the UV above main-

sequence dwarf stars (Ingleby et al., 2011). Here, I use spectra from three WTTS with spectral types similar to those of the CTTS targets: RECX 1 (K5), HBC 427 (K7), and TWA 7 (M1). All of these objects have V-band extinctions, A_V, close to zero and have previously been used as spectral standards within the framework of the Calvet & Gullbring (1998) shock models (Ingleby et al., 2013). These spectra were obtained as part of a large *Hubble Space Telescope* (*HST*) program: Disks, Accretion, and Outflows of T Tau Stars (PI: G. Herczeg, proposal ID: 11616).

3.2.3 *HST* Space Telescope Imaging Spectrograph

For each object, I obtained multiepoch low-resolution spectra covering roughly 1100 Å to 10000 Å using the Space Telescope Imaging Spectrograph (STIS) on board the *HST*. The spectra were primarily taken using four overlapping grating settings: FUV-MAMA G140L, NUV-MAMA G230L, CCD G430L, and CCD G750L, which cover the FUV, NUV, optical and NIR, respectively. The observations for each grating were obtained in consecutive orbits, resulting in a near-contemporaneous dataset for each observational epoch. Note that these observations are not truly simultaneous since they are taken over several *HST* orbits spanning roughly 2.5 hr, and photometric and spectral variability on shorter timescales has been observed in CTTS (e.g., Bouvier et al., 2003; Alencar et al., 2005; Dupree et al., 2012; Cody et al., 2014; Siwak et al., 2018). In regions where gratings overlap, I find good agreement between orbits, suggesting that this effect is minimal within this set of observations.

The observations presented here are taken from five separate *HST* programs. A summary of the *HST* proposals, dates, objects, and naming conventions used for epochs in this publication is shown in Tab. 3.1. The first three epochs of the GM Aur data (from Program 11608) have been previously studied by Ingleby et al. (2015) using techniques similar to that used in this work. The WTTS used as templates in

this analysis were observed as a part of *HST* proposal 11616, PI: G. Herczeg. Fig. 3.1 shows all of the spectra for each epoch stacked on top of each other.

Defringing

Fringe patterns were present in the longer wavelength regions of the NIR G750L spectra. These were removed by following the prescription presented in Goudfrooij & Christensen (1998) using fringe flats and the STSDAS PyRAF tools. Further reduction of the observations followed the standard STScI `calstis` pipeline.

VW Cha

One irregularity in the standard reduction process occurred while extracting the spectrum of Epoch 5 for VW Cha. Observations of VW Cha in the first four epochs were taken with similar slit position angles ($140° - 145°$). The final epoch was taken with a 40° deviation from this. The change in slit position caused a companion star to align with the slit. This companion is brighter in the NIR grating observation than VW Cha, which caused the companion to be extracted under the standard automated spectral extraction process. Using the STIS PyRAF tools, VW Cha was manually reextracted from the 2D spectra with very little contamination from the companion. Although the companion is present in the 2D spectra of the G140L, G230L, and G430L observations, it is faint, and VW Cha was correctly selected and extracted by the automated pipeline. All of the other observations do not show visible contributions from companions in the 2D spectra.

TW Hya

The FUV order for TW Hya was not taken with the G140L grating and was instead done with the higher resolution E140M grating because it would saturate if observed with the lower resolution grating. In order to facilitate comparisons

Table 3.1. Observation Log

Target	Epoch	Date (UT)	Proposal ID	Exposure Times (s)	Notes
DM Tau	1	2011 Sep 08	11608	25, 400, 821, 2994	
DM Tau	2	2011 Sep 15	11608	25, 400, 821, 2994	
DM Tau	3	2012 Jan 04	11608	25, 400, 821, 2994	
GM Aur	1	2011 Sep 11	11608	8, 35, 1231, 3020	
GM Aur	2	2011 Sep 17	11608	8, 35, 1231, 3020	
GM Aur	3	2012 Jan 05	11608	8, 35, 1231, 3020	
GM Aur	4	2016 Jan 05	14048	8, 35, 1207, 2967	
GM Aur	5	2016 Jan 09	14048	8, 35, 1207, 2967	
GM Aur	6	2018 Jan 04	15165	8, 35, 1093, 2950	
GM Aur	7	2018 Jan 11	15165	8, 35, 1093, 2950	
GM Aur	8	2018 Jan 19	15165	8, 35, 1093, 2950	
SZ 45	1	2016 May 14	14193	3, 45, 1549, 3298	
SZ 45	2	2016 May 17	14193	3, 45, 1549, 3298	
SZ 45	3	2016 May 18	14193	3, 45, 1549, 3298	
SZ 45	4	2016 May 20	14193	3, 45, 1549, 3298	
SZ 45	5	2016 Jul 06	14193	3, 45, 1549, 3298	
TW Hya	1	2010 Jan 29	11608	1, 20, 100, 150	E140M
TW Hya	2	2010 Feb 04	11608	1, 20, 100, 150	E140M
TW Hya	3	2010 May 28	11608	1, 20, 150, 548	E140M
TW Hya	4	2015 Apr 18	13775	1, 20, 150, 485	E140M
VW Cha	1	2016 Jan 23	14193	2, 25, 1671, 3298	
VW Cha	2	2016 Jan 25	14193	2, 25, 1671, 3298	
VW Cha	3	2016 Jan 27	14193	2, 25, 1671, 3298	
VW Cha	4	2016 Jan 29	14193	2, 25, 1671, 3298	
VW Cha	5	2016 Mar 11	14193	2, 25, 1671, 3298	Companion in slit
HBC 427	1	2011 Mar 29	11616	60, 1475	WTTS
RECX 1	1	2010 Jan 22	11616	14, 808	WTTS
TWA 7	1	2011 May 05	11616	8, 1490	WTTS

Note. — FUV observations of TW Hya used the higher resolution E140M grating instead of the G140L grating that was used for the other objects to avoid saturation. A companion star landed on the slit during Epoch 5 of the VW Cha observations. The PIs for the proposals are as follows: 11608: N. Calvet, 13775: C. Espaillat, 14048: C. Espaillat, 14193: C. Espaillat, and 15165: C. Espaillat. Exposure times for the CTTS observations are listed in the following order: G750L, G430L, G230L, and G140L/E140M. The two listed exposure times for the WTTS are G230L and G140L observations, respectively. More details on the observations are included in §3.2.3.

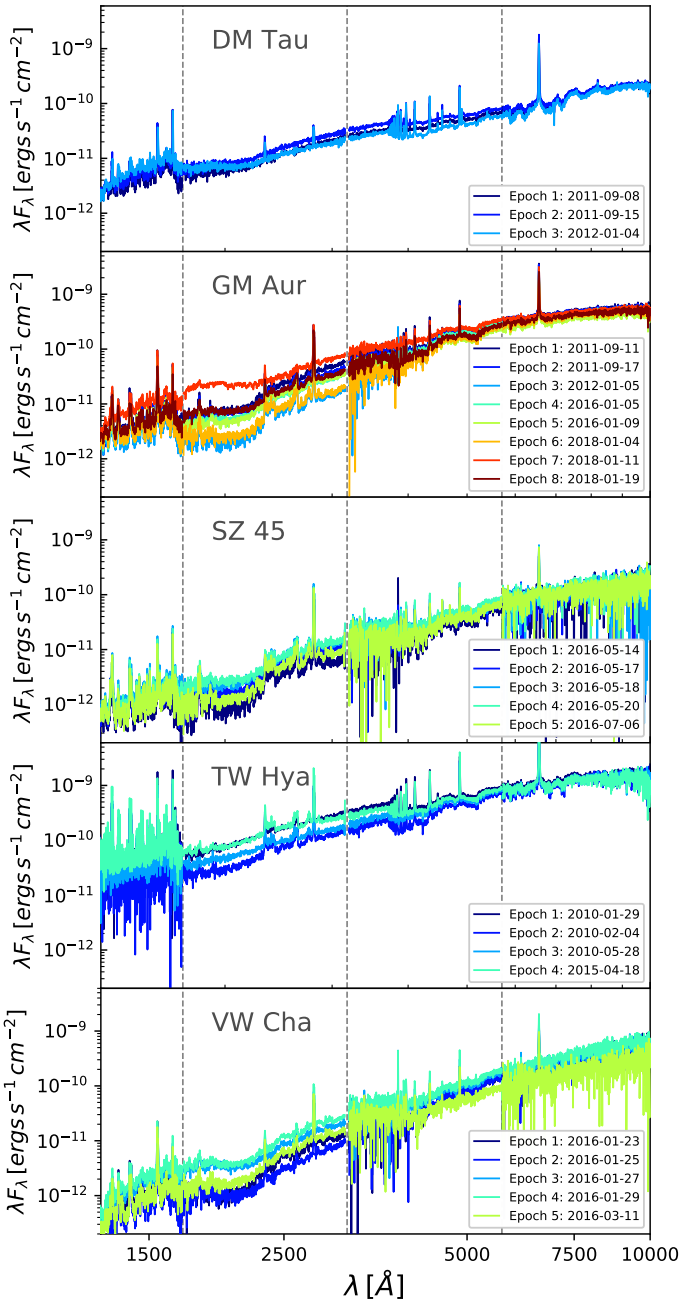

Fig. 3.1: All 25 epochs of *HST* STIS spectra with separate panels for each object. The gray dashed lines mark the edges of the STIS gratings.

between other objects, the spectra were resampled onto the same wavelength grid as the G140L spectra using SpecTres, a Python spectral resampling tool (Carnall, 2017).

3.3 Model

The optical and NUV continua were modeled using an updated version of the Calvet & Gullbring (1998) shock models. This model consists of three regions: the preshock region, the postshock region, and the underlying photosphere, which is heated by emission from the postshock region. The shock is described by the strong shock fluid Rankine-Hugoniot jump conditions and the preshock density and velocity, which can be used to solve for the structure of the postshock region. Emission from the shock itself is not explicitly included because of the limitations imposed by the fluid approach taken by Calvet & Gullbring (1998). A fully kinetic approach would be required to reproduce the conditions and emission in the shock itself.

I have updated the treatment of the preshock and postshock regions presented in Calvet & Gullbring (1998). The method used to model the heated photosphere remains unchanged. Additionally, I make the same assumption that flux from the undisturbed photosphere outside of the accretion columns is identical to that of nonaccreting WTTS. Previous iterations of these models interpolated over a pre-solved grid of preshock and postshock solutions. The updated model now solves for the conditions in these regions for each unique parameter combination.

3.3.1 Postshock Region

The fluid equations governing the postshock structure are solved using a fourth-order Runge-Kutta solver. I have incorporated an adaptive mesh since the temperature in the postshock region near the photosphere changes rapidly over small scales.

Volume emissivities, emergent spectra, and optical depths for each cell were found by interpolating between a grid of models generated using Cloudy (release c17.00, Ferland et al., 2017) for a wide range of temperatures and densities. This grid covers $T = 5 \times 10^3 - 1 \times 10^7$ K and $n = 10^{10} - 10^{17}\,\mathrm{cm}^{-3}$ in logarithmic steps. The postshock region is assumed to be optically thin, so the emission from each cell is summed to find the emergent radiation field. The emission is assumed to be isotropic, which results in the heated photosphere and the overlying preshock region each receiving half of the total emission generated in the postshock. The volume emissivities from the c17.00 release of Cloudy for plasma in this temperature regime are generally higher than the emissivities used in the original models (Raymond & Smith, 1977). The result is that the postshock region is roughly a factor of two smaller than previous estimates produced using this model. Figure 3.2 shows an example the structure of the preshock and postshock structures for GM Aur with these updates.

3.3.2 Preshock Region

The structure and emission, both toward and away from the stellar surface, of the preshock region is found using the built-in radiative transfer methods of Cloudy (Ferland et al., 2017). The incident radiation field on the preshock region is the emission from the postshock region. The density is fixed in this region to a value set by the energy flux of the column and the freefall velocity. The outer boundary stopping condition is set when the depth of the modeled accretion column reaches $0.1\,R_\star$ or when the temperature of the gas reaches 4000 K.

3.3.3 Filling Factors

These models solve for the outgoing emission from $1\,\mathrm{cm}^2$ of the star while ignoring geometric viewing effects. Surface coverage for different energy flux columns is included using multiplicative filling factors, f_i. These filling factors represent the

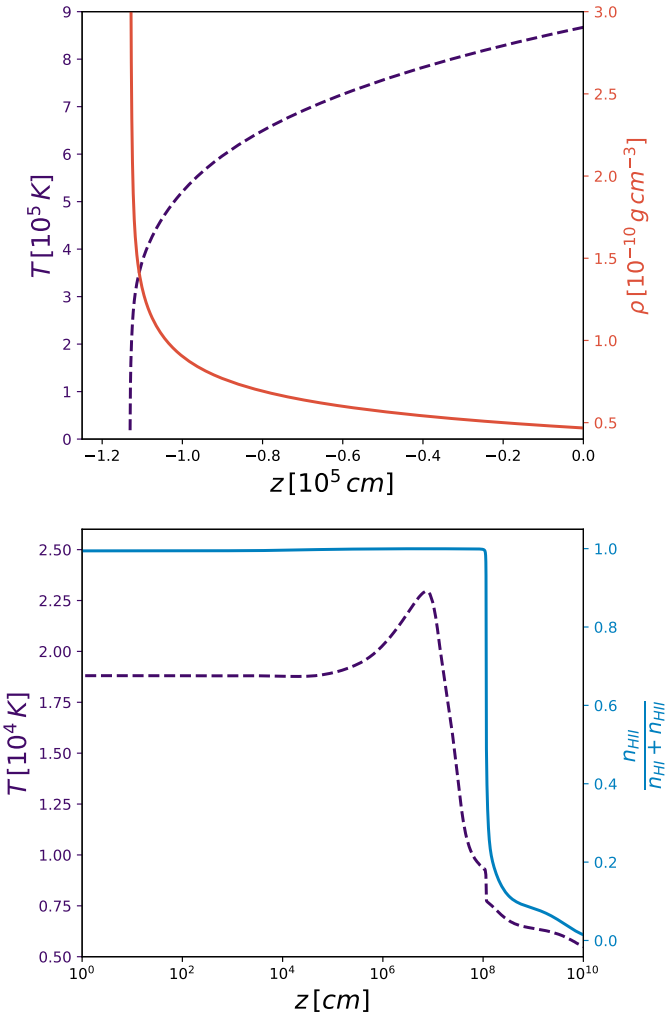

Fig. 3.2: (*Top:*) Temperature (dashed purple line) and density (solid red line) structure of the postshock region. (*Bottom:*) Temperature (dashed purple line) and ionization fraction (solid blue line) structure for the preshock regions. These structures were solved using newly updated volume emissivities from Cloudy version c17.00 (Ferland et al., 2017) for the case of GM Aur. This model was generated with an energy flux of $1 \times 10^{11}\,\mathrm{erg\,s^{-1}\,cm^{-2}}$.

fraction of the star that is covered by accretion columns with that energy flux. By construction, an individual filling factor cannot be less than zero, and the sum of all filling factors cannot be greater than one. Because these are simple multiplicative scaling factors, these filling factors can be changed after the radiative transfer modeling has finished. The emission is further scaled to account for the distance and radius of the star.

3.3.4 Photospheric emission

I include emission from the undisturbed stellar photosphere using a WTTS with a similar spectral type as a template. Photospheric emission of CTTS is veiled by emission from accretion shocks (Hartigan et al., 1989). Veiling is a measure of how much shallower absorption lines look due to an additional continuum source. The degree of spectral line veiling is often used to scale WTTS template spectra to the appropriate level for the CTTS. Previous attempts at fitting continuum levels using the shock models of Calvet & Gullbring (1998) often assume a constant value for veiling at the V band, r_V, between epochs (e.g., Ingleby et al., 2013, 2015), where $F_{V,WTTS} = F_{V,CTTS}/(1+r_V)$ since simultaneous high-resolution spectra can be difficult to obtain. The goal of this work is to measure changes in the mass accretion rate, which should be highly correlated with veiling given that optical emission is produced by accretion shock models (Calvet & Gullbring, 1998). This means that if a constant V-band veiling is assumed, the inferred mass accretion rates measured will be systematically inaccurate.

To approach this issue, I include the scaling of the undisturbed photospheric emission in my fitting as a parameter. First, the WTTS template is reddened to the measured extinction of the CTTS. Next, the template is scaled by a factor, s, of the maximum flux at 5500 Å(roughly V band) for all epochs of *HST* STIS observations of that object. This approach fixes the emission from each cm^2 of the undisturbed

Table 3.2. Stellar parameters

Star	RA (J2000)	Dec. (J2000)	Distance (pc)	SpT	T (K)	Mass ($M_\odot$)	Radius ($R_\odot$)	A_v	WTTS	i (deg.)	Ref.
DM Tau	04:33:48.7	+18:10:10.0	145.1 ± 1.1	M2	3560	0.56	1.63	1.1	TWA 7	34^{+2}_{-2}	(1), (4)
GM Aur	04:55:11.0	+30:21:59.5	159.6 ± 2.1	K5	4350	1.36	2.0	0.6	RECX 1	$52.77^{+0.05}_{-0.04}$	(2),(5)
TW Hya	11:01:51.9	-34:42:17.0	60.09 ± 0.15	K7	4060	0.79	0.929	0.0	HBC 427	7^{+3}_{-3}	(2),(5)
SZ 45	11:17:37.0	-77:04:38.1	188.4 ± 0.9	M0.5	3780	0.85	1.78	0.7	TWA 7	–	(2)
VW Cha	11 08 01.5	-77 42 28.9	190 ± 5	K7	4060	1.24	3.08	1.9	HBC 427	–	(3)

Note. — Stellar parameters were collected from (1): Manara et al. (2014), and (2): Manara et al. (2017) using the Baraffe et al. (1998) evolutionary tracks. Distances were taken from the GAIA DR2 (Gaia Collaboration et al., 2016, 2018) for all targets except VW Cha, which did not have a parallax available, and instead uses the median distance for the Chamaeleon I star-forming region of 190 pc (Roccatagliata et al., 2018). Inclinations were collected when available from (3): Tripathi et al. (2017), (4): Macías et al. (2018), and (5): Andrews et al. (2016).

Table 3.3. Weak-line T Tauri Stellar Parameters

Star	RA (J2000)	Dec. (J2000)	SpT	T (K)	A_v	Ref.
HBC 427	04:56:02	+30:21:03	K7	4060	0	(2)
RECX 1	08:36:56	-78:56:45	K5	4350	0	(1)
TWA 7	10:42:30	-33:40:16	M1	3720	0	(3)

Note. — Sources for stellar parameters: (1) Luhman & Steeghs (2004), (2)Kenyon & Hartmann (1995), (3)Webb et al. (1999). Conversion from spectral type to temperature was done with the tables in Kenyon & Hartmann (1995).

photospheric flux of the star at a single level across all observational epochs. By construction, s should only take values between zero and one. The emission from this photospheric template is then multiplied by the fraction of the star that is not covered by accretion shocks ($1 - \sum_i f_i$). The WTTS photospheres used in this analysis can be seen in Figure 3.3.

3.3.5 Combining the Model Components

Combining the components from the shock model and the undisturbed photosphere, the surface-averaged outgoing flux corrected for extinction for a given wave-

length for a single epoch can be written as

$$F_{tot} = 10^{-0.4A_\lambda}\Big[\Big(1 - \sum_i^n f_i\Big) s F_{phot} + \sum_i^n f_i F_i\Big] \tag{3.1}$$

where each i represents a different column density used in the construction of the model spectra, and n is the total number of contributing column densities (in this case, three). Here, F_i is the sum of $F_{i,hp}$ and $F_{i,pre}$ which are the flux from the heated photosphere and the emission from the preshock region, respectively. F_{phot} represents the emission arising from undisturbed photosphere, here scaled by s and the fraction of the star not covered by accretion shocks. A_λ is the extinction at each wavelength. Extinction is applied to the model using the extinction parameters for HD 29647 from Whittet et al. (2004) using the formulation from Fitzpatrick & Massa (1988) and Fitzpatrick & Massa (1990). Emission from the postshock region is not explicitly included in this equation because the outgoing emission from the postshock forms the incident radiation field for the preshock region and the heated photosphere.

3.4 Analysis and Results

3.4.1 Stellar Parameters

Stellar parameters for the CTTS for this sample are included in Tab. 3.2. Relevant stellar parameters for WTTS used as templates are listed in Tab. 3.3. These parameters were collected from the literature (Manara et al., 2014, 2017) and were calculated by those authors using the Baraffe et al. (1998) evolutionary models. Distances were calculated using parallax measurements from the *Gaia* Data Release 2 (Gaia Collaboration et al., 2016, 2018). Stellar radii from these sources were scaled to be self-consistent with the new *Gaia* distances. Stellar temperature estimates were found using the relationships between T_{eff} and spectral type for pre-main-sequence stars in Kenyon & Hartmann (1995).

3.4.2 Fitting the NUV/Optical Continuum

I model the excess NUV/optical continuum emission with the sum of emission from accretion columns with three different energy fluxes, F_i, in logarithmic steps, $1\times10^{10}, 1\times10^{11}, 1\times10^{12}\,\mathrm{erg\,s^{-1}\,cm^{-2}}$ along with the scaled, undisturbed photosphere template. The velocity at the shock is assumed to be the freefall velocity, and the energy of the flow is assumed to be solely kinetic. This causes the energy flux to be directly related to the density of the column. Regions with strong line emission were masked (the mask can be seen in Figure 3.4) and were not included when fitting models to data. To fit the data, I employ a Bayesian Markov chain Monte Carlo (MCMC) approach, which is described in the following sections.

Likelihood

Under the assumption that the emission from the undisturbed photosphere does not change between observations, I treat s as a single parameter that affects all of the epochs simultaneously for a single object. Fractional uncertainty in the model, w, is included as a nuisance parameter. This uncertainty is added in quadrature with the measurement uncertainty when calculating the likelihood of a given model. Assuming Gaussian and independent uncertainties, the likelihood function is written

$$P(D|\{f_{ij}\},s,w,I) = \prod_{j}^{q}\prod_{k}^{r_j}\frac{1}{\sqrt{2\pi(\sigma_{jk}^2+w^2F_{jk}^2)}}\cdot\exp\Big[-\frac{1}{2}\frac{(F_{jk}-D_{jk})^2}{(\sigma_{jk}^2+w^2F_{jk}^2)}\Big] \tag{3.2}$$

where j indexes over q observational epochs, k indexes over r_j data points for each epoch, i again indexes over the different accretion column energy fluxes, σ_{jk} is the measurement uncertainty in each point from the *HST* pipeline, $\{f_{ij}\}$ represents the complete set of filling factors for all epochs, D is the data, and F is the model (which is a function of $\{f_{ij}\}$ and s; see Eqn. 1). The number of free parameters in the fit

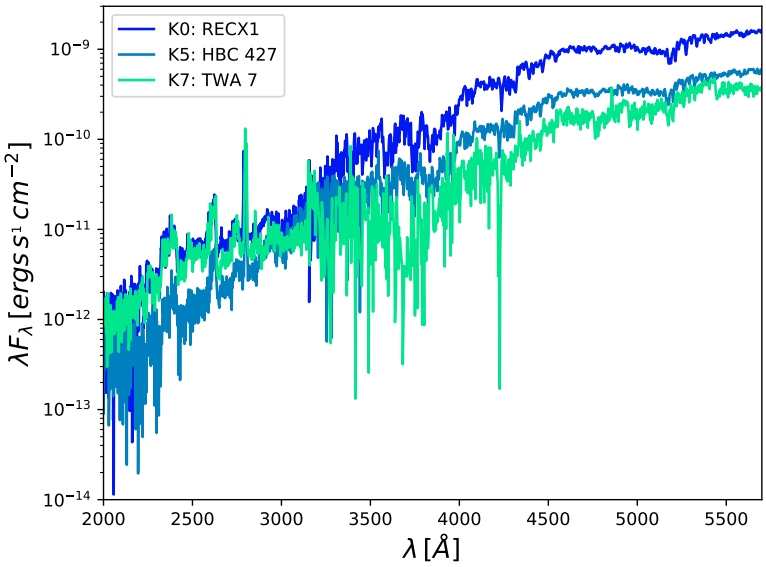

Fig. 3.3: Weak-line T Tauri star spectra used as photospheric templates.

scales as $2 + 3q$ because I have chosen to include contributions from three-column densities and s and w remain single parameters for all epochs.

Priors

Priors for each filling factor, s, and w were included in this analysis. Priors allow us to include prior known information about model parameters when calculating posterior distributions. Each parameter was evaluated in log space, and had a cutoff placed at zero which limits the values of the parameters in regular space to be between zero and one. For the filling factors, this prior removes the nonphysical possibility of both negative emission and surface coverage larger than the surface of the star. In the case of s, the lower bound enforces that the photospheric contribution is not negative, while the upper bound is set because one would not expect the undisturbed photosphere to be brighter than a model that includes additional energy input from the accretion shock. In addition to these cutoffs, I include a prior consisting of a Gaussian centered at the expected value for s based on previous shock modeling by

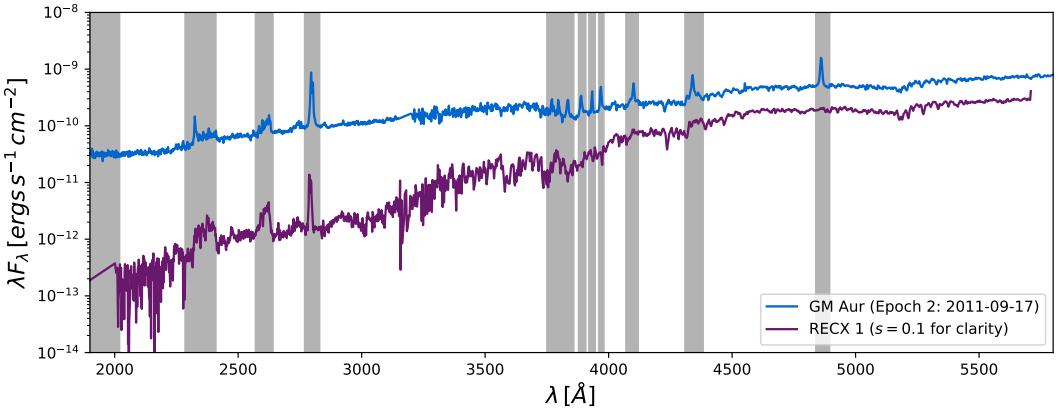

Fig. 3.4: Accreting star (GM Aur; blue line) with an example nonaccreting template photosphere (RECX 1; purple line). Gray shaded areas show regions that were not included when fitting filling factors and were selected to avoid spectral features that were not included in the modeling process. The WTTS is shown scaled to an s value of 0.1 for clarity, and the CTTS spectrum has been dereddened.

Manara et al. (2014, 2016) with a width of 0.1 in s space. Limiting w between zero and one ensures that the uncertainty is positive and that the emission from the shock model is also positive within the uncertainties. In practice, w does not approach one.

Sampling the posterior

To sample the posterior, I employ the widely used ensemble sampler `emcee` (Foreman-Mackey et al., 2013), which uses the Goodman & Weare (2010) affine-invariant sampling algorithm. I used 100 walkers to sample the parameter space for each object. A generous burn-in period before convergence was removed from each walker for each object. Fig. 3.5 shows 2D marginalized posteriors for the subset of the parameters representing Epoch 2 of the GM Aur observations. Marginalized posteriors represent the probability of drawing a particular value of a parameter without reference to parameters that have been marginalized over. In Fig. 3.5, all of the filling factors for the other epochs have been marginalized over. Anticorrelations between f_{1e10} and f_{1e11} and between f_{1e11} and f_{1e12} appear due to some degree of

degeneracy within the models. I find that typical values of the nuisance parameter, w, which represents the fractional uncertainty in the model, generally fall in the range of 10% – 20% for each object.

Mass accretion rates

Mass accretion rates for each epoch can be calculated by summing the contributions from all the columns via

$$\dot{M} = 8\pi\Big(\frac{R_\star}{v_{ff}}\Big)^2 \sum_i^n f_i F_i \tag{3.3}$$

where V_{ff} is the freefall velocity from the inner edge of the gas disk, R_{in}, written as

$$V_{ff} = \sqrt{\frac{2GM_\star}{R_\star}}\sqrt{1 - \frac{R_\star}{R_{in}}}. \tag{3.4}$$

Here, R_{in} is assumed to be five stellar radii. It is important to note that the mass accretion rates reported here are calculated under the assumption that the surface coverage of the columns is identical on the far side of the star. In addition, these models are 1D and ignore geometrical effects, which would require a much more detailed analysis.

Mass accretion rates and filling factors are reported in Tab. 3.4. The median of the posterior distribution is reported for each of these parameters. Reported uncertainties are the difference between the median and the 16^{th} and 84^{th} percentiles (roughly equivalent to 1σ uncertainties for Gaussian distributions). Values of veiling for each epoch at the V-band, parameterized by r_V, are also presented in Table 3.4. The degree of veiling is related to the parameter s, the photospheric scaling factor described earlier, and the amount of excess continuum flux from the accretion shocks. One of the V-band veiling values for VW Cha was found to be negative, which is unusual. This peculiar epoch is further discussed in §3.5.2.

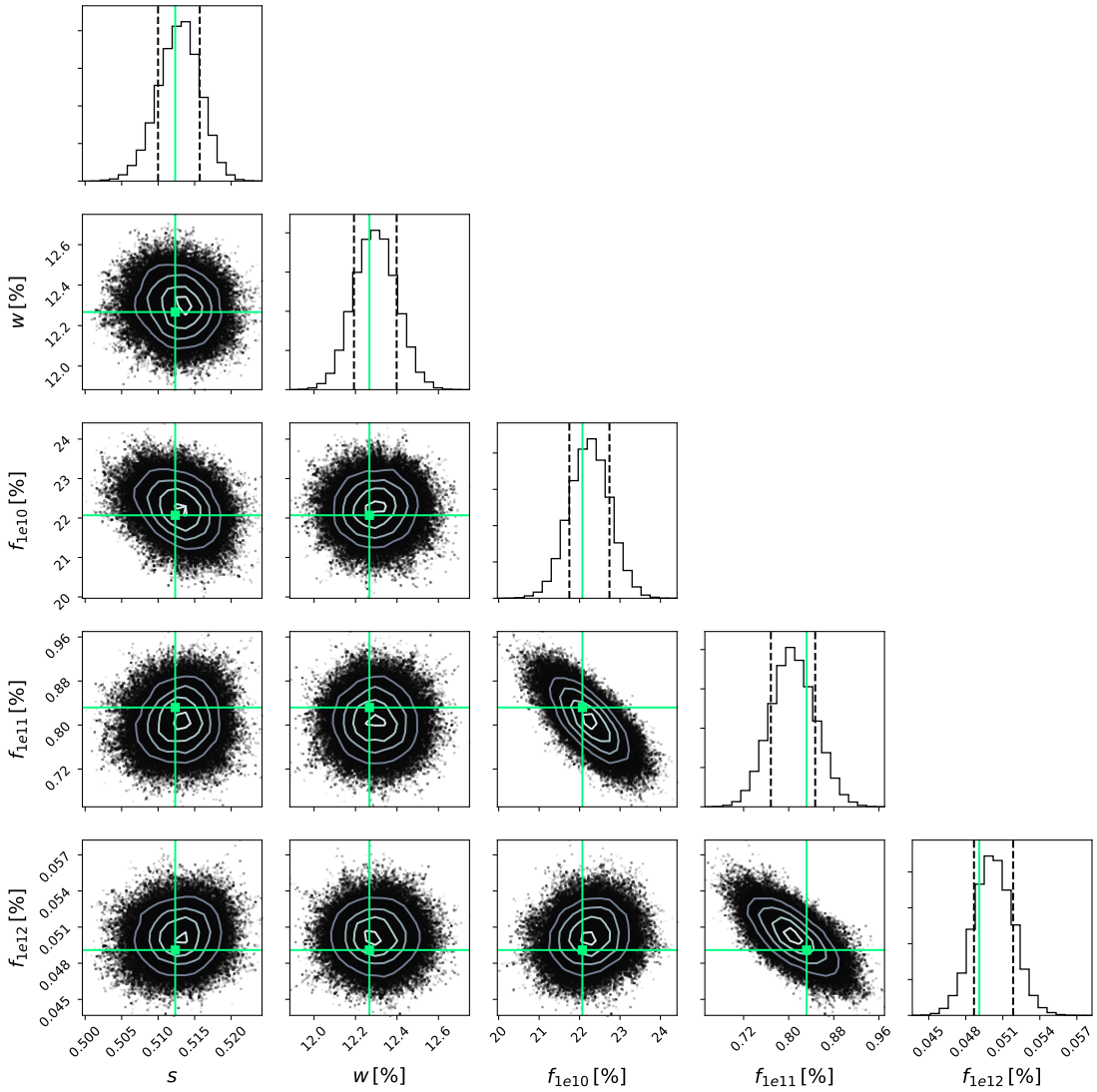

Fig. 3.5: Two-dimensional marginalized posteriors of the photospheric scaling factor s, fractional model uncertainty w, and filling factors for Epoch 2 of the GM Aur observations (written as percentages). The most likely model is marked in green. Note that filling fractions for all epochs for each object were fit simultaneously and that only a subset parameters included in the analysis is shown here as an example.

Table 3.4. Mass Accretion Rates and Filling Factors

Object	Epoch	$\dot{M}$ (10^{-8} $M_\odot$ yr^{-1})	f_{1E10}	f_{1E11}	f_{1E12}	r_V
DM Tau	1	$2.770^{+0.026}_{-0.025}$	$0.211^{+0.007}_{-0.007}$	$0.000066^{+0.00004}_{-0.000015}$	$0.003638^{+0.000027}_{-0.000026}$	$1.41^{+0.05}_{-0.05}$
DM Tau	2	$3.582^{+0.029}_{-0.029}$	$0.259^{+0.008}_{-0.008}$	$0.000069^{+0.00005}_{-0.000018}$	$0.00485^{+0.00003}_{-0.00003}$	$1.81^{+0.06}_{-0.05}$
DM Tau	3	$2.011^{+0.028}_{-0.028}$	$0.036^{+0.008}_{-0.008}$	$0.000059^{+0.000024}_{-0.000010}$	$0.003808^{+0.000027}_{-0.000027}$	$1.06^{+0.04}_{-0.04}$
GM Aur	1	$1.546^{+0.011}_{-0.011}$	$0.214^{+0.006}_{-0.006}$	$0.0164^{+0.0005}_{-0.0005}$	$0.000459^{+0.000019}_{-0.000018}$	$0.893^{+0.011}_{-0.011}$
GM Aur	2	$1.291^{+0.010}_{-0.010}$	$0.223^{+0.005}_{-0.005}$	$0.0081^{+0.0004}_{-0.0004}$	$0.000502^{+0.000016}_{-0.000016}$	$0.847^{+0.011}_{-0.010}$
GM Aur	3	$0.660^{+0.007}_{-0.007}$	$0.142^{+0.003}_{-0.003}$	$0.00342^{+0.00015}_{-0.00015}$	$0.0000462^{+0.0000013}_{-0.0000006}$	$0.643^{+0.010}_{-0.009}$
GM Aur	4	$1.021^{+0.009}_{-0.009}$	$0.183^{+0.004}_{-0.004}$	$0.0057^{+0.0003}_{-0.0003}$	$0.000390^{+0.000013}_{-0.000013}$	$0.690^{+0.010}_{-0.010}$
GM Aur	5	$0.768^{+0.008}_{-0.008}$	$0.044^{+0.004}_{-0.004}$	$0.0127^{+0.0003}_{-0.0003}$	$0.000395^{+0.000013}_{-0.000013}$	$0.303^{+0.008}_{-0.007}$
GM Aur	6	$0.564^{+0.007}_{-0.007}$	$0.087^{+0.003}_{-0.003}$	$0.00528^{+0.00021}_{-0.00020}$	$0.000147^{+0.000008}_{-0.000008}$	$0.428^{+0.008}_{-0.008}$
GM Aur	7	$1.961^{+0.012}_{-0.012}$	$0.303^{+0.005}_{-0.005}$	$0.00009^{+0.00008}_{-0.00003}$	$0.002326^{+0.000022}_{-0.000022}$	$0.950^{+0.011}_{-0.011}$
GM Aur	8	$0.979^{+0.009}_{-0.009}$	$0.125^{+0.005}_{-0.005}$	$0.0070^{+0.0004}_{-0.0004}$	$0.000726^{+0.000017}_{-0.000016}$	$0.551^{+0.009}_{-0.009}$
SZ 45	1	$0.923^{+0.015}_{-0.015}$	$0.172^{+0.006}_{-0.006}$	$0.00452^{+0.00028}_{-0.0003}$	$0.000057^{+0.000009}_{-0.000007}$	$1.71^{+0.10}_{-0.10}$
SZ 45	2	$1.187^{+0.018}_{-0.018}$	$0.191^{+0.007}_{-0.007}$	$0.0064^{+0.0005}_{-0.0005}$	$0.000321^{+0.000018}_{-0.000017}$	$2.08^{+0.12}_{-0.11}$
SZ 45	3	$1.490^{+0.019}_{-0.019}$	$0.247^{+0.008}_{-0.008}$	$0.0060^{+0.0006}_{-0.0006}$	$0.000528^{+0.000024}_{-0.000023}$	$2.70^{+0.14}_{-0.13}$
SZ 45	4	$1.639^{+0.020}_{-0.020}$	$0.300^{+0.008}_{-0.008}$	$0.0034^{+0.0006}_{-0.0006}$	$0.000631^{+0.000026}_{-0.000025}$	$2.86^{+0.15}_{-0.14}$
SZ 45	5	$1.157^{+0.018}_{-0.017}$	$0.204^{+0.007}_{-0.007}$	$0.0058^{+0.0004}_{-0.0004}$	$0.000172^{+0.000015}_{-0.000014}$	$2.27^{+0.13}_{-0.11}$
TW Hya	1	$0.330^{+0.004}_{-0.004}$	$0.275^{+0.014}_{-0.016}$	$0.0113^{+0.0011}_{-0.0011}$	$0.001319^{+0.00003}_{-0.000028}$	$0.962^{+0.020}_{-0.022}$
TW Hya	2	$0.1384^{+0.0028}_{-0.003}$	$0.083^{+0.009}_{-0.010}$	$0.0093^{+0.0006}_{-0.0006}$	$0.000427^{+0.000013}_{-0.000014}$	$0.500^{+0.015}_{-0.017}$
TW Hya	3	$0.2206^{+0.0028}_{-0.004}$	$0.256^{+0.008}_{-0.013}$	$0.0007^{+0.0009}_{-0.0006}$	$0.000852^{+0.000016}_{-0.000023}$	$0.695^{+0.017}_{-0.019}$
TW Hya	4	$0.262^{+0.005}_{-0.004}$	$0.153^{+0.016}_{-0.013}$	$0.0120^{+0.0010}_{-0.0012}$	$0.00140^{+0.00004}_{-0.00003}$	$0.818^{+0.019}_{-0.020}$
VW Cha	1	$8.5^{+0.3}_{-2.0}$	$0.25^{+0.03}_{-0.25}$	$0.0016^{+0.012}_{-0.0014}$	$0.00303^{+0.00008}_{-0.00008}$	$0.441^{+0.022}_{-0.021}$
VW Cha	2	$7.46^{+0.20}_{-0.20}$	$0.324^{+0.017}_{-0.018}$	$0.00010^{+0.00011}_{-0.00004}$	$0.00180^{+0.00005}_{-0.00004}$	$0.408^{+0.021}_{-0.020}$
VW Cha	3	$15.1^{+0.3}_{-0.3}$	$0.386^{+0.029}_{-0.028}$	$0.00014^{+0.00019}_{-0.00008}$	$0.00638^{+0.00009}_{-0.00010}$	$0.747^{+0.027}_{-0.025}$
VW Cha	4	$19.9^{+0.4}_{-0.4}$	$0.54^{+0.04}_{-0.04}$	$0.00027^{+0.0006}_{-0.00019}$	$0.00804^{+0.00013}_{-0.00012}$	$0.941^{+0.03}_{-0.028}$
VW Cha	5	$6.91^{+0.06}_{-0.05}$	$0.0006^{+0.004}_{-0.0005}$	$0.00010^{+0.00011}_{-0.00004}$	$0.00465^{+0.00004}_{-0.00004}$	$-0.074^{+0.014}_{-0.013}$

Note. — Mass accretion rates are presented in units of $10^{-8} M_\odot\ yr^{-1}$ Filling factors are unitless, representing the fraction of the star covered by shocks with that energy flux. Reported values are the median of the distributions, while the uncertainties are the difference between the median and the 16^{th} and 84^{th} percentiles (similar to 1σ uncertainties). The negative values of veilings for VW Cha are discussed in depth in §3.5.2. It is important to note that uncertainties reported here only reflect the width of the 1D marginalized posterior as found from my MCMC analysis and do not take other systematic effects into account (e.g., extinction, optical depth effects, evolutionary track). I find that typically a change in A_v of 0.5 leads to systematic shifts in the absolute value of $\dot{M}$ by approximately a factor of two, while relative shifts between epochs remain around 10%.

3.4.3 Model Fits for Each Epoch

The fits for each epoch are shown in Fig. 3.6. The median for each component of the model is shown, along with the total model in red. The undisturbed photospheric contribution is also shown. It is important to keep in mind that the undisturbed photospheric contribution may be different between epochs because it is also scaled by the fraction of the star not covered by accretion columns. The unscaled version of the photosphere remains the same between all epochs of the same object, due to my

treatment of the photospheric scaling factor as a single parameter, which is described in depth in §3.4.2.

3.4.4 Higher-energy Columns for DM Tau and GM Aur

The fits for all three epochs of DM Tau and Epoch 7 of GM Aur using columns with $F = 10^{10}, 10^{11}$ and $10^{12}\,\mathrm{erg\,s^{-1}\,cm^2}$ are unable to reproduce some of the excess emission observed at the shortest wavelengths in the NUV. One possible explanation for this excess for DM Tau is an incorrect value of extinction. However, this does not appear to be the case, as refitting the data with $A_V = 0$ for DM Tau still resulted in a dearth of model emission in these wavelengths. Including a fourth model component with energy fluxes of $3 \times 10^{12}\,\mathrm{erg\,s^{-1}\,cm^{-2}}$ better reproduces the observed emission. While the overall mass accretion rate does increase with the inclusion of these high-density columns, this does not significantly change the interpretation presented above. The revised filling factors and mass accretion rates are shown in Tab. 3.5, and the updated fits with these components are shown in Fig. 3.7.

Except for Epoch 7, I am able to successfully reproduce the emission in all of the other epochs for GM Aur using the three-column models. Although the change in the fit due to the addition of the higher energy column is more subtle for GM Aur Epoch 7 compared to DM Tau, the overall fit is improved and is consistent with the interpretation that a dense clump of material was accreted onto the star during this epoch, which has the highest accretion rate. I find better agreement with the addition of the higher energy column between the model and data in shorter wavelength regions excluded from the fitting procedures. The inability to fit the shortest wavelength regions reiterates that this epoch is unique relative to the other seven epochs of observations, and more data would be needed to study this further.

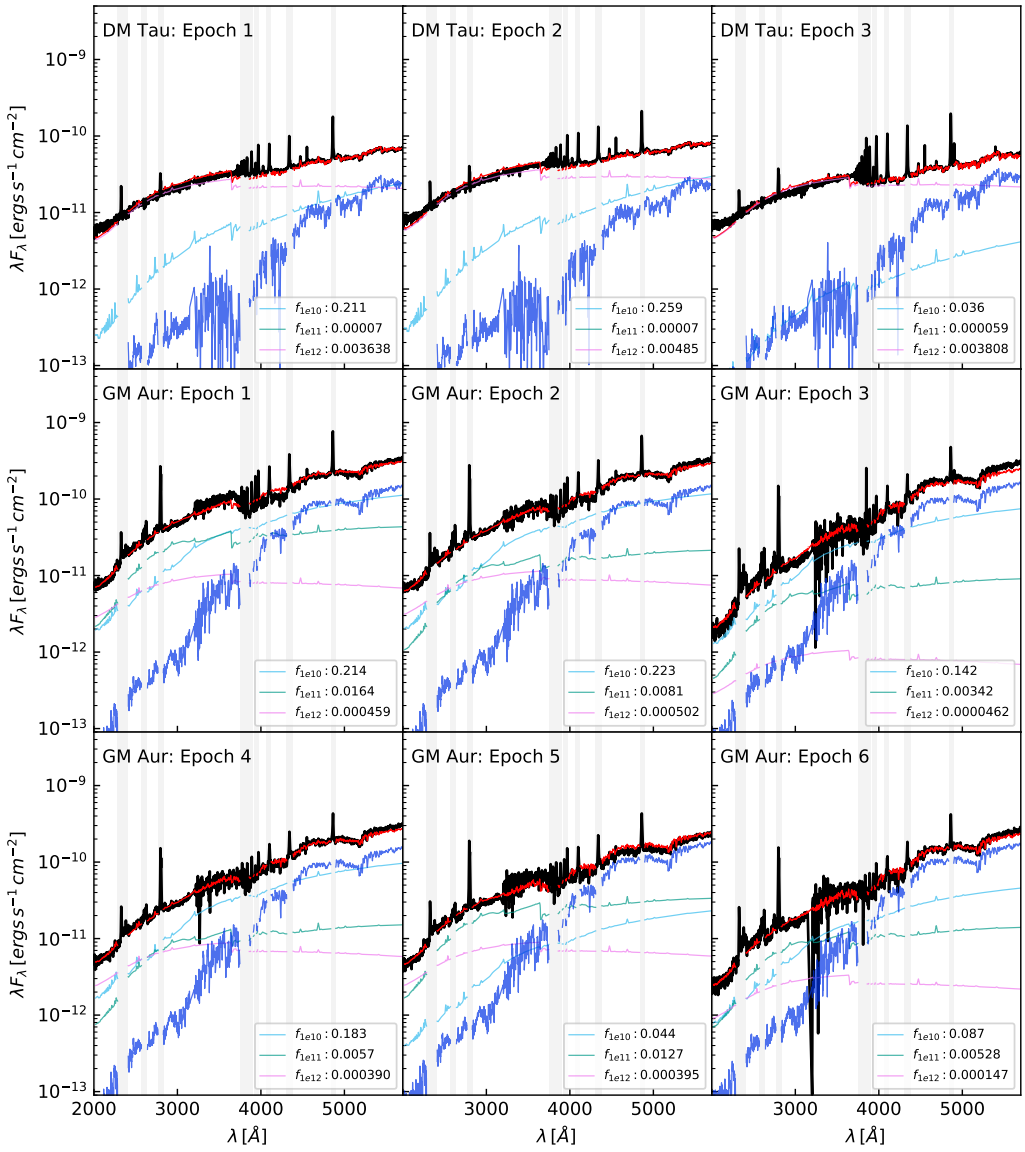

Fig. 3.6: Observed spectra (in black) and model fits showing the median model. The total model is shown in red, and the contribution from the undisturbed photosphere is shown in blue. Contributions from different column energy fluxes are shown as light blue, light green, and light magenta.

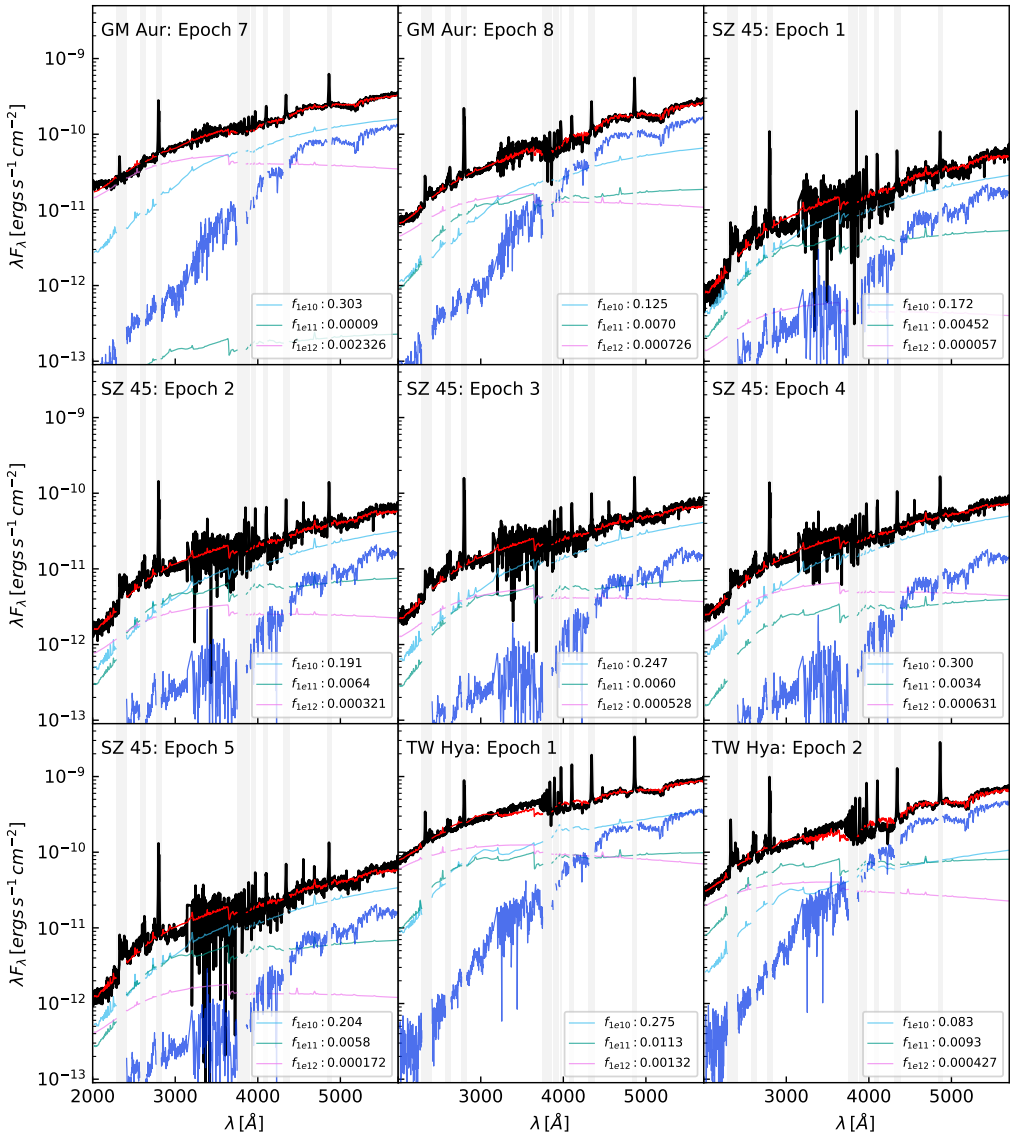

Fig. 3.6: continued.

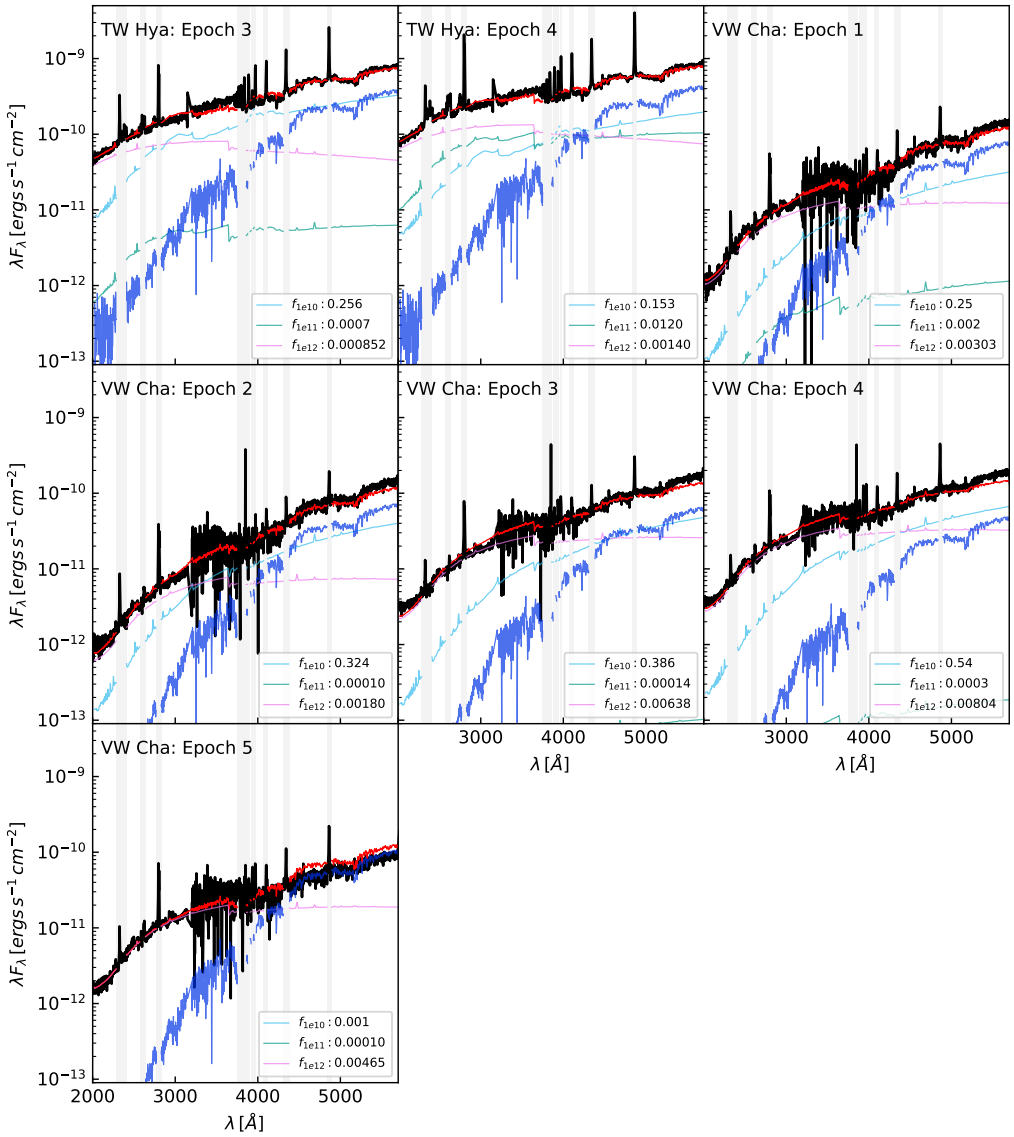

Fig. 3.6: continued.

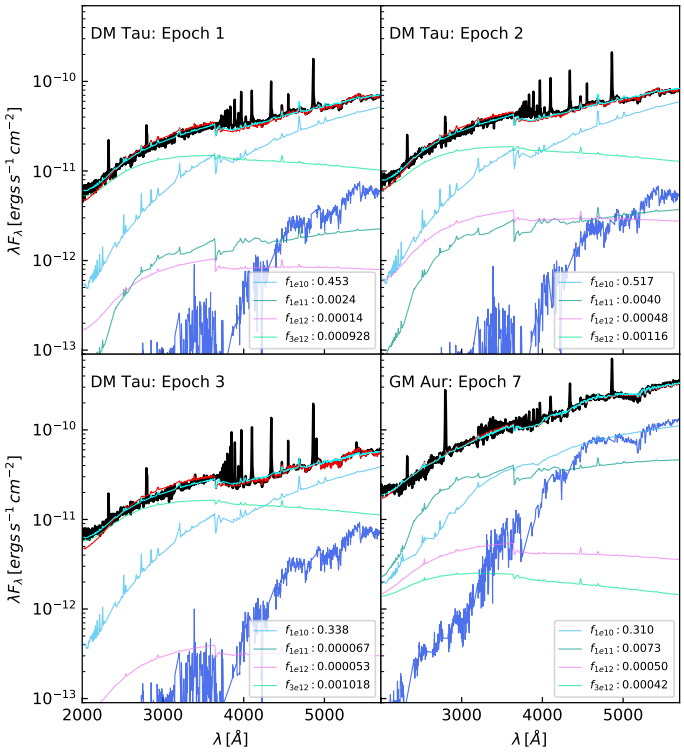

Fig. 3.7: Models including a fourth higher column energy flux for select epochs with excess in the shortest wavelength regions. The total for the four-column model is shown in cyan, while the median of the three-column models is shown in red for comparison. The blue line represents the photospheric contribution. The contributions from each column are labeled.

Table 3.5. Mass Accretion Rates and Filling Factors

Object	Epoch	$\dot{M}$ (10^{-8} $M_\odot$ yr^{-1})	f_{1E10}	f_{1E11}	f_{1E12}	f_{3E12}	r_v
DM Tau	1	$3.707^{+0.023}_{-0.023}$	$0.453^{+0.009}_{-0.009}$	$0.0024^{+0.0008}_{-0.0013}$	$0.00014^{+0.00019}_{-0.00007}$	$0.000928^{+0.000018}_{-0.00004}$	$5.7^{+0.5}_{-0.4}$
DM Tau	2	$4.595^{+0.023}_{-0.024}$	$0.517^{+0.013}_{-0.012}$	$0.0040^{+0.0019}_{-0.0024}$	$0.00048^{+0.0003}_{-0.00028}$	$0.00116^{+0.00006}_{-0.00007}$	$6.8^{+0.6}_{-0.5}$
DM Tau	3	$3.129^{+0.019}_{-0.018}$	$0.338^{+0.005}_{-0.005}$	$0.000067^{+0.00004}_{-0.000016}$	$0.000053^{+0.000014}_{-0.000006}$	$0.001018^{+0.000007}_{-0.000007}$	$4.8^{+0.4}_{-0.4}$
GM Aur	7	$2.045^{+0.015}_{-0.016}$	$0.310^{+0.008}_{-0.007}$	$0.0073^{+0.0019}_{-0.0019}$	$0.00050^{+0.0004}_{-0.00024}$	$0.00042^{+0.00005}_{-0.00008}$	$0.937^{+0.013}_{-0.012}$

Note. — Mass accretion rates and filling factors for four-column models for the observational epochs that showed excess at the shortest wavelengths under the three-column models. Mass accretion rates are presented in units of $10^{-8} M_\odot\, yr^{-1}$.

3.4.5 NUV and FUV Line Luminosities

Correlations have previously been found between NUV and FUV emission features and the mass accretion rate (e.g., Calvet et al., 2004; Ingleby et al., 2013). Repeated observations of the same stars separate trends that might appear due to systematic effects from those caused by changes in mass accretion rate. Here, I measure line luminosities for several NUV and FUV emission lines and H_α (Tab. 3.6) by subtracting a continuum and directly integrating the feature across the relevant wavelength range. Kinematic information about the preshock region is also carried by these lines (Ardila et al., 2013), but the spectra presented here lack the resolution to permit a detailed line shape study.

The continuum was fit with a third-degree polynomial. Although the model produces physically motivated continuum estimates, polynomial fits allow for more accurate representations of the observed continuum level near emission lines. In addition, the FUV was not included when fitting the filling fractions because of the large number of strong spectral features and thus should not be used for continuum subtraction with the shock model. Separate polynomials were used to fit the FUV and the NUV wavelength ranges for each observation to help ensure accurate continuum subtraction. The continuum regions were located by-eye by selecting a set of points for each observation that appeared to be representative of the continuum level across the spectrum. About 15 points were selected for each of the FUV and NUV spectra. These points were then fit with linear regression techniques. The resulting posterior distribution describes the probability of a model with a given set of parameters based on the available data and the prior. By randomly sampling the posterior and computing models, one can construct a set of models that begins to resemble the posterior placed in wavelength space. The width of these random draws from the posterior distribution is representative of the uncertainty in the continuum fit. Given

Table 3.6. Line Luminosities

Obj.	E.	C_{II} 1335 Å	C_I 1463 Å	C_{IV} 1548 Å	He_{II} 1640 Å	O_{III} 1666 Å	Si_{II} 1808 Å	$Si_{III]}$ 1892 Å	$C_{III]}$ 1908 Å	$C_{II]}$ 2325 Å	$Al_{III]}$ 2670 Å	Mg_{II} 2796 Å	H_α 6563 Å
DM Tau	1	$18.3^{+0.8}_{-0.8}$	$5.6^{+1.0}_{-1.0}$	$58.3^{+2.2}_{-2.2}$	$42.5^{+1.1}_{-1.1}$	$1.8^{+0.7}_{-0.7}$	$3.7^{+2.0}_{-2.0}$	$0.5^{+0.9}_{-0.9}$	$1.5^{+1.4}_{-1.4}$	$11.6^{+0.9}_{-0.9}$	$2.0^{+0.9}_{-0.9}$	$9.3^{+1.0}_{-1.0}$	$423.7^{+2.5}_{-2.5}$
DM Tau	2	$16.7^{+1.0}_{-1.0}$	$5.2^{+1.2}_{-1.2}$	$56.1^{+2.6}_{-2.7}$	$44.9^{+1.3}_{-1.3}$	$1.8^{+0.9}_{-0.9}$	$-0.0^{+2.4}_{-2.4}$	$0.3^{+1.1}_{-1.1}$	$0.8^{+1.8}_{-1.7}$	$10.8^{+1.0}_{-1.0}$	$0.3^{+0.8}_{-0.8}$	$7.4^{+0.9}_{-0.9}$	$480.1^{+2.5}_{-2.5}$
DM Tau	3	$12.9^{+0.9}_{-0.9}$	$3.2^{+1.3}_{-1.3}$	$48.5^{+2.7}_{-2.7}$	$36.4^{+1.3}_{-1.3}$	$-0.2^{+1.1}_{-1.1}$	$3.0^{+2.1}_{-2.1}$	$1.9^{+1.1}_{-1.1}$	$3.8^{+1.4}_{-1.4}$	$8.9^{+0.9}_{-0.9}$	$0.3^{+0.7}_{-0.7}$	$12.5^{+0.8}_{-0.8}$	$338.3^{+2.3}_{-2.3}$
GM Aur	1	$8.97^{+0.20}_{-0.20}$	$3.63^{+0.28}_{-0.28}$	$42.9^{+0.5}_{-0.5}$	$10.6^{+0.3}_{-0.3}$	$1.18^{+0.25}_{-0.25}$	$5.4^{+0.4}_{-0.4}$	$1.92^{+0.22}_{-0.22}$	$2.0^{+0.3}_{-0.3}$	$11.5^{+0.3}_{-0.3}$	$2.1^{+0.3}_{-0.3}$	$76.3^{+0.5}_{-0.5}$	581^{+5}_{-5}
GM Aur	2	$8.75^{+0.22}_{-0.21}$	$2.81^{+0.27}_{-0.27}$	$33.3^{+0.5}_{-0.5}$	$10.59^{+0.29}_{-0.29}$	$0.88^{+0.23}_{-0.23}$	$4.3^{+0.5}_{-0.5}$	$1.56^{+0.22}_{-0.22}$	$1.8^{+0.3}_{-0.3}$	$10.05^{+0.28}_{-0.27}$	$0.8^{+0.3}_{-0.3}$	$74.8^{+0.4}_{-0.4}$	559^{+6}_{-6}
GM Aur	3	$5.52^{+0.16}_{-0.16}$	$1.82^{+0.19}_{-0.19}$	$16.5^{+0.4}_{-0.4}$	$6.93^{+0.22}_{-0.22}$	$0.50^{+0.16}_{-0.16}$	$2.10^{+0.28}_{-0.28}$	$0.64^{+0.15}_{-0.15}$	$0.97^{+0.19}_{-0.19}$	$9.11^{+0.19}_{-0.19}$	$0.87^{+0.20}_{-0.19}$	$43.5^{+0.3}_{-0.3}$	426^{+6}_{-6}
GM Aur	4	$5.64^{+0.17}_{-0.17}$	$1.76^{+0.22}_{-0.22}$	$32.0^{+0.5}_{-0.5}$	$12.26^{+0.29}_{-0.29}$	$0.28^{+0.19}_{-0.19}$	$2.1^{+0.4}_{-0.4}$	$0.67^{+0.18}_{-0.18}$	$1.55^{+0.29}_{-0.29}$	$8.55^{+0.27}_{-0.27}$	$1.0^{+0.3}_{-0.3}$	$44.4^{+0.4}_{-0.4}$	340^{+6}_{-6}
GM Aur	5	$7.76^{+0.21}_{-0.21}$	$2.4^{+0.4}_{-0.4}$	$37.0^{+0.6}_{-0.6}$	$12.9^{+0.4}_{-0.4}$	$0.4^{+0.4}_{-0.4}$	$3.4^{+0.4}_{-0.4}$	$1.23^{+0.19}_{-0.19}$	$1.75^{+0.29}_{-0.29}$	$11.03^{+0.26}_{-0.26}$	$1.9^{+0.3}_{-0.3}$	$62.9^{+0.4}_{-0.4}$	458^{+5}_{-5}
GM Aur	6	$5.58^{+0.17}_{-0.17}$	$1.64^{+0.23}_{-0.23}$	$18.3^{+0.4}_{-0.4}$	$5.87^{+0.23}_{-0.23}$	$0.22^{+0.19}_{-0.19}$	$2.6^{+0.3}_{-0.3}$	$0.51^{+0.17}_{-0.17}$	$0.96^{+0.22}_{-0.22}$	$10.12^{+0.22}_{-0.22}$	$1.08^{+0.22}_{-0.22}$	$46.0^{+0.3}_{-0.3}$	375^{+5}_{-5}
GM Aur	7	$7.6^{+0.3}_{-0.3}$	$1.5^{+0.5}_{-0.5}$	$44.5^{+0.8}_{-0.8}$	$11.8^{+0.4}_{-0.4}$	$0.9^{+0.4}_{-0.4}$	$5.2^{+0.9}_{-0.9}$	$3.3^{+0.5}_{-0.5}$	$4.6^{+0.6}_{-0.6}$	$9.6^{+0.6}_{-0.5}$	$3.8^{+0.5}_{-0.5}$	$75.3^{+0.6}_{-0.6}$	529^{+6}_{-6}
GM Aur	8	$7.54^{+0.20}_{-0.20}$	$2.66^{+0.28}_{-0.28}$	$24.9^{+0.5}_{-0.5}$	$9.80^{+0.29}_{-0.3}$	$0.37^{+0.24}_{-0.24}$	$2.9^{+0.5}_{-0.5}$	$0.68^{+0.28}_{-0.28}$	$1.3^{+0.4}_{-0.4}$	$9.6^{+0.3}_{-0.3}$	$1.5^{+0.4}_{-0.4}$	$71.3^{+0.5}_{-0.5}$	432^{+5}_{-5}
SZ 45	1	$2.02^{+0.16}_{-0.16}$	$1.63^{+0.21}_{-0.21}$	$8.7^{+0.4}_{-0.4}$	$7.00^{+0.27}_{-0.27}$	$0.53^{+0.17}_{-0.17}$	$2.9^{+0.3}_{-0.3}$	$0.67^{+0.15}_{-0.15}$	$1.11^{+0.23}_{-0.23}$	$5.07^{+0.19}_{-0.20}$	$1.14^{+0.21}_{-0.21}$	$44.3^{+0.3}_{-0.3}$	128^{+9}_{-9}
SZ 45	2	$2.32^{+0.18}_{-0.18}$	$1.32^{+0.26}_{-0.26}$	$11.9^{+0.5}_{-0.5}$	$9.3^{+0.3}_{-0.3}$	$0.45^{+0.20}_{-0.20}$	$3.0^{+0.5}_{-0.5}$	$0.20^{+0.22}_{-0.22}$	$1.0^{+0.4}_{-0.4}$	$5.5^{+0.3}_{-0.3}$	$1.1^{+0.3}_{-0.3}$	$57.5^{+0.4}_{-0.4}$	158^{+9}_{-9}
SZ 45	3	$2.53^{+0.22}_{-0.22}$	$1.7^{+0.3}_{-0.3}$	$12.1^{+0.6}_{-0.6}$	$10.4^{+0.4}_{-0.4}$	$0.08^{+0.29}_{-0.29}$	$3.8^{+0.5}_{-0.5}$	$0.79^{+0.23}_{-0.23}$	$1.9^{+0.4}_{-0.4}$	$6.52^{+0.3}_{-0.29}$	$2.9^{+0.4}_{-0.4}$	$67.9^{+0.5}_{-0.5}$	191^{+12}_{-12}
SZ 45	4	$2.34^{+0.20}_{-0.20}$	$1.6^{+0.3}_{-0.3}$	$11.4^{+0.5}_{-0.5}$	$9.3^{+0.4}_{-0.4}$	$0.46^{+0.27}_{-0.27}$	$3.8^{+0.6}_{-0.6}$	$1.29^{+0.27}_{-0.28}$	$1.3^{+0.4}_{-0.4}$	$5.6^{+0.3}_{-0.3}$	$1.7^{+0.4}_{-0.4}$	$60.6^{+0.5}_{-0.5}$	183^{+10}_{-10}
SZ 45	5	$2.02^{+0.18}_{-0.18}$	$1.74^{+0.25}_{-0.26}$	$9.7^{+0.5}_{-0.5}$	$7.3^{+0.3}_{-0.3}$	$0.66^{+0.20}_{-0.20}$	$4.8^{+0.4}_{-0.4}$	$1.43^{+0.21}_{-0.21}$	$1.36^{+0.27}_{-0.27}$	$5.42^{+0.26}_{-0.26}$	$0.8^{+0.3}_{-0.3}$	$60.6^{+0.5}_{-0.5}$	195^{+10}_{-10}
TW Hya	1	$1.87^{+0.24}_{-0.24}$	$2.2^{+0.5}_{-0.5}$	$12.9^{+0.7}_{-0.7}$	$7.1^{+0.5}_{-0.5}$	$0.8^{+0.4}_{-0.4}$	$0.11^{+0.16}_{-0.16}$	$0.03^{+0.08}_{-0.08}$	$0.31^{+0.11}_{-0.11}$	$2.94^{+0.10}_{-0.10}$	$0.02^{+0.11}_{-0.11}$	$8.51^{+0.13}_{-0.13}$	$162.5^{+1.7}_{-1.7}$
TW Hya	2	$1.98^{+0.21}_{-0.20}$	$1.5^{+0.3}_{-0.3}$	$7.4^{+0.6}_{-0.6}$	$4.0^{+0.4}_{-0.4}$	$0.43^{+0.25}_{-0.25}$	$0.61^{+0.14}_{-0.14}$	$0.09^{+0.05}_{-0.05}$	$0.39^{+0.09}_{-0.09}$	$2.92^{+0.07}_{-0.07}$	$0.02^{+0.09}_{-0.09}$	$9.82^{+0.11}_{-0.11}$	$164.6^{+1.6}_{-1.6}$
TW Hya	3	$1.80^{+0.09}_{-0.09}$	$1.12^{+0.14}_{-0.15}$	$8.33^{+0.26}_{-0.26}$	$4.29^{+0.16}_{-0.16}$	$0.22^{+0.12}_{-0.12}$	$0.35^{+0.10}_{-0.10}$	$0.09^{+0.05}_{-0.05}$	$0.37^{+0.07}_{-0.08}$	$3.03^{+0.08}_{-0.08}$	$-0.09^{+0.09}_{-0.09}$	$8.06^{+0.11}_{-0.11}$	$158.4^{+1.7}_{-1.7}$
TW Hya	4	$2.93^{+0.14}_{-0.14}$	$1.53^{+0.20}_{-0.21}$	$8.3^{+0.4}_{-0.4}$	$4.09^{+0.21}_{-0.21}$	$-0.01^{+0.17}_{-0.17}$	$0.77^{+0.12}_{-0.12}$	$0.10^{+0.06}_{-0.06}$	$0.42^{+0.09}_{-0.09}$	$5.21^{+0.10}_{-0.10}$	$0.27^{+0.13}_{-0.13}$	$25.67^{+0.17}_{-0.17}$	$294.8^{+1.8}_{-1.8}$
VW Cha	1	93^{+7}_{-7}	21^{+4}_{-5}	338^{+9}_{-10}	44^{+4}_{-5}	9^{+4}_{-4}	24^{+6}_{-6}	$8.7^{+2.6}_{-2.6}$	24^{+4}_{-4}	78^{+3}_{-3}	$6.6^{+2.2}_{-2.2}$	$209.2^{+2.7}_{-2.7}$	1232^{+51}_{-50}
VW Cha	2	70^{+5}_{-5}	12^{+3}_{-3}	152^{+7}_{-7}	32^{+3}_{-3}	$3.8^{+2.4}_{-2.4}$	15^{+6}_{-6}	8^{+3}_{-3}	11^{+4}_{-4}	$65.6^{+2.3}_{-2.3}$	$3.1^{+1.6}_{-1.6}$	$134.0^{+2.1}_{-2.2}$	890^{+60}_{-60}
VW Cha	3	78^{+7}_{-7}	14^{+5}_{-5}	232^{+10}_{-10}	43^{+5}_{-5}	11^{+4}_{-4}	29^{+9}_{-9}	5^{+5}_{-5}	22^{+6}_{-6}	76^{+4}_{-4}	12^{+3}_{-3}	268^{+4}_{-4}	1260^{+60}_{-50}
VW Cha	4	76^{+11}_{-11}	26^{+7}_{-7}	280^{+12}_{-12}	66^{+6}_{-7}	14^{+6}_{-6}	48^{+10}_{-10}	14^{+5}_{-5}	23^{+7}_{-7}	95^{+5}_{-5}	13^{+4}_{-4}	380^{+5}_{-5}	1750^{+60}_{-60}
VW Cha	5	80^{+6}_{-6}	13^{+4}_{-4}	221^{+7}_{-7}	49^{+4}_{-4}	12^{+3}_{-3}	26^{+7}_{-7}	12^{+3}_{-3}	20^{+5}_{-5}	62^{+3}_{-3}	4^{+3}_{-3}	232^{+4}_{-4}	880^{+60}_{-60}

Note. — Integrated line luminosities are presented in units of $10 \times 10^{29}\, ergs s^{-1}$. Listed uncertainties are the 16^{th} and 84^{th} percentiles of the posterior, which is nearly symmetric for all lines included here. Line luminosities reported here have been corrected for extinction. The values reported here for the doublet/multiplet features are the blended line luminosities integrated over a narrow wavelength range covering the feature.

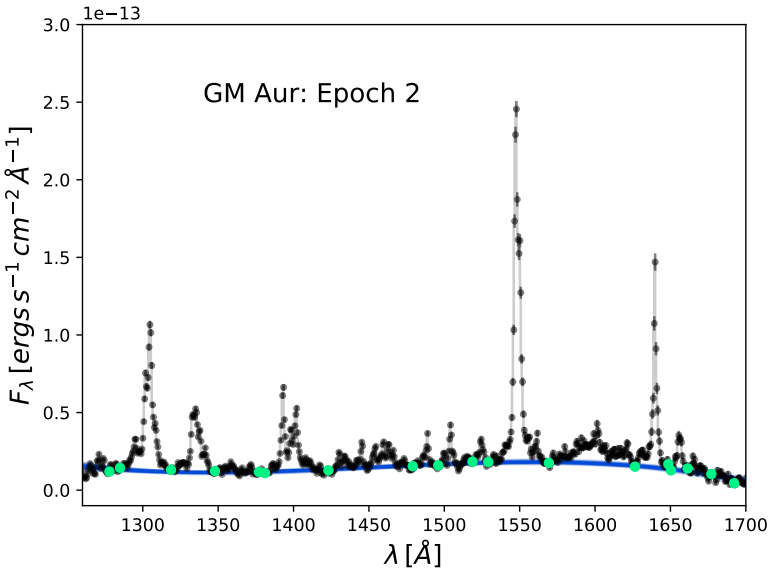

Fig. 3.8: FUV (MAMA G140L) spectrum for the GM Aur Epoch 2 observation (in black), shown as an example of the continuum fitting process. Points selected as being representative of the continuum level are in green. A representative sample (100 models) drawn from the posterior for a third-degree polynomial fit is shown in blue. The width of the posterior is representative of the uncertainty in the fit of the continuum.

the plethora of spectral lines, this approach appears to give a reasonable estimate of the uncertainty in the true level of the continuum. To ensure that the effect of line contamination in the continuum estimates is minimal, I compared my continuum fit to the non-convolved, high-resolution observations of TW Hya and found good agreement between the two. Additional tests consisting of resampling the data at resolutions between the Cosmic Origins Spectrograph (COS) resolution and STIS resolution with higher signal-to-noise ratios returned similar results. An example of the selected points and a representative set of draws from the posterior for the FUV wavelengths for Epoch 2 of the GM Aur observations are shown in Fig. 3.8.

Line luminosities and uncertainties were measured through a Monte Carlo approach. First, each data point in the relevant wavelength range was randomly re-

sampled from a Gaussian centered on the measured value with width given by the measurement uncertainties from the *HST* STIS pipeline. Next, a draw from the posterior for the continuum is selected and subtracted, and the line is integrated using a trapezoidal integration scheme. This was repeated many times, resulting in a posterior distribution for the line luminosity. Due to line blending by the low-resolution nature of the spectra, multiplet lines were measured and reported as individual spectral features by integrating over a narrow wavelength range covering the width of the feature. This includes the bright doublet lines Mg_{II} and C_{IV}.

3.4.6 Correlations with Observables

Plotting luminosities for many of the readily distinguishable lines in the spectra against mass accretion rate reveals relatively strong correlations. These correlations were quantified using the Pearson correlation coefficient (ρ) in Tab. 3.7. As a reminder, a perfect positive correlation will have a ρ of 1. Fig. 3.9 shows the line luminosities normalized by the stellar luminosity against $\dot{M}$.

I found that many of the NUV lines had strong correlations with the mass accretion rate. In particular, Si_{II}, $Si_{III]}$ $C_{III]}$, $Al_{III]}$ all had values of ρ greater than 0.7, with $Si_{III]}$ having the strongest correlation. C_{IV} was found to have the strongest correlation between any of the FUV lines and the mass accretion rate, with a median ρ of 0.620. C_{IV} is quite bright and has been previously observed and characterized in higher resolution studies (Ardila et al., 2013). This makes it useful as a mass accretion rate indicator when simultaneous NUV – optical measurements are not available (e.g., spectra from COS, Green et al., 2012). Other possible options for relating FUV lines to $\dot{M}$ include C_{II} and O_{III}.

One possible explanation for the changes in line luminosity is contamination from the variable continuum level in the line measurements, especially in the narrow partially forbidden lines. However, the regions chosen for continuum subtraction were

selected for each epoch individually with care to avoid line centers and wings while selecting points across the entire wavelength range (see Fig. 3.8 for an example). This makes it unlikely that the continuum extraction would be biased toward over predicting line fluxes for higher accretion rates.

In addition to correlations, I produced log-linear relationships between accretion rates and line strengths. The slope m and offset b which are also listed in Tab. 3.7. These relationships take the form

$$\log_{10}\left(\frac{\dot{M}}{10^{-8}\,\mathrm{M}_{\odot}\,\mathrm{yr}^{-1}}\right) = m \cdot \log_{10}\left(\frac{L_{line}}{L_{\star}}\right) + b. \tag{3.5}$$

These fits are shown plotted on top of the data in Fig. 3.9. Uncertainties on both the fit and the correlation coefficient were found using a Monte Carlo approach using draws from the model fit posterior and the line luminosity posterior. The scatter around the lines in some cases is large relative to uncertainties in the fit, suggesting systematic effects outside measurement uncertainties. This is somewhat expected given the simplicity of this approach. I find that line luminosities for individual objects follow relationships that are generally closer to monotonically increasing functions of mass accretion rate, as expected.

H_{α} in particular has been a useful accretion tracer because it is bright and easily observable from the ground. I found a limited correlation between H_{α} and $\dot{M}$, with a ρ of 0.149, which is in contrast to other studies (e.g., White & Basri, 2003; Natta et al., 2004; Ingleby et al., 2013). However, I note that a strong correlation would be readily apparent if the points belonging to TW Hya in the lower right corner of the final panel in Fig. 3.9 were not included. Doing so results in a ρ of $.780^{+0.013}_{-0.011}$ and a slope and offset of $1.25^{+0.03}_{-0.05}$ and $2.67^{+0.08}_{-0.18}$ respectively. TW Hya is in a pole-on viewing geometry (Andrews et al., 2016). Modeling suggests that sources with low inclinations should have stronger H_{α} emission (Lima et al., 2010), which is consistent

Table 3.7. Pearson correlation coefficients and log-linear fits for FUV/NUV lines

Line	λ [Å]	ρ	m	b
C_{II}	1335	$0.619^{+0.013}_{-0.018}$	$0.660^{+0.018}_{-0.05}$	$2.46^{+0.06}_{-0.17}$
C_{I}	1463	$0.32^{+0.05}_{-0.07}$	$0.39^{+0.08}_{-0.07}$	$1.7^{+0.3}_{-0.3}$
C_{IV}	1548	$0.620^{+0.012}_{-0.017}$	$0.758^{+0.014}_{-0.05}$	$2.36^{+0.04}_{-0.17}$
He_{II}	1640	$0.376^{+0.023}_{-0.021}$	$0.480^{+0.029}_{-0.03}$	$1.72^{+0.09}_{-0.11}$
O_{III}	1666	$0.48^{+0.11}_{-0.07}$	$0.41^{+0.09}_{-0.11}$	$2.0^{+0.4}_{-0.5}$
Si_{II}	1808	$0.77^{+0.05}_{-0.09}$	$0.93^{+0.10}_{-0.17}$	$3.8^{+0.4}_{-0.6}$
$Si_{III]}$	1892	$0.78^{+0.08}_{-0.14}$	$0.74^{+0.13}_{-0.18}$	$3.4^{+0.6}_{-0.8}$
$C_{III]}$	1908	$0.71^{+0.05}_{-0.07}$	$0.80^{+0.07}_{-0.10}$	$3.47^{+0.26}_{-0.4}$
$C_{II]}$	2325	$0.595^{+0.012}_{-0.020}$	$0.933^{+0.022}_{-0.09}$	$3.31^{+0.08}_{-0.3}$
$Al_{III]}$	2670	$0.69^{+0.09}_{-0.10}$	$0.74^{+0.13}_{-0.19}$	$3.4^{+0.6}_{-0.8}$
Mg_{II}	2796	$0.408^{+0.013}_{-0.025}$	$0.71^{+0.04}_{-0.07}$	$2.10^{+0.10}_{-0.19}$
H_{α}	6563	$0.149^{+0.016}_{-0.010}$	$0.309^{+0.027}_{-0.04}$	$0.71^{+0.05}_{-0.08}$

Note. — Pearson correlation coefficients (ρ) and log-linear fit parameters (m, b) between FUV and NUV emission lines and the mass accretion rate. These coefficients include all 25 epochs of HST observations and are calculated in $\log_{10}$ space. While m and b are unitless, the line luminosities and mass accretion rates for these log-linear relations are written in terms of $L_{line}/L_{\star}$ and $\dot{M}/1 \times 10^{-8}\, M_{\odot}\, yr^{-1}$ (see Eqn. 5).

with my findings. In general, TW Hya appears to have stronger line emission than the trends shown in other objects, suggesting it is an outlier. Lines where TW Hya is less apparent as an outlier include Si_{II}, S_{III}, Al_{III}. Measured H_α line luminosities are also affected by changes in wind opacity along the line of sight, which can appear as variable blue–red line asymmetries. This effect likely increases the scatter in the measured relationship between accretion luminosity and H_α.

One notable spectral feature is a broad continuum bump centered near 1600 Å with a width of ~ 30 Å produced by H_2 (Bergin et al., 2004; France et al., 2017). A planned companion paper will address this feature within the scope of this sample in more depth.

U-band excess as an accretion diagnostic

Empirical relations between excess flux in the Johnson U band (Johnson & Morgan, 1953) and the mass accretion rate are commonly used to infer mass accretion rates from the ground (Gullbring et al., 1998). The sample of 25 observations provides an opportunity to test and revise these relations. After dereddening, I subtracted the non-accreting photospheric template from the stars and convolved the spectrum of the excess in the optical with the Johnson U-band filter. Next, accretion continuum luminosities were found from the shock models by assuming

$$L_{acc} = \frac{GM_\star \dot{M}}{R_\star}\Big(1 - \frac{R_\star}{R_{in}}\Big). \tag{3.6}$$

From my observations, I found the following linear relation for converting from excess U-band luminosity to total accretion luminosity, written using the natural log for comparison against the Gullbring et al. (1998) relation (unlike the relationships in the previous section):

$$\ln(L_{acc}/L_\odot) = 0.93^{+0.03}_{-0.03}\ \ln(L_U/L_\odot) + 0.50^{+0.03}_{-0.03}. \tag{3.7}$$

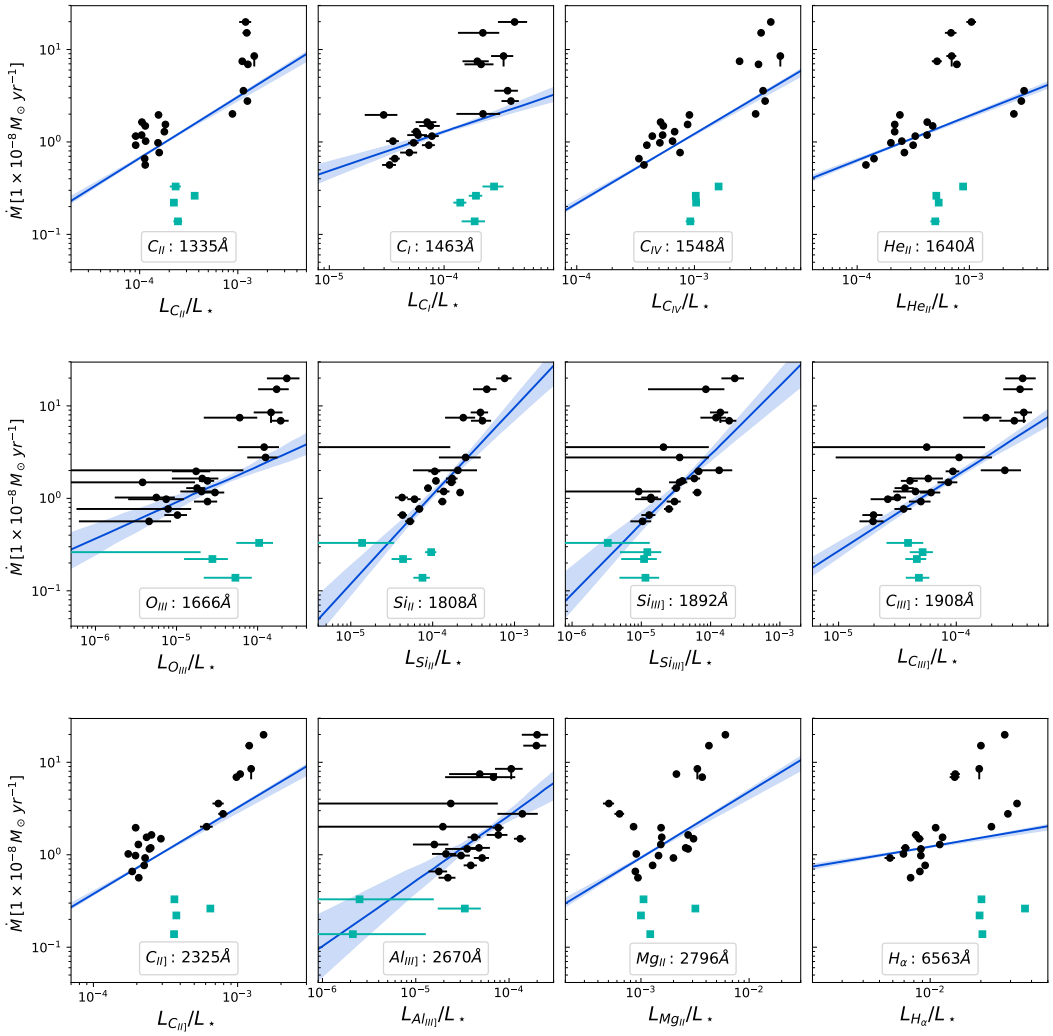

Fig. 3.9: Log-log fits to emission line luminosities and $\dot{M}$. The line luminosities have been divided by the stellar luminosity. The black dots represent observations for all of the objects except for TW Hya, which is shown as teal squares. TW Hya may be an outlier for several lines due to its viewing geometry. The log-linear fits shown here, whose coefficients are listed in Tab. 3.7, include the points from TW Hya during the fitting process. The error bars on the points in this figure reflect the values presented in Tab. 3.4 and Tab. 3.6.

I then compare my results to the commonly used empirical relation for measuring accretion rates from Gullbring et al. (1998). These two relations and the accretion luminosity measurements as a function of convolved U-band flux are shown in Fig. 3.10. I find that my results and those of Gullbring et al. (1998) are similar given the complexities of this type of analysis. An identical analysis was performed using the Sloan *u'* filter response function and recovered a slope of $0.91^{+0.03}_{-0.03}$ and an offset of $0.42^{+0.03}_{-0.11}$ (again in ln-space).

One major issue with using this type of method to obtain mass accretion rates is that it is highly dependent on the ability to accurately remove the photospheric contribution. Here, I use the posterior of the photospheric scaling factor s from my analysis, but clearly that will not be available for most objects. Alternatives include more conventional measurements of photospheric line veiling, or photosphere fitting from longer wavelength observations that are less veiled by the accretion shock. Using longer wavelength photometric observations (i.e., NIR) comes with its own risks, namely the possibility of veiling from the protoplanetary disk rather than the accretion shock. Accurate measurements of the extinction are also important for any determination of the accretion rate relying on continuum excess.

3.5 Discussion

I have presented measurements of the accretion rate and surface coverage of accretion columns of the stellar surface for a sample of five young stars with multiple contemporaneous FUV to NIR observations. In addition, I have measured contemporaneous line luminosities for several spectral features in the NUV and FUV that have previously been used as diagnostics for accretion. Here I interpret the results, examine correlations, and discuss interesting epochs.

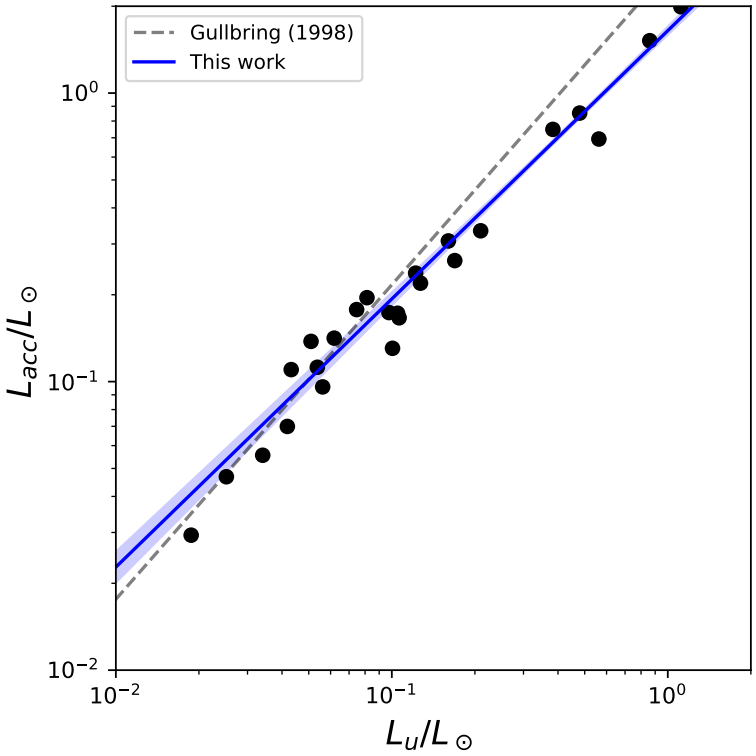

Fig. 3.10: Accretion luminosity as a function of excess U-band luminosity for the 25 observations. The relation found from the analysis is shown in blue (see Eqn. 7), and the commonly used relation from Gullbring et al. (1998) is shown by a broken black line

.

3.5.1 Overall Variability

I found significant amounts of mass accretion variability in all of the objects, even on the shortest timescales included in this study. Even the objects that showed the least amount of variance still changed by 50% on timescales of a week and showed large changes in FUV – NIR continuum and line fluxes. In addition to large changes in the mass accretion rate, significant changes in how mass is distributed between columns of different densities were observed on short timescales. As indicated by previous studies of this nature (Ingleby et al., 2015), these rapid timescales suggest

that variability is induced by changes in the very inner parts of the disk, since the viscous timescale is on the order of years for a standard disk model near 1 au (Hartmann et al., 1998). Whether this variability is induced by a changing magnetosphere or inhomogeneities or the inner disk structure or perhaps more likely a combination of both is more difficult to ascertain from these observations alone. Observed variability is further complicated by rotational modulation from hot spots and cool star spots rotating in and out of view. Spectropolarimetric observations of these objects would greatly help place the observed UV variability in the context of magnetic field structure.

3.5.2 Remarks on Individual Objects

In the following sections I discuss each object in depth, focusing on the mass accretion rate and surface coverage by columns of different densities. When possible, I attempt to place the observations in context with broad photometric surveys of variable young stars by providing suggestions as to the nature of the objects in my sample based on the classification schemes from Cody et al. (2014). Within the sample presented here, I identify GM Aur as a candidate burster and SZ 45 as likely either a quasi-periodic or stochastic source. TW Hya has already been identified as being dominated by flicker noise with semiperiodic changes attributed to instabilities in the inner disk (Rucinski et al., 2008; Siwak et al., 2011b,a, 2014, 2018). The results for TW Hya are consistent with those findings. Other sources are harder to identify because of the limited number of observations (DM Tau) or irregular signatures (VW Cha). Although some of the differences between the measurements and previous measurements of the mass accretion rate can be attributed to systematic differences between accretion diagnostics, I do find large changes between the observations from epoch to epoch. I also find that the mass accretion rates presented here can be used to derive similar relationships found for previous diagnostics (see Fig. 3.10). This

suggests that the primary driver in differences between my inferred mass accretion rates and previous works is likely changes in the overall mass accretion rate and how much of the accretion excess is visible because of rotational effects.

DM Tau

DM Tau is an M1 star (Ingleby et al., 2013) in the Taurus-Auriga region with an inner disk cavity (Andrews et al., 2011). DM Tau has previously been modeled using the Calvet & Gullbring (1998) accretion shock models, finding a value of $2.9 \times 10^{-9}\,M_\odot\,yr^{-1}$ (Ingleby et al., 2013). An earlier accretion measurement by Valenti et al. (1993) found a similar accretion rate.

The mass accretion rate for DM Tau measured here ranges from $\sim 2.0 - 3.6 \times 10^{-8}\,M_\odot\,yr^{-1}$ over three observational epochs. Epoch 1 is separated from Epoch 2 by one week, and Epoch 3 was obtained roughly three months later. DM Tau is an example of a transitional disk with significant accretion. The change in mass accretion rate observed in DM Tau between Epochs 1 and 2 is comparable to much of the variability observed in this sample of full/pre-transitional disks and GM Aur, aside from the outburst during Epoch 7 (see §3.5.2).

One unique feature about DM Tau is the high fraction of mass accreted via high-density columns. Over 60% of the mass/energy deposited onto DM Tau is carried by the high-density columns for all observational epochs, with a maximum of 91% during Epoch 3. I speculate that this might be a signature of a magnetic field with strong higher-order multipole (e.g., octupole) components. Analytic work and simulations predict that magnetically controlled accretion flows with higher order multipole components should have higher energy fluxes at the surface of the star with smaller surface coverages than dipole-controlled flows (Adams & Gregory, 2012; Robinson et al., 2017). At the shortest wavelengths included in my analysis, I find some degree of excess that cannot be explained with the three-component model.

A discussion of four-column fits with a higher column energy flux is presented in §3.4.4. The results from this additional analysis are consistent with the interpretation presented here, but with slightly higher mass accretion rates and higher degrees of surface coverage by low-density shocks.

GM Aur

GM Aur is a well-studied system containing a transitional disk around a young K5 (Manara et al., 2014) solar-analog star in the Taurus-Auriga complex. SED modeling and submillimeter observations of GM Aur show the presence of a large ($\sim$ 35 au) cavity with some remnant optically thin dust near the star (Calvet et al., 2005; Hughes et al., 2009; Andrews et al., 2011; Espaillat et al., 2011; Macías et al., 2018).

My measured accretion rates for the transitional disk GM Aur range from $\sim 0.6 \times 10^{-8}$ to $2.0 \times 10^{-8}\,\mathrm{M_\odot\,yr^{-1}}$ with significant changes in accretion over week- and month-long timescales. The first three epochs of observations presented here have previously been modeled using the Calvet & Gullbring (1998) shock models (Ingleby et al., 2015) resulting in measured accretion rates of 1.1×10^{-8}, 8.5×10^{-9}, and $3.9 \times 10^{-9}\,\mathrm{M_\odot\,yr^{-1}}$. I find higher degrees of surface coverage by low-density columns ($1 \times 10^{10}\,\mathrm{erg\,s^{-1}\,cm^{-2}}$) and higher values of accretion rate overall. These differences are likely primarily due to differences in how photospheric scaling was treated in each respective analysis, in addition to the other updates to the model discussed in §3.3. I find higher degrees of veiling than the constant value of $r_V = 0.2$ adopted by Ingleby et al. (2015). Because the shape of the emission from low-density columns most closely resembles photospheric emission, it seems reasonable that I would measure higher contributions in this work given the different fitting procedure. Surface coverage for the medium- and high-density accretion columns remains largely unchanged between the two analyses. The accretion behavior of GM

Aur during Epochs 4 and 5, taken 4 yr later than Epoch 3, appears fairly consistent with observations taken in Epochs 1 and 2.

Some of the more striking features from my analysis are the changes in emission observed over Epochs 6, 7, and 8 of the GM Aur observations (see Fig. 3.1). These data were taken over two weeks with roughly a week separation between each observation. Continuum levels in the FUV are higher in Epoch 7 than in the other epochs by roughly a factor of three, while emission in the NUV during this epoch is higher than previous epochs by between a factor of three and ten (depending on the epoch or wavelength). The inferred accretion rate increased from ~ 0.6 to $2.0 \times 10^{-8}\,\mathrm{M_\odot\,yr^{-1}}$ between Epochs 6 and 7, and then returned to $\sim 1.0 \times 10^{-8}\,\mathrm{M_\odot\,yr^{-1}}$ during Epoch 8.

An upper limit, set by the observational cadence, can be placed on the relevant timescale for this event of about two weeks. The rotation rate of GM Aur has been measured to be 6.1 d (Percy et al., 2010), which is roughly the same as the cadence for these three epochs. My interpretation is that we are seeing roughly the same region of the star in each of my observations. This implies that the changes in the spectrum are due to changes in the mass accretion rate rather than stable hot spots rotating in and out of view.

My analysis for Epoch 7 indicates that roughly 30% of the surface of the star is covered in low- density columns, which is the highest ever measured for this object. My analysis shows that $\sim$ 0.2% of the star is covered by high-density accretion columns, which is a full order of magnitude higher than Epoch 6 and roughly triples the next highest coverage ever measured in all epochs. Epoch 7 also has the largest percentage (43%) of mass/energy contributed by the high- density columns while most of the other epochs have contributions of $10 - 20\%$. Epoch 8 has the second highest contribution at 27%, perhaps consistent with residual higher density material

from the event that occurred during Epoch 7. Discussion and fits for a model of Epoch 7 with contributions from a fourth column with an even higher energy flux of $3 \times 10^{12}\,\mathrm{erg\,s^1\,cm^{-2}}$ is included in §3.4.4. The inclusion of this higher density column does not significantly change the interpretation presented here.

GM Aur appears to satisfy the trends that would classify it as a burster as described by Cody et al. (2014). This type of object is categorized by rapid increases in the accretion rate followed by a slower decay with moderate degrees of veiling and face-on inclinations (see Stauffer et al., 2014). GM Aur has a measured inclination of $52.77^{\circ}{}^{+0.05}_{-0.04}$ from radio interferometry observations (Macías et al., 2018) which is consistent with the picture of bursters.

SZ 45

SZ 45 (alternative name: T56) is a system in Chamaeleon composed of an M0.5 star (Manara et al., 2014) surrounded by a pre-transitional disk (Kim et al., 2009). Detailed SED modeling of the IR excess estimates the extent of the gap between the inner and outer disk to be 20 au (Espaillat et al., 2011). Previous measurements of $\dot{M}$ found $5 \times 10^{-9}\,\mathrm{M_\odot\,yr^{-1}}$ (Manara et al., 2014).

The mass accretion rate from my measurements for SZ 45 varies between $\sim 0.9 - 1.6 \times 10^{-8}\,\mathrm{M_\odot\,yr^{-1}}$ during the five epochs that it was observed. During the first four epochs, which were taken over the course of 1 week, the mass accretion rate steadily increases up to roughly a factor of 2 higher than the first observation. During the fifth and final observation (1.5 months later), $\dot{M}$ returned to a similar value as Epoch 2 of $\sim 1.2 \times 10^{-8}\,\mathrm{M_\odot\,yr^{-1}}$.

One possible explanation for the slow, consistent rise of the mass accretion rate over timescales of days is a stable hot spot rotating into view. Rotation rates of CTTS and WTTS from large photometric surveys reveal a distribution of rotation periods centered around 5.2 d (Venuti et al., 2017), which is comparable to the total

amount of time covered by the first four epochs of observations. A large fraction of the variability in young stars has been found to be simply due to rotational effects (Venuti et al., 2015). SZ 45 on average has moderate surface coverage during all of the observations, ranging from 17% to 30% surface coverage. With no magnetic field topography readily available for this object, one might speculate that this smooth increase in accretion rate and surface coverage is a signature of an ordered field perhaps with dipolar field components. A multipole field with predominantly dipole contributions is thought to lead to hot spots concentrated toward the poles with limited surface coverage (e.g., TW Hya; Donati et al., 2011c). Additionally, an object with a strong dipole field should have smaller contributions from high-density columns compared to an object with a strong, higher-order field, due to the decreased amount of compression of the flow near the star (Adams & Gregory, 2012; Robinson et al., 2017), which is observed in this object, with typical energy contributions from low-density columns comprising roughly 70% of the total energy budget.

One discrepancy in this interpretation is that my analysis suggests that the ratio of mass being transferred by the medium and high column densities is changing throughout these epochs. These changes perhaps indicate that instead of solely rotationally induced changes, SZ 45 is closer to the quasi-periodic variability class described by Cody et al. (2014) or possibly the stochastic object class. Both classifications exhibit some degree of stochastic variability over these timescales analogous to what was observed. Longer term photometric monitoring of this system would be helpful for further interpreting these results.

TW Hya

TW Hya is one of the closest examples of a protoplanetary disk at a distance of 60 pc (Gaia Collaboration et al., 2016, 2018). It is a transitional disk system in the TW Hya association with a K7 central star (Manara et al., 2014). TW Hya has been

studied extensively due to its proximity and relative isolation (e.g., Calvet et al., 2002; Andrews et al., 2016). Accretion rates from UV/optical spectra for TW Hya have been measured before with values of $2.3 \times 10^{-9}\,M_\odot\,yr^{-1}$ (Ingleby et al., 2013) and $1.3 \times 10^{-9}\,M_\odot\,yr^{-1}$ (Manara et al., 2014). Other measurements of the mass accretion rate from secondary indicators give similar values of $\sim 1 \times 10^{-9}\,M_\odot\,yr^{-1}$ (e.g., Curran et al., 2011; Donati et al., 2011c).

The inferred mass accretion rates across the four epochs of observations of TW Hya were consistently the lowest in my sample, with values ranging between ~ 1.4 and $3.3 \times 10^{-9}\,M_\odot\,yr^{-1}$, which are roughly consistent with previous measurements. Changes in the accretion rate on the order of about two were observed across all of the epochs, which is fairly typical within this sample. Separations between the observations include $\sim$ 1 week, 3 months, and 5 yr. The total surface coverage of accretion columns varies from 9% to 29%. TW Hya has been observed to be nearly face-on ($i = 7^\circ \pm 3^\circ$, Andrews et al., 2016), which should limit variability produced by hot spots or star spots rotating in and out of view.

No single column density greatly dictates the influx of material/energy onto TW Hya. There are moderate changes in the percentage of mass contributed by each component. Epochs 1, 2, and 3, which were all taken within a few months of each other, have roughly equal relative contributions to the total mass influx from the high-density columns (20% – 25%), while the remainder varies greatly between the medium- and low-density columns. Epoch 4, taken 5 yr later, has a slightly higher contribution from high-density columns at 34%.

TW Hya is the only object in the sample that has detailed mapping of the magnetic field topography through spectropolarimetric observations (Donati et al., 2011c). Those observations indicate the presence of a predominantly poloidal field dominated by a rotation-axis-aligned octopolar component with a weaker

antiparallel-rotation-axis-aligned dipolar component. Those authors found accretion-powered hot spots with coverage on the order of 2%, which is similar to the coverage by medium- and high-density columns indicated by my analysis. It was also found that accretion occurred primarily at the poles of the star, but there was some evidence of variable accretion at lower latitudes, possibly consistent with the modest surface coverage of low-density columns that I have found with my analysis. Long-term photometric surveys of TW Hya indicate flicker noise behavior and longer term quasi-periodic behavior, which are consistent with the type of variability observed during these four epochs (Rucinski et al., 2008; Siwak et al., 2011b,a, 2014, 2018).

VW Cha

VW Cha is system that includes a full disk around a K7 star located in Chamaeleon (Manoj et al., 2011). Previous observations of VW Cha have measured mass accretion rates of $1.1\times10^{-7}\,M_\odot\,yr^{-1}$ (Hartmann et al., 1998), $2.5\times10^{-8}\,M_\odot\,yr^{-1}$ (Manara et al., 2016), and $3.2\times10^{-8}\,M_\odot\,yr^{-1}$ (Salyk et al., 2013).

My analysis for VW Cha reveals a robust accretor with significant contributions from both low- and high-density accretion columns. VW Cha is the strongest accretor in the sample, with median mass accretion rates ranging between $\sim 6.9-20\times10^{-8}\,M_\odot\,yr^{-1}$ over the five epochs that it was observed. The first four epochs were observed over roughly one week and Epoch 5 was obtained 1.5 months later.

While all of the epochs display variability in the FUV and NUV typical of all of the objects in the sample, the NIR and optical wavelengths show interesting behavior. The first four epochs of VW Cha are roughly consistent with each other in the optical and NIR, but I find a large decrease in both wavelength ranges during Epoch 5 (see Fig. 3.1). The FUV and NUV emission during Epoch 5 is higher than two out of four of the previous epochs. This is inconsistent with the typical variability observed in other objects in this sample. To explain this curious behavior, I consider

several possibilities: (1) pointing error, (2) contamination from a companion, (3) star spots, (4) variable global extinction, and (5) a partial chance occultation by the magnetosphere or a disk warp along the line of sight.

(1) Pointing Error I inspected the centering of the object on the slit from the *HST* acquisition images, and VW Cha appears to be well centered in the slit. Aperture photometry of VW Cha using the acquisition images in the F28X50OII observing mode (centered on O_{II} at 3727 Å) is consistent with the flux changes observed in the spectrum, suggesting that the object was indeed well centered in the slit.

(2) Companions VW Cha is a known triple system (Brandeker et al., 2001). The primary and secondary stars are separated by 0.″7, and the tertiary is tightly bound to the second star with a projected separation of 0.″1. The secondary star is well resolved and readily apparent in the acquisition images. The tertiary star remains undetected by eye due to its dimness and proximity to the secondary. During Epochs 1, 2, 3, and 4, the position angle of the slit was set such that only the primary star fell onto the slit. During Epoch 5, the position angle of the slit changed significantly, causing the secondary to also align with the slit, which was visible in the 2D spectra. The stars are far enough apart on the detector to avoid significant contamination from the secondary during extraction, and care was taken to ensure that the background level selected for subtraction was also far away from either star. The background emission was faint and relatively flat across the detector. In addition, if there was contamination from the secondary in the extraction of the primary, it would instead act to increase the flux, which was opposite of what was observed. All of this suggests that contamination from the secondary (or the dim tertiary) is not responsible for the changes in flux. Additional companions falling onto the slit due to changes in the

position angle are ruled out by high-resolution (0.″1) images of VW Cha obtained by Brandeker et al. (2001).

(3) Star Spots Typical star spots are $\sim$ 500 K cooler than the photosphere (Venuti et al., 2015) and will decrease the emission in the optical and NIR. Both the star spots and the undisturbed photosphere contribute little to the observed UV excess compared to the contributions from the accretion shock (see Calvet & Gullbring, 1998; Ingleby et al., 2013). Since I have made the assumption that the undisturbed photosphere is not changing between different epochs, this is not something that the model can recover. Lifetimes of star spots on TTS are on the order of years (Bradshaw & Hartigan, 2014). Given this, it seems unlikely that changes of this magnitude would occur in spot coverage over a period of 1.5 months, making this a less plausible explanation for the observed changes. A large spot hidden on the opposite side of the star during the first four epochs is also an unlikely explanation for the observed changes. Epochs 1-4 span roughly one week, which is comparable to the typical rotation rate observed in young stars (see Bouvier, 2007). If there was a large cool spot, its effects likely would have been observed during those epochs.

(4) Changes in Global Extinction Changing extinction column densities are a common source of variability in young stars (e.g., AA Tau; Grankin et al., 2007; Bouvier et al., 2013). The expected signature of an increase in extinction is a large decrease in the observed FUV and NUV, with a smaller decrease in the optical and NIR. This is inconsistent as the sole cause of the observed changes in Epoch 5 because the FUV and NUV are similar to previous epochs while the optical decreases, and I would expect to see the largest changes in the UV.

(5) Partial Occultation The situation changes if only part of the star is extincted. If the degree of accretion is similar to other epochs, one could imagine a scenario where a chance alignment of the cooler magnetosphere or an inner disk warp covers a large fraction of the undisturbed photosphere, but not the regions of the star covered by high-energy flux accretion columns. This would result in suppressed photospheric emission in the optical/IR while the emission in the NUV/FUV would remain primarily unchanged, which is consistent with my observations. The amount of material blocking stellar emission along the line of sight is difficult to directly measure due to degeneracies between accretion, the fraction of the star that is occulted, and occulting column density. However, if I make the simplifying assumption that the extincting screen is fully opaque to the stellar emission, I can estimate the fraction of the star that is blocked and obtain lower limits on the mass of the screen. To make this approximation, f_i, w, and s for Epochs 1 - 4 were refit simultaneously, while the parameters for Epoch 5 were fit separately. Assuming all of the changes in the photospheric scaling factor s for Epoch 5 are solely due to occultation, I find that approximately 60% of the emission from the stellar surface is blocked. Using the typical relation between A_v and column density for $R_V = 3.1$ ISM dust (Weingartner & Draine, 2001) and a uniform extinction across the screen of 3 magnitudes (in A_v, such that $\sim$ 95% of the light is absorbed at V band), I find a very rough estimate of the minimum amount of occulting dust of $M_{occult} > 1 \times 10^{-14}\,\mathrm{M}_\odot$.

The fraction of coverage observed in VW Cha is comparable to the inferred coverage of the young star V354 Mon, where disk warps were invoked to explain changes in observed flux (Fonseca et al., 2014; Schneider et al., 2018). One complication in this explanation for VW Cha is that V354 Mon is extincted by the disk warp about half of the time with a period of 5.25 d, where I only observe these changes in one out of five epochs. The first four epochs span roughly one week, which is similar to

typical rotation rates of CTTS. To avoid this issue, one might speculate that the disk warp has a longer period than seven d (giving a Keplerian radius of $>\sim 0.08$ au.)

Extinction by the magnetosphere requires a moderate amount of dust grains within the accretion column to sufficiently extinct the light from the photosphere. Previous observations have suggested that large grains may be able to survive near the corotation region (e.g., Ingleby et al., 2015; Stauffer et al., 2015). This would suggest that the canonical picture of a dust-free inner gas disk may be oversimplified. If occultation by a dusty column is more sensitive to geometric alignment than disk warps, it might explain why we do not see its effects during the previous four epochs as the duration of the occultation would be reduced.

While extinction by the accretion column is the preferred explanation, I note that the above is qualitative and speculative since my models do not recover this sort of geometric effect and we cannot discern between different alignment scenarios under the current framework. In any case, the changes in the observed flux appear to be astrophysical in nature and not a by-product of calibration. Given the strange behavior observed for this object, it is difficult to speculate with any certainty on a variability class, but if the observed changes are indeed due to extinction, then it may fall into the "dipper" class. Additional observations, particularly photometric monitoring to better constrain occultation timescales and submillimeter interferometric observations to measure the inclination of the disk, would greatly help with the interpretation of these observations.

3.5.3 Star Spots and Caveats

Previous efforts with similar modeling processes have scaled the photospheric flux by a constant veiling value generally measured from a high-resolution and often nonsynchronously obtained optical spectrum. This approach results in undisturbed photospheric fluxes that are inconsistent if variability in the accretion shock emission

occurs. The analysis presented here makes the assumption that the continuum fluxes from the undisturbed photosphere for an individual star remain constant between observations. In reality, the emission from the photosphere will likely be modulated by star spots. Surface coverage from star spots can be large ($\sim 20\%$) for young stars, and star spots are typically very long lived (Bradshaw & Hartigan, 2014). While changes in mass accretion rates may happen on shorter timescales than changes in star spot distributions, rotational modulation of existing star spots occurs on similar timescales.

Disk warps are another possible source of variability that were not considered in this analysis for objects other than VW Cha. If the disk is not symmetric, raised regions of the disk can pass between the star and the observer, manifesting as changes in the extinction as a function of disk rotational phase (e.g., AA Tau Grankin et al., 2007; Bouvier et al., 2013). This effect primarily occurs if the inclination is such that the disk is being viewed nearly edge-on. It is difficult to infer the importance of disk warps with the limited cadence of the *HST* observations, but additional photometric monitoring or millimeter observations to obtain inclinations for these objects would make it possible to identify cases where disk warps are an important component of the variability.

Another important caveat to the work done here to keep in mind is that stars are inherently 3D objects, and I am inferring the accretion rates and surface coverage based only on the excess visible to us as the observer. Based on the paradigm of magnetospheric accretion and the localization of magnetic footprints shown by spectropolarimetric measurements (e.g., Donati et al., 2011b) and hot-spot-modulated light curves, it is very possible that surface coverage on the far side of the star is different from surface coverage on the front side. Likewise, the filling factors provide only a crude method of adjusting the amount of excess produced by the model com-

pared to a a full 3D model with geometric effects, as discussed in the context of VW Cha in §3.5.2.

With this in mind, some of the variability observed here can likely be explained by changes in which parts of the star are visible to us instead of changes in the amount of material falling onto the star. Higher cadence observations and measurements of the rotation rate for individual stars would help eliminate some of these concerns and aid in the interpretation of these spectra.

3.6 Conclusions

Using multiple *HST* UV spectra of individual young stars, I have explored accretion variability from three approaches: the overall mass accretion rate, coverage of the different density accretion columns, and FUV/NUV emission lines. Here I summarize the main points of this chapter:

1. I have updated the Calvet & Gullbring (1998) shock models and include veiling and model uncertainty as parameters when fitting multiepoch observations.

2. I find that mass accretion rates are highly variable, with typical spreads of roughly a factor of two individual objects. As such, future studies considering an effect that may be sensitive to FUV/NUV emission (e.g., infrared H_2 line emission; Nomura et al., 2007) should consider obtaining a simultaneous diagnostic of the accretion rate.

3. U-band photometry and FUV, NUV, and H_α line luminosities have been found to be indicators of mass accretion rates, a result that is consistent with previous findings.

4. The transitional disk GM Aur underwent a factor of 3.5 increase in the mass accretion rate during one epoch of the observations, relative to all other sampled epochs, which I interpret as an accretion burst.

5. VW Cha demonstrated interesting behavior during Epoch 5 in which the optical flux significantly decreased while the NUV/FUV fluxes remained comparable to previous epoch's values. The qualitative interpretation that I offer to explain this event is a chance alignment of the accretion column, leading to selective extinction of the undisturbed photosphere along the line of sight, while high-energy shocks remain free from extinction.

6. I offer suggestions as to the morphological variability classes of GM Aur as a burster and SZ 45 as either a quasi-periodic or stochastic source. The observed behavior of TW Hya is consistent with the previous interpretations of a pole-on quasi-periodic source punctuated by short-timescale flicker noise. DM Tau and VW Cha are more difficult to classify, due to the limited number of epochs and unique behavior, respectively.

My results continue to demonstrate the near-ubiquitous nature of variability in TTS and highlight the need for continued UV monitoring of accreting young stars.

4

HST, LDT, and Short-cadence *TESS* Observations of T Tauri Stars in Taurus

A similar version of this chapter is currently under review in the Astrophysical Journal.

4.1 Introduction

Nearly all CTTS show some manner of variability. Sources of the variability include rotational modulation from hot/cool spots, changes in the mass accretion rate, stellar activity, and variable extinction from material in the surrounding disk or dust entrained within the stellar magnetosphere (e.g., Herbst et al., 1994; Cody et al., 2014). The different sources of variability can be disentangled by their light curve shapes and characteristic timescales. Month-timescale photometric satellite-based monitoring campaigns of CTTS with CoRoT and K2 (Cody et al., 2014; Cody & Hillenbrand, 2018) have been successful in characterizing variability on timescales longer than 30 minutes through the development of statistical metrics that can be used to sort light curves into several categories of empirical variability classifications. Simulations of the inner regions of disks have been able to explain some of the observed variability caused by changes in the mass accretion rate on hour- and day-timescales via instabilities in the inner regions of the disk and overdensities in the accretion column powered by turbulence (e.g., Kurosawa & Romanova, 2013; Robinson et al., 2017).

Despite the above progress, variability on minute- to hour- timescales and the driving forces behind it remain relatively poorly characterized. Thermal instabilities have been predicted to be a source of variability within the accretion column Langer et al. (1981); Chevalier & Imamura (1982) with predicted timescales varying from 0.02 s to 900 s, given model assumptions (Sacco et al., 2008; Koldoba et al., 2008; Orlando et al., 2013; Costa et al., 2017). Studies searching for these instabilities have had mixed results. Drake et al. (2009) and Günther et al. (2010) did not find any evidence of periodic behavior on these timescales, while Siwak et al. (2018) identified quasi-periodicity on 11-to-30-minute timescales. Their results suggest that these types of events may not occur all of the time and have small amplitudes ($\sim$ 1% changes in flux), making high precision, continuous, short-cadence monitoring necessary. However, only a handful of multi-day, short-cadence observations of CTTS exist from K2, which primarily targeted atypical systems, making it difficult to draw more general conclusions on short-timescale accretion variability behavior.

The Transiting Exoplanet Survey Satellite (*TESS* Ricker et al., 2015) has begun to eliminate some of these concerns by providing high-quality light curves of many CTTS, including continuous, 2-minute cadence observations which can probe variability that may have been missed by previous studies. With the continuous monitoring observing strategy of *TESS*, it is also feasible to obtain simultaneous, multi-wavelength, multi-observatory, short-timescale observations for multiple, well-studied targets which are critical for interpreting observations of short-timescale accretion variability.

To link the short-timescale variability as observed by *TESS* to accretion diagnostics, I present *TESS* observations with simultaneous photometric observations from the Lowell Discovery Telescope (LDT) for 14 well-studied T Tauri Stars in the Taurus-Auriga star-forming region. Additionally, I present six new epochs of *HST*

STIS spectra taken simultaneously with *TESS* that provide NUV - NIR coverage of the CTTS GM Aur, which has been the focus of several previous variability studies (see Ingleby et al., 2015; Robinson & Espaillat, 2019, and Chapter 3). In §4.2, information about the data sets and reduction processes are presented. In §4.3, I detail the steps taken to analyze these data sets. In §4.4, I present the results. I discuss the significance of these results in regards to previous studies and upcoming observations in §4.5 and summarize my key findings in §4.6.

4.2 Observations

The sample presented in this chapter consists of the 14 brightest TTS in the Taurus-Auriga star-forming region that were observed by *TESS* in Cycle 2. The well-studied Taurus star-forming region is located roughly 140 pc away, and is 1-2 Myr old (Torres, 2007; Andrews et al., 2013). Tab. 4.1 contains the coordinates and stellar parameters (discussed in more detail in §4.3.1). GM Aur, a young K5 star with a transitional disk containing residual optically thin dust in the cavity (Calvet et al., 2005; Hughes et al., 2009; Andrews et al., 2011; Espaillat et al., 2011; Macías et al., 2018), was selected for additional monitoring efforts to follow up on previous UV studies of accretion, where it showed significant changes in $\dot{M}$ (Ingleby et al., 2015; Robinson & Espaillat, 2019). GM Aur is an ideal target for accretion studies because of its robust accretion rate, similarity to the young Sun, inner cavity, and moderate inclination of $52^{\circ}.77^{+0.05}_{-0.04}$, which limits the chance for disk occultation of the star (Macías et al., 2018).

4.2.1 *TESS*

Short-cadence (2-minute) light curves of the objects in the sample were obtained through *TESS* GO program 22216 (PI: C. Robinson). These observations occurred

Table 4.1. Coordinates and Stellar Parameters

Object Name	2MASS Name	α $[hms]$	δ $[^\circ]$	SpT	A_v	$T_\star$ $[K]$	$L_\star$ $[L_\odot]$	Distance $[pc]$	$R_\star$ $[R_\odot]$	$M_\star$ $[M_\odot]$
BP Tau	J04191583+2906269	4:19:15.8	+29:06:26.9	M0.5	0.45	3900	0.4	129.1	1.38	0.66
CW Tau	J04141700+2810578	4:14:17.0	+28:10:57.8	K3	1.8	4543	0.46	132.4	1.09	0.98
CY Tau	J04173372+2820468	4:17:33.7	+28:20:46.8	M2.3	0.35	3560	0.26	128.9	1.32	0.4
CoKu Tau 4	J04411681+2840000	4:41:16.8	+28:40:00.1	M1.1	1.75	3720	0.48	170.5	1.67	0.48
DD Tau	J04183112+2816290	4:18:31.1	+28:16:29.0	M4.8	0.75	3190	0.25	123.1	1.66	0.19
DE Tau	J04215563+2755060	4:21:55.6	+27:55:06.1	M2.3	0.35	3560	0.5	127.4	1.86	0.38
DS Tau	J04474859+2925112	4:47:48.6	+29:25:11.2	M0.4	0.25	3900	0.24	159.1	1.08	0.72
FO Tau	J04144928+2812305	4:14:49.3	+28:12:30.6	M3.9	2.05	3410	0.76	156.9	2.5	0.28
FM Tau	J04141358+2812492	4:14:13.6	+28:12:49.2	M4.5	0.35	3190	0.07	131.9	0.88	0.18
FN Tau	J04141458+2827580	4:14:14.6	+28:27:58.1	M3.5	1.15	3410	0.53	131.2	2.09	0.29
GM Aur	J04551098+3021595	4:55:11.0	+30:21:59.5	K5	0.6	4350	1.28	159.6	2.0	1.36
RY Tau	J04215740+2826355	4:21:57.4	+28:26:35.5	G0	1.85	5930	11.04	133.0	3.16	2.07
V819 Tau	J04192625+2826142	4:19:26.3	+28:26:14.3	K8.0	1.0	3960	0.48	131.7	1.48	0.69
UY Aur	J04514737+3047134	4:51:47.4	+30:47:13.6	K7.0	1.0	4020	1.05	155.6	2.12	0.63

Note. — Stellar parameters were adopted from Herczeg & Hillenbrand (2014), except for GM Aur, which are adopted from Manara et al. (2014) (see §4.3.1). Distances were derived from parallaxes from *Gaia* DR2 (Gaia Collaboration et al., 2016, 2018), and luminosities were updated based on those distances. The exception to this is RY Tau, whose *Gaia* parallax is suspected to be erroneous. Masses were obtained by interpolating between models in the MIST isochrone tracks (Choi et al., 2016; Dotter, 2016).

during *TESS* Sector 19 (Nov. 28th - Dec 23rd, 2019). The *TESS* spectral response curve is very broad, and covers roughly between 0.6μm and 1.1μm with a steep cutoff at the blue end. An orbital gap in the data is present in each of the otherwise continuous light curves during perigee. The light curves for each object are shown in Fig. 4.1.

To verify the quality of the data, the 30-minute cadence target pixel files from the Full Frame Images (FFI) for each object were individually inspected using the Python package `Lightkurve` (Lightkurve Collaboration et al., 2018). Several of the data sets include transient (presumably solar-system) objects that cross through the frame. From visual inspection, these transient objects do not significantly impact the quality of any of the target light curves. For each object, I applied a variety of test apertures to the FFI to produce light curves for comparison against the short-cadence light curve produced by the Science Processing Operations Center (SPOC) pipeline. I found that some contamination is present from nearby stars for several of the objects, but in all cases the target is the dominant source of photons. The light curve from the FFI using the ideal aperture from this testing closely matched the short-cadence light curve produced by the SPOC pipeline for each object. Given this, I adopt the SPOC pipeline reduction. I also monitored the background flux in the FFI to determine the length of time around the orbit gaps to mask and find the standard SPOC mask is suitable to avoid contamination. Erroneous observations (e.g., single-frame sudden brightening/dimming events) were identified by visual inspection and masked. Flares were identified by eye and stored as a separate mask. I leave detailed analysis of these flares for later work.

4.2.2 *HST*

Six NUV - NIR spectra of GM Aur were obtained using the STIS aboard *HST* , with a 1-3 d separation between epochs These spectra were taken with the 52" x

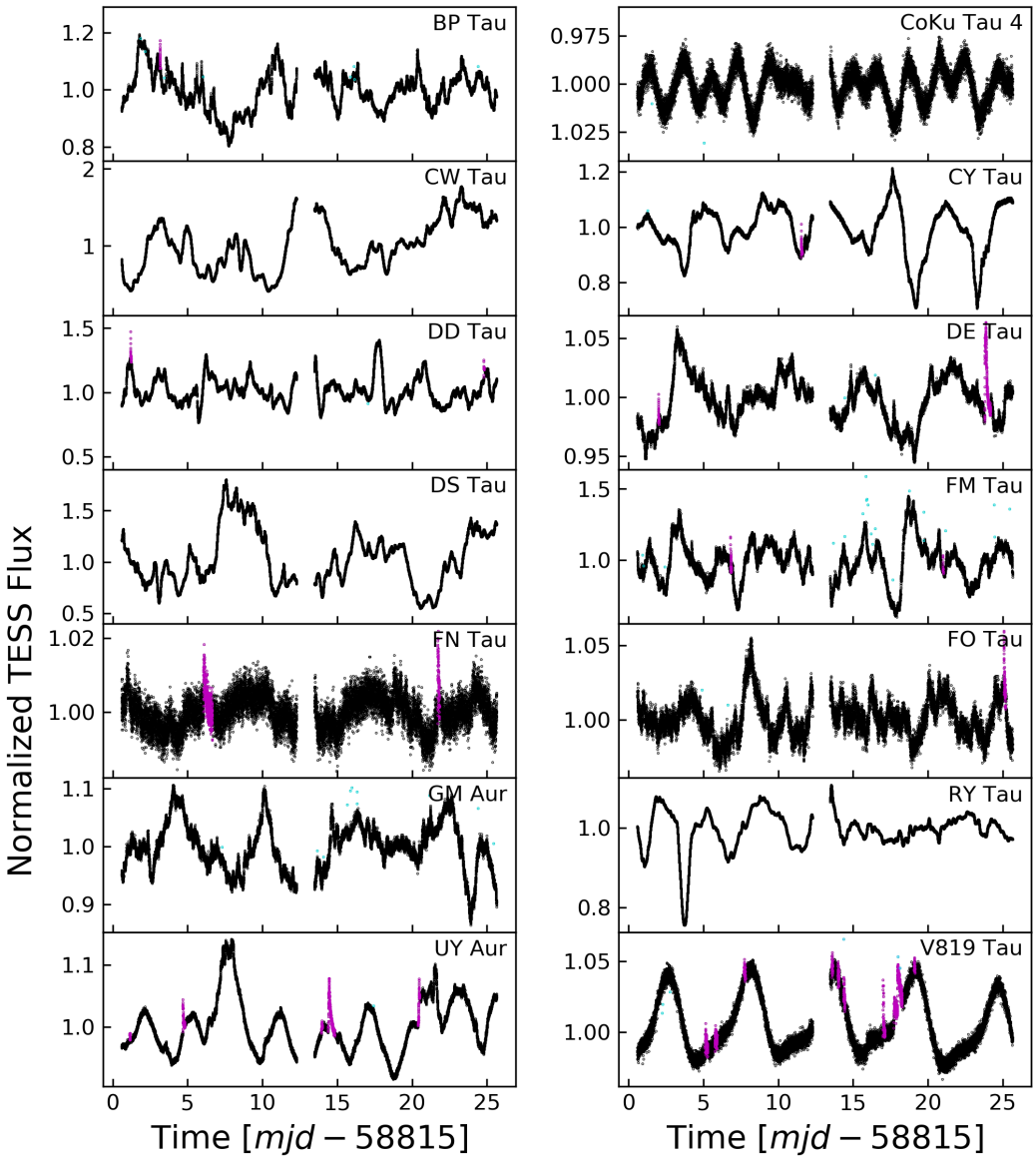

Fig. 4.1: Short-cadence (2 minute) *TESS* light curves for the 14 objects in the sample. The photometry shown here was produced using the standard SPOC pipeline. The timestamps of the data are presented in the Barycentric Dynamical Time (TDB) scale and account for travel time to the barycenter of the solar system. Flares identified by eye have been flagged in magenta, and single-point outliers have been flagged in cyan.

2" slit using the G230L grating with the NUV-MAMA detector and the G430L and G750L gratings with the CCD detector. Each set of the three spectral orders were taken sequentially within a single orbit, making the observations contemporaneous to within roughly 50 minutes. Moderate fringing occurs at the red end of the NIR spectrum. To correct this, I follow the standard procedure described in Goudfrooij & Christensen (1998) using a contemporaneous fringe flat taken alongside the observations during terrestrial occultations. The NUV data were taken in the time-tag mode of the NUV-MAMA detector, which records photon arrival times, making it possible to break a single long exposure into several shorter sub-exposures. The initial delay and exposure times for these sub-exposures were chosen such they are exactly simultaneous with overlapping *TESS* exposures. See §4.2.4 for details on matching time frames between *HST*, *TESS*, and LDT.

I refer to these observations as Epochs 9 - 14 to remain consistent with the eight previous observations presented in Ingleby et al. (2015) and Robinson & Espaillat (2019). Tab. 4.2 summarizes the six new *HST* STIS observations of GM Aur. Fig. 4.2 shows the six new epochs of *HST* STIS spectra overlaid on the range of the eight previous *HST* STIS observations. These observations were obtained during the *HST* Director's Discretionary time GO program 16010 (PI: C. Robinson).

Non-accreting WTTS are preferred as spectral templates due to significant chromospheric emission in young stars in the UV (Ingleby et al., 2011). A NUV - optical *HST* STIS spectrum of the WTTS RECX 1 was used as a spectral template in my analysis of GM Aur. This spectrum was taken with the matching 52" x 2" slit and the G230L and G430L gratings using the CCD detector during the *HST* GO program 11616 (PI: G. Herczeg).

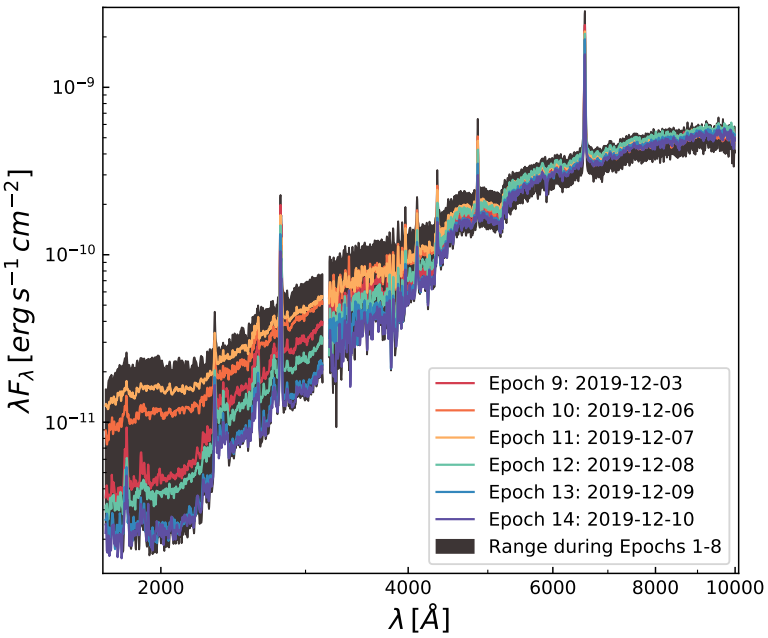

Fig. 4.2: Six epochs (Epochs 9 - 14) of new *HST* STIS spectra with contemporaneous NUV - NIR coverage of GM Aur observed during December 2019. The dark solid region represents the range between the maximum and minimum values observed during the previous *HST* STIS observations (Epochs 1 - 8) of GM Aur presented in Ingleby et al. (2015) and Robinson & Espaillat (2019). The spectra presented in this figure have been convolved with a Gaussian kernel to improve readability.

4.2.3 LDT

Multiwavelength images of all 14 targets were taken using the Large Monolithic Imager (LMI) on the 4.3m Lowell Discovery Telescope (LDT) using U, B, V, R, and I filters. These images were obtained during six nights spread over Dec. 2019 (specifically 2019-12-01, 2019-12-06, 2019-12-09, 2019-12-12, 2019-12-17, and 2019-12-20 in UT). I also obtained longer 1-2 hour-long U-band light curves of GM Aur during each of the nights. Standard flat fielding and bias subtraction were applied to the images before extraction of photometry. The median value from a set of three consecutive images was chosen to mitigate outliers and cosmic rays. Differential photometric

Table 4.2. HST Observation Summary

Target	Epoch	Proposal ID	Date (UT)	Gratings
GM Aur	9	16010	2019 Dec 03	G230L, G430L, G750L
GM Aur	10	16010	2019 Dec 06	G230L, G430L, G750L
GM Aur	11	16010	2019 Dec 07	G230L, G430L, G750L
GM Aur	12	16010	2019 Dec 08	G230L, G430L, G750L
GM Aur	13	16010	2019 Dec 09	G230L, G430L, G750L
GM Aur	14	16010	2019 Dec 10	G230L, G430L, G750L
RECX 1	–	11616	2010 Jan 22	G230L, G430L

Note. — Summary of the *HST* STIS observations of the CTTS GM Aur and the WTTS RECX 1. The reported start and end times encompass all of of the exposures completed during the visit. Each visit was completed within a single orbit. The epoch naming scheme is adopted from Ingleby et al. (2015) and Robinson & Espaillat (2019), which discuss epochs 1-3 and epochs 4-8 in more detail, respectively.

observations were tethered to observations of the objects during photometric nights using the photometric standard field centered on GD 64 (Landolt, 2013). Tables containing the U, B, V, R, and I tethered magnitudes and their uncertainties are shown in Tab. 4.3, 4.4, 4.5, 4.6, and 4.7, respectively. An observation log containing the start and end of the exposures for each set of observations for each night and object is included in Tab. 4.8.

4.2.4 Time

Because this is a multi-observatory study with importance placed on simultaneity, the timestamps for each observation must be placed into the same time scale. I choose to adopt the Barycentric Dynamical Time (TDB) scale and account for pho-

Table 4.3. U-Band LDT photometry

Object	2019 Dec 01	2019 Dec 06	2019 Dec 09	2019 Dec 12	2019 Dec 17	2019 Dec 20
BP Tau	12.35 ± 0.26	12.8 ± 0.4	12.01 ± 0.19	12.44 ± 0.28	12.43 ± 0.27	12.28 ± 0.24
CW Tau	14.4 ± 0.7	14.5 ± 0.7	13.8 ± 0.6	14.2 ± 0.7	14.1 ± 0.7	13.2 ± 0.6
CY Tau	14.4 ± 0.3	–	–	–	–	–
CoKu Tau 4	18.0 ± 0.3	17.79 ± 0.24	–	–	–	18.1 ± 0.3
DD Tau	15.9 ± 0.7	14.6 ± 0.7	15.5 ± 0.7	15.8 ± 0.7	15.6 ± 0.7	15.5 ± 0.7
DE Tau	13.46 ± 0.26	14.0 ± 0.4	13.8 ± 0.3	13.8 ± 0.3	13.7 ± 0.3	13.8 ± 0.3
DS Tau	14.3 ± 0.6	12.6 ± 0.5	14.0 ± 0.6	13.9 ± 0.6	14.7 ± 0.8	14.1 ± 0.6
FM Tau	14.4 ± 0.7	14.1 ± 0.7	14.9 ± 0.8	14.3 ± 0.7	14.5 ± 0.8	15.1 ± 0.8
FN Tau	16.2 ± 0.5	16.0 ± 0.5	–	14.9 ± 0.4	16.4 ± 0.6	16.2 ± 0.5
FO Tau	16.7 ± 0.3	16.7 ± 0.3	16.92 ± 0.12	16.38 ± 0.25	16.8 ± 0.3	16.9 ± 0.4
RY Tau	11.4 ± 0.8	–	11.6 ± 0.9	11.3 ± 1.2	11.4 ± 0.8	11.3 ± 0.8
UY Aur	15.3 ± 2.0	15.2 ± 1.6	15.6 ± 1.2	14.9 ± 1.1	15.4 ± 0.8	14.7 ± 1.1
V819 Tau	16.0 ± 0.5	15.56 ± 0.29	15.8 ± 0.3	15.8 ± 0.3	15.9 ± 0.4	15.56 ± 0.28

Note. — Tab. 4.3, 4.4, 4.5, 4.6, and 4.7 contain the U, B, V, R, and I photometry, respectively, for each night of observerations for each of the objects taken by the LDT. The U band data for GM Aur is not included here due to the amount of data collected for that object (see Fig. 4.9 for mass accretion rates for GM Aur). The uncertainties reported here include the systematic uncertainty from tethering multiple nights of differential photometry together.

Table 4.4. B-Band LDT photometry

Object	2019 Dec 01	2019 Dec 06	2019 Dec 09	2019 Dec 12	2019 Dec 17	2019 Dec 20
BP Tau	12.67 ± 0.25	13.1 ± 0.4	12.44 ± 0.21	13.0 ± 0.3	12.80 ± 0.28	12.63 ± 0.25
CW Tau	14.1 ± 0.7	14.1 ± 0.7	13.7 ± 0.7	14.3 ± 0.8	14.1 ± 0.7	13.1 ± 0.6
CY Tau	14.7 ± 0.3	14.7 ± 0.3	–	15.1 ± 0.4	–	14.8 ± 0.3
CoKu Tau 4	16.3 ± 0.7	16.4 ± 0.7	16.3 ± 0.4	16.4 ± 0.7	16.4 ± 0.7	16.4 ± 0.7
DD Tau	16.1 ± 0.8	15.0 ± 0.8	15.8 ± 0.8	15.9 ± 0.8	15.8 ± 0.8	15.8 ± 0.8
DE Tau	13.98 ± 0.25	14.2 ± 0.3	14.09 ± 0.28	14.08 ± 0.27	14.08 ± 0.27	14.16 ± 0.29
DS Tau	14.4 ± 0.9	12.8 ± 0.7	14.0 ± 0.8	14.0 ± 0.8	14.6 ± 0.9	14.2 ± 0.8
FM Tau	14.8 ± 0.7	14.8 ± 0.7	15.2 ± 0.8	14.6 ± 0.7	14.8 ± 0.7	15.7 ± 0.9
FN Tau	15.7 ± 0.5	15.6 ± 0.5	15.7 ± 0.5	15.7 ± 0.5	15.7 ± 0.5	15.7 ± 0.5
FO Tau	16.7 ± 0.4	16.7 ± 0.4	16.8 ± 0.4	16.6 ± 0.4	16.7 ± 0.4	16.8 ± 0.4
GM Aur	13.30 ± 0.26	13.15 ± 0.23	13.6 ± 0.3	13.24 ± 0.25	13.39 ± 0.28	13.4 ± 0.3
RY Tau	11.0 ± 0.4	11.0 ± 0.4	11.0 ± 0.4	10.7 ± 0.4	10.8 ± 0.4	10.7 ± 0.4
UY Aur	14.5 ± 1.7	14.5 ± 1.2	14.5 ± 1.2	14.4 ± 1.2	14.4 ± 1.2	14.2 ± 1.2
V819 Tau	14.7 ± 0.3	14.5 ± 0.3	14.7 ± 0.3	14.8 ± 0.4	14.7 ± 0.3	14.5 ± 0.3

Note. — See Tab. 4.3 for details.

Table 4.5. V-Band LDT photometry

Object	2019 Dec 01	2019 Dec 06	2019 Dec 09	2019 Dec 12	2019 Dec 17	2019 Dec 20
BP Tau	12.03 ± 0.27	12.2 ± 0.3	11.85 ± 0.23	12.2 ± 0.3	12.04 ± 0.27	11.93 ± 0.25
CW Tau	12.7 ± 0.8	12.6 ± 0.8	12.3 ± 0.8	12.8 ± 0.8	12.6 ± 0.8	11.9 ± 0.8
CY Tau	13.5 ± 0.5	13.5 ± 0.4	13.6 ± 0.4	13.8 ± 0.5	13.8 ± 0.5	13.7 ± 0.5
CoKu Tau 4	14.6 ± 0.5	14.6 ± 0.5	14.6 ± 0.5	14.7 ± 0.5	14.6 ± 0.5	14.6 ± 0.5
DD Tau	15.0 ± 0.8	14.1 ± 0.7	14.8 ± 0.7	14.8 ± 0.7	14.7 ± 0.7	14.8 ± 0.7
DE Tau	12.86 ± 0.27	12.95 ± 0.29	12.90 ± 0.28	12.88 ± 0.27	12.89 ± 0.28	12.96 ± 0.29
DS Tau	13.1 ± 0.4	11.89 ± 0.14	12.81 ± 0.29	12.8 ± 0.3	13.2 ± 0.4	12.9 ± 0.3
FM Tau	14.1 ± 0.7	14.1 ± 0.7	14.6 ± 0.8	13.9 ± 0.7	14.1 ± 0.7	14.6 ± 0.8
FN Tau	14.2 ± 0.4	14.2 ± 0.4	14.2 ± 0.4	14.2 ± 0.4	14.2 ± 0.4	14.2 ± 0.4
FO Tau	15.2 ± 0.3	15.2 ± 0.4	15.2 ± 0.4	15.1 ± 0.3	15.2 ± 0.4	15.2 ± 0.4
GM Aur	12.17 ± 0.25	12.18 ± 0.25	12.36 ± 0.29	12.22 ± 0.26	12.28 ± 0.27	12.25 ± 0.27
RY Tau	10.0 ± 0.3	9.9 ± 0.3	9.9 ± 0.3	9.69 ± 0.29	9.7 ± 0.3	9.67 ± 0.29
UY Aur	13.3 ± 1.8	13.3 ± 1.2	13.0 ± 1.2	13.0 ± 1.7	13.2 ± 1.2	13.0 ± 1.2
V819 Tau	13.1 ± 0.4	13.1 ± 0.4	13.1 ± 0.4	13.2 ± 0.4	13.1 ± 0.4	13.0 ± 0.4

Note. — See Tab. 4.3 for details.

Table 4.6. R-Band LDT photometry

Object	2019 Dec 01	2019 Dec 06	2019 Dec 09	2019 Dec 12	2019 Dec 17	2019 Dec 20
BP Tau	11.22 ± 0.25	11.40 ± 0.29	11.21 ± 0.25	11.39 ± 0.29	11.28 ± 0.27	11.22 ± 0.25
CW Tau	11.7 ± 0.9	11.7 ± 0.9	11.3 ± 0.8	11.7 ± 0.9	11.5 ± 0.8	11.0 ± 0.8
CY Tau	12.5 ± 0.4	12.4 ± 0.4	12.5 ± 0.4	12.6 ± 0.4	12.7 ± 0.4	12.8 ± 0.4
CoKu Tau 4	13.3 ± 0.4	13.3 ± 0.4	13.3 ± 0.3	13.33 ± 0.29	13.3 ± 0.4	13.3 ± 0.4
DD Tau	13.5 ± 0.5	13.0 ± 0.5	13.5 ± 0.5	13.4 ± 0.5	13.4 ± 0.5	13.4 ± 0.5
DE Tau	11.9 ± 0.3	11.9 ± 0.4	11.9 ± 0.3	11.87 ± 0.28	11.9 ± 0.3	11.9 ± 0.4
DS Tau	12.3 ± 0.4	11.27 ± 0.14	12.01 ± 0.28	11.99 ± 0.28	12.3 ± 0.4	12.00 ± 0.28
FM Tau	13.1 ± 0.6	13.1 ± 0.6	13.6 ± 0.7	13.2 ± 0.6	13.2 ± 0.6	13.8 ± 0.7
FN Tau	12.9 ± 0.3	12.9 ± 0.3	12.9 ± 0.3	12.9 ± 0.3	12.9 ± 0.3	12.9 ± 0.3
FO Tau	13.61 ± 0.26	13.62 ± 0.27	13.65 ± 0.27	13.60 ± 0.26	13.64 ± 0.27	13.65 ± 0.27
GM Aur	11.30 ± 0.25	11.34 ± 0.26	11.45 ± 0.28	11.4 ± 0.4	11.40 ± 0.27	11.36 ± 0.26
RY Tau	9.3 ± 0.5	9.2 ± 0.5	9.3 ± 0.5	9.0 ± 0.4	9.1 ± 0.4	9.0 ± 0.4
UY Aur	12.0 ± 1.0	12.0 ± 0.7	12.0 ± 0.7	12.0 ± 0.7	11.8 ± 0.7	11.8 ± 0.7
V819 Tau	12.1 ± 0.3	12.1 ± 0.3	12.1 ± 0.3	12.2 ± 0.3	12.1 ± 0.3	12.0 ± 0.3

Note. — See Tab. 4.3 for details.

Table 4.7. I-Band LDT photometry

Object	2019 Dec 01	2019 Dec 06	2019 Dec 09	2019 Dec 12	2019 Dec 17	2019 Dec 20
BP Tau	10.26 ± 0.24	10.52 ± 0.28	10.44 ± 0.26	10.54 ± 0.28	10.46 ± 0.26	10.46 ± 0.26
CW Tau	10.8 ± 0.6	10.7 ± 0.9	10.2 ± 0.6	10.7 ± 0.6	10.5 ± 0.6	10.1 ± 0.6
CY Tau	11.3 ± 0.3	11.2 ± 0.4	11.2 ± 0.3	11.5 ± 0.4	11.3 ± 0.3	11.6 ± 0.4
CoKu Tau 4	11.9 ± 0.4	11.9 ± 0.4	11.9 ± 0.4	11.9 ± 0.4	11.9 ± 0.4	11.9 ± 0.4
DD Tau	11.9 ± 0.7	11.7 ± 0.6	12.0 ± 0.7	11.8 ± 0.6	11.8 ± 0.6	11.8 ± 0.6
DE Tau	10.52 ± 0.28	10.55 ± 0.28	10.54 ± 0.28	10.55 ± 0.28	10.53 ± 0.28	10.54 ± 0.28
DS Tau	11.3 ± 0.3	10.59 ± 0.17	11.17 ± 0.28	11.12 ± 0.27	11.4 ± 0.3	11.12 ± 0.27
FM Tau	12.0 ± 0.4	12.1 ± 0.5	12.2 ± 0.5	12.2 ± 0.5	12.1 ± 0.5	12.6 ± 0.6
FN Tau	11.2 ± 0.3	11.19 ± 0.29	11.2 ± 0.3	11.2 ± 0.3	11.2 ± 0.3	11.2 ± 0.3
FO Tau	11.79 ± 0.27	11.79 ± 0.27	11.81 ± 0.28	11.79 ± 0.27	11.80 ± 0.28	11.77 ± 0.27
GM Aur	10.56 ± 0.25	10.62 ± 0.26	10.67 ± 0.27	10.61 ± 0.26	10.66 ± 0.27	10.62 ± 0.26
RY Tau	8.5 ± 0.4	8.4 ± 0.4	8.5 ± 0.4	8.3 ± 0.3	8.3 ± 0.3	8.3 ± 0.3
UY Aur	10.8 ± 0.6	10.8 ± 0.4	10.9 ± 0.4	10.8 ± 0.4	10.7 ± 0.4	10.7 ± 0.4
V819 Tau	11.0 ± 0.4	11.0 ± 0.4	11.0 ± 0.4	11.0 ± 0.4	11.0 ± 0.4	11.0 ± 0.4

Note. — See Tab. 4.3 for details.

ton travel time to the barycenter of the solar system. For *TESS*, timestamps were transformed into this system using the `Lightkurve` package (Lightkurve Collaboration et al., 2018). For *HST*, this was accomplished by following the steps laid out in Dashevsky et al. (2000) using the orbital information of *HST* during epochs 9-14. Finally, the LDT data were transformed to this time scale using the `astropy.time` package (Astropy Collaboration et al., 2018).

4.3 Analysis

4.3.1 Stellar Parameters

Stellar luminosities and spectral types for each object except GM Aur were adopted from Herczeg & Hillenbrand (2014). Those authors considered the effects of extinction and accretion when determining stellar parameters, both of which are critical for further accurate characterization of accretion. I scaled the stellar luminosities from that work using the distances derived from parallaxes from *Gaia* DR2 (Gaia Collaboration et al., 2016, 2018) and obtained new stellar radii based on this correction. Spectral types were converted into effective stellar temperatures by lin-

Table 4.8. LDT Observation Log

Object	2019 Dec 01		2019 Dec 06		2019 Dec 09		201 Dec 12		2019 Dec 17		2019 Dec 20	
	First	Last	First	Last	First	Last	First	Last	First	Last	First	Last
BP Tau	4.45804	4.46615	9.12398	9.13042	12.12787	12.13533	15.11495	15.12185	20.10784	20.11471	23.11365	23.12041
CW Tau	4.4411	4.44784	9.14606	9.15378	12.1446	12.15185	15.13227	15.1394	20.12482	20.13143	23.12991	23.13697
CY Tau	4.41579	4.4225	9.16374	9.17345	12.16747	12.17605	15.15165	15.1631	20.14797	20.15701	23.16531	23.17352
CoKu Tau 4	4.3454	4.35566	9.20511	9.21578	12.21385	12.22382	15.20066	15.21874	20.197	20.20937	23.2026	23.21461
DD Tau	4.38206	4.38901	9.1948	9.20337	12.20413	12.21208	15.18882	15.19829	20.18563	20.19463	23.19149	23.20037
DE Tau	4.39057	4.39832	9.18466	9.19291	12.19424	12.20226	15.17785	15.18665	20.17515	20.18371	23.18165	23.18973
DS Tau	4.44944	4.45658	9.13814	9.14462	12.13672	12.14332	15.12335	15.13093	20.11649	20.1233	23.12192	23.12874
FM Tau	4.40629	4.4144	9.17505	9.18287	12.1778	12.18659	15.16524	15.17504	20.15844	20.1666	23.1546	23.16341
FN Tau	4.37329	4.38044	9.21824	9.22872	12.23172	12.24209	15.22191	15.23735	20.21972	20.22954	23.22393	23.23597
FO Tau	4.35681	4.36403	9.23092	9.24111	12.24418	12.25471	15.24003	15.25049	20.2319	20.24279	23.23898	23.25073
GM Aur	4.32681	4.33263	9.07463	9.09695	12.0886	12.09358	15.07471	15.08359	20.06984	20.07538	23.06768	23.07606
RY Tau	4.48481	4.49059	9.09841	9.10349	12.10019	12.10531	15.08514	15.09087	20.05713	20.06266	23.09132	23.09684
UY Aur	4.47247	4.49911	9.11259	9.12235	12.11276	12.12045	15.1026	15.11301	20.09158	20.09984	23.09802	23.10602
V819 Tau	4.42408	4.43357	9.15537	9.16214	12.15951	12.16588	15.14119	15.15001	20.13959	20.14661	23.14546	23.15261

Note. — Times of the start of the first and last exposures in each set of LDT U, B, V, R, and I exposures for each object during each night. The times are shown in the TDB time frame in days since MJD 58815 and include a correction for the light travel time to the barycenter of the solar system. This table does not include the LDT U-band monitoring of GM Aur.

early interpolating between the grid of WTTS presented in Tab. 4 of Herczeg & Hillenbrand (2014). Following that work, I include K8 as an intermediate spectral type between K7 and M0. Stellar masses were obtained by interpolating between the grid of models which comprise the Mesa Isochrones and Stellar Tracks (MIST) model set (Choi et al., 2016; Dotter, 2016). For GM Aur, I adopt the stellar parameters from Manara et al. (2014) to remain consistent with the analysis of the *HST* STIS spectra presented in Robinson & Espaillat (2019) during Epochs 1-8. I note that this choice of stellar parameters has limited impact on the results presented in this chapter. As discussed by Garufi et al. (2019), the parallax from *Gaia* DR 2 for RY Tau is known to be inconsistent with previous measurements and is assumed to be erroneous. I follow the those authors and adopt the value of 133 pc from Hipparcos (esa, 1997). The adopted stellar parameters are listed in Tab. 4.1.

As a comparison to the adopted values, estimates of extinction were measured from the B, V, R, and I LDT photometry using colors from Kenyon & Hartmann (1995). In most cases, I find values of A_v consistent with the values from Herczeg & Hillenbrand (2014), who modeled flux-calibrated spectra to measure extinction, spectral type, and veiling. In regards to discrepancies, I note that the estimates using the Kenyon & Hartmann (1995) colors do not include the effects of accretion, which motivates the choice to adopt the values from Herczeg & Hillenbrand (2014).

4.3.2 Measuring Q, M, and Rotation Periods

Q and M are statistical metrics that measure periodicity and symmetry around the mean of a light curve, respectively. These metrics were measured from the *TESS* light curves for each of the objects. These metrics were developed by Cody et al. (2014) and have been used to characterize several other star-forming regions (e.g., NGC 2264 and Ophiuchus, Cody et al., 2014; Cody & Hillenbrand, 2018). These metrics can be used to separate objects into empirical variability classes. These clas-

sifications include burster (B), purely periodic (P), quasi-periodic stochastic (QPS), stochastic (S), quasi-periodic dipper (QPD) and aperiodic dipper (APD). In addition to these classifications, I also note the possibility of several other variability classes, including multi-periodic (MP), which would not be identified by these metrics. I adopt the regions of Q and M parameter space as defined by Cody & Hillenbrand (2018) to determine variability classifications for the objects. More specifics on the algorithms used to measure these metrics can be found in that work and in Chapter 5.

One of the steps for measuring Q requires determining the stellar rotation period. Following Cody et al. (2014), I measured the period by interpolating the *TESS* data onto a uniform grid and autocorrelating the data, and the first significant peak of the autocorrelation function is identified. Next, I applied a Lomb-Scargle periodogram (Lomb, 1976; Scargle, 1982). The resulting periodogram was then weighted by a Gaussian centered at the peak of the autocorrelation function with a width of 30% of the peak period. This was found to more accurately recover rotational periods of models of accreting young stars (see Chapter 5) when compared to the box-car weighting of Cody et al. (2014).

4.3.3 Continuous Wavelet Transforms

The relatively short duration of the possible detection of thermal instabilities by Siwak et al. (2018) suggests that the phenomenon may be transient. While the commonly used Fourier transform is very effective at identifying stationary periodic signals, it misses short-lived, quasi-periodic behavior. To identify this variability, I apply a continuous wavelet transform (CWT) to the *TESS* light curves. The CWT is a signal processing technique that localizes quasi-periodic signatures through the convolution of the light curve with wavelets over a range of characteristic time scales. The result from applying this technique is a 2D spectrum with time increasing on

the x-axis, increasing characteristic wavelet timescale on the y-axis, and amplitude on the z-axis. I order to employ this method, I linearly interpolated over missing and masked data in the *TESS* light curve.

Siwak et al. (2018) used a CWT to identify quasi-periodic variability patterns on 11- to 30-minute timescales. I follow that work, Rucinski et al. (2008), and Siwak et al. (2011b, 2014, 2016), and adopt a Morlet-6 wavelet for my analysis. The Morelet-6 wavelet is described by a complex exponential multiplied by a Gaussian whose width is determined by the period of the complex exponential to have 6 six distinct peaks. In this chapter, references to wavelet scale refer to the period of the complex exponential term, not the width of the Gaussian envelope (i.e., the CWT will identify regions where the period of the quasi-periodicity matches the wavelet scale).

Here, I identified regions of significant short-timescale quasi-periodic behavior by dividing the 1D spectrum at each wavelet scale by its standard deviation and then searching for regions above a threshold (here I choose a value of 7). I found this approach to be very effective for identifying signals on wavelet scales of 8-120 minutes. An example of the CWT is shown in Fig. 4.3 for DS Tau, which shows strong quasi-period signals on these timescales. Contours representing the significance of the signals are overlaid. While Fig. 4.3 shows the CWT from the smallest wavelet scale (Nyquist limited) to the largest possible scale (1/2 the observation length), the discussion focuses on quasi-periodicity on timescales from 8 minutes to 120 minutes which can be uniquely probed by the short-cadence *TESS* observations. Notable lengths of time that demonstrate strong quasi-periodic signals for each object over this range of wavelet scales are discussed in §4.4.3.

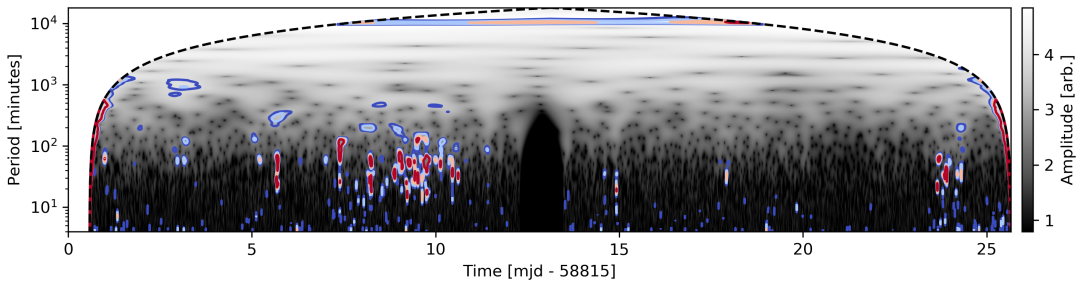

Fig. 4.3: 2D wavelet spectrum of the *TESS* lightcurve of DS Tau. Short-timescale regions are highlighted by "significance" contours found by dividing the power in the row for each wavelet scale by its standard deviation. The dark blue, light blue, pink, and red contours mark regions with greater than 5, 6, 7, and 8 significance, respectively. The cone of influence is shown by the dashed black lines. Strong regions of significance are found near 8 d, which is associated with a large accretion event. The large dark region between roughly 12-13 d is the data gap in the *TESS* light curve.

4.3.4 Measuring $\dot{M}$ from U-band Excess

Excess emission in the Johnson U band can be used to measure $\dot{M}$ through empirical relationships (e.g., Gullbring et al., 1998). I approximate the photospheric emission with the BT-Settl model grid at solar metallicity with no α enhancement scaled to the correct distance and stellar radius. The excess is then measured by subtracting the photospheric spectrum convolved with the U-band transmission curve from the observed photometry. Here I apply the relationship from Robinson & Espaillat (2019) to convert from U-band excess to accretion luminosity/mass accretion rate. Uncertainties for $\dot{M}$ were estimated using a Monte Carlo approach in which $L_\star$, T_{eff}, A_v, parallax, the observed flux, and the slope/y-intercept of the empirical excess-$\dot{M}$ relationship were resampled using their respective uncertainties. With this approach, I find typical uncertainties for $\dot{M}$ are on the order of 30%. Mass accretion rates for each night are listed in Tab. 4.9.

Table 4.9. By-night Mass Accretion Rates from U-band Excess

Object	2019 Dec 01	2019 Dec 06	2019 Dec 09	2019 Dec 12	2019 Dec 17	2019 Dec 20
BP Tau	$2.6^{+1.2}_{-0.8}$	$1.8^{+1.1}_{-0.7}$	$3.5^{+1.6}_{-0.9}$	$2.5^{+1.3}_{-0.8}$	$2.5^{+1.1}_{-0.8}$	$2.7^{+1.3}_{-0.9}$
CW Tau	$1.6^{+1.4}_{-0.8}$	$1.5^{+1.5}_{-0.9}$	$2.4^{+2.5}_{-1.2}$	$1.6^{+1.6}_{-0.7}$	$1.9^{+1.6}_{-1.0}$	$4.4^{+3}_{-1.9}$
CY Tau	$0.54^{+0.4}_{-0.22}$	–	–	–	–	–
CoKu Tau 4	$0.18^{+0.16}_{-0.11}$	$0.23^{+0.19}_{-0.13}$	–	–	–	$0.14^{+0.15}_{-0.09}$
DD Tau	$0.6^{+0.9}_{-0.4}$	$2.2^{+2.0}_{-1.1}$	$1.0^{+1.2}_{-0.6}$	$0.8^{+0.8}_{-0.4}$	$0.8^{+1.1}_{-0.5}$	$0.9^{+0.7}_{-0.5}$
DE Tau	$1.8^{+1.0}_{-0.6}$	$1.0^{+0.7}_{-0.5}$	$1.4^{+0.8}_{-0.5}$	$1.4^{+0.9}_{-0.6}$	$1.4^{+0.8}_{-0.5}$	$1.3^{+0.8}_{-0.5}$
DS Tau	$0.37^{+0.4}_{-0.22}$	$1.7^{+0.9}_{-0.7}$	$0.52^{+0.4}_{-0.26}$	$0.54^{+0.5}_{-0.26}$	$0.25^{+0.3}_{-0.15}$	$0.45^{+0.3}_{-0.22}$
FM Tau	$1.0^{+1.1}_{-0.5}$	$1.1^{+1.4}_{-0.6}$	$0.6^{+0.8}_{-0.3}$	$1.0^{+1.1}_{-0.5}$	$0.9^{+0.8}_{-0.5}$	$0.52^{+0.5}_{-0.29}$
FN Tau	$0.7^{+0.7}_{-0.4}$	$0.7^{+0.7}_{-0.4}$	–	$2.4^{+1.4}_{-1.1}$	$0.5^{+0.5}_{-0.3}$	$0.7^{+0.6}_{-0.4}$
FO Tau	$2.5^{+1.7}_{-0.9}$	$2.8^{+1.7}_{-1.1}$	$2.2^{+1.1}_{-0.7}$	$3.8^{+2.0}_{-1.3}$	$2.4^{+1.3}_{-0.9}$	$2.2^{+1.4}_{-1.1}$
GM Aur	$0.54^{+0.022}_{-0.04}$	$0.96^{+0.14}_{-0.12}$	$0.22^{+0.019}_{-0.03}$	$0.968^{+0.03}_{-0.029}$	$0.70^{+0.022}_{-0.06}$	$0.387^{+0.012}_{-0.018}$
", ", ", ", ", "] RY Tau	30^{+73}_{-30}	–	30^{+70}_{-20}	44^{+100}_{-32}	28^{+60}_{-21}	30^{+60}_{-20}
UY Aur	$1.7^{+7}_{-1.4}$	$1.4^{+5}_{-1.1}$	$0.9^{+1.9}_{-0.6}$	$1.0^{+2.3}_{-0.8}$	$0.7^{+1.0}_{-0.6}$	$1.6^{+3}_{-1.1}$
V819 Tau	$0.14^{+0.17}_{-0.09}$	$0.23^{+0.14}_{-0.11}$	$0.17^{+0.17}_{-0.10}$	$0.16^{+0.18}_{-0.09}$	$0.13^{+0.14}_{-0.08}$	$0.23^{+0.16}_{-0.12}$

Note. — Mass accretion rates in units of $10^{-8} M_{\odot}\, yr^{-1}$ found using the relationship between U-band excess and accretion rate in Robinson & Espaillat (2019). With the exception of GM Aur, the listed uncertainties are the 16^{th} and 84^{th} percentile confidence intervals. The values listed for GM Aur are the median mass accretion rates from the by-night continuous U-band monitoring. The associated uncertainties for GM Aur are the 16^{th} and 84^{th} percentiles of those observations.

4.3.5 Measuring $\dot{M}$ from *HST*

To probe the accretion columns and the circumstellar environment of GM Aur, the mass accretion rate and surface coverage of accretion shocks with different densities were measured with the *HST* STIS spectra using the accretion shock models and fitting methods of Robinson & Espaillat (2019). These models are an updated version of the models of Calvet & Gullbring (1998). The model and fitting methods are briefly described here.

The structure and emission arising from the post-shock region is solved under a given kinetic energy flux, $F_i = \frac{1}{2}\rho u^3$ where ρ is density and u is velocity. These models work under assumption that the accretion flow is in freefall in the pre-shock region, making the kinetic energy flux directly proportional to the density of the column.

Half of the emission is radiated toward the star, where it heats the underlying photosphere, and the other half irradiates the pre-shock region. The outgoing, reprocessed emission from these two regions is then summed and scaled by a multiplicative filling factor, f_i, which is treated as a free parameter. This is repeated for each value of F_i. A non-accreting WTTS, multiplied by a free parameter scaling factor, s, is used as a template for the non-accreting regions of the stellar photosphere. The emission from each component is then summed to produce an estimate of the continuum emission. Finally, the spectrum is reddened using the extinction parameters of Whittet et al. (2004), which are typically used for UV observations.

In this approach, the photosphere is assumed to remain constant between epochs, i.e., the value of s is multiplied uniformly by the photospheric template for each epoch. Treating s as a single free parameter requires that f_i for all epochs and s be fit simultaneously. To identify models that fit the observations well in this high-dimensional parameter space, posteriors for f_i, s, and model uncertainty w were sampled using a Markov Chain Monte Carlo approach. In particular, I adopt the affine-invariant Goodman & Weare (2010) sampling algorithm via the Python-based ensemble sampler `emcee` (Foreman-Mackey et al., 2013). Each parameter is evaluated in log-space (limiting possible values to positive quantities) and I impose priors such that s, w, and f_i cannot be larger than 1 to remain physical. Additionally, I impose a Gaussian prior on s with a width of 0.1 centered on the value of s derived from the analysis of the Epochs 1-8 from Robinson & Espaillat (2019). The model uncertainty, w, is marginalized over as a nuisance parameter. It is important to note that the resulting reported posteriors do not include the systematic uncertainty arising from the stellar parameters and extinction. Robinson & Espaillat (2019) found an additional $\sim 10\%$ systematic uncertainty in the fitted parameters is appropriate

in most cases. For more discussion on the fitting technique and the model, see that work, Calvet & Gullbring (1998), and Chapter 3.

4.4 Results

4.4.1 $\dot{M}$ Across the Sample

To test if *TESS* is sensitive to variability caused by changes in accretion, I plot the normalized *TESS* flux against $\dot{M}$ as measured by the simultaneous U-band excess, normalized to the mean observed $\dot{M}$ in Fig. 4.4. I exclude objects with MP, P, QPD, and APD classifications from this analysis, since their variability is not thought to be driven by accretion. I find a positive correlation between the two quantities, with some scatter, which can be understood in part by the systematic uncertainties in the stellar parameters and observational uncertainties. I did not attempt to subtract a photospheric component or obtain a flux-calibratation measurement from the *TESS* light curve because of the broad-band nature of the filter pass-band, coupled with the known contamination from nearby sources. By not considering the absolute flux arising from accretion in the *TESS* bandpass, the slope between the *TESS* flux and $\dot{M}$ will vary as a function of intrinsic stellar brightness. I also expect some astrophysical scatter from starspots and changes in extinction. While this positive correlation suggests that the *TESS* flux is sensitive to accretion variability in young stars, I strongly caution against deriving a one-to-one relation between the *TESS* flux and normalized $\dot{M}$. This warning holds for individual objects as well. I found that the slope of relationships between the *TESS* flux and $\dot{M}$ can vary between observations on different nights (see §4.4.4). Encouragingly, I note that these measurements of $\dot{M}$ and the *TESS* flux when taken over 1-2 consecutive hours do generally show linear trends.

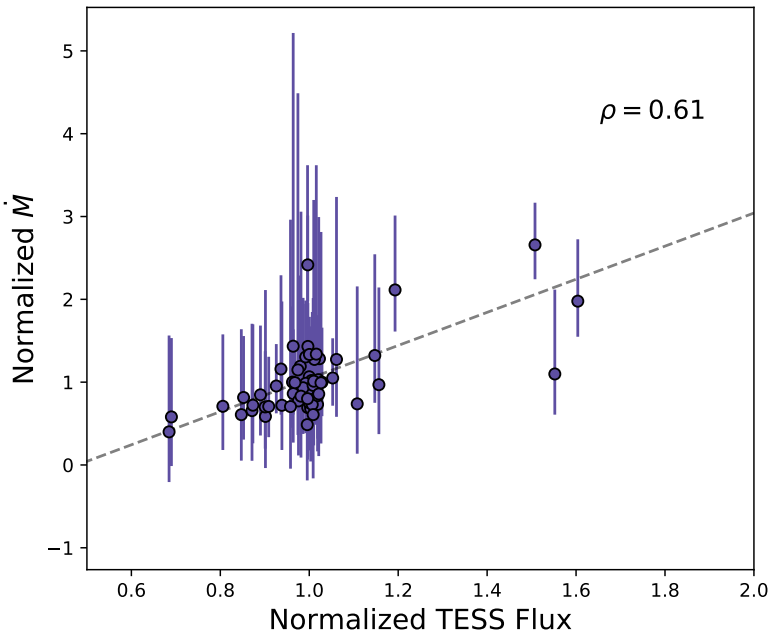

Fig. 4.4: Mass accretion rate against *TESS* flux, both normalized to the observed mean value. This figure includes the LDT measurements of $\dot{M}$ for all of the objects except GM Aur, which has been excluded because of its large number of observations compared to the other objects. I find a correlation between the two quantities with a Pearson correlation coefficient of 0.61. This suggests that *TESS* flux is sensitive to accretion variability. The dashed line is a linear regression to help display the trend.

4.4.2 Results from the CWT Analysis

Applying a CWT to the light curves reveals a rich variety of quasi-periodic oscillations on timescales from minutes to hours. I find that the majority of the events selected by the significance criteria are associated with local maxima in the *TESS* light curves. Fig. 4.5 shows the distribution of by-eye estimates of the lower and upper period bounds for significant events identified during the CWT analysis. From the middle panel, I identify possible clumps of quasi-periodic events with mean periods centered roughly around 20, 50, and 90 minutes. From the bottom panel of Fig. 4.5 I show that the majority of the identified timescales are relatively localized

in timescale-space, with most events having a period spread of fewer than 20 minutes. Light curves with the regions of significant quasi-periodicity from the CWT analysis for each object are shown in Fig. 4.6. I focus on wavelet scales between 8 and 120 minutes because these are timescales that can be uniquely probed by the short-cadence *TESS* photometry.

4.4.3 Remarks on Individual *TESS* Light Curves

Here, I discuss individual objects with regards to their observed variability classifications, quasi-periodicity, and stellar activity. Derived statistical metrics Q and M, periods, and empirical variability classifications can be found in Tab. 4.10. This section refers to events occurring in terms of days since MJD 58815 in the TDB time scale. GM Aur is discussed in more detail in §4.4.4.

BP Tau Using Q and M, BP Tau is classified as a QPS object. Periodic behavior in the light curve is not immediately obvious by-eye. Some features that resemble both dips and accretion bursts are present. A bright flare was observed near 3.5d. Typical changes in brightness are on the order of 10%. Several other smaller events that resemble flares are visible in the CWT. Most of the quasi-periodic behavior appears near peaks in the light curve, with typical scales ranging from 17 - 85 minutes.

Coku Tau 4: I distinctly see periodic behavior with two frequencies and thus classify CoKu Tau 4 as an MP object rather than the QPS that Q and M would suggest. The amplitudes of observed changes for this object are small, on the order of 1%. I do not see obvious evidence for flaring in this object. Only one region, which is short-lived ($\sim$ 0.7 hours long), is deemed significant in the CWT, with a wavelet scale of 30 minutes. I used a Lomb-Scargle Periodogram (Lomb, 1976; Scargle, 1982) to identify both periods of the signals present in the light curve.

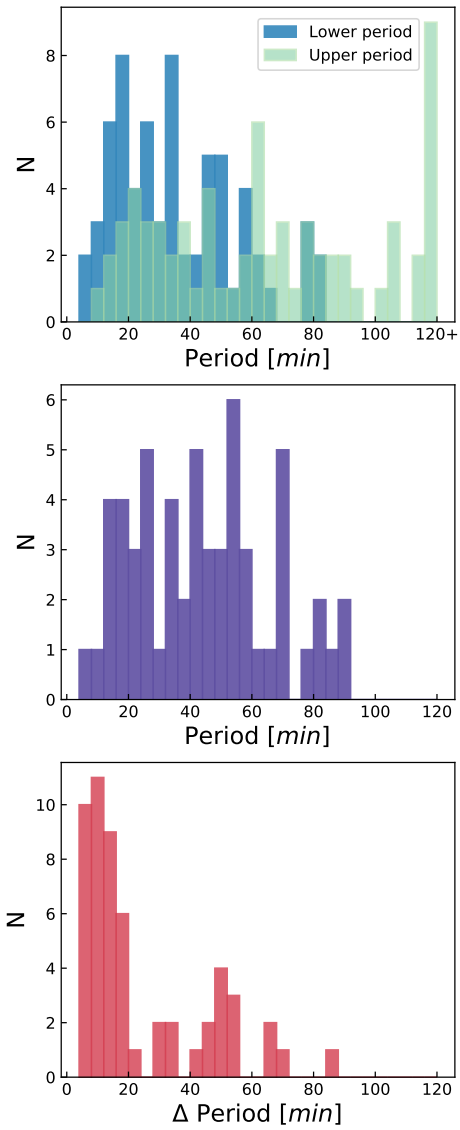

Fig. 4.5: *Top:* Histograms of estimates on upper and lower periods for significant quasi-periodic events identified during the CWT analysis for all of the objects. Events associated with flares have been pruned. *Middle:* Average of the upper and lower period, excluding those with upper periods longer than 120 minutes. *Bottom:* Difference between the upper and lower periods for these events, excluding those with upper periods greater than 120 minutes.

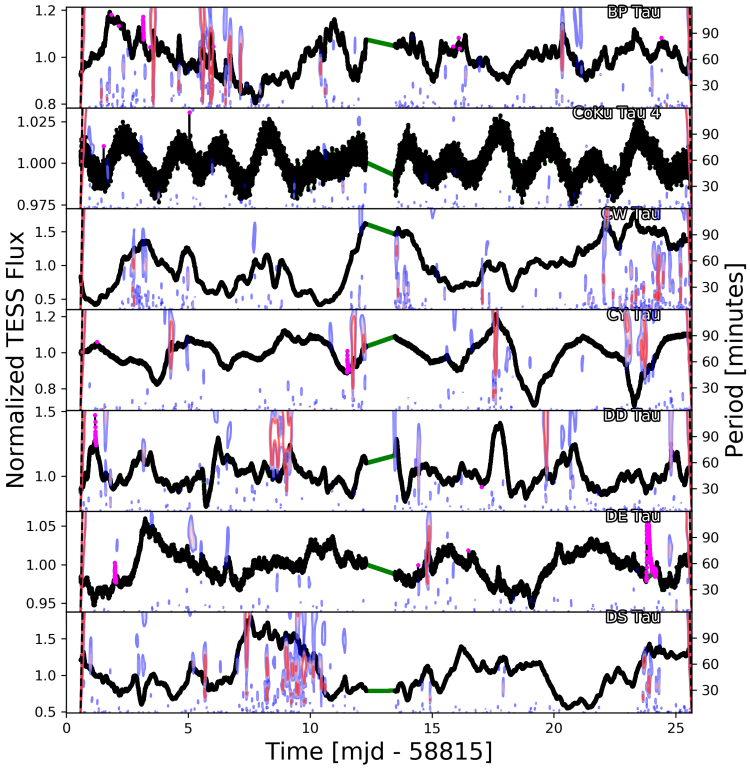

Fig. 4.6: Significance contours for wavelet scales with periods between 8 and 120 minutes overlaid on the *TESS* light curve for each object (see §4.3.3). Like Fig. 4.3, the dark blue, light blue, pink, and red contours mark regions of significance greater than 5, 6, 7, and 8, respectively. Most of the these regions coincide with local maxima in the light curve. Regions containing flares and single-observation outliers are flagged in magenta. These flares and other regions of missing data were linearly interpolated over with the new values shown in green.

Table 4.10. Statistical Metrics, Periods, and Empirical Classifications from *TESS* Light Curves

Object	Q	M	Period [d]	Empirical Class
BP Tau	0.83	-0.03	4.39	QPS
CoKu Tau 4	0.33	-0.14	1.91/3.02	MP (QPS)[a]
CW Tau	0.56	-0.10	9.40	QPS
CY Tau	0.38	0.50	3.99	QPD
DD Tau	0.85	-0.49	5.95	B
DE Tau	0.39	-0.06	5.79	QPS
DS Tau	0.36	-0.27	8.65	B
FM Tau	0.70	-0.02	5.37	QPS
FN Tau	< 0.6[b]	0.03	8.65	P/QPS
FO Tau	0.32	-0.29	4.18	B
GM Aur	0.46	0.02	5.79	QPS
RY Tau	0.82	0.61	3.33	QPD
UY Aur	0.74	-0.49	3.04	B
V817 Tau	0.03	-0.27	5.48	P (B)[a]

Note. — (a) I adopt the classification of MP for CoKu Tau 4 and P for V817 Tau via by-eye inspection over their assigned classification from Q and M. The classifications derived for these objects are included in parentheses. (b) The SPOC pipeline uncertainties in the *TESS* light curve are overestimated for FN Tau compared to the observed scatter, leaving us with an upper limit on Q. Note that periods are generally increasingly uncertain with increasing values of Q due to astrophysical noise.

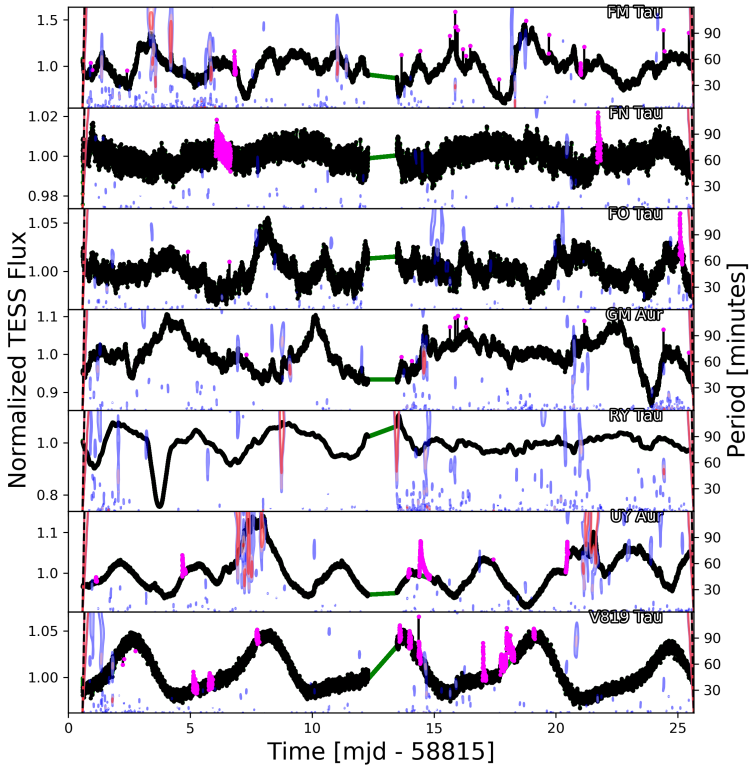

Fig. 4.6: *Continued.*

CW Tau: This object exhibits very large changes in flux (up to 50%) with limited obvious periodicity, hence its classification as a QPS. Most of the changes resemble accretion events, but some events may be dips. I do not see evidence of flaring, but they might be masked by the large-scale variability. Several patches of significant quasi-periodicity are found in the CWT. These are predominantly found near the peaks of the accretion curves with scales spanning nearly the entire range considered here (8 - 120 minutes). A particularly interesting region begins near 24.0d, where near-continuous 20-minute oscillations are present for 6 hours. This region is located during a bright part of the light curve and also exhibits overlapping quasi-periodicity on timescales of 30-60 minutes. 20-minute timescale quasi-periodicity is also observed earlier in the light curve (near 2.5d and 13.6d) at lower significance.

CY Tau: This object exhibits periodicity and shows evidence for both accretion bursts and dips, resulting in a classification of QPD. A single flare was identified near 11.5d. While some of the regions of significant periodicity are associated with peaks in the light curve (typically 60-minute wavelet scales), the largest appear on either side of the dip that occurs near 23.2d. These regions both show extended periods of significance, roughly 5 hours long, with power in wavelet scales between 60 - 100 minutes. The second region with clear quasi-periodicity is co-located with a longer, roughly 4 hour period which persists for 10 hours.

DD Tau: Some degree of periodicity is visible for this object. Most of the variability resembles accretion bursts, resulting in a B classification. Two flares were identified near 1.2d and 24.8d. A large region of significant quasi-periodic behavior was observed starting near 8.4d. 90-minute scale quasi-periodicity persists (with varying significance) for the next 20 hours. Longer and shorter timescale regions also occur sporadically during this time frame, with periods ranging from 30 minutes to over 120 minutes. This event occurs on the rise of a brightening event. After the peak, there is very little behavior on these timescales, but slower ($\sim$ 3 hour) oscillations can be seen. A small localized event was observed near 19.7d, with a 17-minute weakly-significant signal.

DE Tau: This object shows a periodic signal with accretion bursts and was classified as a QPS object. Two flares are present near 2.0d and 24.0d. A quasi-periodic signal is present beginning near 14.7d and persists for about 4 hours with wavelet scales between 36 and 100 minutes. This occurs near a local maximum in the light curve. A less-significant 90-minute period signal, which persisted for 4 hours, was observed near 5.1d on the downward descent from a peak in the light curve.

DS Tau: A possible period can be identified for this object, but it is somewhat masked by changes in the accretion rate. This object displays large changes in flux

(up to 50%) and was assigned a B classification. During the largest peak, significant multi-period quasi-periodic behavior is observed. This persists over much of the 80 hours that encompass the peak of the light curve. While quasi-periodicity is observed over the entire range of scales from 14 minutes to 120 minutes, the dominant periods are roughly 30 and 60 minutes. Additional short-timescale variability was observed close to a peak near 23.6d. During this time, a 60-minute scale region persists for 2.5 hours. A second region exhibiting 30- to 45-minute quasi-periodicity persists for roughly 3.5 hours.

FM Tau: Clear periodicity is difficult to identify for this object. The light curve is stochastic with both dimming and brightening events, resulting in a QPS classification. Two flares were observed, near 6.8d and 21.0d. Relative changes for this object are moderate (on the order of 25%). Quasi-periodic signals were identified over a ~ 7 hour period near a peak in the light curve at 3.2d, with separate wavelet scales of 35, 60, and 100 minutes. Short-lived regions of significance were also observed near 4.1d, 11.0d, and 18.2d, which may be associated with small flares. A short-lived region was also observed near 5.8d, with a wavelet scale of about 45 minutes.

FN Tau: While the changes in this object are quite small (on the order of 1%), a periodic signal is identifiable. I found that the *TESS* flux uncertainties from the SPOC pipeline were slightly overestimated compared to the observed scatter, causing the algorithm used to measure Q to fail. To account for this, I report an upper limit on Q for this object and note that both P and QPS are possible variability classifications. Two potential flares were identified near 6.0d and 21.7d. While no quasi-periodicity was detected above the threshold of 6 standard deviations, some quasi-periodicity is detected with lower confidence near 20.4d at 60-minute wavelet scales.

FO Tau: A period is identifiable and accretion bursts are present in the *TESS* light curve, resulting in a B classification via Q and M. A single flare was identified near 25.0d. No quasi-periodicity is detected above a significance of 6 standard deviations. Possible lower significance quasi-periodicity was observed over the 12 hours starting near 14.9d on timescales of 35, 70, and 120+ minutes.

RY Tau: Deep dips are visible during the first half of the *TESS* observations which contributes to the classification of QPD. During the second half, almost no period is visible. RY Tau has been previously observed to show dipping behavior thought to be associated with variations in the upper layers of the inner disk (Davies et al., 2020) which matches the observed behavior here. No flares were identified for this object. This object displays very limited short-timescale quasi-periodic signals. The regions that are identified in the CWT are associated with small discontinuities rather than a quasi-periodic signal. The exception is a short-lived region near 24.4d with a period of 50 minutes.

UY Aur: A clear periodic signal can be identified, punctuated by flares and accretion events, resulting in a classification of B. I identified 5 events that resemble flares in this object, one of which appears to be at the beginning of a major accretion event. This object displays strong quasi-periodic signals only during the largest accretion bursts which last on the order of 30 hours. Observed periods during these events range from 25 minutes to over 120 minutes. A single dominant wavelet timescale is difficult to identify, but some scale of short-timescale variability persists over the majority of the peaks. I find very few significant quasi-periodic signals on the explored timescales outside of the accretion bursts.

V819 Tau: V819 Tau is a very periodic source with many flares. I identified 10 events that resemble the characteristic rapid rise and exponential decay of flares. I see very limited variability that resembles dipping/accretion. A single moderately-

significant quasi-periodic signal is detected near 20.8d with a wavelet scale of ~ 87 minutes. While the use of Q and M would suggest this is a B object, the classification is on the edge, and by-eye inspection of the light curve reveals that a classification of P is more appropriate.

4.4.4 GM Aur

GM Aur is unique within the sample because of the NUV - NIR *HST* STIS data obtained simultaneously with the *TESS* observations. From the *TESS* light curve, a period can be identified. On top of the periodic behavior, I see accretion bursts, resulting in a classification of QPS. No obvious flares were identified for this object. Several regions of quasi-periodicity are located near local maxima in the light curve, but unfortunately do not overlap with the *HST* observations. Two of the most significant regions, near 9.1 d and 14.5 d had periods on the order of 50 - 60 minutes.

Contribution of Accretion Columns

The contemporaneous NIR - NUV coverage of the STIS spectrograph allows us to break the degeneracy between accretion column density and accretion shock surface coverage. Tab. 4.11. contains the fitted mass accretion rates, accretion shock filling factors, and veilings for *HST* Epochs 9 - 14. The model with the maximum posterior probability is overlaid on the observations in Fig. 4.7. Individual contributions from low-, medium-, and high-density accretion shocks are shown separated from the total.

I find the total surface coverage by accretion shocks to be between 10% and 17%. The largest contributor to the surface coverage is the low-density column, while the relative contribution from each column density bin to the total mass accretion rate varies between epochs. Figure 4.8 shows the breakdown of the contribution to the total mass accreted from each column density bin on top of the *TESS* light curve.

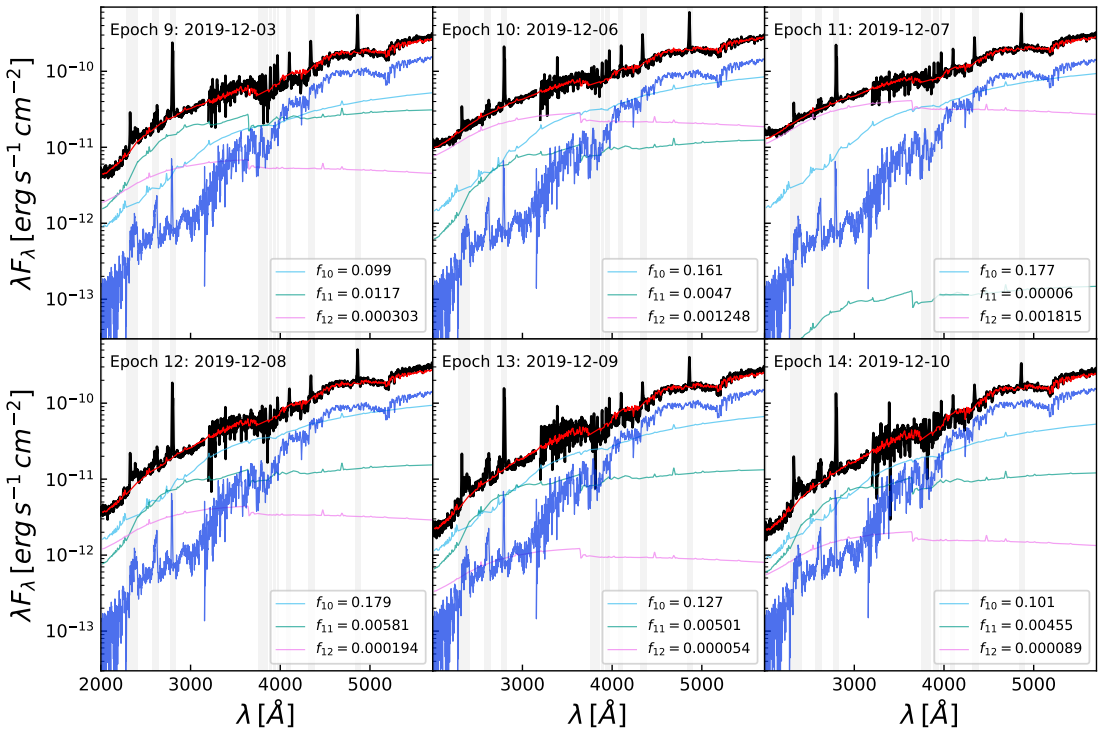

Fig. 4.7: Model fits to the continuum emission of GM Aur during Epochs 9 - 14 as observed by STIS on *HST* . The data are shown in black, and the total model is shown by the red line. The model components, $F = 10^{10}$, 10^{11}, and $10^{12}\,\mathrm{erg\,s^{-1}\,cm^{-2}}$ are shown in cyan, light blue, and pink respectively. The undisturbed photosphere model is displayed in dark blue. The total model shown here maximizes the posterior probability (i.e., the mode of the distribution). Filling fractions for this model for each epoch are included in the legend. The light grey bars mark regions that were masked during the fitting procedure due to line emission.

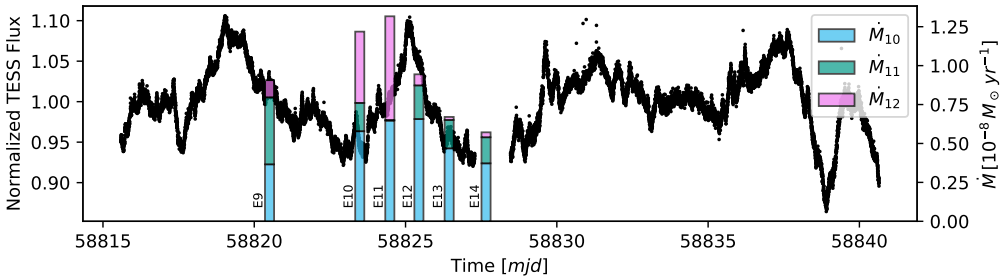

Fig. 4.8: Contribution to the total mass accretion rate from the low-, medium-, and high-density accretion columns on top of the *TESS* light curve for GM Aur. The total mass accretion rate is given by the height of the bar and each bar is placed at the time of observation (see the axis on the right).

I find that the peak accretion rate occurs roughly one day before the peak of the *TESS* curve. However, the peak of the low density accretion columns is better-aligned with the peak of the *TESS* light curve. Given that the *TESS* response curve is centered near 9000 Å, this is somewhat expected since the spectrum of the low-density accretion column peaks at longer wavelengths compared to its medium- and high-energy counterparts. This also explains some of the scatter in the slopes between the *TESS* photometry and the excess in the U-band, which should be more sensitive to all of the accretion column densities considered here compared to the *TESS* bandpass.

$\dot{M}$ from U-band Excess

The bottom panel of Figure 4.9 shows the *TESS* light curve with the simultaneous *HST* and LDT mass accretion rates marked. The top panel shows the derived mass accretion rates against the simultaneous *TESS* observations. While correlations are present between the mass accretion rate and the observed *TESS* flux during all of the individual nights of LDT observations, significantly more scatter is present when the entire sample is considered. The *HST* observations mirror this and display significant scatter. $\dot{M}$ measurements from the LDT U-band excess and those from

Table 4.11. GM Aur Fitted Model Parameters

Epoch	$\dot{M}$	f_{1E10}	f_{1E11}	f_{1E12}	r_v
9	$0.900^{+0.009}_{-0.009}$	$0.100^{+0.004}_{-0.004}$	$0.0117^{+0.0003}_{-0.0003}$	$0.000300^{+0.000012}_{-0.000011}$	$0.548^{+0.009}_{-0.009}$
10	$1.210^{+0.010}_{-0.010}$	$0.157^{+0.005}_{-0.005}$	$0.0049^{+0.0005}_{-0.0005}$	$0.001246^{+0.000022}_{-0.000021}$	$0.552^{+0.009}_{-0.009}$
11	$1.309^{+0.010}_{-0.010}$	$0.176^{+0.004}_{-0.004}$	$0.00009^{+0.00010}_{-0.00004}$	$0.001813^{+0.000016}_{-0.000017}$	$0.664^{+0.010}_{-0.010}$
12	$0.938^{+0.009}_{-0.009}$	$0.179^{+0.004}_{-0.004}$	$0.00588^{+0.00027}_{-0.00026}$	$0.000194^{+0.000010}_{-0.000011}$	$0.665^{+0.010}_{-0.010}$
13	$0.666^{+0.008}_{-0.007}$	$0.127^{+0.003}_{-0.003}$	$0.00495^{+0.00018}_{-0.00019}$	$0.000053^{+0.000006}_{-0.000005}$	$0.477^{+0.009}_{-0.009}$
14	$0.568^{+0.007}_{-0.007}$	$0.101^{+0.003}_{-0.003}$	$0.00455^{+0.00019}_{-0.00018}$	$0.000087^{+0.000007}_{-0.000007}$	$0.441^{+0.008}_{-0.009}$

Note. — Mass accretion rates, filling factors, and veiling for GM Aur from the analysis of the *HST* STIS observations with the accretion shock models presented in Calvet & Gullbring (1998) and Robinson & Espaillat (2019). Note that the uncertainties presented here are the 16^{th} and 84^{th} percentiles of the posteriors (roughly analogous to 1σ) recovered from the MCMC analysis, and do not include systematic uncertainties (e.g., extinction and stellar parameters). Robinson & Espaillat (2019) found that $\sim$ 10% systematic uncertainties are appropriate in derived parameters from this type of analysis.

HST that are close in time are in moderate agreement given the uncertainties in measuring the mass accretion rate (e.g., 2019-12-06 UT and Epochs 10 & 11).

Sub-exposure Time-tag Analysis

The STIS NUV-MAMA detector records photon arrival timestamps while in the time-tag mode, which can be used to break long, single exposures into multiple, shorter sub-exposures. By breaking the longer NUV exposure into 120 s chunks and adding a delay to the first sub-exposure, I obtain exactly simultaneous NUV-*TESS* observations to identify correlations on minute-timescales. Fig. 4.10 shows the integrated NUV flux between $1700 - 3100$ Å plotted against the simultaneous *TESS*

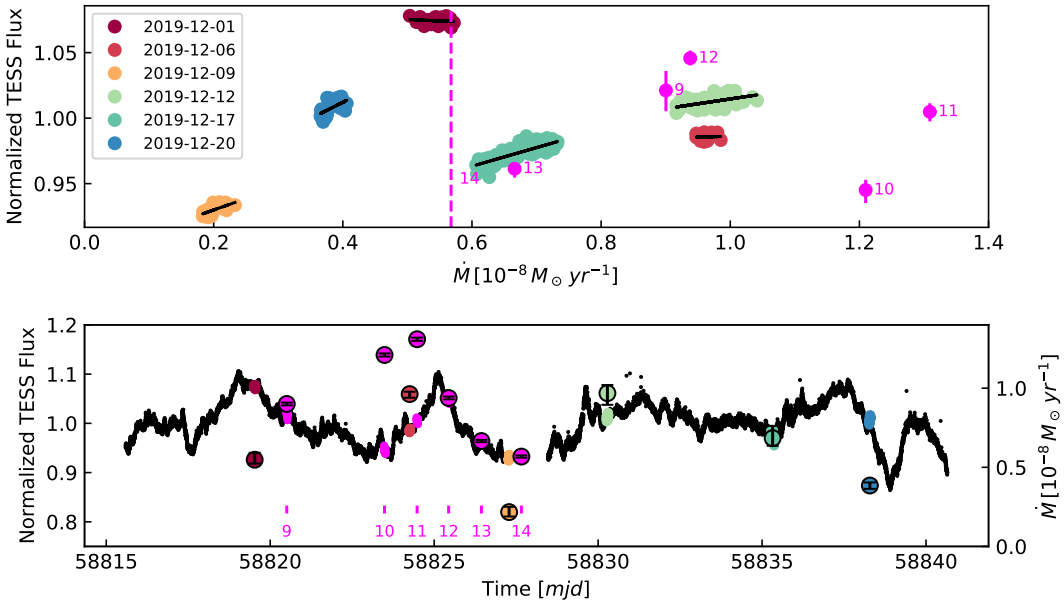

Fig. 4.9: *Top:* Mormalized *TESS* flux vs. mass accretion rate. Colored points represent mass accretion rates obtained through U-band excess, while the magenta points represent *HST* STIS epochs 9-14. The black lines on top of the loci of LDT points show a night-by-night linear regression to help display trends. While I find strong positive correlations between *TESS* flux and U-band excess during individual nights, significant scatter is found across the entire sample, and the slope of the correlations changes between nights. *HST* Epoch 14, which fell into the *TESS* gap, is marked by the dashed line. The error bars on the *HST* points represent the range of observed *TESS* fluxes during the exposure. *Bottom: TESS* light curve with the simultaneous measurements highlighted in the same color scheme as the top panel. Mass accretion rates are overlaid as colored points with black outlines (right axis). The error bars for the LDT data are the width of the observed mass accretion rates during that night, while those for the *HST* points are the fitted uncertainties.

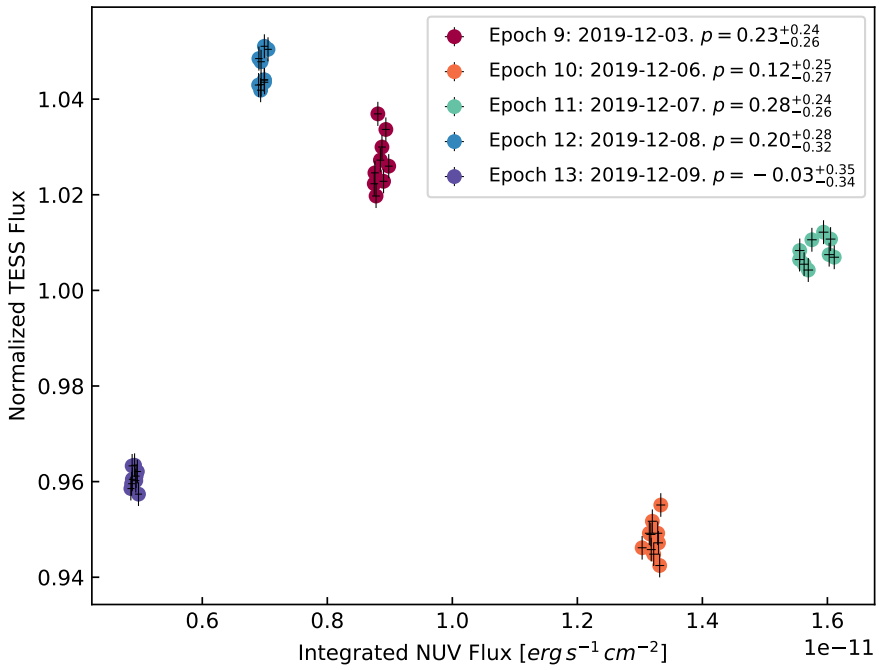

Fig. 4.10: Integrated NUV flux from 120s sub-exposures of the NUV *HST* STIS observations of GM Aur plotted against the simultaneous *TESS* observations. Pearson correlation coefficients for each visit are included in the legend. I find weak positive trends during 4/5 epochs, but note large uncertainties in the significance of these correlations.

observation. The existence of a trend between *HST* and *TESS* within individual *HST* visits is tested by calculating the Pearson correlation coefficient within a Monte Carlo simulation. I find a weak, positive trend between *TESS* and *HST* within most individual exposures, but note that the Monte Carlo analysis suggests large uncertainties on the significance of this result. Values of the correlation coefficients for each epoch are included in Fig. 4.10.

4.5 Discussion

I obtained continuous short-cadence *TESS* and simultaneous LDT observations of 14 TTS in the Taurus star-forming region during December 2019 to study accretion

variability. Additionally, I obtained contemporaneous NUV - NIR *HST* STIS spectra simultaneously with the *TESS* observations of the CTTS GM Aur. I found that much of the variability observed in the *TESS* light curves can be attributed to changes in the accretion rate, but note that *TESS* primarily traces low-density accretion shocks. Within these light curves, I identified regions of significant quasi-periodicity that primarily occur near the maxima in some light curves using a CWT analysis. Below I discuss the implications of these findings with regards to future work and other studies.

4.5.1 *TESS* as a Tracer of Accretion

While positive correlations between $\dot{M}$ and *TESS* fluxes are observed in nearly all of the *TESS* - LDT observations, I note significant scatter in the measured slope between the two quantities. This does not appear to be solely caused by systematic differences between different stars since different slopes between $\dot{M}$ and *TESS* were also observed between different sessions of the hour-timescale LDT U-band monitoring of GM Aur. Likewise, on even shorter scales I find different slopes from the time-tag analysis (see §4.4.4 and note that the correlations are quite weak in this case). The results of the decomposition of the accretion columns into individual components presented in §4.4.4 also shows that *TESS* misses some of the information about accretion encoded in the shorter wavelengths. Based on the spread of the measured slopes between objects, I suggest that any global, linear relationship between normalized *TESS* flux and the relative mass accretion rate would likely be unreliable. However, I note that the *TESS* flux does trace facets of the accretion behavior, particularly on shorter timescales. Longer timescale observations appear to suffer from additional astrophysical noise, e.g., starspots.

4.5.2 Quasi-periodicity & ULLYSES

Siwak et al. (2018) identified quasi-periodic variability in TW Hya on 11-to-30-minute timescales superimposed on both the rising and falling slopes near accretion maxima. This variability is similar to much of the quasi-periodicity found in my sample, although I also find significant periods of quasi-periodicity on slightly longer timescales. Siwak et al. (2018) found these events show the largest changes in U and B bands, with decreasing amplitude as a function of wavelength, suggesting that this variability is associated with the accretion process. Thermal instability oscillations within the accretion shock have been proposed as a possible source of this quasi-periodicity (Langer et al., 1981; Chevalier & Imamura, 1982). Depending on the assumptions made by different models of this instability, predictions for the timescale range from 0.02s up to 900s (Sacco et al., 2008; Koldoba et al., 2008; Matsakos et al., 2013; Orlando et al., 2013; Costa et al., 2017). The longest timescale predictions come from the models of Matsakos et al. (2013) which included an oblique impacting surface.

The lack of previous detections of quasi-periodicity by Drake et al. (2009) and Günther et al. (2010) may in part be attributed to the oscillations generally only appearing near maxima in the light curve, which in turn occur in a stochastic manner. Additionally, I do not find this quasi-periodicity near all of the maxima in the *TESS* light curves, which also increases the chances of a non-detection with a non-continuous monitoring observational strategy. Regrettably, uncertainties regarding under what accretion column conditions these quasi-periodicities (and thus the instabilities) can occur still persist. None of the GM Aur *HST* observations, which can be used to probe the density of the accretion column, aligned with regions of significant quasi-periodicity. Detailed analysis of individual objects that display these

quasi-periodicities may help answer some of these questions, but I defer such analysis for future work.

This uncertainty may also be remedied by the upcoming *HST* Ultraviolet Legacy Library of Young Stars as Essential Standards (ULLYSES) program. The ULLYSES program has been allocated 400 *HST* orbits to obtain contemporaneous FUV - NIR *HST* STIS and Cosmic Origins Spectrograph (COS) spectra for a large number of CTTS to produce the largest-ever UV spectral library of YSOs. An additional 100 orbits have been allocated to monitor four well-studied targets, which include GM Aur, BP Tau, TW Hya, and RU Lup. Based on the results for GM Aur and objects that demonstrated quasi-periodicity on short timescales, I recommend that when possible, these *HST* observations should be scheduled to be simultaneous with short-cadence photometric observations. While longer-cadence (e.g., 30-minute cadence *TESS* FFI) observations will provide context with regards to slower accretion trends and variability classification, those observations miss the quasi-periodicity detected in this chapter. Ultimately, without short-cadence photometry data, we lack the critical broader context for the additional information we gain from the more detailed *HST* observations necessary to interpret these results. I also recommend continued use of the NUV time-tag mode on STIS when observing CTTS since the overhead costs are minimal/zero, and I found potential correlations between the NUV *HST* STIS spectra and *TESS* during individual sub-exposures (see §4.4.4).

It is worth noting that a second possibility for the observed quasi-periodicity on these timescales exists in the form of small, well-organized clumps of material striking the star in rapid succession. This would give rise to rapid, quasi-periodic increases in flux. However, like Siwak et al. (2018), I must defer until a clear method of distinguishing between the two cases is developed, likely involving more modeling and multi-wavelength, simultaneous measurements during one of these events.

4.5.3 Comparisons to Previous *HST* GM Aur Observations

The values of the mass accretion rates of GM Aur measured from the *HST* data are consistent with the previously observed range during epochs 1-8, which spans from $0.6 - 2.0 \times 10^{-8}\,\mathrm{M_\odot\,yr^{-1}}$ Ingleby et al. (2015); Robinson & Espaillat (2019). Likewise, the distribution of accretion column densities and the measured veiling is also consistent with much of the behavior that has been observed before. Robinson & Espaillat (2019) found a large increase in $\dot{M}$ during Epoch 7. The measured mass accretion rate during that event was still roughly 50% times higher than the peak accretion rate observed in this chapter, which highlights the uniqueness of that event. That work also considered the inclusion of accretion columns with even higher densities during Epoch 7, with kinetic energy fluxes of $3 \times 10^{12}\,\mathrm{erg\,s^{-1}\,cm^{-2}}$, which I do not find during any of the epochs observed here. The empirical classification of QPS is consistent with the previously observed behavior and the inclination of $52^\circ.77^{+0.05}_{-0.04}$ obtained from radio observations under the assumption that the stellar rotation axis is aligned with the disk (Macías et al., 2018).

4.6 Summary

I monitored 14 objects using the short-cadence mode on *TESS* for 26 d. During that time, I also observed these objects with UBVRI photometric bands on the LDT on six nights. I obtained simultaneous *HST* STIS observations with contemporaneous NUV - NIR coverage of GM Aur. With the *TESS* data, I estimate rotational periods and determine empirical variability classifications through the use of previously developed statistical metrics. With the LDT data, I measured mass accretion rates through the measured U-band excess. With the *HST* STIS data, I employ detailed accretion shock models to measure surface coverage of accretion shocks for GM Aur. My primary findings are as follows.

1. Some of the variability present in the *TESS* light curves can be linked to accretion down to timescales of minutes. However, a single clear relationship between *TESS* flux and $\dot{M}$ is not readily apparent. This is further demonstrated by the U-band monitoring of GM Aur where the slope between these two quantities changes between nights.

2. *TESS* is more sensitive to accretion from low-density accretion columns than medium- and high-density columns.

3. Quasi-periodic events on timescales from $10 - 120+$ minutes were identified within the *TESS* light curves for most of the objects in the sample. The majority of these events occur near maxima in the light curve. These events may be associated with thermal instabilities within the accretion column, but I still cannot rule out ordered, clumpy accretion.

4. Simultaneous short-cadence light curves remain an important tool for providing context for multi-wavelength studies of accretion in young low mass stars.

5

Synthetic Light Curves of Accretion Variability in T Tauri Stars

5.1 Introduction

Variability has been a nearly ubiquitous feature CTTS since their discovery (Joy, 1945; Herbig, 1962), and has been observed on timescales ranging from minutes to decades (Siwak et al., 2018). One of the major sources of variability that occurs on timescales of hours to weeks is variability in the accretion rate onto the star (Herbst et al., 1994). These changes are most readily apparent in NUV and the optical.

Recent space-based long-timescale optical photometric monitoring campaigns from CoRoT (Cody et al., 2014; Stauffer et al., 2014, 2015, 2016; McGinnis et al., 2015) and K2 (Cody & Hillenbrand, 2018) have been successful in classifying CTTS variability in several categories based on their light curve symmetry and periodicity by eye and subsequently using statistical metrics to separate objects by light curve periodicity and symmetry (Q and M, respectively). These classifications include bursters, quasiperiodic symmetric objects, purely stochastic objects, and purely periodic objects, whose variability has in part been attributed to changes in the accretion rate and/or to rotational effects from stable accretion hot spots (Stauffer et al., 2014; Venuti et al., 2015). Young stars that predominantly show decreases in observed flux are classified as quasiperiodic dippers and aperiodic dippers (e.g., Stauffer et al., 2015; Kesseli et al., 2016; Nagel & Bouvier, 2019). Objects that do not fit into these

categories are placed into the classes of long timescale, unclassifiable, non-variable, or eclipsing binary (e.g., Cody & Hillenbrand, 2018).

Many works have described the accretion variability and the inner regions of protoplanetary disks under the constraint of magnetically controlled accretion. Steady-state solutions of 1D flow along the accretion column have been studied analytically by several authors (e.g., Hartmann et al., 1994; Li, 1996; Koldoba et al., 2002). Additional work has been done with 3D MHD simulations of the inner regions of the disk (e.g., Romanova et al., 2003, 2004, 2008; Long et al., 2011; Romanova et al., 2011; Kurosawa & Romanova, 2013; Romanova et al., 2013). These works identify numerous sources of variability including rotational modulation and Rayleigh Taylor instabilities. Adams & Gregory (2012) developed semi-analytic steady-state 1D solutions within a coordinate system that follows along a corotating magnetic field line connecting the star to the disk. That work was expanded upon by Robinson et al. (2017) using simulations that demonstrated the formation of traveling shocks along the magnetospheric accretion column under smoothly varying disk input conditions (see Chapter 2). These shocks cause rapid sawtooth-like changes in the accretion rate that qualitatively resemble the variability seen in objects under the burster classification. However, the variability in those simulations is induced through density perturbations controlled by an overly simplified sinusoidal driving function. Additionally, those simulations were not used to make direct predictions of the accretion events to compare against observations.

Here, I combine the 1D HD fluid simulations of the accretion column of Robinson et al. (2017) and radiative transfer accretion shock models (Calvet & Gullbring, 1998; Robinson & Espaillat, 2019) to produce the expected excess from accretion under a variety of physical conditions in the inner disk. This excess is then characterized using the same metrics that have been applied in long-timescale optical monitoring

studies of CTTS. In §5.2, I present the models and describe the process of obtaining the metrics. In §5.3, I demonstrate how different physical parameters affect light curves. In §5.4, I discuss my findings within the context of other studies and possible future work. I conclude with a summary of the primary findings in §5.5.

5.2 Methods

5.2.1 Overview

To create synthetic light curves, I couple three models together. These include a 1D HD simulation of the accretion column; nLTE accretion shock models of the preshock, postshock, and heated photosphere; and a geometric rotational modulation model. I run the 1D HD simulations of the accretion column to obtain the density and velocity of the flow near the surface of the star. The emission arising from the shock is then found with the nLTE accretion shock model by using the conditions of the flow from the HD simulations as input. That emission is then scaled by the fraction of the accretion hot spot that is visible based on the rotational phase, inclination and spot latitude (i.e., a filling factor). Note that no feedback is included in the HD simulations from the nLTE shock models and that the solutions from the nLTE models are obtained in a time-independent manner. If the radiative timescales are longer than the accretion variability then this approach may break down. I finish this section by describing the metrics and relevant variability classes that have been developed to describe observed light curves of CTTS that I then apply to the light curves from the models. Definitions for commonly reoccurring symbols used in this work are listed in Tab. 5.1.

[h]

Table 5.1. Reoccurring symbols used in this work

Symbol	Definition
Coordinate Systems & Magnetic Field	
θ	Polar angle
ϕ	Azimuthal angle
r	Radial coordinate
p	Distance from origin along field line
q	Coordinate that selects the field line
ξ	Dimensionless radial coordinate
B_{dip}	Dipolar magnetic field coefficient
B_{oct}	Octupole magnetic field coefficient
Γ	Ratio of B_{oct} to B_{dip}
Star, Disk, & Fluid	
R_{disk}	Truncation & co-rotation radius
i	Inclination
A	Turbulent perturbation amplitude
n_0	Number density at the disk
F	Kinematic energy flux of the flow
Rotational Modulation	
f	Accretion shock filling factor
α	Angular spot radius
γ	Angle between spot center and rotation axis

Table 5.1 (cont'd)

Symbol	Definition
β	Angle between spot center and line of sight
Light Curve Metrics	
Q	Periodicity metric
M	Symmetry Metric
σ	Injected white noise
GP	Gaussian Processes

5.2.2 Hydrodynamic Simulations

To model the accretion column connecting the star to the inner edge of the disk, I turn to the 1D HD fluid simulations of Robinson et al. (2017). These simulations follow along the magnetic field line that connects the inner gas to the star, following the curvilinear coordinate system developed by Adams & Gregory (2012). These simulations operate under several simplifying assumptions that enable the use of the 1D approach. The assumptions and the implication for each assumptions are described below.

Assumptions

The magnetic field is assumed to be current free, and therefore curl free, and thus can be expressed as the gradient of a scalar field. I take advantage of this assumption by constructing a set of orthogonal curvilinear coordinates to describe the magnetic field lines. The coordinate p describes the distance from the origin (which is at the center of the star) along a field line, while the orthogonal coordinate

q describes which field line is being traced. The third coordinate, ϕ, describes the position in the azimuthal direction.

The magnetic field is assumed to be strong enough to force flow solely along the field line, which allows us to work in a 1D space described solely by p under a fixed q and ϕ. Thus, many complexities that can arise in higher dimensions (e.g., several types of instabilities) are suppressed. Compression from converging field lines is included through curvilinear scale factors. The assumed magnetic field structure is that of a rotation-axis-aligned multipolar field. While measurements of the magnetic field structure of some CTTS have shown evidence for complex toroidal fields (Donati et al., 2011a), many CTTS can be well described by composite fields consisting of dipole and octupole components (e.g., Donati et al., 2010a, 2011b). The ratio between the two associated coefficients is parameterized by $\Gamma \equiv \frac{B_{oct}}{B_{dip}}$ with the magnetic field described by

$$\mathbf{B} = \frac{B_{oct}}{2}\xi^{-5}\Big[(5\cos^2\theta - 3)\cos\theta\,\hat{r} + \frac{3}{4}(5\cos^2\theta - 1)\sin\theta\,\hat{\theta}\Big] + \frac{B_{dip}}{2}\xi^{-3}(2\cos\theta\,\hat{r} + \sin\theta\,\hat{\theta}), \tag{5.1}$$

where $\xi \equiv \frac{r}{R_\star}$.

The final assumption is that the corotation point is colocated with the magnetic truncation radius. This forces the magnetic footprints at both the star and the disk to stay fixed, which eliminates the possibility of shear flows at either boundary. A more complete description of the simulations is shown in Robinson et al. (2017), and more discussion on the curvilinear coordinate system can be found in Adams & Gregory (2012). The top panel of Fig. 5.1 shows a schematic of the system under several magnetic field constructions and magnetic truncation radii, R_{disk}.

1D HD Simulation Scheme and Boundary Conditions

A ZEUS-style upwind finite difference scheme was used to solve the 1D fluid equations (Stone & Norman, 1992). Under this scheme, the density, velocity, and internal energy of the flow are solved on a staggered mesh. In this work, I restrict the flow along the accretion column to be isothermal at a temperature of 10,000K from UV heating, which sets the sound speed in the simulation. The internal structure of the solver remains unchanged between this work and Robinson et al. (2017), with the exception of the boundary conditions.

The new boundary condition that has been implemented at the outer boundary mimics Kolmogorov turbulence (see Kolmogorov, 1941) in the inner disk by using a velocity driving function. The upper bound on the turnover frequency is set by a cutoff on events happening on timescales shorter than 30 minutes. The lower frequency bound is set by the travel time of a sound wave around the circumference of the inner disk of the base model (described in §5.3.2). A turbulence spectrum with these bounds is then used to generate velocity-driving functions composed of sine curves with random phase offsets. I do not restrict outflow from the system, and as such, these boundary conditions result in solutions similar to those under steady-state boundary conditions with the addition of stochastic perturbations. The system is allowed to evolve for 18 d (roughly 14 sound crossing times) to allow transients from initialization to disappear before the simulation is sampled. An example of one of the driving functions that mimics turbulence is shown in the bottom panel of Fig. 5.1.

5.2.3 Accretion Shock Model

The nLTE accretion shock models of Calvet & Gullbring (1998), which were recently adapted by Robinson & Espaillat (2019) (see Chapter 3) to use a recent

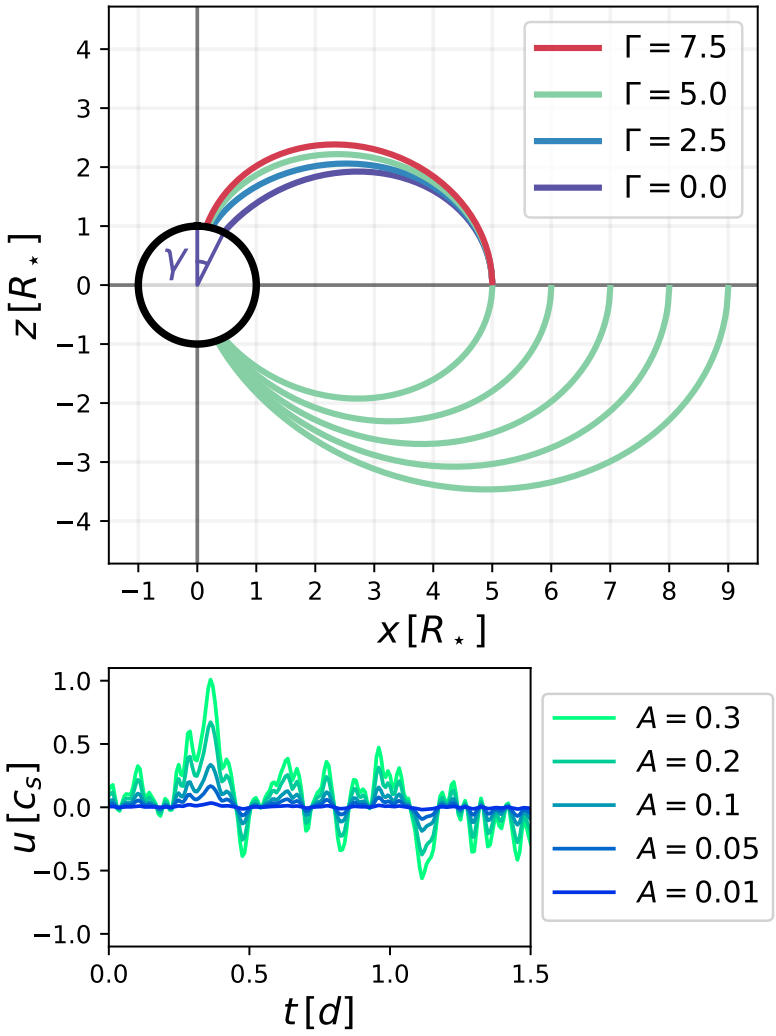

Fig. 5.1: *Top:* Magnetic field line geometry for several values of the ratio between dipole and octupole components, Γ, and inner disk radius, R_{disk}. Changing γ, the angle between the center of the hot spot and the rotation axis, changes the rotational modulation of the model (see Fig. 5.2). After normalizing the magnetic footprint at the disk, the effective cross-sectional area near the star decreases with increasing Γ and R_{disk}. This schematic is to scale, and the axes are in Cartesian coordinates in units of stellar radii. *Bottom:* A 1.5 d sample of the turbulent driving function with several Mach number rms amplitudes, A.

release of Cloudy (Ferland et al., 2017), were used to generate the emission from accretion. This model consists of a 1D plane-parallel accretion column with three parts: the preshock, the postshock, and the heated photosphere. The postshock is hot due to the kinetic energy of the flow being converted into thermal energy in the shock. As the material cools and falls, it re-radiates that energy (primarily as X-rays) into the preshock region and the underlying photosphere. The combined emission from these two regions forms the outgoing flux. Previous work has required the inclusion of accretion columns with different densities to reproduce observations (Ingleby et al., 2013, 2015; Robinson & Espaillat, 2019).

Here, I slightly modify the Robinson & Espaillat (2019) models by using the density and velocity information from the 1D fluid simulations as the preshock conditions rather than assuming that the flow is at the freefall velocity. In general, this causes the accretion column to be denser and slower than previous models at the same kinetic energy flux. This in turn causes the postshock region to narrow since the region is assumed to be optically thin and the velocity at the top of the region depends on the preshock velocity via the Rankine-Hugoniot strong shock conditions. Apart from this change, the accretion shock model remains unchanged from the version presented in Robinson & Espaillat (2019).

5.2.4 Rotational Modulation Model

The emission from the accretion shock model is scaled by a filling factor f, which represents the fraction of the visible stellar disk covered by accretion shocks. To do this, I have modeled the accretion hot spots on the surface of the star using an spherical cap geometry which is offset from the rotation axis. The filling factors can be calculated by integrating the projected area of the cap along the line of sight. The following solution follows a similar procedure and much of the nomenclature of Ureña & Georgiev (2018).

On a unit sphere, the spot is described by the angle between the center of the spot and the line of sight, β, and the angular radius of the spot, α. The integral to obtain the projected area can be separated into four cases: an ellipse (i), an ellipse + lune (ii), lune only (iii), or entirely hidden (iv). The specific case depends on the values of α and β. The functional forms of the solutions to the integral can be written as

$$f(\alpha,\beta) = \begin{cases} \pi a_x a_y, \text{ (i)} \\ \pi a_x a_y + 2I(y_L) - 2x_e y_L - 2a_x a_y I(y_L/a_y), \text{ (ii)} \\ 2I(y_L) - 2x_e y_L - 2a_x a_y I(y_L/a_y), \text{ (iii)} \\ 0, \text{ (iv)} \quad , \end{cases} \tag{5.2}$$

where the region for each case is described by

$$\begin{aligned} &\text{(i)}\, 0 \leq \beta \leq 90^\circ - \alpha \\ &\text{(ii)}\, 90^\circ - \alpha < \beta \leq 90^\circ \\ &\text{(iii)}\, 90^\circ < \beta \leq 90^\circ + \alpha \\ &\text{(iv)}\, \beta > 90^\circ + \alpha \quad , \end{aligned} \tag{5.3}$$

and the terms for the semiminor axis, semimajor axis, ellipse center, and lune height (a_x, a_y, x_e, and y_L, respectively) can be written as

$$a_x = \sin\alpha \cos\beta \tag{5.4}$$

$$a_y = \sin\alpha \tag{5.5}$$

$$x_e = \cos\alpha \sin\beta \tag{5.6}$$

$$y_L = \sqrt{1 - \frac{\cos^2\alpha}{\sin^2\beta}} \quad . \tag{5.7}$$

The ancillary function $I(\eta)$ is defined as

$$I(\eta) \equiv \int_0^\eta \sqrt{1-\eta'^2} d\eta' = \frac{1}{2}\left[\eta\sqrt{1-\eta^2} + \sin^{-1}\eta\right] \quad . \tag{5.8}$$

Next, I move into a coordinate system where the z axis is pointing toward the observer and the rotational pole is in the xz plane. The inclination, i, takes the standard definition of the angle between the rotational pole and the z axis. If the angular separation from the center of the spot and the rotation axis, γ, is specified, the x, y, and z positions of the spot center can be written as a function of rotational phase ϕ as

$$x(\phi) = \sin\gamma \sin\phi \tag{5.9}$$

$$y(\phi) = -\sin\gamma\cos i\cos\phi + \cos\gamma\sin i \tag{5.10}$$

$$z(\phi) = \sin\gamma\sin i\cos\phi + \cos i\cos\gamma \quad . \tag{5.11}$$

The phase zero point is defined such that when $\phi = 0$, y is at its minimum value. Using these functions, β can be written as a function of rotational phase via

$$\beta(\phi) = \begin{cases} \sin^{-1}\left(\sqrt{x(\phi)^2 + y(\phi)^2}\right), \; z \geq 0 \\ 180^\circ - \sin^{-1}\left(\sqrt{x(\phi)^2 + y(\phi)^2}\right), \; z < 0 \quad . \end{cases} \tag{5.12}$$

By combining this result with the expression for Eqn. 5.2, the projected area can be written as a function of ϕ, γ, α, and i.

The value of γ can be calculated under the assumption of flow solely along rotation axis-aligned dipole + octupole fields. The general expression for the coordinate q, which is constant along field lines, is given by

$$q = \frac{1}{4}\xi^{-3}\Gamma(5\cos^2\theta - 1)\sin^2\theta + \xi^{-1}\sin^2\theta \quad . \tag{5.13}$$

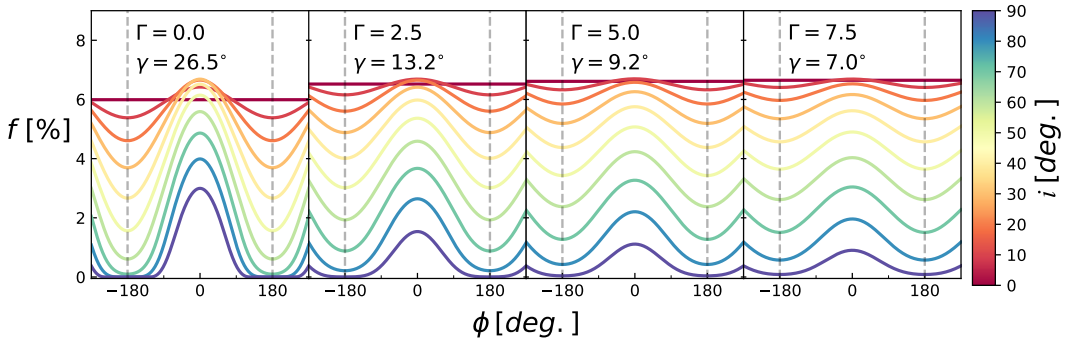

Fig. 5.2: Filling factor as a function of rotational phase, inclination, and magnetic field geometry for a single hot spot modeled as a spherical cap (expressed as a percentage). The examples shown here have a fixed spot radius of 15° and inner disk radius of $5R_\star$. As Γ increases, the magnetic footprint of the corotating field line on the star approaches the rotation axis, which diminishes the changes in projected spot area caused by rotation. The angle between the rotation axis and the center of the spot is γ. Due to the construction of the magnetic field, γ is also anticorrelated with the inner disk radius.

The value of the coordinate q that describes the field line that crosses the disk at the corotation point is fixed at

$$q = \frac{R_\star}{R_{disk}} \left(1 - \frac{\Gamma R_\star^2}{4 R_{disk}^2} \right) \quad . \tag{5.14}$$

Because q is a fixed quantity along field lines, Eq. 5.13 can be numerically solved for θ at the stellar surface with the value of q from Eq. 5.14. This θ is identical to γ under the definitions above. This reduces additional parameters that must be specified to include hot spot modulation to just i and α. Examples of the filling factor as a function of ϕ, Γ, and i with a fixed α are shown in Fig. 5.2.

5.2.5 Statistical Metrics Q and M

The metrics Q and M have recently been developed to classify light curves obtained using K2 and CoRoT (see Cody et al., 2014; Cody & Hillenbrand, 2018).

Here, I apply these metrics to light curves produced using my simulations and models to provide physical insight to previous classifications of observations. I also described several minor changes in the method of obtaining these metrics.

Determining Q

Q is calculated following the steps outlined in Cody et al. (2014), with a few modifications. The first step is identifying the rotation period. While the rotation period is known a priori in the simulations, the goal is to replicate the conditions present for real observations and conduct the analysis without including this prior knowledge. Additionally, I have injected white noise into the synthetic light curves with amplitudes of $\sigma = 0.5\%$ of the mean value to replicate typical observing conditions. The process to measure Q is described below and an example of the process is depicted visually in its entirety in Fig. 5.3. The unmodified light curve is shown in Fig. 5.3a.

The rotation period is estimated using two approaches: the autocorrelation function (ACF) (Fig. 5.3b) and a Lomb-Scargle periodogram (Lomb, 1976; Scargle, 1982) (Fig. 5.3c). The synthetic light curve is resampled to a linear grid when calculating the ACF and is smoothed using a Savitzky-Golay filter with a window size of 3 points to help avoid issues with local minima (Savitzky & Golay, 1964). The local maximum with the shortest lag of the smoothed ACF that is 0.05 larger than the surrounding local minima is identified. In the method of Cody et al. (2014), the largest peak in the Lomb-Scargle periodogram that is within $\pm 20\%$ of the previously identified period in the ACF is chosen as the rotation period of the star. However, I found that this method occasionally selected harmonics rather than the true period of my models, so I deviate from the approach of those authors slightly. Instead, I multiply the periodogram by a Gaussian centered on the selected peak of the ACF with a width of 30% of the period from the ACF, and then select the peak of this

weighted periodogram. I found that this method was effective at recovering the true period of the models even in the cases where the selected peak of the ACF was a harmonic.

The periodic behavior of the light curve was then identified by horizontally stacking three copies of the phase-folded data and modeling the trend using Gaussian Processes (GP), as shown by Figs. 5.3d and e. By stacking the phased light curve in this manner and making predictions with GP for the central copy of the stacked curves, I avoid edge effects and recover a smooth, periodic, non-parametric curve that can be modified to smooth over features with different timescales. The covariance function selected for this approach is a Gaussian with a characteristic covariance length of 0.3 in phase space. The predicted values from this GP approach for the central copy of the stacked phased light curve are then subtracted from the original light curve, as shown by Fig. 5.3f to eliminate periodic components. Using the results from this analysis, Q is defined by

$$Q = \frac{(\mathrm{rms}^2_{\mathrm{resid}} - \sigma^2)}{(\mathrm{rms}^2_{\mathrm{raw}} - \sigma^2)} \quad , \tag{5.15}$$

where $\mathrm{rms}_{\mathrm{resid}}$ is the rms value of the residuals after subtracting the periodic behavior and $\mathrm{rms}_{\mathrm{raw}}$ is the rms of the original light curve. Q is smaller for curves with stronger periodic components and larger for more stochastic light curves. The derived Q value for the example shown in Fig. 5.3 is 0.59.

Determining M

Again following Cody et al. (2014) and Cody & Hillenbrand (2018), the first step for calculating M is to remove outliers. This is accomplished by subtracting a smoothed version of the light curve from the raw light curve (Figs. 5.4a and b). I again employ GP with a Gaussian covariance function to produce a smooth version

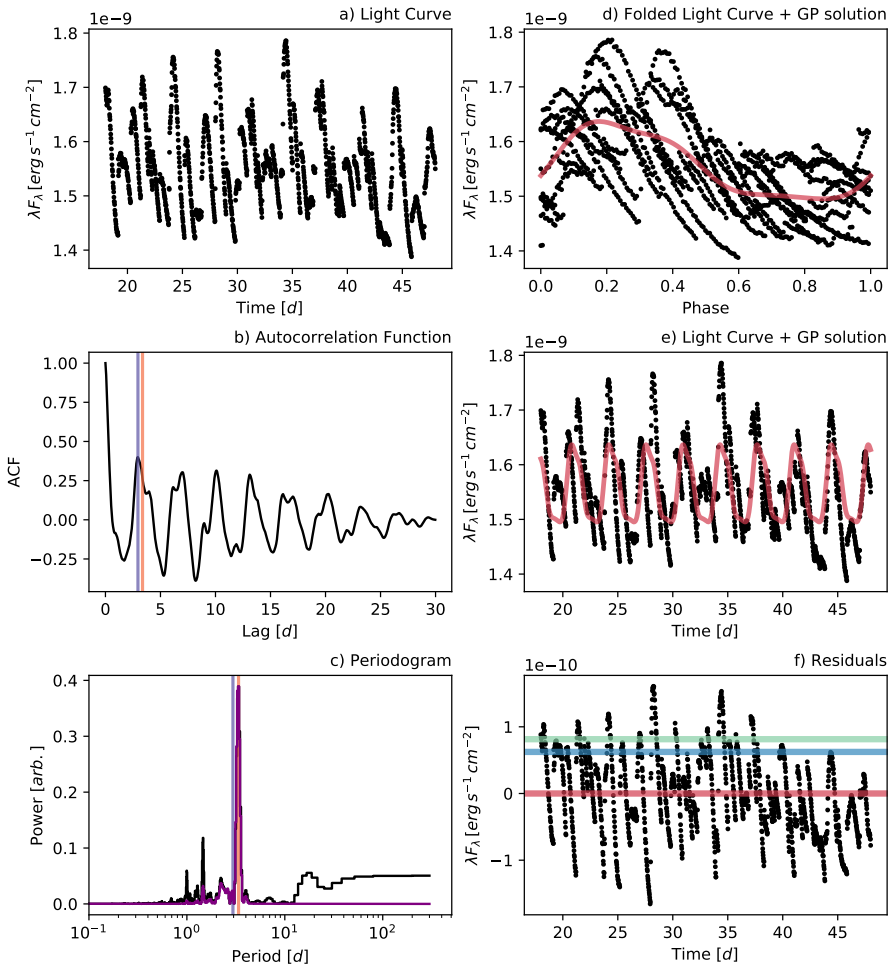

Fig. 5.3: Illustration of the steps to obtain the metric Q, which measures the periodicity of the light curve (see §5.2.5 for details on the process). This light curve is the base model described in §5.3.2 viewed from an inclination of 60°. Panel a) shows the raw light curve. Panel b) is the autocorrelation function (ACF) with the period as measured by the ACF and the Lomb-Scargle periodogram marked by purple and orange lines, respectively. Panel c) shows the Lomb-Scargle periodogram with the periods marked in the same fashion. I show the periodogram weighted by a Gaussian whose parameters are derived from the ACF in purple. Panel d) shows the folded light curve with the GP solution shown in red. Panel e) shows the raw light curve with the GP solution overlaid in red. Panel (f) shows the residuals after removing the GP solution. The horizontal red, blue, and green lines show the mean, $\mathrm{rms}_{\mathrm{resid}}$, and $\mathrm{rms}_{\mathrm{raw}}$, respectively. The derived Q value for this synthetic light curve is 0.59.

of the light curve that is subtracted from the original curve (Fig. 5.4c) in a flexible manner. The covariance length in this case was selected to be 2 hours. Outliers were identified as points in the residuals whose absolute values were greater than 5 times the rms. After clipping these outliers, the mean of the top and bottom 5% of points from the original curve is found, $\langle d_{5\%} \rangle$ (Fig. 5.4d). Using this mean, the median of the entire clipped light curve, d_{med}, and the rms of the clipped light curve, σ_d, the metric M is defined

$$M = -\frac{\langle d_{5\%} \rangle - d_{med}}{\sigma_d} \quad . \tag{5.16}$$

Here a negative sign is included since the original metric was constructed for use with magnitudes in Cody et al. (2014). More negative values of M indicate that the light curve features bursting behavior, while positive values of M suggest preferential dimming. Values of M closer to 0 indicate symmetric variability. The derived M value for the example shown in Fig. 5.4 is -0.31.

5.2.6 Variability Classes

The bivariate plot of Q vs. M can be broken into rough regions that display different forms of variability (e.g., Cody et al., 2014; Cody & Hillenbrand, 2018) based on visual classification. The definitions for the regions that I adopt from Cody & Hillenbrand (2018) are:

- *Burster*

  $M < -0.25$

- *Purely periodic symmetric*

  $Q < 0.15$ and $-0.25 < M < 0.25$

- *Quasiperiodic symmetric*

  $0.15 < Q < 0.85$ and $-0.25 < M < 0.25$

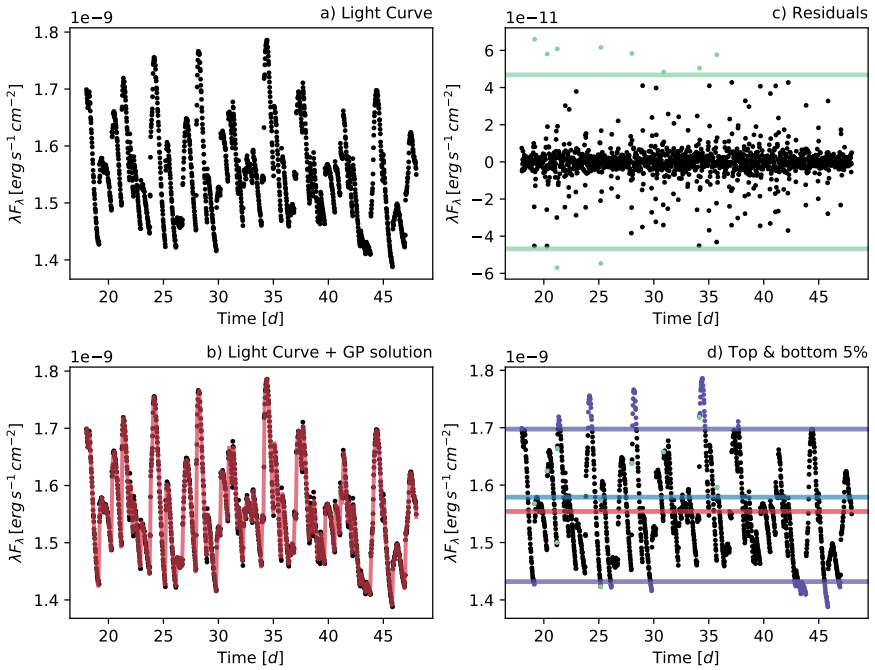

Fig. 5.4: Illustration of the steps to obtain the metric M, which measures the symmetry of the light curve around the mean (see §5.2.5). This light curve is produced using the base model described in §5.3.2 with an inclination of 60°. Panel a) shows the raw light curve. Panel b) shows the light curve with the GP solution overlaid in red. Panel c) shows the residuals after subtracting this fit. Points above the 5σ green lines are considered outliers. Panel d) identifies the top and bottom 5% of photometry points in purple, with the mean, $\langle d_{5\%} \rangle$, shown by the blue line. The median of all of the data, d_{med}, is shown by the red line. The derived M value for this synthetic light curve is -0.31.

- *Purely stochastic*

  $Q > 0.85$ and $-0.25 < M < 0.25$

- *Quasiperiodic dipper*

  $0.15 < Q < 0.85$ and $M > 0.25$

- *Aperiodic dipper*

  $Q > 0.85$ and $M > 0.25$.

In addition to these categories, which can be sorted by their position in Q and M space, Cody & Hillenbrand (2018) and Cody et al. (2014) include classifications by-eye for long-timescale, unclassifiable, nonvariable, and eclipsing binaries. Here I primarily focus on the types of variability that are thought to be caused in part by accretion-related phenomena (burster, purely periodic symmetric, quasiperiodic symmetric, and purely stochastic).

5.3 Results

After linking the HD simulation, the nLTE shock model, and the model of rotational modulation, I explored which parameters had an effect on the observed variability through the Q and M metrics. Below I discuss each of the parameters and their effect on the light curve.

5.3.1 Free Parameters

The relevant parameters that can be readily changed in the models are the following: the magnetic field geometry, Γ; the inner disk radius, R_{disk}; the rms of the turbulent driving function, A; the stellar parameters, $M_\star$, $R_\star$, and T_{eff}; the density of the accretion column at the disk, n_0; the inclination, i, of the star; the spot latitude (measured from the rotational axis), γ; the angular radius of the spot, α; and the filter bandpass.

While the number of free parameters initially appears daunting, several of them can be eliminated or combined into a single variable. The three stellar parameters, $M_\star$, $R_\star$, and T_{eff} can be reduced to the single parameter of $M_\star$ if an age is assumed using isochrones. Here, I use the MESA Isochrones and Stellar Tracks (MIST) with solar metallicity at an age of 2 Myr (Choi et al., 2016; Dotter, 2016). As noted in §5.2.4, under the assumption of a multipolar field, the spot latitude can be numer-

ically solved, eliminating γ as a free parameter. The fluid equations can be solved in a dimensionless manner, which means that changing n_0 does not affect the flow structure along the column, but only the output spectra. Here, I fix n_0 to a single value of $10^{13}\,\mathrm{cm}^{-3}$, which results in kinetic energy fluxes between roughly 10^{10} and $10^{12}\,\mathrm{erg\,s^{-1}\,cm^{-2}}$ which is a typical range for young stars (Ingleby et al., 2013, 2015; Robinson & Espaillat, 2019). Unless stated otherwise, the light curves are generated using the Johnson V filter (Johnson & Morgan, 1953). I explored a range of viewing inclinations, i, and found that changing α only strongly affects Q and M for models at high inclinations. Such inclinations are typically unobservable because of disk obscuration. Given this, I fix $\alpha = 15°$.

5.3.2 Base Model

After the above simplifications, five relevant free parameters remain: Γ, R_{disk}, A, $M_\star$, and i. To explore this parameter space, I first construct a base model with parameters thought to be somewhat typical of young stars. The base model has $\Gamma = 5.0$, $R_{disk} = 5.0R_\star$, and $M_\star = 1.0\,\mathrm{M}_\odot$. Ten inclinations were evenly sampled between 0° and 90°. Figure 5.5 shows the $U-V$ color against V for this base model viewed at an inclination of 60° for synthetic observations lasting 30 d. Fig 5.5 also demonstrates the degeneracy between the filling factor, f, and the kinetic energy flux of the flow at the shock, F, which can be written as

$$F = \frac{1}{2}\rho v^3 \tag{5.17}$$

where ρ and v are taken from the HD simulation at the stellar surface.

My base model was then run three times using the turbulent driving functions described above, each with a different random seed value. Q and M were then calculated for each of these models. As a rough estimate of the uncertainty in Q and

M, I adopt the mean of the standard deviations between the three realizations at each inclination. The process of determining Q and M for one of the light curves from a model realization at $i = 60°$ is illustrated in Figs 5.3 and 5.4, respectively.

5.3.3 Variants on the Base Model

Next, I consider variants on the base model, where one parameter is changed at a time. To gain insight on the parameters, simulations were first run with simple steady input/output boundary conditions that do not restrict the flow. These simulations converge to steady state and match both the analytic results from Adams & Gregory (2012) and the simulations from Robinson et al. (2017). The density and velocity solutions are shown in Fig. 5.6. Next, the steady-state boundary conditions were replaced with the turbulent boundary conditions described in §5.2.2. To minimize variation from random effects between models, the random number seed selected for the generation of the turbulent driving function for each model variant is fixed to be the same as the model shown in Figs. 5.3 and 5.4.

In the following sections, the importance of each parameter on variability classification is discussed. The results for all of the models are shown in Fig. 5.7 displayed in the form of Q vs. M bivariate plots. Fig. 5.8 shows Q and M as a function of i for the model variants, while Fig. 5.9 demonstrates the effect of changing the other model parameters parameters (Γ, r_{disk}, A, and $M_\star$).

Inclination, i

Under the model construction, i plays a strong role in determining how periodic the observed signal appears. Objects with low inclinations typically show weaker periodic variations, while objects that are more edge-on show significant rotational modulation. While the inclination at which the model turns from aperiodic to quasiperiodic to periodic depends on the other parameters described above, the

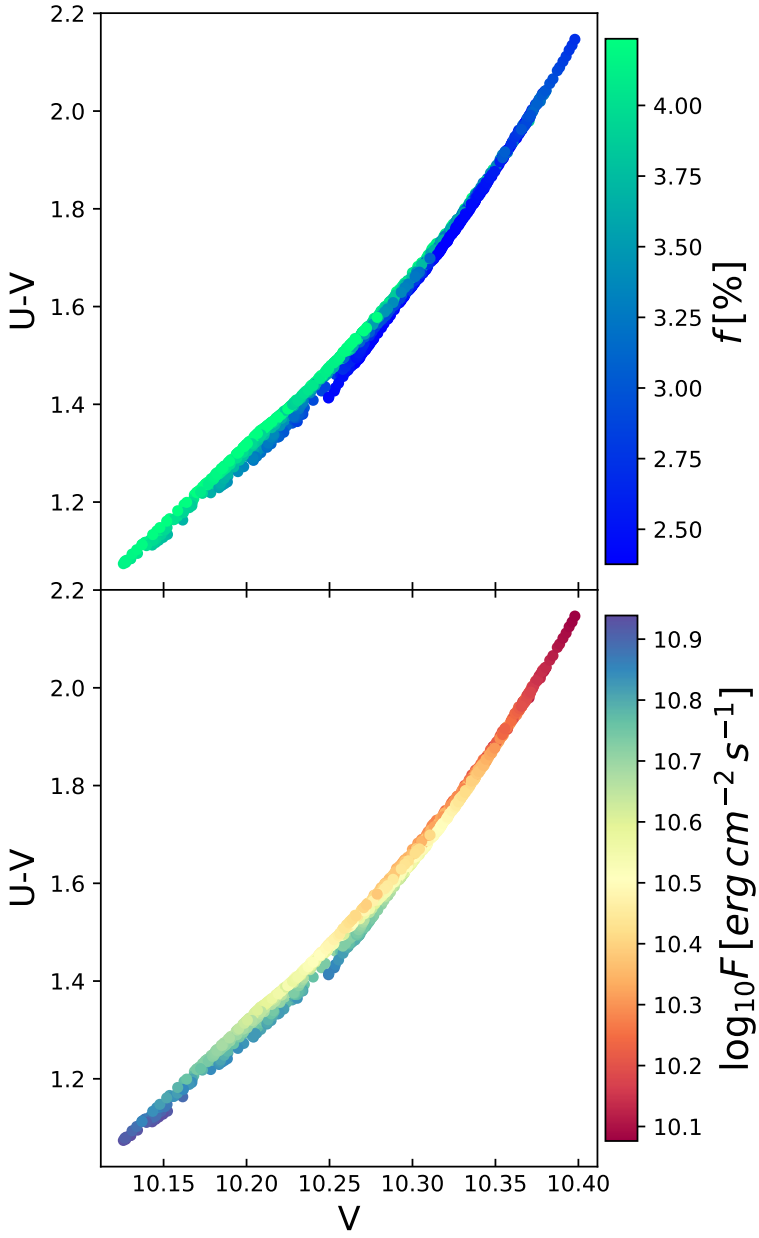

Fig. 5.5: $U-V$ vs. V diagrams created using 30 d of synthetic observations of the base model at an inclination of 60°. The top panel is colored by the filling factor, f (expressed as a percentage), while the bottom panel is colored by the kinetic energy flux, F. I find a gradient along the narrow diagonal locus of points for both of these quantities, demonstrating the degeneracy between both parameters at these wavelengths.

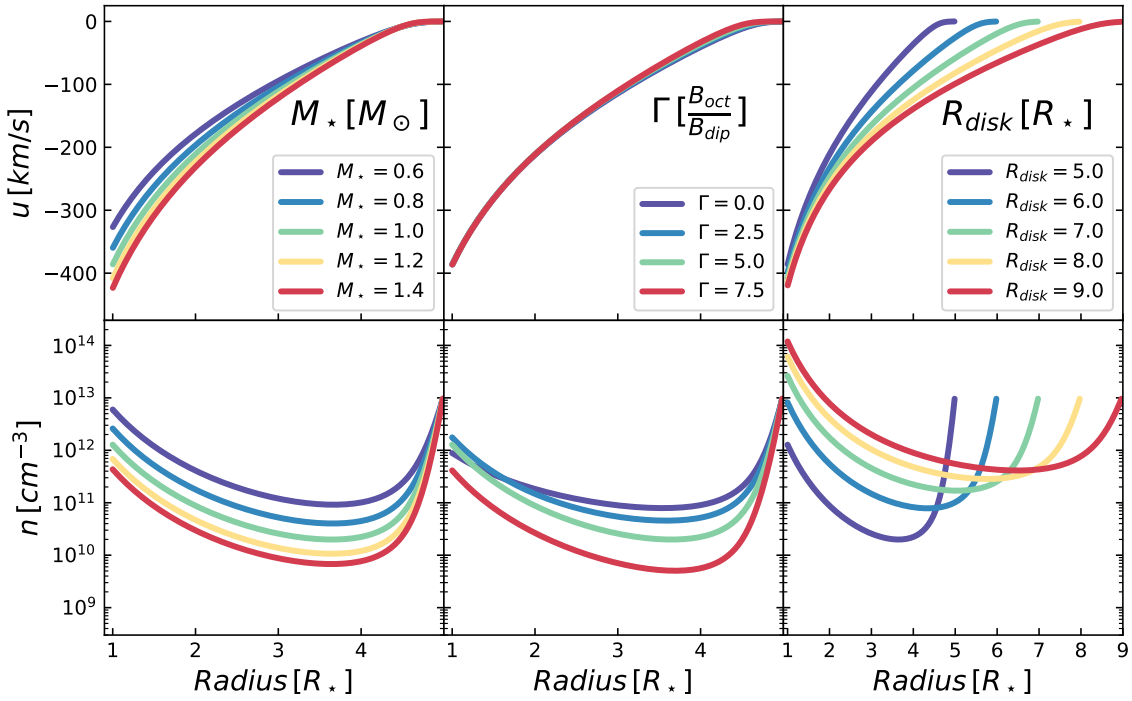

Fig. 5.6: Steady-state solutions for the different values of $M_\star$, Γ, and R_{disk} from the set of models discussed in §5.3.3. For the set of parameters I have explored, changes in the kinetic energy flux, F, are primarily caused by differences in the density near the star rather than the velocity.

trend of an increasing i leading to decreasing Q holds true for all of the models. This is demonstrated in Fig. 5.8. I also find that increasing the inclination tends to lead to light curves that appear more burst dominated. Note that the breaking of symmetry around the mean of the visible area of the hot spot is not responsible for this effect, as it only occurs at very large inclinations, ($i \geq 70°$, see Fig. 5.2).

Stellar Mass, $M_\star$

At a fixed age, increasing the stellar mass also increases the effective temperature and the radius of the star. This changes the depth of the potential well, which changes the flow structure along the accretion column. Under the unitless approach I have taken in the 1D HD simulations, the depth of the potential well is parameterized

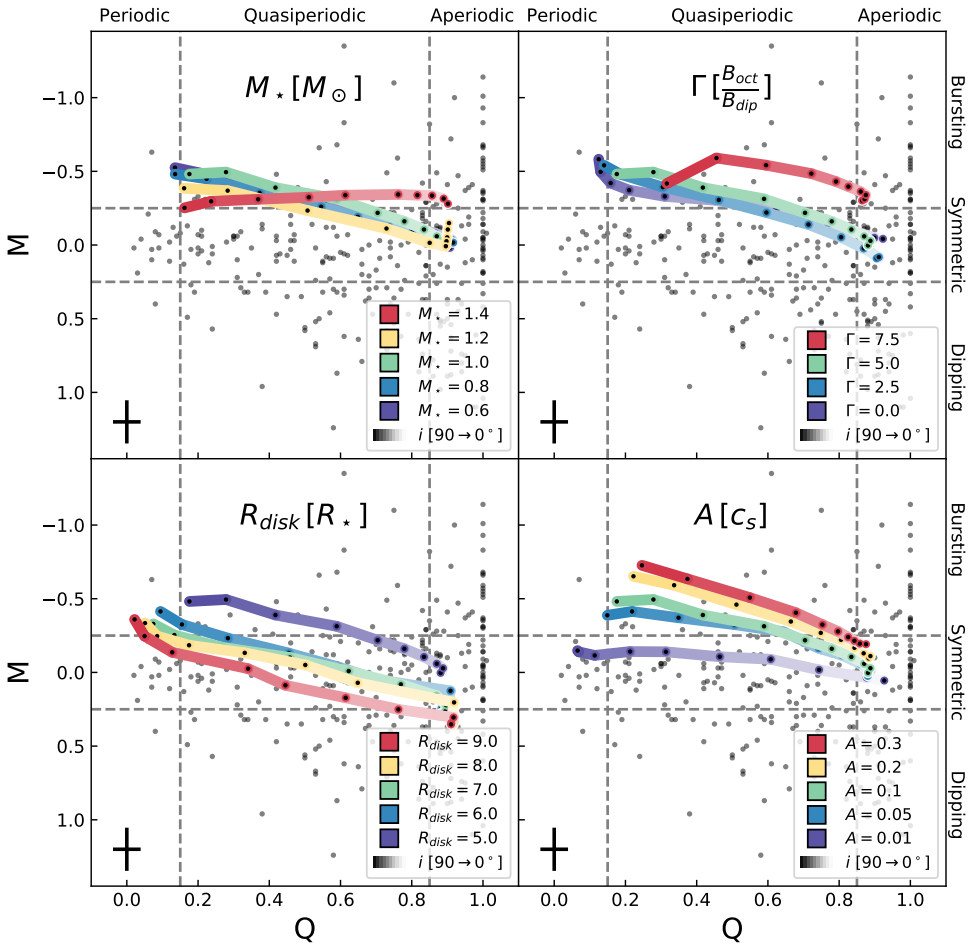

Fig. 5.7: Bivariate plots of metrics Q and M that describe the degree of periodicity and symmetry of the light curves for different parameters. Here, variants on $M_\star$, Γ, R_{disk}, and A are shown from a base model of $M_\star = 1.0\,\mathrm{M}_\odot$, $\Gamma = 5.0$, $R_{disk} = 5.0$ and $A = 0.1$. Individual model realizations are shown as black points along the colored lines. The inclination, i, is shown by the darkness of the lines. The dashed grey lines mark the boundaries between variability classes listed on the top and right axes. An estimate of the model uncertainty is shown by the symbol in the lower left (see §5.3.2). Q and M values from K2 light curves from Cody & Hillenbrand (2018) are shown as gray points.

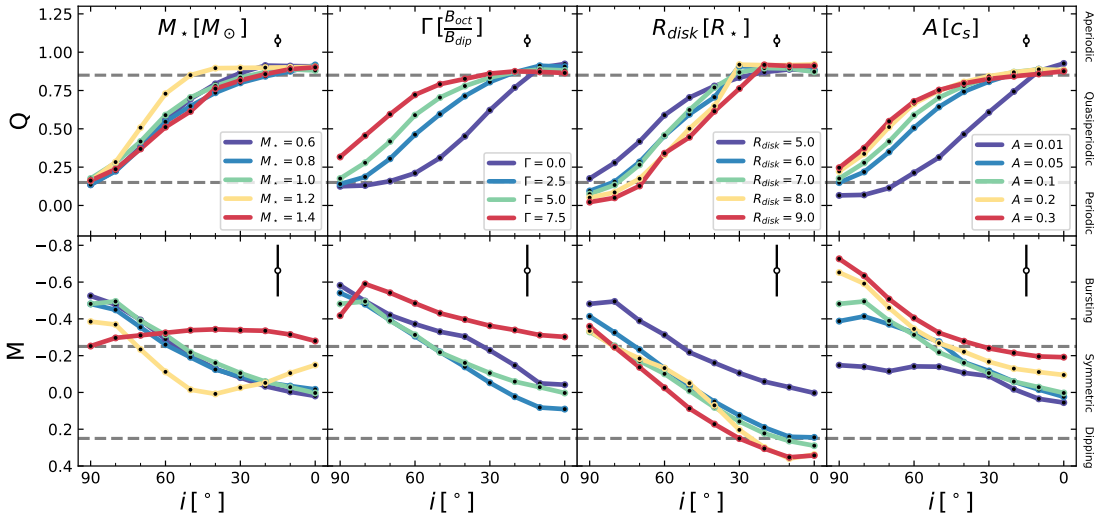

Fig. 5.8: Q and M values as functions of the inclination. Each vertical pair of panels shows model variants of $M_\star$, Γ, R_{disk}, and A. Individual model realizations are shown by the black points. An estimate of the uncertainty is shown in the upper right which was derived by changing the seed value of the turbulent driving function for the base model. The dashed grey lines mark the boundaries between the variability classes listed on the far right axis.

by the single dimensionless quantity $b \equiv \frac{GM_\star}{R_\star c_s^2}$. The effect on b from changing $M_\star$ depends on the age of the star because the radius is set using stellar isochrones (Choi et al., 2016; Dotter, 2016). At an age of 2 Myr, as $M_\star$ increases, b also increases. Here, I have explored values of $M_\star = 0.6$, 0.8, 1.0, 1.2, and $1.4\,\mathrm{M}_\odot$, which results in $b = 511$, 618, 711, 794, and 855.

The first-order effect of increasing b on the flow structure is an increase in the steady-state Mach number of the flow at the stellar surface due to the deeper potential well. However, under the assumption that the magnetospheric truncation radius is colocated with the corotation radius, changing the stellar mass also affects rotation. The effect of this on the simulations is parameterized with a dimensionless rotation parameter $\omega \equiv \left(\frac{\Omega R_\star}{c_s}\right)^2$, where Ω is the rotation rate of the star. Under

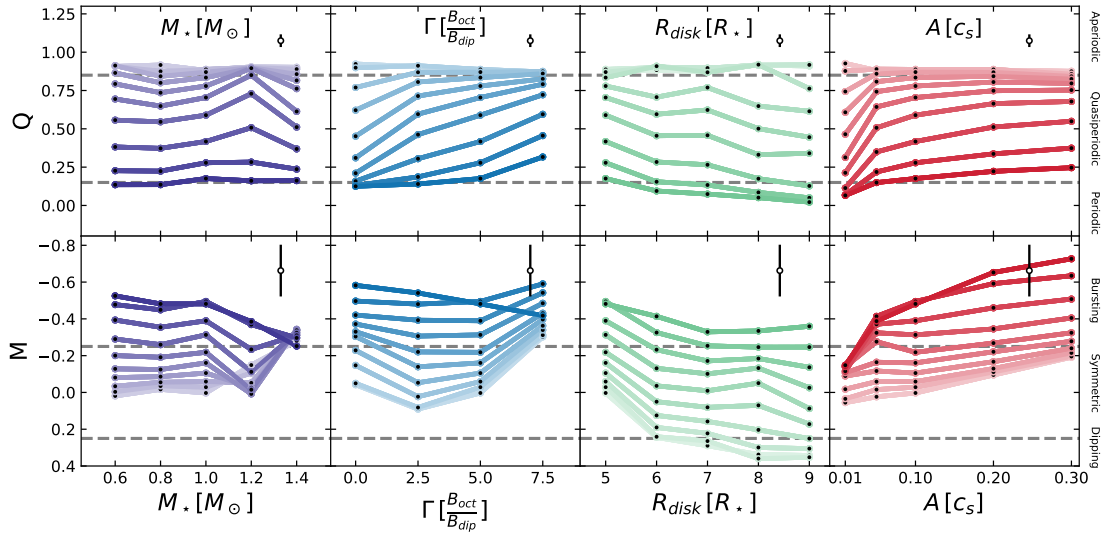

Fig. 5.9: Q and M values as functions of $M_\star$, Γ, R_{disk}, and A. Individual model realizations are shown by the black points. Darker colors represent models with higher inclinations, with values evenly sampled between 0 and 90°. Estimates of the model uncertainties on Q and M are shown by the marker in the upper right corner of each panel. The dashed grey lines mark the boundaries between the variability classes listed on the far right axis.

these assumptions, this can be written as $\omega = \frac{bR_\star^3}{R_{disk}^3}$. While increasing $M_\star$ creates a stronger outward centrifugal force in the non-inertial frame, ultimately the effect of increasing gravity is stronger, and the Mach number of the flow increases along the column with increasing $M_\star$. Changing the rotation rate via $M_\star$ in part also controls spot modulation since it sets the rotation period of the star under the constraint of corotation. The coordinate system that is used to describe the system is independent of b, so changing $M_\star$ does not affect the degree of compression by the magnetic field nor does it change γ (the latitude of the hot spot).

I find that linear relationships between both Q and M and $M_\star$ are not readily apparent. This is shown in Fig. 5.9. At $M_\star = 1.4\,\mathrm{M}_\odot$, I find that the model lies near the boundary between bursting and symmetric as measured by M for all inclinations,

which is in contrast to most of the other models which generally show decreasing M with increasing i. The Q metric shows a small peak for the $M_\star = 1.2\,\mathrm{M}_\odot$ model at moderate inclinations, but returns to the typical value at $M_\star = 1.4\,\mathrm{M}_\odot$. As $M_\star$ increases, the density near the star decreases (see Fig. 5.6). Interestingly, this leads to a column with a lower kinetic energy flux, since the increased speed of the flow from the larger gravitational potential does not offset the decreased density. This result matches the analytic results presented by Adams & Gregory (2012).

Magnetic Field Configuration, Γ

The ratio between the dipole and octupole components, Γ, sets the overarching magnetic field structure of the model. The scale factors of the curvilinear coordinate system set the effective cross-sectional area of the accretion column as a function of radius. These scale factors are a function of Γ, and as Γ increases, the flow becomes more constricted near the star (see Robinson et al., 2017, for more discussion regarding scale factors). Changing Γ also changes the shape of the accretion column, which affects components of force vectors along the magnetic field line ($\hat{x} \cdot \hat{p}$ term in the centrifugal force and $\hat{r} \cdot \hat{p}$ term in the gravitational force term). As shown by Fig. 5.1, increasing Γ also decreases γ.

Here, I explore variants with $\Gamma = 0$, 2.5, 5.0, and 7.5. As Γ increases, the steady-state velocity distribution remains relatively unchanged and the density across most of the column decreases (see Fig. 5.6). However, near the star, the relation between density and Γ is no longer monotonic, and I find a peak around $\Gamma = 2.5$. After implementing the turbulent boundary conditions, I find a maximum in the M metric near $\Gamma = 2.5$. For values of Γ greater than this, I find that as Γ increases, M decreases, and the light curve appears more dominated by accretion bursts. The pure dipole case shows a more negative value of M than both the $\Gamma = 2.5$ and 5.0 cases. In the case of $\Gamma = 7.5$, I find that all models appear as bursters. The slight

increase in the M parameter shown by the $\Gamma = 5.0$ and 7.5 models at $i = 90°$ in Figs. 5.8 and 5.9 is caused by the combination of the low-density accretion columns and small projected area of the hot spot. This leads the variability generated by accretion to be comparable to the symmetric $\sigma = 0.5\%$ uncertainty that was injected into the light curves. As expected, based on the relationship between Γ and γ, objects appear more aperiodic as Γ increases as measured by the Q metric (see the the top panel of Fig. 5.9).

Inner Disk Radius, R_{disk}

The models are constructed under the assumption that the accretion column follows a single magnetic field line that connects the star to the corotation point in the disk. As such, the choice of R_{disk} influences both the rotation rate of the star and which magnetic field line is traced (see Fig. 5.1). As a consequence, γ monotonically decreases with R_{disk}. Here, I have explored inner disk radii of $R_{disk} = 5.0$, 6.0, 7.0, 8.0, and 9.0 $R_\star$. For these values of R_{disk}, $\gamma = 9.2$, 8.6, 8.1, 7.7, and 7.3°, respectively.

Changing the inner disk has large consequences on the density distribution along the column in the steady-state solution (see Fig. 5.6). The density at the stellar surface spans a full two orders of magnitude between $R_{disk} = 5.0R_\star$ and $R_{disk} = 10.0R_\star$. This is in part because of the decreased effective area of the accretion column near the star in the $R_{disk} = 10.0R_\star$ case due to the associated curvilinear scale factors. However, the additional compression in the larger inner disk radius case is only a factor of about 5, which implies that the model is less restrictive to additional mass entering the simulation through the outer boundary as R_{disk} increases.

As the inner disk radius increases, the models tend to be slightly more periodic. This is counter to what the changes in γ would suggest, but the changes in γ are relatively small (e.g., compared to the changes in γ from changing Γ). I found that

models with small values of R_{disk} showed much stronger bursting behavior for all inclinations.

Turbulent Amplitude, A

The turbulent driving function introduces gradients in velocity and density structure near the disk. These gradients lead to the formation of traveling shocks along the accretion column (see Robinson et al., 2017, or Chapter 2). The turbulent amplitude, A, is the Mach number of the rms velocities of these perturbations at the boundary. Under a Shakura & Sunyaev (1973) α-disk prescription, turbulent perturbations scale as $A = \sqrt{\alpha}$. This α, not to be confused with the spot size, is a dimensionless parameterization of turbulent viscosity. Typical values of α from modeling protoplanetary disks are on the order of 0.01 with some amount of scatter (e.g., Hartmann et al., 1998; Andrews et al., 2009). Motivated by this, I tested model variants with values of A = 0.01, 0.05, 0.10, 0.20, and 0.30, but caution that α is generally inferred much further out in the disk than the region that I am simulating. Recall that the random number seed used to generate the turbulent driving function is fixed across all model variants.

As A increases, I find that models monotonically appear more aperiodic, as described by the Q metric. Likewise, as A increases, I find that the objects are more dominated by bursts (i.e., M decreases). I find that increasing A also increases the amount of material entering the simulation available for accretion (see Fig. 5.10), which may lead to the some of the scatter in the measured Q and M values. Additionally, larger values of A lead to steeper gradients in the outer disk, which aid the formation of the travelling shocks.

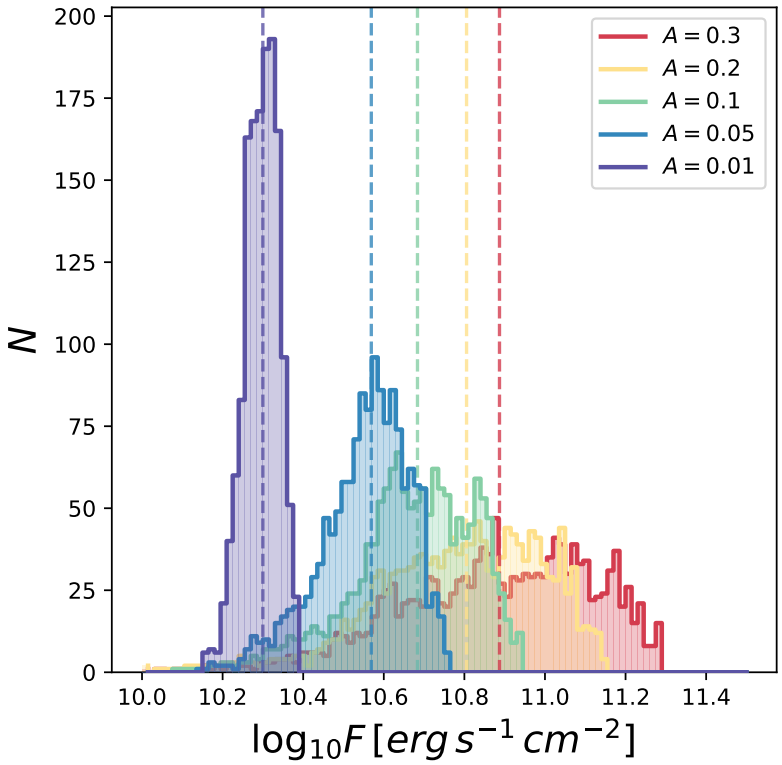

Fig. 5.10: Histograms showing kinematic energy flux, F, at the surface of the star for each time step for different values of turbulent driving amplitude, A. The changes in the median value of F (shown by the dashed lines) are nearly entirely due to increased density, as the median velocity at the star changed very little between different values of A.

5.4 Discussion

I have connected a simple 1D HD simulation of the accretion column (first presented in Robinson et al., 2017) to the accretion shock models of Robinson & Espaillat (2019) and introduced rotational modulation by modeling accretion hot spots as spherical caps. The output from these simulations was studied using the same tools that have been applied to recent photometric monitoring surveys of accreting young stars in nearby low-mass star-forming regions. Here, I place the results from my simulations in context with these campaigns and discuss implications on variabil-

ity classifications for different parameters. I also consider two additional complexities that could be explored more in the future: non-rotation axis-aligned fields and multiple accretion columns.

5.4.1 Implications for Variability Classes

Within this work, I have included only mechanisms that can result in variability caused by changes in the mass accretion rate and rotational effects, so I focus on objects with burster, purely periodic symmetric, quasiperiodic symmetric, and purely stochastic classes. Several of the other classes (quasiperiodic dipper, aperiodic dipper, and eclipsing binary) likely rely on the presence of occulting bodies (Cody et al., 2014). Because I do not include any such bodies in my analysis, discussion of these types of objects in general is not included here. Likewise, the choice of the boundary condition and fixed parameters likely exclude objects that would be classified as long-timescale, unclassifiable, and nonvariable.

Under the constraints imposed by this model, I found that inclination plays a large role in determining the periodic behavior of the star, as quantified by Q. Under the parameters that I explored, I found that typically only objects with low inclinations ($i \leq 30°$) would be classified as purely stochastic objects. Objects with intermediate inclinations ($30° < i < 80°$) tend to fall into the quasiperiodic symmetric classification. Finally, objects that have the highest inclinations ($i \geq 80°$) tend to fall into the category of purely periodic. However, while i is the primary parameter that determines Q, the inclination at which the model appears as periodic, quasiperiodic, or aperiodic depends strongly on the other parameters considered here (see Fig. 5.8). For example, the model variant with $\Gamma = 7.5$ is on the border of being classified as stochastic up to an inclination of roughly 50°. Therefore, inclination is likely not the only driver when determining periodic variability class.

I found that the magnetic field geometry (parameterized by Γ and R_{disk}) and the amplitude of the turbulent driving function all had a large impact on M, while $M_\star$ did not. I found that models with small R_{disk} or large Γ both exhibit bursting behavior with relatively low accretion column densities near the star (see Fig. 5.6). In contrast, models with large values of A also show bursts with increasing column density (Fig. 5.10). Contemporaneous NUV - NIR spectra can be used to break degeneracies between accretion column density and surface coverage (e.g., Ingleby et al., 2013, 2015; Robinson & Espaillat, 2019), and the magnetic field can be directly probed with spectropolarimetric observations, (e.g., Donati et al., 2010a). Combined, these techniques may be able to distinguish between these scenarios. With regards to $M_\star$, Cody & Hillenbrand (2018) did not find an obvious relationship between variability classification and $M_\star$, using K2 observations and spectral types as proxies for stellar masses. This is in agreement with the non-monotonic relationship I found between $M_\star$ and M.

While the range of models that I explored does not cover all of parameter space, basic generalizations can be speculated about variability class populations given that the selection of base model parameters are somewhat representative of a typical CTTS. I found that most of my models fell into the QPS classification, suggesting that these types of light curves might be common. This is in agreement with previous photometric monitoring campaigns that also showed the largest fraction of stars in the QPS class ($17 \pm 3\%$ to $29 \pm 3\%$ from observations, depending on the region; Cody & Hillenbrand, 2018). I also find that under the range of parameters that I explored, this model can produce light curves that fall into all of the classifications associated with changes in the mass accretion rate. At the very least, this suggests that the some of the observed variability could feasibly be driven by Kolmogorav-style turbulence in the inner disk. However, I caution further conjecture at this point regarding the

entire population because the variability classification of the model variants strongly depend on the base model parameters. Additionally, observational biases that affect studies of variability in young stars are not considered here (e.g., the star is unlikely to be observable at high inclinations due to disk obscuration). These models also lack the ability to reproduce fluid instabilities that 3D simulations can reveal.

5.4.2 Non-aligned Magnetic Field Structure

One of the largest assumptions in the model is the presence of a perfectly rotation-axis aligned magnetic field that can be described using a multipole decomposition. Zeeman-Doppler imaging of the magnetic field structure of young stars has shown that the magnetic fields are not necessarily perfectly aligned with the rotation axis (Kenyon et al., 1994; Johns & Basri, 1995b; Bouvier et al., 1999; Donati et al., 2010c). This misalignment, along with any possible toroidal components, causes the accretion hot spot geometry to become significantly more complex.

We can begin to consider the effects that such a misaligned field might have on the simulations. If deviations from a purely rotation-axis–aligned magnetic field are included, the easiest effect to consider without detailed HD simulations is the change in γ. Models with larger values of γ tend to be more periodic since the effect of rotational modulation of the light curve is enhanced. With the introduction of a misalignment, the magnetic field connecting the disk to the star becomes a function of ϕ in the co-rotating frame. If magnetic field lines further from the axis of rotation are favored for mass loading because the gravitational force vector is more closely aligned with the magnetic field line at the magnetic footprint at the inner edge of the disk (predicted by 3D MHD simulations, e.g., Romanova et al., 2003, 2004), then misalignments would tend to increase the periodicity of the observed light curve. However, as demonstrated in this work, changing the magnetic field geometry can

drastically change the flow along the accretion column, thus making more detailed modeling required for more concrete predictions.

5.4.3 Multiple Columns

The mass deposited onto the star in these models is uniformly spread across a single hot spot. Modeling of NUV spectra, which can break the degeneracy in Fig. 5.5, has shown that multiple accretion column densities are typically necessary to fully reproduce observations within single observations (Ingleby et al., 2013, 2015; Robinson & Espaillat, 2019). This suggests either that multiple accretion columns exist with different densities and/or that gradients occur across the accretion columns. Adding more accretion columns introduces several new free parameters that were not necessary to consider in the single column case.

Using two of the base model realizations (see §5.3.2), I performed exploratory tests to examine the effect of adding a second non-overlapping column. The phase offset and the ratio between spot areas was varied while the total area covered is fixed to be the same as a single spot with $\alpha = 10°$. I also fix $i = 60°$ for simplicity. Q and M were then measured for each phase-ratio pair. I explored five spot ratios cases: $5:1$, $3:1$, $1:1$, $1:3$ and $1:5$ and five evenly sampled phase offsets between $120°$ and $240°$ for each ratio. I find limited impact on Q and M between different phase offsets of the spots. The mean standard deviation for Q and M when fixing the spot size ratio and varying the phase offset was 0.03 and 0.04, respectively. Changing the ratio of spot sizes has a larger effect on Q and M. The mean standard deviation of Q and M between models with a fixed phase offset and a varied spot ratio is 0.10 and 0.17, respectively. The mean Q and M values for the two column realizations were 0.77, and -0.32, which is similar to the the two single column models with values of 0.60 and 0.75 for Q and -0.31 and -0.33 for M. However, trends between the spot ratio and the change in Q and M are not easily identified. Even light

curves of conjugate pairs of spot size ratios (e.g., 3 : 1 and 1 : 3) with the same phase offset can appear remarkably different. This reflects the dependence on the stochastic nature of the chosen driving functions and the spread in the metrics is similar to that calculated between single column models with different random seeds §5.3.2. Ultimately, adding additional columns tends to act as a contributing source of uncertainty that has not been considered in the single column analysis presented in this work and merits further exploration.

5.5 Summary

I created synthetic light curves of accreting pre-main-sequence stars using a set of 1D HD simulations of the magnetosphere that are coupled with an nLTE accretion shock model and a simple model for rotational modulation. The models were constructed under the assumption of a dipole or a dipole + octupole rotation-axis-aligned magnetic field. Perturbations were introduced to steady-state flow solutions using boundary conditions that aimed to mimic turbulence in the inner disk. Specifically, I tested the effect of the stellar mass, inclination, magnetic field geometry, the inner disk radius, and the level of turbulence in the inner disk.

I then used the previously developed metrics Q and M to measure the light curve periodicity and symmetry around the mean, respectively, in order to facilitate comparisons between the model variants and the results from month-long photometric monitoring campaigns of young stars. (see Cody et al., 2014; Cody & Hillenbrand, 2018). I focused on variability classes that can, in part, be explained by changes in the mass accretion rate. These classes include bursters, purely periodic symmetric, quasiperiodic symmetric, and purely stochastic classes. I found that Kolmogorav turbulence in the inner disk can drive a wide degree of variability behavior associated with these classes. My major findings are summarized as follows.

1. Clear monotonic trends between $M_\star$ and the Q and M metrics are difficult to identify, which is in agreement with previous observations of CTTS. This suggests that accretion variability class is not dependent on stellar mass.

2. I found that the periodic behavior of the light curve as measured by Q is primarily controlled by the inclination, i. Typically, I find that objects with $i \leq 30^\circ$ appear as purely stochastic, $30^\circ < i < 80^\circ$ as quasiperiodic, and $i \geq 80^\circ$ as purely periodic. However, the value of i where the object appears periodic, quasiperiodic, or aperiodic depends to some degree on the magnetic field geometry, the inner disk radius, and the level of turbulence in the inner disk.

3. I found that the symmetric behavior of the light curve as measured by M is also a function of the inclination, magnetic field composition, inner disk radius, and turbulent amplitude. Objects with either a pure dipole field, large octupole components, or a small truncation radius tend to exhibit more burst-dominated behavior. Increasing the amplitude of the turbulent perturbations also led to more bursts.

4. These models suggest that it may be possible to separate driving parameters behind variability observed in light curves using NUV spectra to measure the kinetic energy flux of the accretion flow and spectropolarimetric measurements of the magnetic field.

5. Complexities such as multiple columns and non-axis aligned magnetic fields can modify the measured Q and M parameters. I suggest that a non-axis aligned field may lead to more periodic light curves. The initial tests find that when additional columns are included, Q remains similar to the single column model

while M varies widely as a function of the ratio between spot sizes, but note that more work is necessary to make further predictions.

6. I suggest a slight adjustment to the algorithm for measuring rotation periods when measuring Q. I found that weighting the Lomb-Scargle periodogram with a Gaussian whose parameters are derived from the ACF gave a more accurate estimate than previous methods for the synthetic light curves (whose true period is known a priori).

More continuous light curves of well-studied CTTS will become available from *TESS* in the upcoming years. This work attempts to establish the groundwork for characterization of those objects with a relatively simple approach.

6

Summary

6.1 Goals and Questions

The goal of this dissertation was to investigate drivers of accretion variability and the structure of the inner disk. To accomplish this, I used simulations, observations, and models of the inner disk, with a focus on the emission arising from the accretion column at the stellar surface. In particular, I address the following three questions raised in Chapter 1:

1. *Is the accretion column connecting the disk to the star inherently unstable?*
2. *What are the observable accretion signatures of variability driven by the inner disk?*
3. *Is the material in the inner disk clumpy or homogenous?*

6.2 Scientific Results

Below, I outline how the results from Chapters 2, 3, 4, and 5 begin to address these questions.

6.2.1 Is the accretion column connecting the disk to the star inherently unstable?

I address this question in Chapters 2 and 4 using simulations and observations. These chapters address different facets of this question.

Chapter 2 describes simulations that I used to test the prediction from Adams & Gregory (2012) that the large-scale magnetospheric accretion structure may spontaneously give rise to hydrodynamic instabilities. I found that under reasonable physical parameters, no spontaneous variability was generated, suggesting that the accretion column is inherently stable under the assumptions of my model.

In Chapter 4, I searched for variability on minute-timescales using continuous wavelet transforms of short-cadence *TESS* observations of 14 objects in the Taurus star-forming region. If detected, such variability would provide observational support of a predicted thermal instability near the accretion shock that has eluded several previous attempts to observe it. I identified significant regions of quasi-periodicity in the *TESS* light curves with timescales reminiscent of those predicted for the thermal instability. These events occurred almost exclusively near local maxima in the light curves, which may explain some of the previous difficulties in identifying this variability.

6.2.2 What are the observable accretion signatures of variability driven by the inner disk?

I address this question within Chapters 2, 3, 4, and 5. Chapter 5 is the most focused on answering this question.

By introducing time-variable boundary conditions that mimic turbulence in the inner disk to the simulations in Chapter 2, I found that traveling shocks form within the accretion column. These shocks collide with the star, causing sudden increases in the accretion rate followed by slower declines. These changes are qualitatively similar to the observed variability in the Burster classification.

In Chapter 3, I develop an updated version of the Calvet & Gullbring (1998) accretion shock models to produce more accurate measurements of the accretion excess. I also provide updated relations between $\dot{M}$ and U- and u'-band excess.

Correlations between FUV, NUV, and optical emission lines and $\dot{M}$ are presented, with the strongest correlation involving several of the NUV emission lines. I also developed a new approach when using these models to self-consistently include the stellar photosphere and incorporate prior knowledge through a Bayesian statistical framework.

In Chapter 4, I find a positive correlation between variability in *TESS* light curves, which are widely available for many TTS, and simultaneous ground- and space-based observations of accretion in TTS. I also find weak, positive correlations down to the shortest possible timescale for the *TESS* light curves by breaking the NUV *HST* STIS observations into simultaneous sub-exposures.

Motivated by the results of Chapter 2, I describe a coupled model in Chapter 5 formed through the combination of simulations of the accretion column, described in Chapter 2; the accretion shock model of Chapter 3; and a treatment of rotational modulation of hot spots. This model produces synthetic light curves that can reproduce many to most of the empirical variability classifications from Cody et al. (2014) associated with changes in the mass accretion rate. I found that the type of variability produced by these models is a function of the magnetic field geometry, the stellar mass, the inclination, and the strength of the turbulent perturbations in the inner disk.

6.2.3 Is the material in the inner disk clumpy or homogenous?

This question is primarily addressed by Chapter 3, where I use accretion shock models to measure the mass accretion rate and distribution of accretion columns on the surface of the star as a function of time through multiple epochs of *HST* STIS FUV-NIR spectra. I find that on week-timescales, variability in $\dot{M}$ of 10% is common and that the distribution of accretion columns with different densities can change significantly. In particular, the CTTS GM Aur displayed a rapid rise and

fall of the mass accretion rate by a factor of 4 on week timescales with drastically increased high-density accretion column filling factors, which indicates a clumpy inner disk. Additionally, one of the *HST* observations of VW Cha showed dimming in the optical/NIR, while the UV emission remained unchanged. I interpret events such as this as the partial occultation by a highly-collimated dusty accretion column. Such an occultation suggests that dust may be able to survive in the inner disk.

Through the *TESS* light curves presented in Chapter 4, I measured empirical variability classifications. Like previous studies of accretion variability (e.g., Herbst et al., 1994; Cody et al., 2014), I found a range of accretion-powered behavior. Several TTS exhibit rapid bursts in their accretion rates, suggesting inhomogeneities in their inner disks. Other TTS contrastingly show smoothly varying periodic light curves. This raises the question of why some objects appear to be more homogenous in the inner disk than others. I begin to address this question with the models presented in Chapter 5.

6.3 Concluding Remarks

Accretion variability provides a lens to study the traditionally unresolvable inner disk and processes that power the transport of mass and angular momentum. Continuous, high-cadence monitoring by observatories like *TESS* alongside simultaneous multi-wavelength observations and the development of more advanced models will continue to help answer new questions about accretion and the drivers of accretion variability. Through the study of accretion onto TTS, we can form a clearer picture of the beginnings of our solar system.

List of Journal Abbreviations

Abbreviation	Full Name
ARA&A	Annual Review of Astronomy and Astrophysics
AJ	Astronomical Journal
A&A	Astronomy and Astrophysics
ApJ	Astrophysical Journal
ApJL	Astrophysical Journal, Letters
ApJS	Astrophysical Journal, Supplement
Ap&SS	Astrophysics and Space Science
MNRAS	Monthly Notices of the Royal Astronomical Society
PASP	Publications of the Astronomical Society of the Pacific

7

Appendix

7.1 Numerical Details for the HD Simulations of the Accretion Column

Included here are details and tests associated with the simulations presented in Chapter 2.

7.1.1 Finite-Difference Equations

In this section, I describe the finite-difference scheme used to solve the system of hydrodynamic equations and discuss the associated scale factors and ancillary functions. The majority of the difference equations and their implementation were detailed in Owen & Adams (2016); here I detail the changes that have been made to include the magnetospheric accretion geometry and the energy equation. Variables are subscripted with the location on the grid (i.e. $i-1$). Time-dependant variables (u, α, ϵ, and P) are superscribed with the time step (i.e., $n+1$). Time independent variables are superscribed with a or b, depending on if the variable is face-centered or zone-centered, respectively (see also Stone & Norman, 1992). Recall in this staggered scheme, α and ϵ (and thus P) are zone-centered, while u is face-centered (e.g, Stone & Norman, 1992; Owen & Adams, 2016).

During the source step, the velocity is updated due to forces from pressure, gravity, rotation, and viscosity. The velocity is first updated using the following finite-differenced version of the momentum equation:

$$u_i^{n+1} = u_i^n - \frac{\Delta t}{h_{p,i}^a}\frac{2}{(\alpha_i^n + \alpha_{i+1}^n)}\left(\frac{P_i^n - P_{i+1}^n}{p_i^b - p_{i+1}^b}\right)$$
$$-\frac{\Delta t}{h_{p,i}^a}\left(\frac{b}{(\xi_i^a)^2}\right)\left((\xi_i^a)^{-5}\frac{f_i^a\cos\theta_i^a}{H}\right) + \omega\Delta t\xi_i^a\sin\theta_i^a(\hat{x}\cdot\hat{p}_i^a). \tag{7.1}$$

where ω is a dimensionless parameter that measures rotation,

$$\omega = \left(\frac{\Omega R_*}{a_1}\right)^2. \tag{7.2}$$

The component of x along the field line, $\hat{x}\cdot\hat{p}$, can be written as a function of ξ, θ, and the ancillary functions f, g, and H:

$$\hat{x}\cdot\hat{p} = \frac{\xi^{-5}\sin\theta\cos\theta(f+g)}{\sqrt{H}} \tag{7.3}$$

where

$$f \equiv \Gamma(5\cos^2\theta - 3) + 2\xi^2$$
$$g \equiv \frac{3}{4}\Gamma(5\cos^2\theta - 1) + \xi^2 \tag{7.4}$$

. The ancillary functions, f and g, recur often when using these coordinates and can be used in both the pure dipole case ($\Gamma = 0$) and the octupole plus dipole case. These functions can be combined to write $|\nabla p|^2$, defined as H:

$$H \equiv |\nabla p|^2 = \xi^{-10}[f^2\cos^2(\theta) + g^2\sin^2(\theta)]. \tag{7.5}$$

The functional forms of the scale factors for p, q and ϕ can be written as

$$h_p = \xi^5[f^2\cos^2\theta + g^2\sin^2\theta]^{-1/2} \tag{7.6}$$

$$h_q = \frac{\xi^4}{\sin\theta}[f^2\cos^2\theta + g^2\sin^2\theta]^{-1/2} \tag{7.7}$$

$$h_\phi = \xi\sin\theta \tag{7.8}$$

Derivatives of these scale factors for both the face-centered and zone-centered grids were computed by finite differencing using the following expressions:

$$\begin{aligned} \frac{\partial h^a_{x,i}}{\partial p} &= \frac{h^b_{x,i} - h^b_{x,i-1}}{p^b_i - p^b_{i-1}} \\ \frac{\partial h^b_{x,i}}{\partial p} &= \frac{h^a_{x,i} - h^a_{x,i-1}}{p^a_i - p^a_{i-1}}. \end{aligned} \tag{7.9}$$

Owen & Adams (2016) showed, at sufficient resolution, the derivatives of the scale factors found by finite differencing are accurate enough for these geometric constructions for use in these simulations. This is useful since analytically o btaining these derivatives can be cumbersome.

The velocity and internal energy are then updated using an artificial viscosity tensor. More discussion on this tensor and the velocity update itself are included in Appendix A of Owen & Adams (2016). The source step is finished with the addition of the compressional heating update for the internal energy, performed using the explicit finite-difference expression shown in Stone & Norman (1992). Finally, the transport step, which solves for changes in the time-dependant variables due to fluid advection, follows the finite-difference equations described in Stone & Norman (1992).

7.1.2 Analytic vs. Simulation Comparison

In order to be sure the numerical method is working as expected, one can compare my solution to an analytic solution that exists for isothermal accretion. A relatively simple solution for the velocity structure of the accretion column for the case of isothermal flow along dipole magnetic field geometry can be obtained using the procedure of Adams & Gregory (2012). Following Adams & Gregory (2012), an analytic solution for the velocity u in the isothermal case can be written as

$$u^2 = -W[-\lambda^2 (q\xi)^{-6}(4 - 3q\xi)\exp(-2\varepsilon - \frac{2b}{\xi} - \omega q\xi^3)] \tag{7.10}$$

where W is the Lambert W special function (see also Cranmer, 2004), ξ is the dimensionless radius, b is the dimensionless depth of the potential well, and ε is an integration constant written as

$$\varepsilon = \frac{1}{2}\lambda^2 - \frac{3}{2}bq. \tag{7.11}$$

I note the Lambert W function has two real branches, the '0' branch corresponds to subsonic flow and the '-1' branch to supersonic flow. This solution for the velocity assumes the location where the field line intercepts the disk is the co-rotation radius such that $\omega = bq^3$. The integration constant λ can be written in the transcendental form

$$\ln\lambda - \frac{\lambda^2}{2} = 3\ln q\xi_s - \frac{1}{2}\ln\left(4 - 3q\xi_s\right) - \frac{1}{2} + b(-\frac{3}{2}q + \frac{1}{\xi_s} + \frac{1}{2}q^4\xi_s^3), \tag{7.12}$$

where ξ_s is the sonic point radii. Using the Lambert W function, the solution for λ takes the form

$$\lambda^2 = -W\Big[-\exp\big(-6\ln q\xi_s - \ln(4 - 3q\xi_s) - 1 + b(3q + \frac{2}{\xi_s} + q^4\xi_s)\big)\Big], \tag{7.13}$$

where the sonic point ξ_s is calculated using a numeric solution to the matching condition for the sonic point. The matching conditions is written as

$$3\xi_s(\frac{8 - 5q\xi_s}{4 - 3q\xi_s}) + 3\omega q\xi_s^4 = 2b. \tag{7.14}$$

An isothermal dipole simulation with $b = 250$, a disk radius of $\xi_{\rm d} = 10$ and 1024 cells was run using a constant density outer boundary condition and outflow inner boundary conditions. For this value of b, the sonic point is at a radius of 8.71 stellar radii. The excellent agreement of the analytic solution and the simulation result can be seen in Figure 7.1.

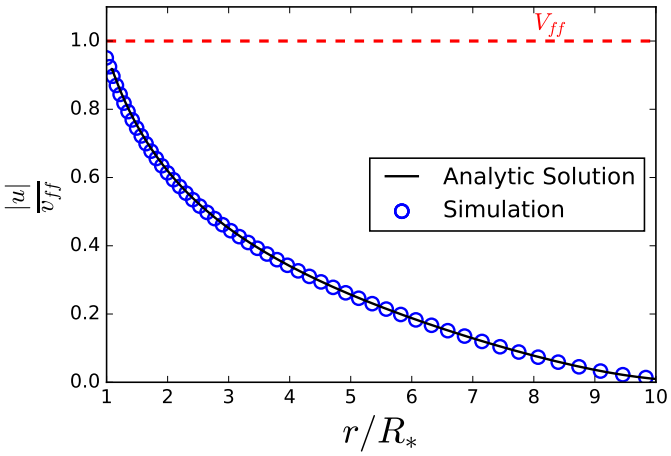

Fig. 7.1: Analytic solution for the case of isothermal transonic accretion compared with the result from the simulation. The simulation result converges to this analytic solution, ensuring the simulation is returning physical results. Median deviations from the analytic solution are on the order of 0.7%. The true resolution of the simulation is 20 times finer than indicated by the number of open circles.

References

1997, ESA Special Publication, Vol. 1200, The HIPPARCOS and TYCHO catalogues. Astrometric and photometric star catalogues derived from the ESA HIPPARCOS Space Astrometry Mission

Adams, F. C., & Gregory, S. G. 2012, ApJ, 744, 55

Alencar, S. H. P., Basri, G., Hartmann, L., & Calvet, N. 2005, A&A, 440, 595

Alencar, S. H. P., Teixeira, P. S., Guimarães, M. M., et al. 2010, A&A, 519, A88

Ambartsumian, V. A. 1947, The evolution of stars and astrophysics

—. 1949, AZh, 26, 3

—. 1952, Teoreticheskaia astrofizika.

Ambartsumian, V. A. 1954, in Liege International Astrophysical Colloquia, Vol. 5, Liege International Astrophysical Colloquia, 293

Andre, P., Ward-Thompson, D., & Barsony, M. 1993, ApJ, 406, 122

Andrews, S. M., Rosenfeld, K. A., Kraus, A. L., & Wilner, D. J. 2013, ApJ, 771, 129

Andrews, S. M., Terrell, M., Tripathi, A., et al. 2018, ApJ, 865, 157

Andrews, S. M., Wilner, D. J., Espaillat, C., et al. 2011, ApJ, 732, 42

Andrews, S. M., Wilner, D. J., Hughes, A. M., Qi, C., & Dullemond, C. P. 2009, ApJ, 700, 1502

Andrews, S. M., Wilner, D. J., Zhu, Z., et al. 2016, ApJ, 820, L40

Ardila, D. R., Herczeg, G. J., Gregory, S. G., et al. 2013, ApJS, 207, 1

Armitage, P. J. 2019, Saas-Fee Advanced Course, 45, 1

Astropy Collaboration, Price-Whelan, A. M., Sipőcz, B. M., et al. 2018, AJ, 156, 123

Balbus, S. A., & Hawley, J. F. 1991, ApJ, 376, 214

Bally, J., Sutherland, R. S., Devine, D., & Johnstone, D. 1998, AJ, 116, 293

Banzatti, A., Pontoppidan, K. M., Bruderer, S., Muzerolle, J., & Meyer, M. R. 2015, ApJ, 798, L16

Baraffe, I., Chabrier, G., Allard, F., & Hauschildt, P. H. 1998, A&A, 337, 403

Bergin, E., Calvet, N., Sitko, M. L., et al. 2004, ApJ, 614, L133

Bertout, C., Basri, G., & Bouvier, J. 1988, ApJ, 330, 350

Bondi, H. 1952, MNRAS, 112, 195

Bouvier, J. 2007, in IAU Symposium, Vol. 243, Star-Disk Interaction in Young Stars, ed. J. Bouvier & I. Appenzeller, 231–240

Bouvier, J., Grankin, K., Ellerbroek, L. E., Bouy, H., & Barrado, D. 2013, A&A, 557, A77

Bouvier, J., Chelli, A., Allain, S., et al. 1999, A&A, 349, 619

Bouvier, J., Grankin, K. N., Alencar, S. H. P., et al. 2003, A&A, 409, 169

Bradshaw, S. J., & Hartigan, P. 2014, ApJ, 795, 79

Brandeker, A., Liseau, R., Artymowicz, P., & Jayawardhana, R. 2001, ApJ, 561, L199

Calvet, N., D'Alessio, P., Hartmann, L., et al. 2002, ApJ, 568, 1008

Calvet, N., & Gullbring, E. 1998, ApJ, 509, 802

Calvet, N., & Hartmann, L. 1992, ApJ, 386, 239

Calvet, N., Muzerolle, J., Briceño, C., et al. 2004, AJ, 128, 1294

Calvet, N., D'Alessio, P., Watson, D. M., et al. 2005, ApJ, 630, L185

Camenzind, M. 1990, Reviews in Modern Astronomy, 3, 234

Carnall, A. C. 2017, ArXiv e-prints

Chamberlin, T. C. 1901, ApJ, 14, 17

Chevalier, R. A., & Imamura, J. N. 1982, ApJ, 261, 543

Choi, J., Dotter, A., Conroy, C., et al. 2016, ApJ, 823, 102

Cleeves, L. I., Bergin, E. A., Öberg, K. I., et al. 2017, ApJ, 843, L3

Cody, A. M., & Hillenbrand, L. A. 2018, AJ, 156, 71

Cody, A. M., Hillenbrand, L. A., David, T. J., et al. 2017, ApJ, 836, 41

Cody, A. M., Stauffer, J., Baglin, A., et al. 2014, AJ, 147, 82

Costa, G., Orlando, S., Peres, G., Argiroffi, C., & Bonito, R. 2017, A&A, 597, A1

Courant, R., Friedrichs, K., & Lewy, H. 1928, Mathematische Annalen, 100, 32

Cranmer, S. R. 2004, American Journal of Physics, 72, 1397

Curran, R. L., Argiroffi, C., Sacco, G. G., et al. 2011, A&A, 526, A104

D'Alessio, P., Calvet, N., Hartmann, L., Franco-Hernández, R., & Servín, H. 2006, ApJ, 638, 314

Dashevsky, I., Sahu, K., & Smith, E. 2000, STIS Time-Tag Analysis Guide, Space Telescope STIS Instrument Science Report

Davies, C. L., Kraus, S., Harries, T. J., et al. 2020, ApJ, 897, 31

Del Zanna, L., Velli, M., & Londrillo, P. 1998, A&A, 330, L13

Donati, J. F., Jardine, M. M., Gregory, S. G., et al. 2007, MNRAS, 380, 1297

Donati, J. F., Skelly, M. B., Bouvier, J., et al. 2010a, MNRAS, 402, 1426

Donati, J.-F., Skelly, M. B., Bouvier, J., et al. 2010b, MNRAS, 409, 1347

Donati, J. F., Skelly, M. B., Bouvier, J., et al. 2010c, MNRAS, 409, 1347

Donati, J. F., Gregory, S. G., Montmerle, T., et al. 2011a, MNRAS, 417, 1747

Donati, J. F., Gregory, S. G., Alencar, S. H. P., et al. 2011b, MNRAS, 417, 472

Donati, J.-F., Gregory, S. G., Alencar, S. H. P., et al. 2011c, MNRAS, 417, 472

Donati, J. F., Bouvier, J., Alencar, S. H., et al. 2019, MNRAS, 483, L1

Doppmann, G. W., Greene, T. P., Covey, K. R., & Lada, C. J. 2005, AJ, 130, 1145

Dotter, A. 2016, ApJS, 222, 8

Draine, B. T. 1978, ApJS, 36, 595

Draine, B. T., & Lee, H. M. 1984, ApJ, 285, 89

Drake, J. J., Ratzlaff, P. W., Laming, J. M., & Raymond, J. 2009, ApJ, 703, 1224

Dupree, A. K., Brickhouse, N. S., Cranmer, S. R., et al. 2012, ApJ, 750, 73

Edwards, S., Hartigan, P., Ghandour, L., & Andrulis, C. 1994, AJ, 108, 1056

Espaillat, C., Calvet, N., D'Alessio, P., et al. 2007, ApJ, 670, L135

Espaillat, C., Furlan, E., D'Alessio, P., et al. 2011, ApJ, 728, 49

Espaillat, C., Muzerolle, J., Najita, J., et al. 2014, Protostars and Planets VI, 497

Espaillat, C. C., Macías, E., Hernández, J., & Robinson, C. 2019a, ApJ, 877, L34

Espaillat, C. C., Robinson, C., Grant, S., & Reynolds, M. 2019b, ApJ, 876, 121

Ferland, G. J., Chatzikos, M., Guzmán, F., et al. 2017, Revista Mexicana de Astronomía y Astrofísica, 53, 385

Fitzpatrick, E. L., & Massa, D. 1988, ApJ, 328, 734

—. 1990, ApJS, 72, 163

Fogel, J. K. J., Bethell, T. J., Bergin, E. A., Calvet, N., & Semenov, D. 2011, ApJ, 726, 29

Fonseca, N. N. J., Alencar, S. H. P., Bouvier, J., Favata, F., & Flaccomio, E. 2014, A&A, 567, A39

Foreman-Mackey, D., Hogg, D. W., Lang, D., & Goodman, J. 2013, PASP, 125, 306

France, K., Roueff, E., & Abgrall, H. 2017, ApJ, 844, 169

Fromang, S., & Papaloizou, J. 2006, A&A, 452, 751

Gaches, B. A. L., & Offner, S. S. R. 2018, ApJ, 861, 87

Gaia Collaboration, Prusti, T., de Bruijne, J. H. J., et al. 2016, A&A, 595, A1

Gaia Collaboration, Brown, A. G. A., Vallenari, A., et al. 2018, A&A, 616, A1

Gammie, C. F. 1996, ApJ, 457, 355

Garufi, A., Podio, L., Bacciotti, F., et al. 2019, A&A, 628, A68

Ghosh, P., & Lamb, F. K. 1979a, ApJ, 232, 259

—. 1979b, ApJ, 234, 296

Goodman, J., & Weare, J. 2010, Communications in Applied Mathematics and Computational Science, Vol. 5, No. 1, p. 65-80, 2010, 5, 65

Gorti, U., Dullemond, C. P., & Hollenbach, D. 2009, ApJ, 705, 1237

Gorti, U., & Hollenbach, D. 2009, ApJ, 690, 1539

Goudfrooij, P., & Christensen, J. A. 1998, STIS Near-IR Fringing. III. A Tutorial on the Use of the IRAF Tasks, Tech. rep.

Grankin, K. N., Melnikov, S. Y., Bouvier, J., Herbst, W., & Shevchenko, V. S. 2007, A&A, 461, 183

Green, J. C., Froning, C. S., Osterman, S., et al. 2012, ApJ, 744, 60

Greene, T. P., Wilking, B. A., Andre, P., Young, E. T., & Lada, C. J. 1994, ApJ, 434, 614

Gregory, S. G., Donati, J.-F., & Hussain, G. A. J. 2016, arXiv e-prints, arXiv:1609.00273

Gullbring, E., Hartmann, L., Briceño, C., & Calvet, N. 1998, ApJ, 492, 323

Günther, H. M., Lewandowska, N., Hundertmark, M. P. G., et al. 2010, A&A, 518, A54

Günther, H. M., Birnstiel, T., Huenemoerder, D. P., et al. 2018, AJ, 156, 56

Hartigan, P., Edwards, S., & Ghandour, L. 1995, ApJ, 452, 736

Hartigan, P., Hartmann, L., Kenyon, S., Hewett, R., & Stauffer, J. 1989, ApJS, 70, 899

Hartmann, L. 2008, Accretion Processes in Star Formation, 2nd edn., Cambridge Astrophysics (Cambridge University Press)

Hartmann, L., Calvet, N., Gullbring, E., & D'Alessio, P. 1998, ApJ, 495, 385

Hartmann, L., Herczeg, G., & Calvet, N. 2016, Annual Review of Astronomy and Astrophysics, 54, 135

Hartmann, L., Hewett, R., & Calvet, N. 1994, ApJ, 426, 669

Herbig, G. H. 1962, Advances in Astronomy and Astrophysics, 1, 47

Herbst, W., Herbst, D. K., Grossman, E. J., & Weinstein, D. 1994, AJ, 108, 1906

Herczeg, G. J., & Hillenbrand, L. A. 2014, ApJ, 786, 97

Hughes, A. M., Andrews, S. M., Espaillat, C., et al. 2009, ApJ, 698, 131

Ingleby, L., Espaillat, C., Calvet, N., et al. 2015, ApJ, 805, 149

Ingleby, L., Calvet, N., Bergin, E., et al. 2011, ApJ, 743, 105

Ingleby, L., Calvet, N., Herczeg, G., et al. 2013, ApJ, 767, 112

Jackman, J. A. G., Wheatley, P. J., Pugh, C. E., et al. 2019, MNRAS, 482, 5553

Jeans, J. H. 1917, MNRAS, 77, 186

Johns, C. M., & Basri, G. 1995a, AJ, 109, 2800

—. 1995b, ApJ, 449, 341

Johns-Krull, C. M. 2007, ApJ, 664, 975

Johns-Krull, C. M., & Valenti, J. A. 2000, in Astronomical Society of the Pacific Conference Series, Vol. 198, Stellar Clusters and Associations: Convection, Rotation, and Dynamos, ed. R. Pallavicini, G. Micela, & S. Sciortino, 371

Johnson, H. L., & Morgan, W. W. 1953, ApJ, 117, 313

Joy, A. H. 1945, ApJ, 102, 168

Kant, I. 1755, Allgemeine Naturgeschichte und Theorie des Himmels

Kenyon, S. J., & Hartmann, L. 1995, ApJS, 101, 117

Kenyon, S. J., Hartmann, L., Hewett, R., et al. 1994, AJ, 107, 2153

Kesseli, A. Y., Petkova, M. A., Wood, K., et al. 2016, ApJ, 828, 42

Kim, K. H., Watson, D. M., Manoj, P., et al. 2009, ApJ, 700, 1017

Koenigl, A. 1991, ApJ, 370, L39

Koldoba, A. V., Lovelace, R. V. E., Ustyugova, G. V., & Romanova, M. M. 2002, AJ, 123, 2019

Koldoba, A. V., Ustyugova, G. V., Romanova, M. M., & Lovelace, R. V. E. 2008, MNRAS, 388, 357

Kolmogorov, A. 1941, Akademiia Nauk SSSR Doklady, 30, 301

Kulkarni, A. K., & Romanova, M. M. 2008, MNRAS, 386, 673

Kurosawa, R., & Romanova, M. M. 2013, MNRAS, 431, 2673

Lada, C. J. 1987, in IAU Symposium, Vol. 115, Star Forming Regions, ed. M. Peimbert & J. Jugaku, 1

Landolt, A. U. 2013, AJ, 146, 131

Langer, S. H., Chanmugam, G., & Shaviv, G. 1981, ApJ, 245, L23

Laplace, P.-S. 1798, Exposition du système du monde, 2e édition (Duprat)

Li, J. 1996, ApJ, 456, 696

Lightkurve Collaboration, Cardoso, J. V. d. M., Hedges, C., et al. 2018, Lightkurve: Kepler and TESS time series analysis in Python, Astrophysics Source Code Library

Lima, G. H. R. A., Alencar, S. H. P., Calvet, N., Hartmann, L., & Muzerolle, J. 2010, A&A, 522, A104

Liu, H. B., Dunham, M. M., Pascucci, I., et al. 2018, A&A, 612, A54

Lomb, N. R. 1976, Ap&SS, 39, 447

Long, M., Romanova, M. M., Kulkarni, A. K., & Donati, J. F. 2011, MNRAS, 413, 1061

Luhman, K. L., & Steeghs, D. 2004, ApJ, 609, 917

Lyttleton, R. A. 1961, MNRAS, 122, 399

Macías, E., Espaillat, C. C., Ribas, Á., et al. 2018, ApJ, 865, 37

Manara, C. F., Fedele, D., Herczeg, G. J., & Teixeira, P. S. 2016, A&A, 585, A136

Manara, C. F., Frasca, A., Alcalá, J. M., et al. 2017, A&A, 605, A86

Manara, C. F., Testi, L., Natta, A., et al. 2014, A&A, 568, A18

Manoj, P., Kim, K. H., Furlan, E., et al. 2011, ApJS, 193, 11

Matsakos, T., Chièze, J. P., Stehlé, C., et al. 2013, A&A, 557, A69

McGinnis, P. T., Alencar, S. H. P., Guimarães, M. M., et al. 2015, A&A, 577, A11

Moulton, F. R. 1905, ApJ, 22, 165

Muzerolle, J., Calvet, N., Hartmann, L., & D'Alessio, P. 2003, ApJ, 597, L149

Muzerolle, J., Flaherty, K., Balog, Z., et al. 2009, ApJ, 704, L15

Nagel, E., & Bouvier, J. 2019, A&A, 625, A45

Natta, A., Testi, L., Alcalá, J. M., et al. 2014, A&A, 569, A5

Natta, A., Testi, L., Muzerolle, J., et al. 2004, A&A, 424, 603

Nomura, H., Aikawa, Y., Tsujimoto, M., Nakagawa, Y., & Millar, T. J. 2007, ApJ, 661, 334

O'dell, C. R., Wen, Z., & Hu, X. 1993, ApJ, 410, 696

Offner, S. S. R., Gaches, B. A. L., & Holdship, J. R. 2019, ApJ, 883, 121

Orlando, S., Bonito, R., Argiroffi, C., et al. 2013, A&A, 559, A127

Owen, J. E., & Adams, F. C. 2016, MNRAS, 456, 3053

Padovani, M., Marcowith, A., Hennebelle, P., & Ferrière, K. 2016, A&A, 590, A8

Parenago, P. P. 1950, Peremennye Zvezdy, 7, 169

Parker, E. N. 1958, ApJ, 128, 664

Percy, J. R., Grynko, S., Seneviratne, R., & Herbst, W. 2010, PASP, 122, 753

Persson, M. V. 2014

Prentice, A. J. R. 1978, Moon and Planets, 19, 341

Raymond, J. C., & Smith, B. W. 1977, ApJS, 35, 419

Ricker, G. R., Winn, J. N., Vanderspek, R., et al. 2015, Journal of Astronomical Telescopes, Instruments, and Systems, 1, 014003

Robinson, C. E., & Espaillat, C. C. 2019, ApJ, 874, 129

Robinson, C. E., Owen, J. E., Espaillat, C. C., & Adams, F. C. 2017, ApJ, 838, 100

Roccatagliata, V., Sacco, G. G., Franciosini, E., & Randich, S. 2018, A&A, 617, L4

Romanova, M. M., Kulkarni, A. K., & Lovelace, R. V. E. 2008, ApJ, 673, L171

Romanova, M. M., Ustyugova, G. V., Koldoba, A. V., & Lovelace, R. V. E. 2004, ApJ, 610, 920

—. 2011, MNRAS, 416, 416

—. 2012, MNRAS, 421, 63

—. 2013, MNRAS, 430, 699

Romanova, M. M., Ustyugova, G. V., Koldoba, A. V., Wick, J. V., & Lovelace, R. V. E. 2003, ApJ, 595, 1009

Rucinski, S. M. 1985, AJ, 90, 2321

Rucinski, S. M., Matthews, J. M., Kuschnig, R., et al. 2008, MNRAS, 391, 1913

Sacco, G. G., Argiroffi, C., Orlando, S., et al. 2008, A&A, 491, L17

Salyk, C., Herczeg, G. J., Brown, J. M., et al. 2013, ApJ, 769, 21

Savitzky, A., & Golay, M. J. E. 1964, Analytical Chemistry, 36, 1627

Scargle, J. D. 1982, ApJ, 263, 835

Schneider, P. C., Günther, H. M., Robrade, J., Schmitt, J. H. M. M., & Güdel, M. 2018, A&A, 618, A55

Schure, K. M., Kosenko, D., Kaastra, J. S., Keppens, R., & Vink, J. 2009, A&A, 508, 751

Shakura, N. I., & Sunyaev, R. A. 1973, A&A, 500, 33

Shu, F. H., Najita, J., Ruden, S. P., & Lizano, S. 1994, ApJ, 429, 797

Siwak, M., Rucinski, S. M., Matthews, J. M., et al. 2011a, MNRAS, 415, 1119

—. 2011b, MNRAS, 410, 2725

—. 2014, MNRAS, 444, 327

Siwak, M., Ogloza, W., Rucinski, S. M., et al. 2016, MNRAS, 456, 3972

Siwak, M., Ogloza, W., Moffat, A. F. J., et al. 2018, MNRAS, 478, 758

Skrutskie, M. F., Dutkevitch, D., Strom, S. E., et al. 1990, AJ, 99, 1187

Stassun, K. G., Mathieu, R. D., Vrba, F. J., Mazeh, T., & Henden, A. 2001, AJ, 121, 1003

Stauffer, J., Cody, A. M., Baglin, A., et al. 2014, AJ, 147, 83

Stauffer, J., Cody, A. M., McGinnis, P., et al. 2015, AJ, 149, 130

Stauffer, J., Cody, A. M., Rebull, L., et al. 2016, AJ, 151, 60

Stone, J. M., & Norman, M. L. 1992, ApJS, 80, 753

Strom, K. M., Strom, S. E., Edwards, S., Cabrit, S., & Skrutskie, M. F. 1989, AJ, 97, 1451

Swedenborg, E. 1734, Emanuelis Swedenborgii...Principia rerum naturalium, sive: Norvorum tentaminum phænomena mundi elementaris philosophice explicandi cum figuris æneis, Emanuelis Swedenborgii...Principia rerum naturalium, sive: Norvorum tentaminum phænomena mundi elementaris philosophice explicandi cum figuris æneis No. v. 1 (sumptibus Frideric Hekelii)

Thanathibodee, T., Calvet, N., Muzerolle, J., et al. 2019, ApJ, 884, 86

Thanathibodee, T., Calvet, N., Herczeg, G., et al. 2018, ApJ, 861, 73

Torres, G. 2007, ApJ, 671, L65

Tripathi, A., Andrews, S. M., Birnstiel, T., & Wilner, D. J. 2017, ApJ, 845, 44

Ureña, C., & Georgiev, I. 2018, Computer Graphics Forum, 37, 13

Ustyugova, G. V., Koldoba, A. V., Romanova, M. M., & Lovelace, R. V. E. 2006, ApJ, 646, 304

Valenti, J. A., Basri, G., & Johns, C. M. 1993, AJ, 106, 2024

Valenti, J. A., & Johns-Krull, C. M. 2004, Ap&SS, 292, 619

van Leer, B. 1977, Journal of Computational Physics, 23, 276

Velli, M. 1994, ApJ, 432, L55

Venuti, L., Bouvier, J., Irwin, J., et al. 2015, A&A, 581, A66

Venuti, L., Bouvier, J., Cody, A. M., et al. 2017, A&A, 599, A23

Watson, A. M., & Stapelfeldt, K. R. 2007, AJ, 133, 845

Webb, R. A., Zuckerman, B., Platais, I., et al. 1999, ApJ, 512, L63

Weingartner, J. C., & Draine, B. T. 2001, ApJ, 548, 296

Wendeborn, J., Espaillat, C. C., Macías, E., et al. 2020, ApJ, 897, 54

White, R. J., & Basri, G. 2003, ApJ, 582, 1109

Whittet, D. C. B., Shenoy, S. S., Clayton, G. C., & Gordon, K. D. 2004, ApJ, 602, 291

Woolfson, M. M. 1964, Proceedings of the Royal Society of London Series A, 282, 485

Yang, H., Herczeg, G. J., Linsky, J. L., et al. 2012, ApJ, 744, 121

Curriculum Vitae